Title

Macrophage membrane-coated nanoparticles for anti-inflammation treatment

Author

Duan, Yaou

Publication Date

2023

Peer reviewed|Thesis/dissertation

UNIVERSITY OF CALIFORNIA SAN DIEGO

Macrophage membrane-coated nanoparticles for anti-inflammation treatment

A Dissertation submitted in partial satisfaction of the requirements
for the degree Doctor of Philosophy

in

NanoEngineering

by

Yaou Duan

Committee in charge:

Professor Liangfang Zhang, Chair
Professor Shaochen Chen
Professor David Gonzalez
Professor Nisarg Shah

2023

The Dissertation of Yaou Duan is approved, and it is acceptable in quality and form for publication on microfilm and electronically.

University of California San Diego

2023

DEDICATION

This dissertation is dedicated to my parents, Yanwen Duan and Ying Huang, and especially to my beloved wife, Cheng Ma, for their unconditional love and support throughout my academic journey. I am forever grateful to haven them in my life.

TABLE OF CONTENTS

LIST OF FIGURES

LIST OF TABLES

ACKNOWLEDGEMENTS

First and foremost, I would like to thank my PhD advisor, Professor Liangfang Zhang for his guidance and support in every step throughout my graduate journey. Professor Liangfang Zhang kindly accepted my transfer at the third year of my PhD studies and offered me with incredible opportunities and systematic training to pursue cutting-edge nanomedicine research. His constant belief in me shaped me into the capable researcher I am today, and I will always strive to emulate his work ethic, kindness, and integrity.

I would also like to thank my mentor, Dr. Weiwei Gao, whom I owe much of my success. I started to work with Dr. Weiwei Gao when I transferred to Professor Liangfang Zhang's nanomedicine lab at the third graduate school year. During my transition, he patiently taught me knowledge in the field of nanomedicine and guided me through every step of my doctoral studies, while at the same time provided me with the independence to freely explore without repercussions. I'm grateful for his endless patience and the many opportunities he has given to me.

I owe particular thanks to my previous PhD advisor, Professor Kang Zhang. Although Professor Kang Zhang only guided me during my first 3 years of graduate journey, his solid ways of doing research and deep understanding of science not only helped me lay the foundation of my own research, but also showed me how to be a good scholar.

In addition, I'm thankful for my wonderful labmates, Dr. Ronnie Fang, Dr. Hua Gong, Dr. Xiangzhao Ai, Dr. Yao Jiang, Dr. Yue Zhang, Dr. Yijie Chen, Dr. Joon Ho Park, Dr. Maya Holay, Dr. Xiaoli Wei, Edward Zhang, Shuyan Wang, Nishta Krishnan, Zhidong Zhou, Luke Kubiatowicz, Animesh Mohapatra, Audrey Zhu, Anvita Komarla, and Jiyong Heo, for being such an incredibly supportive and inspiring group. It is a valuable experience to work alongside

all of you every day. I'm grateful that I was able to develop personal relationship with several labmates, Dr. Jia Zhuang, Dr. Jiarong Zhou, Dr. Qiangzhe Zhang, Dr. Lei Sun, Dr. Ilkoo Noh, Yiyan Yu, Yifei Peng, Nianfei Xian, Wei-ting Shen, Rui Wang, Mingxuan Kai, Dan Wang, and Zhongyuan Guo, who I can share laughter and struggles with. I owe special thanks to my previous labmates in my first three years of graduate journey, Xin Fu, Zhe Yang, and Zheng Zhong, who have supported and guided me from the very beginning, providing me with essential techniques and habits that served as the foundation for my success.

I would also like to extend gratitude to all my scientific collaborators who I had the pleasure of working with, and without whom, a lot of this research would not be possible: professor David Gonzalez and Dr. Lee Swanson for their expertise on inflammatory bowel diseases, professor Joseph Wang, Dr. Fangyu Zhang, Zhengxing Li, and Hao Luan for their expertise on micromotors and nanorobotics.

I would especially like to thank my parents, who have supported me both morally and financially throughout my doctoral education. I also thank my beloved wife, Cheng Ma, who has always been so encouraging and supportive of my intellectual pursuit. Her understanding and kindness gave me strength and inspiration throughout years of graduate school.

Last, but not least, I would like to offer my enduring gratitude to UC San Diego, where I have spent almost 7 years of my academic life, for being an inspirational and inclusive university. Especially, I'm thankful to Dana Jimenez, Ji Song, Eric Peng, and Graduate Division staff for providing heartwarming support during numerous difficult times throughout my graduate journey.

Chapter 1, in full, is a reprint of the material as it appears in *Advanced Materials*, 2022 by Shuyan Wang, Dan Wang, Yaou Duan, Zhidong Zhou, Weiwei Gao, and Liangfang Zhang. The dissertation author was a major contributor and co-author of this paper.

Chapter 2, in full, is a reprint of the material as it appears in *Nano Letter*, 2020 by Jia Zhuang, Yaou Duan, Qiangzhe Zhang, Weiwei Gao, Shulin Li, Ronnie H. Fang, and Liangfang Zhang. The dissertation author was the co-primary investigator and co-author of this paper.

The first portion of Chapter 3, in full, is a reprint of the material as it appears in *ACS Nano*, 2023 by Yaou Duan, Edward Zhang, Ronnie H. Fang, Weiwei Gao, and Liangfang Zhang. The dissertation author was the primary investigator and author of this paper.

The second portion of Chapter 3, in full, is a reprint of the material as it appears in *Science Robotics*, 2022 by Fangyu Zhang, Zhengxing Li, Yaou Duan, Amal Abbas, Rodolfo Mundaca-Uribe, Lu Yin, Hao Luan, Weiwei Gao, Ronnie H. Fang, Liangfang Zhang and Joseph Wang. The dissertation author was the co-primary investigator and co-author of this paper.

The third portion of Chapter 3, in full, is a reprint of the material as it appears in *Science Advances*, 2022 by Fangyu Zhang, Zhengxing Li, Yaou Duan, Hao Luan, Zhongyuan Guo, Chuanrui Chen, Mingyao Xu, Weiwei Gao, Ronnie H. Fang, Liangfang Zhang, and Joseph Wang. The dissertation author was the co-primary investigator and co-author of this paper.

Chapter 4, in full, is a reprint of the material as it appears in *Small*, 2023 by Yaou Duan, Jiarong Zhou, Zhidong Zhou, Edward Zhang, Yiyan Yu, Nishta Krishnan, Daniela Ailva-Ayala, Ronnie H. Fang, Anthony Griffiths, Weiwei Gao, and Liangfang Zhang. The dissertation author was the primary investigator and author of this paper.

VITA

2015 Bachelor of Science in BioEngineering, University of California Berkeley, USA

2018 Master of Science in NanoEngineering, University of California San Diego, USA

2023 Doctor of Philosophy in NanoEngineering, University of California San Diego, USA

PUBLICATIONS

1. **Duan Y**, Zhang Q, Zhou J, Zhou Z, Yu Y, Krishnan N, Silva-Ayala D, Zhang E, Fang R, Griffiths A, Gao W & Zhang L. (2023) Extending the in vivo residence time of macrophage membrane-coated nanoparticles through genetic modification. ***Small***, 2305551.

2. **Duan Y**, Zhang E, Fang R, Gao W & Zhang L. (2023) Capsulated cellular nanosponges for the treatment of experimental inflammatory bowel disease. ***ACS Nano***, 17, 15893-15904.

3. Krishnan N, Jiang Y, Zhou J, Mohapatra A, Peng F, **Duan Y**, Holay M, Chekuri S, Guo Z, Gao W, Fang R & Zhang L. (2023) A modular approach to enhancing cell membrane-coated nanoparticle functionality using genetic engineering. ***Nature Nanotechnology***, in press.

4. Ai X, Wang D, Noh I, **Duan Y**, Zhou Z, Mukundan N, Fang R, Gao W & Zhang L. (2023) Glycan-modified cellular nanosponges for enhanced neutralization of botulinum toxin. ***Biomaterials***, in press.

5. **Duan Y**, Wang D, Wang S, Zhou Z, Komarla A, Zhou J, Zhang Q, Ai X, Gao W & Zhang L. (2023) Cell membrane-coated nanoparticles and their biomedical applications. ***Encyclopedia of Nanomaterials***, 3, 519-542.

6. Zhang F†, Li Z†, **Duan Y**†, Luan H, Yin L, Guo Z, Chen C, Xu M, Gao W, Fang R & Zhang L. (2022) Extremophile-based biohybrid micromotors for biomedical operations in harsh environments. ***Science Advances***, 8, eade6455.

7. Holay M, Krishnan N, Zhou J, **Duan Y**, Guo Z, Gao W, Fang R & Zhang L. (2022) Single low-dose nanovaccine for long-term protection against anthrax toxins. ***Nano Letters***, 22, 9672-9678.

8. Wang D, Ai X, **Duan Y**, Xian N, Fang R, Gao W & Zhang L. (2022) Neuronal cellular nanosponges for effective detoxification of neurotoxins. ***ACS Nano***, 16, 19145-19154.

9. Zhang F, Zhuang J, Li Z, Gong H, Bsteban-Fernandez de Avila B, **Duan Y**, Zhang Q, Zhou J, Yin L, Karshalev E, Gao W, Nizet V, Fang R, Zhang L & Wang J. Nanoparticle-modified microrobots for in vivo antibiotic delivery to treat acute bacterial pneumonia. ***Nature Materials***, 21, 1324-1332.

10. Zhang F†, Li Z†, **Duan Y**†, Abbas A, Mundaca-Uribe R, Yin L, Luan H, Gao W, Fang R, Zhang L & Wang J. (2022) Gastrointestinal tract drug delivery using algae motors embedded in a degradable capsule. ***Science Robotics***, 7, eabo4160.

11. Wang S, Kai M, **Duan Y**, Zhou Z, Fang R, Gao W & Zhang L. (2022) Membrane cholesterol depletion enhances enzymatic activity of cell-membrane-coated metal-organic-framework nanoparticles. ***Angewandte Chemie International Edition***, 61, e202203115

12. Wang S, Wang D, **Duan Y**, Zhou Z, Gao W & Zhang L. (2022) Cellular nanosponges for biological neutralization. ***Advanced Materials***, 34, 2107719.

13. **Duan Y**, Wang S, Zhang Q, Gao W & Zhang L. (2021) Nanoparticle approaches against SARS-CoV-2 infection. ***Current Opinion in Solid State & Materials Science***, 25, 100964.

14. Ai X, Wang D, Honko A, **Duan Y**, Gavrish I, Fang R, Griffiths A, Gao W& Zhang L. (2021) Surface glycan modification of cellular nanosponges to promote SARS-CoV-2 inhibition. ***Journal of the American Chemical Society***, 143, 17615-17621.

15. Ai X, Wang S, **Duan Y**, Zhang Q, Chen M, Gao W & Zhang L. (2021) Emerging approaches to functionalizing cell membrane-coated nanoparticles. ***Biochemistry***, 60, 941-955.

16. Gong H, Zhang Q, Komarla A, Wang S, **Duan Y**, Zhou Z, Chen F, Fang R, Xu S, Gao W & Zhang L. (2021) Nanomaterial biointerfacing via mitochondrial membrane coating for targeted detoxification and molecular detection. ***Nano Letters***, 21, 2603-2609.

17. Ai X, **Duan Y**, Zhang Q, Sun D, Fang R, Liu-Bryan R, Gao W & Zhang L. (2021) Cartilage-targeting ultra-small lipid-polymer hybrid nanoparticles for the prevention of cartilage degradation. ***Bioengineering & Translational Medicine***, 6, e10187.

18. Wang S, **Duan Y**, Zhang Q, Komarla A, Gong H, Gao W & Zhang L. (2020) Drug targeting via platelet membrane-coated nanoparticles. ***Small Structures***, 1, 2000018.

19. Jiang Y, Krishnan N, Zhou J, Chekuri S, Wei X, Kroll A, Yu C, **Duan Y**, Gao W, Fang R & Zhang L. (2020) Engineered cell-membrane-coated nanoparticles directly present tumor antigens to promote anticancer immunity. ***Advanced Materials***, 32, 2001808.

20. Zhuang J†, **Duan Y**†, Zhang Q, Gao W, Li S, Fang R & Zhang L. (2020) Multimodal enzyme delivery and therapy enabled by cell membrane-coated metal-organic framework nanoparticles. ***Nano Letters***, 20, 4051-4058.

21. Liang H, Tsui B, Ni H, Valentim CCS, Baxter S, Liu G, Cai W, Kermany DS, Sun X, Chen J, He L, Zhu J, Tian P, Shao H, Zheng L, Hou R, Hewett S, Li G, Liang P, Zang X, Zhang Z, Pan L, Cai H, Ling R, Li S, Cui Y, Tang S, Ye H, Huang X, He W, Liang W, Zhang Q, Jiang J, Yu W, Gao J, Ou W, Deng Y, Hou Q, Wang B, Yao C, Liang Y, Zhang S, **Duan Y**, Zhang R, Gibson S, Zhang CL, Li O, Zhang ED, Karin G, Nguyen N, Wu X, Wen C, Xu J, Xu W, Wang B, Wang W, Li J, Pizzato B, Bao C, Xiang D, He W, He S, Zhou Y, Haw W, Goldbaum M, Tremoulet A, Hsu CN, Carter H, Zhu L, Zhang K & Xia H. (2019) Evaluation and accurate diagnoses of pediatric diseases using artificial intelligence. ***Nature Medicine***, 433-438.

22. Wang Z, **Duan Y** & Duan Y. (2018) Application of polydopamine in tumor targeted drug delivery system and its drug release behavior. ***J Control Release***, 56-74.

23. Fu X, Huu ANV, **Duan Y**, Kermany DS, Valentim CCS, Zhang R, Zhu J, Zhang CL, Sun X & Zhang K. (2018) Clinical applications of retinal gene therapies. ***Precision Clinical Medicine***, 1(1), 5-20.

24. Kermany DS, Goldbaum M, Cai W, Valentim CCS, Liang H, Baxter SL, McKeown A, Yang G, Wu X, Yan F, Dong J, Prasadha MK, Pei J, Ting MYL, Zhu J, Li C, Hewett S, Dong J, Ziyar I, Shi A, Zhang R, Zheng L, Hou R, Shi W, Fu X, **Duan Y**, Huu VAN, Wen C, Zhang ED, Zhang CL, Li O, Wang X, Singer MA, Sun X, Xu J, Tafreshi A, Lewis MA, Xia H & Zhang K. (2018) Identifying medical diagnosis and treatable diseases by image-based deep learning. ***Cell***, 172(5), 1122-1131.

25. Xu R, Wei W, Krawczyk M, Wang W, Luo H, Flagg K, Yi S, Shi W, Quan Q, Li K, Zheng L, Zhang H, Caughey B.A., Zhao Q, Hou J, Zhang R, Xu Y, Cai H, Li G, Hou R, Zhong Z, Lin D, Fu X, Zhu J, **Duan Y**, Yu M, Ying B, Zhang W, Wang J, Zhang E, Zhang C, Li O, Guo R, Carter H, Zhu J.K., Hao X & Zhang K. (2017) Circulating tumour DNA methylation markers for diagnosis and prognosis of hepatocellular carcinoma. ***Nature Materials***, 16(11), 1155-1161.

26. Zhu J, Ming C, Fu X, **Duan Y**, Hoang DA, Rutgard J, Zhang R, Wang W, Hou R, Zhang D, Zhang E, Zhang C, Hao X, Xiong W & Zhang K. (2017) Gene and mutation independent therapy via CRISPR-Cas9 mediated cellular reprogramming in rod photoreceptors. ***Cell Research***, 27, 830-833.

27. Li K, **Duan Y**, Ying MYL, Ou Z, Liu L, Zhang K & Fu X. (2017) Future Science Prize goes to non-invasive prenatal testing. ***Sci China Life Sci***, 60(4), 429-431.

28. Shaw PX, Zhang L, Zhang M, Du H, Zhao L, Lee C, Grob S, Lim SL, Hughes G, Lee J, Bedell M, Nelson MH, Lu F, Krupa M, Luo J, Ouyang H, Tu Z, Su Z, Zhu J, Wei X, Feng Z, **Duan Y**, Yang Z, Ferreyra H, Bartsch DU, Kozak I, Zhang L, Lin F, Sun H, Feng H & Zhang K. (2012) Complement factor H genotypes impact risk of age-related macular degeneration by interaction with oxidized phospholipids. ***Proceedings of the National Academy of Sciences***, 109(34), 13757-13762.

29. Lee J, Zeng J, Hughes G, Chen Y, Grob S, Zhao L, Lee C, Krupa M, Quach J, Luo J, Zeng J, Wei X, Zhang X, Zhu J, **Duan Y**, Ferreyra H, Goldbaum M, Haw W, Shaw PX, Tang L &

Zhang K. (2013). Association of LIPC and advanced age-related macular degeneration. ***Eye***, 27, 265-271.

30. Helgason H, Sulem P, Duvvari M, Luo H, Thorleifsson G, Stefansson H, Jonsdottir I, Masson G, Gudbjartsson D, Walters G, Magnusson O, Kong A, Rafnar T, Kiemeney L, Schoenmaker-Koller F, Zhao L, Boon C, Song Y, Fauser S, Pei M, Ristau T, Patel S, Liakopoulos S, P H van de Ven J, Hoyng C, Ferreyra H, **Duan Y**, Bernstein P, Geirsdottir A, Helgadottir G, Stefansson E, den Hollander A, Zhang K, Jonasson F, Sigurdsson H, Thorsteinsdottir U& Stefansson K. (2013) A rare nonsynonymous sequence variant in C3 is associated with high risk of age-related macular degeneration. **Nature Genetics**, 45(11): 1371-1374.

ABSTRACT OF THE DISSERTATION

Macrophage membrane-coated nanoparticles for anti-inflammation treatment

by

Yaou Duan

Doctor of Philosophy in NanoEngineering

University of California San Diego, 2023

Professor Liangfang Zhang, Chair

Cell membrane coating technology is a technique that faithfully replicate the unique biomimicry and biointerfacing properties of natural cell membranes onto synthetic nanoparticulate cores, providing them with additional biological functionalities to create new therapeutic modalities. One major application of cell membrane coating technology is biodetoxification-based therapy, in which cell membrane-coated nanoparticles (CMNP), mimicking susceptible parent cells, are used to capture and retain biotoxins that would

otherwise target parent cells. By serving as decoys to intercept the interaction of harmful molecules and infectious pathogens, CMNPs allow a function-driven and broad-spectrum biodetoxification strategy without the prior knowledge of the threat. These properties of CMNPs are especially valuable in designing novel and efficacious therapy to ameliorate "cytokine storms" in inflammatory diseases, which involves orchestra of multiple cytokines and complex signaling pathways, posing significant challenges for conventional treatment.

Herein, we discuss the development and engineering of a new generation of CMNPs, macrophage membrane-coated nanoparticle (MΦ-NP), for inflammation management via biodetoxification. Firstly, recent development of cell membrane-coated nanoparticles in neutralizing pathogenic biological molecules will be discussed, highlighting their promising roles played in inflammation management. The second portion of this dissertation will demonstrate the development of a local delivery formulation of macrophage membrane-coated metal-organic framework (MΦ-MOF) as a potential enzyme delivery vehicle for therapeutic treatment of gout. The MOF core can efficiently encapsulate and protect the bioactivity of the loaded enzyme, while macrophage cell membrane coatings provide additional cytokine neutralization functionalities that synergize with the encapsulated enzyme to target disease pathology from multiple dimensions. The third section of this dissertation will cover the development of MΦ-NP in oral formulation as an anti-inflammatory strategy for the management of inflammatory bowel diseases (IBD) via their natural cytokine neutralization capability. Along the lines of IBD, the third section will also explore future directions to enhance oral delivery efficacy of MΦ-NP, including the use of encapsulated *C. reinhardtii* and acidophilic *C. pitschmannii* as biomotors. Finally, we will focus on the improvement of current systemic delivery formulation of MΦ-NP through genetic engineering for detoxification.

Macrophages are genetically engineered to express proline-alanine-serine (PAS) peptide chains, which provide additional protection against opsonization and phagocytosis, resulting in prolonged in vivo residence times. The prolonged residence times contribute to enhanced nanoparticle efficacy in inhibiting inflammatory cytokines in mouse models of lipopolysaccharide-induced lung injury and sublethal endotoxemia, respectively.

This dissertation will serve as an example for rational design and engineering of MΦ-NP for therapeutic treatments of various inflammatory disorders. By harnessing the versatile engineering flexibility, this MΦ-NP holds promising potential to become the next generation drug-free anti-inflammatory nanomedicine, which can be easily developed in a plethora of novel formulations to address other unmet clinical needs in inflammatory diseases.

Chapter 1

Cellular Nanosponges for Biological Neutralization

1.1. Introduction

Threats from harmful molecules, either endogenous or exogenous, pose significant health problems. For example, poisoning by toxic chemicals, including drugs, nerve agents, and animal venom, leads to serious and sometimes deadly consequences [1-3]. Meanwhile, excessive production of endogenous molecules, including inflammatory cytokines, digestive enzymes, and auto-antibodies, underlie some of the most critical inflammatory disorders, such as sepsis, rheumatoid arthritis, and immune hypersensitivities [4-6]. The threats can also come from infectious pathogens. For example, in bacterial infections, pathogenic bacteria secrete toxins to manipulate host cell functions favoring their colonization and reproduction [7, 8]. In viral infections, viral particles attach themselves to the host cell membrane for invasion, hijacking host cell machinery to replicate [9, 10]. In order to counteract these threats, biological neutralization represents a general strategy that deploys therapeutic agents to bind with the harmful molecules or pathogens, block their bioactivity, and thus prevent them from causing the diseases [11-14]. Therapeutic platforms, such as antisera, monoclonal antibodies, and small-molecule inhibitors, have been widely used for neutralization [15-19]. Despite their pivotal roles in treating numerous diseases, these platforms sometimes show inadequate efficacy. The reason is attributable, in part, to their design of focusing on the causative molecules or pathogens, which leads to narrow-spectrum neutralization solutions. For example, some antidotes are highly effective in treating poisoning, but most deadly toxicants do not have specific pharmacological antidotes [12]. In inflammatory disorders, existing agents neutralizing one or a few cytokines are insufficient to halt or reverse disease progression due to the multiplicity of cytokine targets and signaling network redundancy [20]. In bacterial infections, bacterial toxins display enormous diversity of molecular structures and epitopic targets [21, 22]. In contrast, current neutralizing agents target specific toxin

structures and require customized design for different toxins, making their wide applications impractical. Similarly, viral neutralization focuses heavily on specific viral species and therefore cannot be deployed across different species or families of viruses or may be rendered ineffective as the virus accumulates mutations and escapes treatments [23]. Overall, these challenges underscore the need for innovative biological neutralization approaches.

Recently, the emergency of cell-membrane-coated nanoparticles offers a unique solution to address the challenges facing current biological neutralization technologies [24]. These nanoparticles are made by first deriving natural cell membranes and then coating them onto synthetic cores. Cell-membrane coated nanoparticles were first developed by coating red blood cell (RBC) membranes onto polymeric cores [25]. The goal was to replicate the long-circulation feature of natural RBCs desirable for drug delivery. However, the success of these biomimetic nanoparticles soon sparked the idea of using them as decoys of susceptible RBCs for biological neutralization [26]. All pathological agents must interact with host cells for their bioactivity. Therefore, researchers can design cell decoys to intercept these harmful agents and divert them away from the intended cellular targets without knowing the molecular structure of the agents. A shift of focus from the causative agents to the host cells makes function-driven and broad-spectrum neutralization solutions possible. Shortly after developing RBC-membrane coated nanoparticles, they were successfully applied to neutralize bacterial toxins, pathological antibodies, and chemical toxicants [27-29]. As membranes of other cell types were successfully coated onto synthetic materials, the cell decoy approach has been applied to neutralize other pathological agents such as inflammatory cytokines and viruses, with favorable outcomes [30-32]. This new class of cell-membrane-coated nanoparticles was named “cellular nanosponges” to emphasize their working mechanisms of “soaking up” harmful toxins or pathogens for neutralization.

In this article, we review recent progress of the development and application of cellular nanosponges for neutralization against numerous pathological agents, including bacterial toxins, chemical toxicants, inflammatory cytokines, pathological antibodies, and viruses (**Figure 1.1**). Under each category, we organize the review based on source cell types used to make the cellular nanosponges and highlight the relationship between nanosponge design and the corresponding biological neutralization functions. Overall, this article demonstrates cellular nanosponges as a nanomedicine platform that can effectively leverage the diverse functions of cell membranes for biological neutralization towards the treatment of various medical problems.

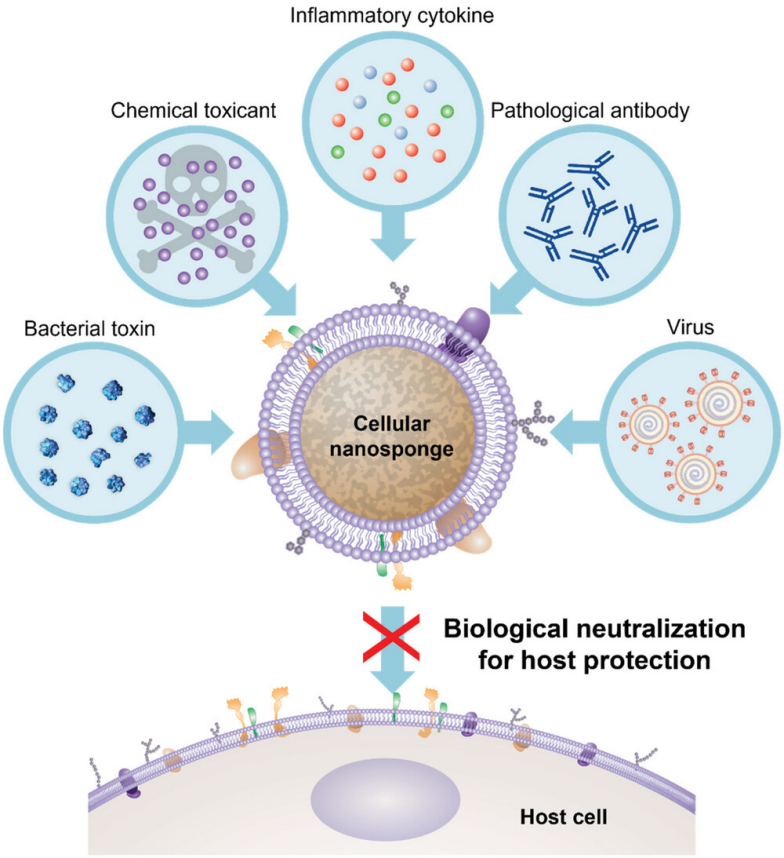

Figure 1.1 A schematic summary of using cellular nanosponges for biological neutralization. Cellular nanosponges are made by coating synthetic nanoparticle cores with the plasma membranes of natural cells. They act as host cell decoys, intercept harmful molecules or infectious pathogens, and divert them away from the intended cellular targets. Cellular nanosponges have been applied to neutralize various pathological agents, including bacterial toxins, chemical toxicants, inflammatory cytokines, pathological antibodies, and viruses.

1.2 Neutralizing Bacterial Toxins

Neutralizing bacterial toxins can suppress bacterial growth without direct disruption of their cycles [33, 34]. Instead, this approach facilitates the host immune system for effective bacterial clearance [35]. Additionally, neutralizing bacterial toxins may create synergy with other compounds for more effective antimicrobial activities [36]. These features make toxin neutralization unlikely to elicit drug resistance as compared to traditional antibiotics. However, conventional approaches for toxin neutralization rely primarily on the toxin structure for design cues [37]. Therefore, they are limited by the substantial diversity of the toxins. In contrast, cellular nanosponges harness the functional similarity among the toxins for neutralization, regardless of toxins' molecular structures or epitopic targets. As a result, the nanosponge has led to function-driver, broad-spectrum, and membrane type-specific toxin neutralization.

Pore-forming toxins (PFTs) are common bacterial toxins specializing in perforating the plasma membranes of the host cells. By interacting with the immune cells, PFTs promote bacterial dissemination and colonization [38]. Therefore, disarming PFTs has been a potential strategy to reduce bacterial infection and halt resistance development [39]. In this regard, RBC-membrane-coated nanosponges (denoted "RBC-NS") were developed to absorb various PFTs. For example, RBC membrane was coated onto poly(lactic-co-glycolic acid) (PLGA) nanoparticles to neutralize alpha-hemolysin (α-toxin) of methicillin-resistant Staphylococcus aureus (MRSA) [26]. In vitro, these nanoparticles decreased RBC hemolysis by absorbing α-toxins. When α-toxin was mixed with RBC-NS and injected subcutaneously into mice, the toxin no longer induced skin lesions. When challenged with a lethal dose of α-toxin intravenously, mice injected with RBC-NS via the same route before the toxin injection showed the highest survival rate than the groups injected with

poly(ethylene glycol) (PEG)-functionalized PLGA nanoparticles (denoted "PEG-NPs") or RBC membrane vesicles.

Following the initial development, RBC-NS were also used to neutralize other PFTs such as Streptolysin O [40, 41], hemotoxin from Candida albicans [42], and cytolysin from Enterococcus faecalis [43]. As an anti-virulence platform, RBC-NS were also applied to neutralize whole secreted proteins (wSP) of bacteria [44, 45]. In this study, RBC-NS inhibited wSP-induced cytotoxicity on human umbilical vein endothelial cells and hemolysis in vitro (**Figure 1.2**) [44]. When the mice were challenged with a lethal dose of wSP, the RBC-NS increased the mouse survival rate. RBC-NS also protected organs from toxin damages when the mice were challenged with a sublethal dose of wSP pre-incubated with the nanosponges.

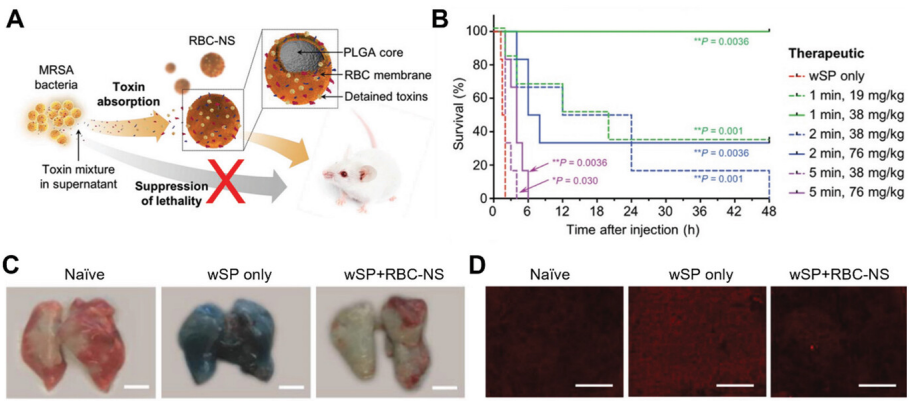

Figure 1.2 RBC-membrane-coated nanosponges (RBC-NS) neutralize hemolytic toxins in MRSA culture for the treatment of MRSA infection. A) Schematic illustration of using RBC-NS to treat MRSA toxin-induced toxic shock in mice. RBC-NS are constructed by wrapping PLGA polymeric cores with natural RBC membrane. They absorb and detain hemolytic toxins in MRSA culture and therefore protect mice from toxic shock induced by the toxins. B) Survival rates of mice over 24 h in a therapeutic regimen with RBC-NS, where mice are first injected with wSP (1.4 mL kg−1, LD100) followed by injections of RBC-NS at different intervals and dosages (n = 6 per cohort). C) Lung photographs from mice injected with sucrose (10%, naïve), wSP only (0.7 mL kg−1), and wSP (0.7 mL kg−1) preincubated with RBC-NS, followed by an injection of Evans Blue dye in 24 h. Mice are euthanized 10 min after the dye injection. The lungs are perfused thoroughly before the photographs are taken. Photographs are representative of three mice. Scale bars = 5 mm. D) Fluorescence-stained spleen sections showed lower NF-kB expression in mice injected with wSP preincubated with RBC-NS than that in mice injected with wSP alone. Each image is representative of three examined sections. Scale bars = 100 μm. A–D) Reproduced with permission [44]. Copyright 2019, Wiley-VCH.

Recently, new designs of RBC-based nanosponges were developed for toxin neutralization. For example, RBC-NS were embedded into polyacrylate hydrogels, resulting in a nanosponge-hydrogel hybrid formulation for bacterial detoxification (denoted "NS-gel") [46]. While the nanosponges absorbed PFTs, the hydrogel retained nanosponges at the infection sites. The synergy of such a combination enhanced localized toxin neutralization for better anti-virulence efficacy. In a subcutaneous MRSA infection mouse model, the skin lesion development of mice treated with NS-gel was slower than those treated with hydrogel without embedded nanosponges. Meanwhile, RBC membrane was coated onto other nanoparticle cores, such as hydrogel nanoparticles [47], iron oxide [45], and anisotropic polymeric nanoparticles [48], for toxin neutralization. In the above examples, PLGA cores stand out for their high encapsulation efficiency of hydrophobic payloads and controlled-release properties, and hydrogel cores are especially suited for encapsulating hydrophilic drugs and delivering them in response to environmental cues. Meanwhile, iron oxide cores confer photothermal lysis upon external laser irradiation, and anisotropic polymeric cores resist cellular uptake and reduce clearance from the blood circulation. In addition, RBC membrane was also coated onto nanomotors made from gold nanowires for guided toxin neutralization [49]. Under ultrasound propulsion, the RBC-motor nanosponges were more effective for PFT neutralization than uncoated motors or regular RBC-NS without active propulsion enabled by the motors.

Besides RBCs, platelets are also an important target of bacterial toxins such as Pertussis toxin and Shiga toxin [50]. Therefore, platelet-membrane-coated nanosponges have also been developed for toxin neutralization. For example, Shiga toxin recognizes specific glycosphingolipid receptors on platelet membrane and thus activates platelet cells, causing thrombocytopenia and microthrombus formation. Platelet-membrane-coated magnetic helical Pd/Ni/Au nanomotor

(denoted "PL-motors") was developed to neutralize Shiga toxin [51]. When guided with a magnetic field, the PL-motors were more effective for Shiga toxin binding and neutralization than the uncoated motors. When challenged with Shiga toxin, cells treated with PL-motors in a magnetic field showed higher viability than those treated with uncoated nanomotor or platelet vesicle.

Bacterial membranes were also used as coating materials to make nanosponges that mimicked source bacteria and competed with them for binding to the host cells or tissues. For example, outer membrane vesicles (OMVs) of Helicobacter pylori were collected and coated onto PLGA nanoparticles (denoted "OM-NPs") for inhibiting bacterial adhesion (**Figure 1.3**) [52]. In the study, the OM-NPs bound with the human gastric epithelial cells (AGS cells) in a dose-dependent manner. By competing with H. pylori bacteria for binding, these OMV-based nanosponges inhibited H. pylori adhesion to the AGS cells. Even after the bacteria bound with the cells, the nanosponges were able to detach them from the AGS cells. When tested on the stomach tissue of C57BL/6 mice, these nanosponges inhibited H. pylori attachment in vivo.

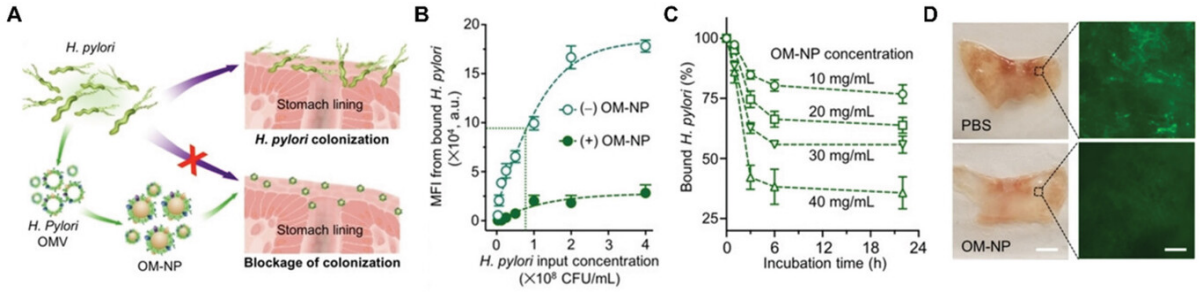

Figure 1.3 Neutralization of bacterial adhesion by bacterial outer membrane coated nanoparticles (OM-NPs). A) Schematic illustration of using OM-NPs to neutralize H. pylori adhesion and inhibit bacterial colonization on the stomach lining. B) Treatment with OM-NPs reduced H. pylori adhesion on AGS cells. C) The remaining H. pylori bacteria on AGS cells after incubation with OM-NPs decreased with the increase of the concentration of OM-NPs. D) OM-NPs reduced H. pylori colonization on the mouse stomach tissue. Mouse stomach tissue was incubated with PBS or OM-NPs before H. pylori bacteria were added. Scale bar = 5 mm. A–D) Reproduced with permission [52]. Copyright 2019, Wiley-VCH.

Table 1.1 summarizes examples of using nanosponges to neutralize bacterial toxins. The nanosponge-toxin complex formation in the neutralization process has also inspired other promising applications. For example, some complexes were developed as "nanotoxoids" to elicit meaningful and safe antibacterial immunity [53]. Moreover, the nanosponge-enabled toxin capture in combination with mass spectrometry has led to a novel "biomimetic virulomics" strategy for identifying bacterial virulence factors with cell-type specificity [54, 55]. Together, these emerging applications indicate that bacterial toxin neutralization by cellular nanosponges plays a significant role in developing nanomedicine against infectious diseases.

Table 1.1 Summary of using cellular nanosponges to neutralize bacterial toxins.

Nanosponge platform [a)]	Bacterial toxins	Mechanisms
RBC-NS	• Alpha-hemolysin [26] • Streptolysin O [40, 41] • Hemotoxin [42] • Cytolysin [43] • Whole secreted proteins of bacteria [44, 45]	• Specific binding of bacterial toxins with toxin receptors on RBC membrane
NS-gel	• *Staphylococcus aureus* secreted toxins [46]	• Specific binding of bacterial toxins with toxin receptors on RBC membrane and hydrogel retaining nanosponges at infectious sites
Motor sponge	• Melittin [49]	• Active motion of the motor increasing toxin adsorption and neutralization efficiency
PL-motor	• Shiga toxin [51]	• Specific binding of Shiga toxin to receptor on platelet membrane and autonomous motion increasing toxin binding and neuralization efficiency
OM-NP	• Adhesion molecules on *Helicobacter pylori* [52]	• Bacterial membrane nanosponges competing with bacteria for binding sites on host cells and tissues

[a)] RBC-NS: red blood cell (RBC) membrane-coated nanosponge; NS-gel: nanosponge-hydrogel hybrid; Motor sponge: RBC-membrane-coated gold nanomotor; PL-motor: platelet-membrane-coated magnetic helical nanomotor; OM-NP: bacteria outer membrane vesicle-coated nanoparticle.

1.3 Neutralizing Chemical Toxicants

Chemical toxicants pose a significant threat to public health. For example, organophosphorus compounds (OPs), commonly found in insecticides and nerve agents, are one of the leading causes of poisoning worldwide [56]. OPs bind with acetylcholinesterase (AChE) expressed on neuromuscular junctions, cholinergic brain synapses, and RBCs. Such binding irreversibly deactivates AChE, leading to the accumulation of acetylcholine (ACh). ACh accumulation disrupts cholinergic synaptic transmissions and induces severe neurotoxicity and

even fatality [57]. Inspired by the presence of AChE on the RBC membrane, researchers have developed cell-mimicking nanoparticles cloaked with the RBC membrane for neutralizing OPs. With membrane-bound AChE, these nanoparticles act as decoys for OP binding, thereby diverting OPs away from endogenous AChE targets and mitigating OP poisoning.

In one study, RBC-membrane-coated PLGA nanoparticles (denoted "RBC-NPs" in the study, which have a similar composition as "RBC-NS" above) were tested for OP neutralization (**Figure 1.4**) [29]. The resulting RBC-NPs retained membrane-bound AChE and its enzymatic activity. These RBC-NPs absorbed dichlorvos (DDVP), a model OP, in a dose-dependent manner. They also reduced the loss of AChE activity on RBC ghosts upon exposure to OP. RBC-NPs absorbed OP and protected AChE activity more effectively than PEG-coated PLGA nanoparticles, indicating the key role of RBC membrane coating in OP neutralization. In mice intravenously or orally challenged with lethal doses of DDVP, RBC-NPs improved the survival of mice and preserved the endogenous AChE activity. This study validated the feasibility of using cell-membrane-coated nanoparticles as decoys for OP neutralization.

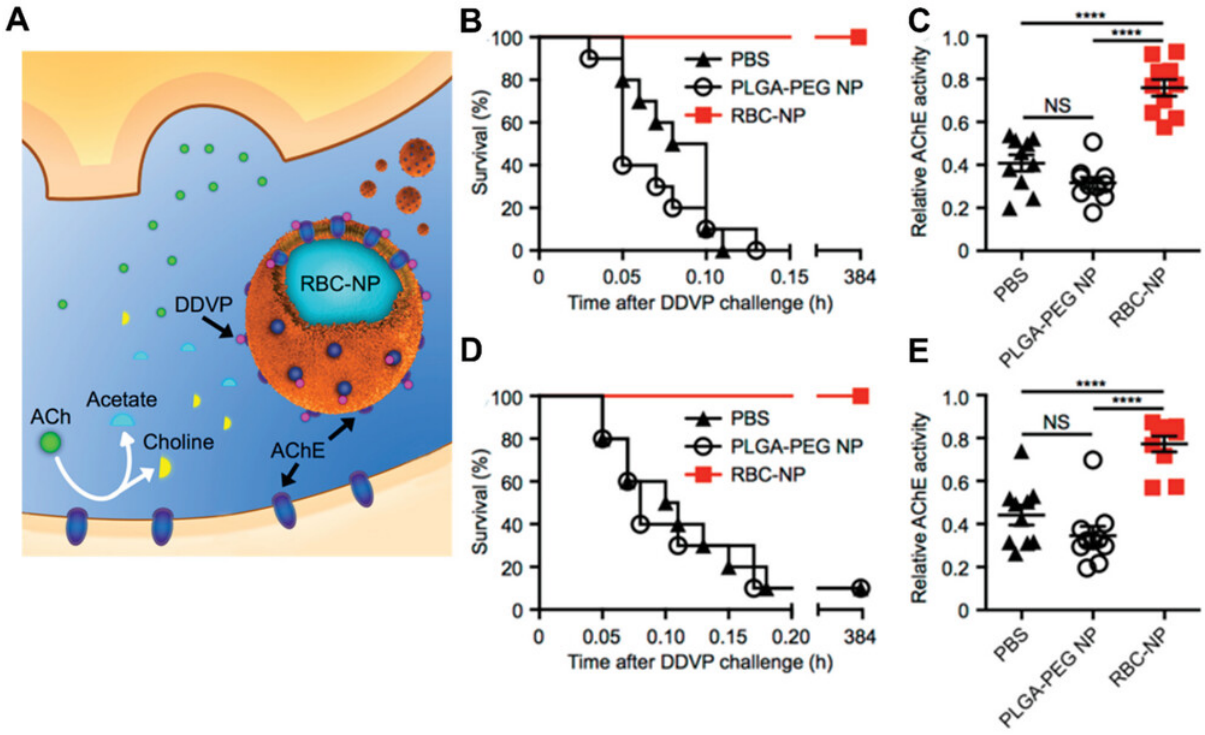

Figure 1.4 RBC-membrane-coated PLGA nanoparticles (RBC-NPs) for neutralizing DDVP, an organophosphorus compound. A) Schematic illustration of DDVP neutralization by RBC-NPs. With membrane-bound AChE receptors, RBC-NPs bind to DDVP molecules in the circulation, thereby preserving the ability of endogenous AChE at the synapse to break down ACh. B) The survival curves and C) relative RBC AChE activity of mice receiving intravenous injection of 200 mg kg−1 RBC-NPs, PEG-coated PLGA nanoparticles (PLGA-PEG NPs) or phosphate-buffered saline (PBS), immediately after intravenous injection of DDVP at a lethal dose (10 mg kg−1). D) The survival curves and E) relative RBC AChE activity of mice receiving intravenous injection of 200 mg kg−1 RBC-NPs, PLGA-PEG NPs or PBS, immediately after oral administration of DDVP at a lethal dose (150 mg kg−1). In all data sets, n = 10. The error bars represent the standard error of the mean. The statistical analysis is performed using the two-tailed t-test (****p ⩽ 0.0001, NS = no statistical significance). A–E) Reproduced with permission [29]. Copyright 2015, American Chemical Society.

In another study, RBC membrane was coated onto olive oil nanodroplets to form oil nanosponges (Oil-NS) for OP neutralization [58]. In this design, the RBC membrane coating provided AChE receptors for specific OP binding while the oil core provided a reservoir for non-specific OP absorption. Such dual-modal detoxification mechanism enhanced the overall detoxification capacity of the nanosponges. Oil-NS were shown to absorb three different OPs, including paraoxon (POX), diisopropyl fluorophosphate (DFP), and DDVP, in a dose-dependent

manner. They also protected the endogenous AChE on RBC ghosts against POX. Compared with RBC-NPs or uncoated oil droplets, Oil-NS performed much better at OP absorption and AChE protection, demonstrating the advantages of dual-modal detoxification. In mice subcutaneously challenged with a lethal dose of POX, Oil-NS mitigated the intoxication symptoms, reduced the loss in the endogenous AChE activity, and improved the survival of mice. Besides a treatment regimen, Oil-NS also showed prophylactic efficacy against POX. Pre-treating mice with Oil-NS before POX exposure improved the survival of mice and retained the endogenous AChE activity. These results show Oil-NS as a promising prophylactic and therapeutic platform against OPs.

In addition to neutralizing OPs, cell-membrane-coated nanoparticles have also been used to absorb small molecule chemotherapeutics to reduce chemotherapy-associated toxicity. For example, RBC-NPs were used to absorb doxorubicin (DOX), a commonly used chemotherapeutic drug (**Figure 1.5**) [59]. In this design, DOX absorption by RBC-NPs was primarily driven by the electrostatic interactions between the negatively charged membrane and cationic DOX. Following initial absorption onto the membrane, DOX diffused into the negatively charged PLGA core, which served as a reservoir for DOX. RBC-NPs maintained their surface charge after DOX absorption due to this reservoir effect and remained well-dispersed in buffers. By contrast, uncoated PLGA nanoparticles aggregated after DOX absorption due to drastic changes in the surface charge. In the study, RBC-NPs were shown to protect B16-F10 melanoma cells from DOX cytotoxicity and improve cell viability. Recently, outer mitochondrial membrane (OMM) from mouse livers was coated onto PLGA nanoparticle cores [60]. These nanoparticles (denoted "OMM-NPs") bound with ABT-263, a B-cell lymphoma protein 2 (Bcl-2) inhibitor that targets the OMM. As a result, OMM-NPs effectively protected the cells from ABT-263-induced cell death and apoptosis in vitro. They also attenuated ABT-263-induced thrombocytopenia in vivo.

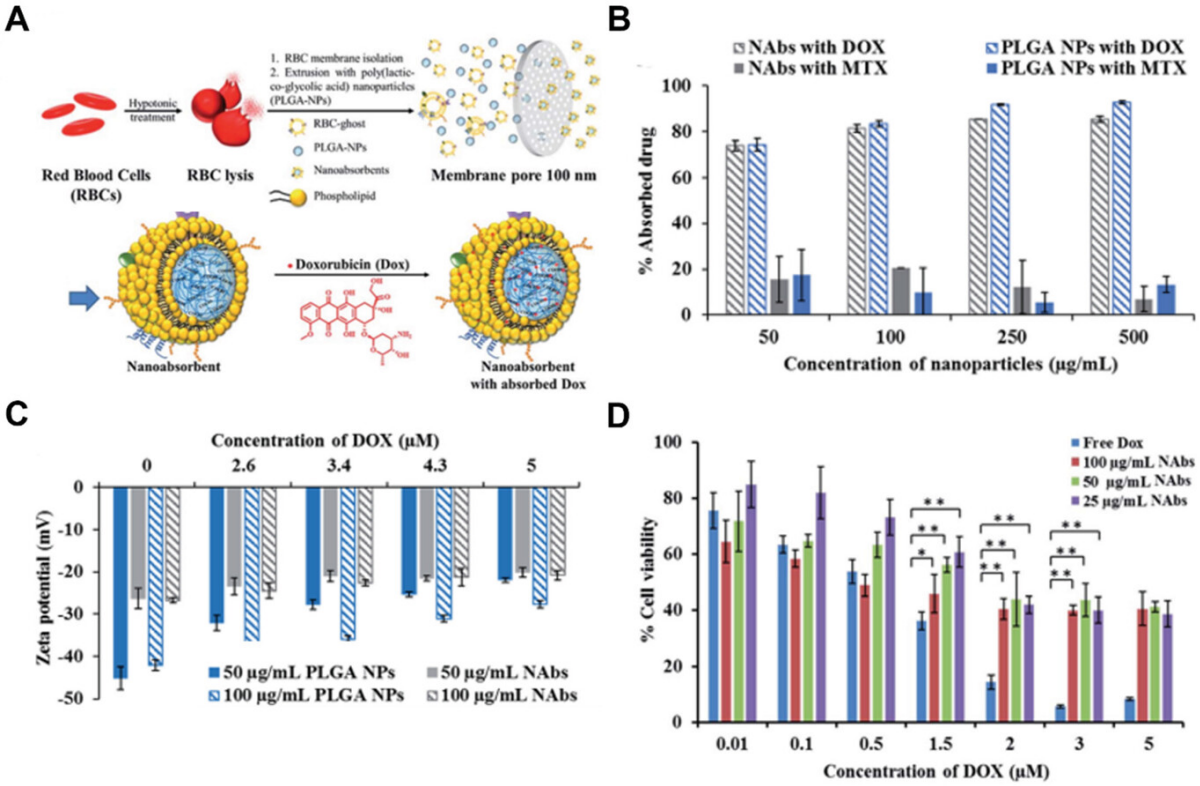

Figure 1.5 RBC-membrane-coated nanoabsorbents (NAbs) for neutralizing DOX. A) Schematic illustration of NAb fabrication and DOX absorption by NAbs. B) Percentage of absorption of cationic DOX or anionic methotrexate (MTX) by NAbs or uncoated PLGA nanoparticles (PLGA NPs), respectively (n = 3, mean ± standard deviation). C) Changes in the surface charge of NAbs or PLGA NPs when incubated with DOX at varying concentrations (n = 3, mean ± standard deviation). D) Viability of B16-F10 melanoma cells when exposed to DOX at varying concentrations in the absence or presence of NAbs (n = 6, mean ± standard deviation). The statistical analysis is performed using the Student's t-test (*$p < 0.01$, **$p < 0.001$). A–D) Reproduced with permission.[59] Copyright 2016, Royal Society of Chemistry.

Table 1.2 summarizes examples of using cellular nanosponges to neutralize chemical toxicants. Overall, these studies have demonstrated RBC-membrane-coated nanoparticles as a versatile detoxification platform for neutralizing chemical toxicants such as OPs and chemotherapeutic compounds. Apart from the RBC membrane, nanoparticles cloaked with other cell membranes can also be used to neutralize chemical toxicants, provided that the membranes possess surface receptors for toxicant recognition. The membranes can be further modified to incorporate more toxicant-specific receptors through lipid insertion, metabolic or genetic engineering for a higher detoxification capacity [61]. Additionally, encapsulating cargo molecules

such as enzymatic scavengers that specifically degrade toxicants can boost the detoxification efficiency [62, 63]. With such engineering flexibility, cell-membrane-coated nanoparticles are expected to make a significant impact in neutralizing chemical toxicants.

Table 1.2 Summary of using cellular nanosponges to neutralize chemical toxicants.

Nanosponge platform [a)]	Chemical toxicant [b)]	Mechanism [c)]
RBC-NP	• DDVP [29] • DOX [59]	• Specific binding of DDVP with AChE receptor on RBC membrane • Electrostatic binding of cationic DOX with negatively charged RBC membrane
Oil-NS	• DDVP [58] • POX [58] • DFP [58]	• Specific binding of toxicants with AChE receptor of RBC membrane and non-specific absorption of toxicants by the oil core
OMM-NP	• ABT-263 [60]	• Specific binding of ABT-263 with Bcl-2 receptor on outer mitochondrial membrane

[a)] RBC-NP: RBC-membrane-coated PLGA nanoparticle; Oil-NS: RBC-membrane-coated oil nanosponge; OMM-NP: outer mitochondrial membrane-coated PLGA nanoparticle; [b)] DDVP: dichlorvos; DOX: doxorubicin; POX: paraoxon; DFP: diisopropyl fluorophosphate; [c)] AChE: acetylcholinesterase; Bcl-2: B-cell lymphoma protein 2.

1.4 Neutralizing Inflammatory Cytokines

Immune cells, such as macrophages, neutrophils, and T cells, secrete inflammatory cytokines to regulate inflammation and remove harmful stimuli during trauma or infection [14, 64]. However, oftentimes, the production of inflammatory cytokines becomes excessive, resulting in pathogenic cytokine storm and serious inflammatory disorders [14]. For example, in sepsis, bacterial endotoxins interact with macrophages through the toll-like receptor 4 (TLR-4) and CD14 receptor. Such interactions induce macrophages to release various inflammatory cytokines, including tumor necrosis factor-alpha (TNF-α), interleukin 6 (IL-6), and interferon-gamma (IFN-γ), which further activate other macrophages. Such signaling propagation and potentiation in

severe sepsis can lead to septic shock, multi-organ failure, and death [65, 66]. Inflammation caused by sustained elevation of inflammatory cytokines can also lead to other disorders, including rheumatoid arthritis [67, 68], inflammatory bowel disease [69, 70], atherosclerosis [71, 72], and muscular dystrophy [73]. With such prominent roles in these diseases, inflammatory cytokines are common targets for neutralization.

Currently, a few cytokine-neutralizing antibodies, including Infliximab (TNF-α antibody), Tocilizumab (IL-6 antibody), and Emapalumab (IFN-γ antibody), have been approved for treating inflammatory disorders [13]. However, the therapeutic efficacies of these cytokine attenuation treatments vary with substantial dose-limiting adverse effects due to non-selective biodistribution [74]. In addition, inflammation is orchestrated by different molecules with complicated sensor and feedback pathways. Inhibiting a single inflammatory cytokine might trigger another compensatory inflammatory response [14, 75]. Antibodies that neutralize a single cytokine are often inadequate in treating inflammatory disorders. In contrast, cell-membrane-coated nanoparticles present identical antigenic profiles as the target cells. As a result, they mimic source cells and neutralize cytokines in a multiplex fashion, leading to effective outcomes in treating various inflammatory disorders.

Among all types of cells, sentinel immune cells interact extensively with inflammatory cytokines during inflammation. Especially, macrophages are naturally rich in cytokine-binding receptors, including CD126, CD130, CD120a, CD120b, and CD119 on the cell surface [76]. As a result, macrophage-membrane-coated nanoparticles (denoted "MΦ-NPs") have been widely studied for anti-inflammation treatment. MΦ-NPs were first developed by coating the membrane of J774 cells, a mouse macrophage cell line, onto PLGA polymeric cores [77]. When applied to treat sepsis, MΦ-NPs bound with bacterial endotoxin and inflammatory cytokines, inhibiting

cytokine functions of potentiating downstream cytokine storms and sepsis. In the study, MΦ-NPs effectively sequestered cell response to lipopolysaccharide (LPS) and inflammatory cytokines in vitro. In mice, MΦ-NPs significantly reduced lethality and serum inflammatory cytokine levels after intravenous injection in an LPS-induced endotoxemia mouse model. In a mouse Escherichia coli bacteremia model, treatment with MΦ-NPs reduced pro-inflammatory cytokine levels, inhibited bacterial dissemination, and ultimately conferred a significant survival advantage to infected mice.

Macrophage membrane has also been coated onto cores fabricated from various materials for broad functionalities. For example, macrophage membrane was coated onto iron oxide nanoparticle cores for sepsis management [78]. Compared to polymeric cores, the positively charged iron oxide cores enhanced the binding affinity of the nanoparticles towards negatively charged LPS. The resulting MΦ-NPs, when administered intravenously into LPS-induced endotoxemic mice, significantly reduced LPS and serum levels of pro-inflammatory cytokines, which led to an improved overall survival rate. Similarly, MΦ-NPs were also synthesized by coating the membrane of mouse RAW 264.7 macrophages onto a composite nanoparticle core containing bactericidal TiO2 to treat bacterial infection in the bone [79]. These MΦ-NPs not only sequestered LPS and inflammatory cytokines but also generated reactive oxygen species (ROS) under UV irradiation to kill bacteria, resulting in enhanced antibacterial activities in vivo.

Recently, MΦ-NPs have also been studied to treat other inflammatory disorders. For example, macrophage-membrane-coated metal–organic framework (MOF) was developed to deliver uricase (denoted “MΦ-MOF-uricase”) to treat gout, inflammatory arthritis mediated by chronic deposition of monosodium urate crystals (**Figure 1.6**) [80]. In this case, MOF effectively encapsulated and delivered uricase while maintaining their bioactivity of degrading monosodium

urate crystals. Simultaneously, the macrophage membrane neutralized inflammatory cytokines associated with gout pathogenesis, such as IL-6, TNF-α, and IL-1β. In a murine gout model generated by intra-articular injection of monosodium urate crystals into the ankle joints, MΦ-MOF-uricase treatment significantly reduced urate level and suppressed joint inflammation, ameliorating gout-mediated joint damage. Furthermore, MΦ-NPs were used to rescue transplanted liver from ischemia-reperfusion injury through LPS neutralization, inflammation suppression, and inhibition of hepatic macrophage activation [81]. Based on a similar working mechanism, macrophage-membrane-coated gold nanocages and amphiphilic chitosan oligosaccharide nanoparticle cores were used to accelerate bone repair and treat atherosclerosis through synergistic cytokine neutralization and controlled anti-inflammation payload delivery [82, 83].

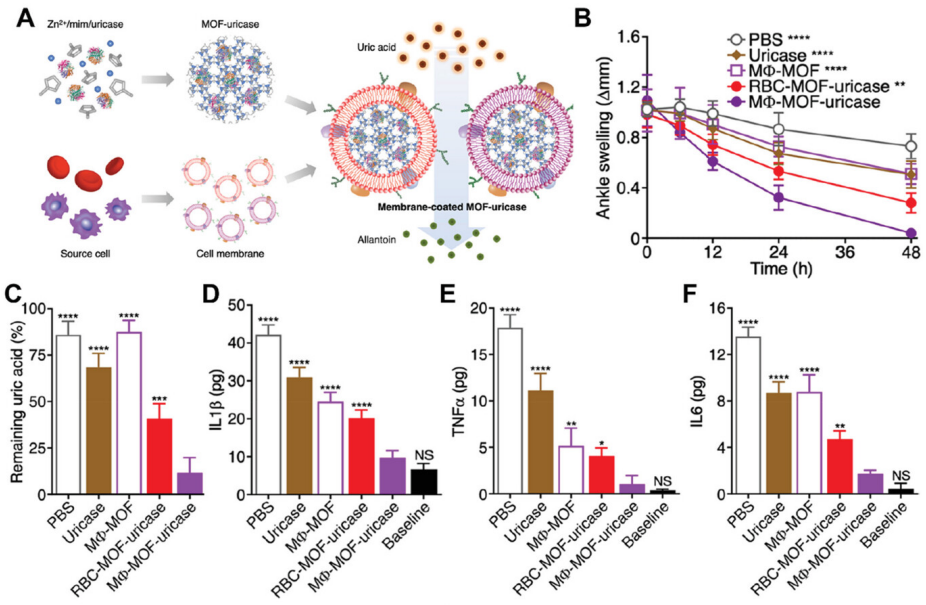

Figure 1.6 Schematic design of macrophage-membrane-coated uricase-loaded MOF nanoparticles (MΦ-MOF-uricase) and in vivo gout management. A) Design features and proposed mechanism of MΦ-MOF-uricase for the neutralization of inflammatory cytokines and enzymatic degradation of uric acid. B) Change in ankle joint diameter of mice with gout after intra-articular treatment with PBS, free uricase, MΦ-MOF, RBC-MOF-uricase, or MΦ-MOF-uricase (n = 4, mean ± standard deviation (SD)). C) Remaining uric acid level in the ankle joints 48 h after the treatment (n = 4, mean ± SD). D–F) Remaining IL1β (D), TNFα (E), and IL6 (F) levels in the ankle joints 48 h after the treatment (n = 4, mean ± SD). A–F) Reproduced with permission [80]. Copyright 2020, American Chemical Society.

Like MΦ-NP, neutrophil membrane-coated nanoparticles (denoted "neutrophil-NPs") were also developed for neutralizing inflammatory cytokines. For example, neutrophil-NPs made with PLGA cores were used to inhibit synovial inflammation and alleviate joint damage in inflammatory arthritis [84]. In this case, neutrophil-NPs inhibited multiple cytokines concurrently. By inheriting chondrocyte-binding ligands from the source cells, neutrophil-NP penetrated deep into the cartilage matrix. In a mouse model of collagen-induced arthritis and a human transgenic mouse model of arthritis, neutrophil-NPs conferred significant therapeutic efficacy by ameliorating joint damage and suppressing overall arthritis severity. Neutrophil-NPs were also used to restore immunosuppression in the tumor microenvironment due to their capability to neutralize granulocyte-macrophage colony-stimulating factor (GM-CSF) and chemokine ligand 2 (CXCL2), two cytokines crucial for myeloid-derived suppressor cells (MDSCs) expansion and tumor-tropic migration (**Figure 1.7**) [85]. In mice with subcutaneous B16F10 tumors, neutrophil-NPs treatment significantly inhibited the expansion and accumulation of MDSCs in tumor sites that would otherwise induce an immunosuppressive environment. This reversion of tumor microenvironments enhanced tumor-filtrating T lymphocytes activity and improved anti-cancer efficacy of checkpoint blockade cancer immunotherapy.

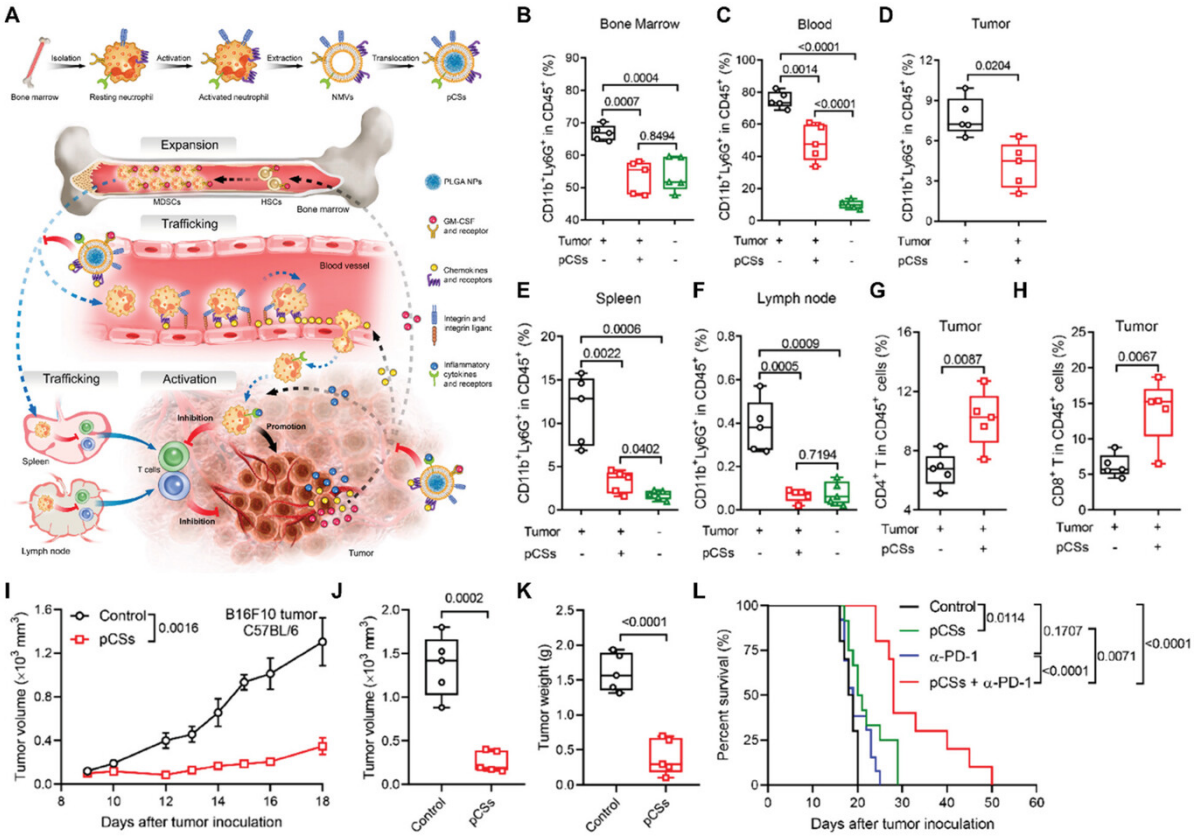

Figure 1.7 Pseudoneutrophil cytokine sponges (pCSs) inhibited the expansion and activation of MDSC, restoring antitumor microenvironment. A) Schematics showing the preparation and cytokine neutralization of pCSs. B–F) pCSs inhibited MDSC expansion in bone marrow (B), peripheral blood (C), tumors (D), spleen (E), and lymph node (F). G, H) Flow cytometry quantification of CD4+ (G) and CD8+ T (H) cells among DAPI−CD45+ tumor-infiltrating leukocytes after pCSs treatment. I) Tumor growth curve of subcutaneously implanted B16F10 tumors from C57BL/6 mice treated with or without pCSs. J, K) The volume (J) and weight (K) of excised B16F10 tumors. L) Kaplan–Meier survival curves for mice treated with pCSs, α-PD-1, pCSs plus α-PD-1, or control. A–L) Reproduced with permission [85]. Copyright 2019, American Chemical Society.

Table 1.3 summarizes examples of using cellular nanosponges to neutralize inflammatory cytokines. Overall, recent studies have demonstrated cell-membrane-coated nanoparticles as a promising approach for anti-inflammation therapy. Particularly, MΦ-NPs and neutrophil-NPs, with inherent inflammatory cytokines binding capability acquired from membrane coating, have shown great potential in treating a wide variety of inflammatory diseases, including sepsis, arthritis, and atherosclerosis. In addition, the successful use of neutrophil-NPs for restoring antitumor

microenvironment suggests that immune cell-membrane-coated nanoparticles may serve as a synergistic therapy for cancer immunotherapy.

Table 1.3. Summary of using cellular nanosponges to neutralize inflammatory cytokines.

Nanosponge platform [a)]	Inflammatory cytokine [b)]	Mechanism
MΦ-NP	• IL-6 [77-83] • TNF-α [77, 78, 81-83] • IFN-γ [77] • IL-1β [83] • oxLDL [83] • MCP-1 [83]	• Specific binding of cytokines with cytokine receptors on macrophage cell membrane
MΦ-MOF-NP	• IL-1β [80] • TNF-α [80] • IL-6 [80]	• Specific binding of cytokines with cytokine receptors on macrophage cell membrane
Neutrophil-NP	• IL-1β [84] • TNF-α [84] • GM-CSF [85] • CXCL2 [85]	• Specific binding of cytokines with cytokine receptors on neutrophil cell membrane

[a)] MΦ-NP: macrophage-membrane-coated nanoparticle; MΦ-MOF-NP: macrophage-membrane coated metal-organic framework nanoparticle; Neutrophil-NP: neutrophil membrane-coated nanoparticle; [b)] IL-6: interleukin 6; TNF-α: tumor necrosis factor alpha; IFN-γ: interferon gamma; IL-1β: interleukin 1 beta; oxLDL: oxidized low-density lipoprotein; MCP-1: monocyte chemoattractant protein-1; GM-CSF: granulocyte-macrophage colony-stimulating factor; CXCL2: C-X-C motif chemokine ligand 2.

1.5 Neutralizing Pathogenic Antibodies

Cellular nanosponges have also been studied to neutralize and deplete pathological antibodies in antibody-induced anemia, where autoantibodies attack surface antigens present on RBCs. The disease may be idiopathic, as in autoimmune hemolytic anemia (AIHA). Treatments start with systemic steroids, then escalate to cytotoxic drugs and B cell-depleting monoclonal antibodies, followed by splenectomy depending on patient response to the therapy. Drug-based immune suppression imposes considerable iatrogenic risk while spleen removal heightens susceptibility to severe infections [86, 87]. The disease may also be drug-induced, as in drug-induced anemia. Treatments include discontinuance of the offending drug and, much more often

than in AIHA, blood transfusions. The latter carries the risks of hemolytic transfusion reactions, the formation of alloantibodies, and iron toxicity [88-90].

To minimize disease burden without the need for drug-based immune suppression, researchers studied the efficacy of RBC-NS to abrogate the effect of pathological antibodies in antibody-induced anemia (**Figure 1.8**) [28]. In vitro experiments showed that RBC-NS bound specifically with anti-RBC antibodies in a dose-dependent manner. While intraperitoneal injection of anti-RBC antibody into mice induced acute anemia, the same amount of antibody preincubated with the nanosponges failed to induce an anemic response. The efficacy of RBC-NS was further tested in a mouse model of antibody-induced anemia, where low-dose antibodies were administrated daily via intraperitoneal injection to keep an antibody level for anemia progression. After the anemia was established, mice treated with RBC-NS via intravenous injection showed significant benefit in anemia-related parameters, such as RBC count, hemoglobin level, and hematocrit. Notably, assessment of autoantibodies against mouse RBCs showed no observable elevation of autologous anti-RBC responses in mice receiving RBC-NS treatment. This result confirms that the RBC-NS/anti-RBC antibody complex does not potentiate a humoral immune response against particle-associated membrane antigens.

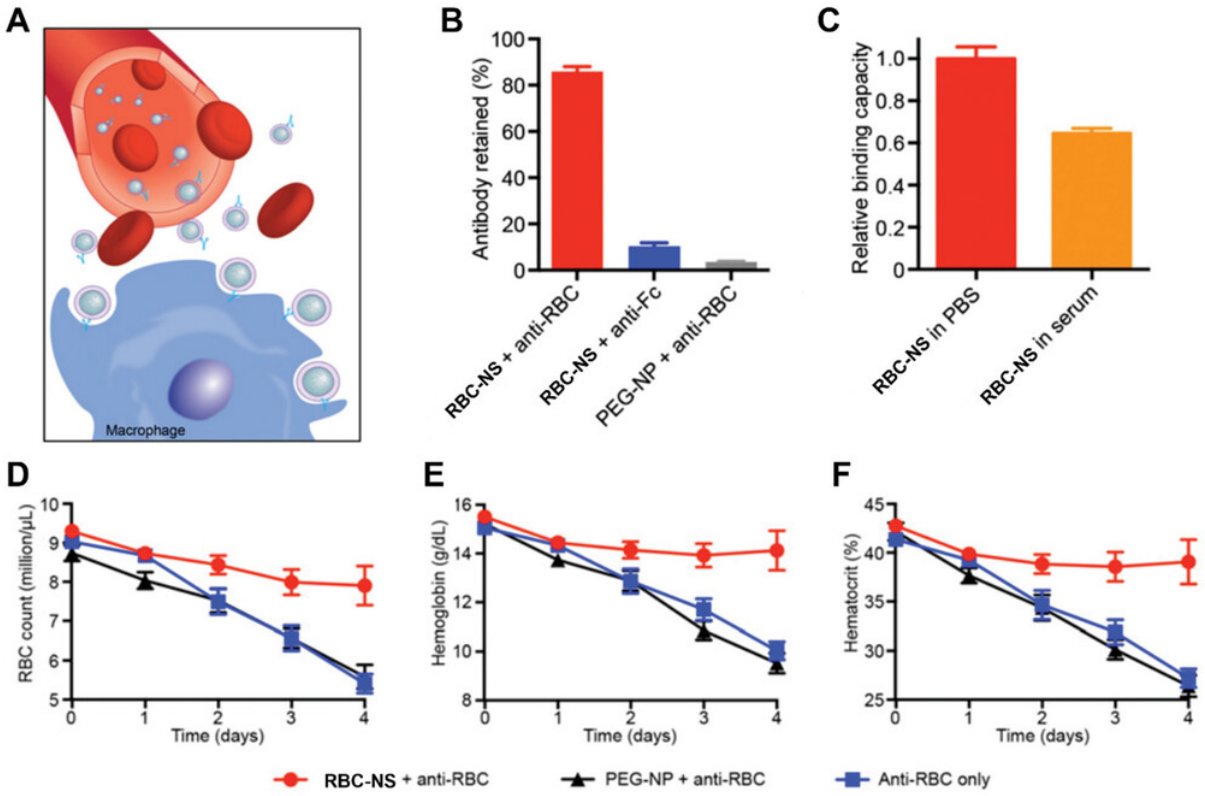

Figure 1.8 RBC-membrane-coated nanosponges (RBC-NS) for clearing pathological antibodies. A) Scheme of RBC-NS neutralizing anti-RBC antibodies (anti-RBCs). These nanosponges contain antigens from RBCs and bind with anti-RBCs, thereby protecting RBCs from phagocytosis. B, C) In vitro characterization of RBC-NS. B) Equivalent amounts of RBC-NS incubated with anti-RBCs or anti-Fc demonstrated significantly greater specific binding than nonspecific binding. The corresponding PEGylated nanoparticles (PEG-NPs) incubated with anti-RBCs served as a negative control. C) The relative binding capacity of nanosponges in PBS versus RBC-NS in serum at saturation. There is no significant difference between the two different environments. D–F) In vivo neutralization of anti-RBCs by RBC-NS. Mice (n = 10) were intraperitoneally (i.p.) injected with 200 μg of anti-RBCs on days 0, 1, 2, and 3. After each dose of the antibody, the mice received 2 mg of RBC-NS (red), PEG-NP (black), or PBS (blue) via tail-vein injection. Blood was collected daily to monitor the RBC count (million cells per microliter) (D), hemoglobin level (grams per deciliter) (E), and hematocrit (%) (F) of the mice. A–F) Reproduced with permission [28]. Copyright 2014, The Authors, published by National Academy of Sciences of the United States of America.

The concept of using nanosponges to neutralize pathological antibodies was recently extended to treat immune thrombocytopenic purpura (ITP) by using platelet membrane-coated nanoparticles (denoted "PNPs") [91]. ITP is an immune-mediated hematological disorder characterized by a low level of platelets and easy or excessive bleeding due to the presence of anti-platelet autoantibodies [92, 93]. These pathological antibodies bind to specific antigens on the

platelet surface, leading to platelet sequestration and destruction by the reticuloendothelial system [94]. Current therapies for the treatment of ITP are non-specific, such as corticosteroids and invasive and irreversible splenectomy for those who fail to respond to the drug treatment [95, 96]. These treatments can, at times, result in complications that are more burdensome than the disease itself. In the study, PNPs acted as decoys that bound pathological antiplatelet antibodies in a dose-dependent manner (**Figure 1.9**) [91]. When the anti-platelet antibodies were preincubated with the PNPs followed by intraperitoneal injection, the mice kept platelet counts similar to the healthy mice. In a mouse model of antibody-induced thrombocytopenia, the mouse group treated with PNPs had significantly higher platelet counts and hemostatic capacity than the control groups treated with PLGA-PEG NPs (without platelet membrane).

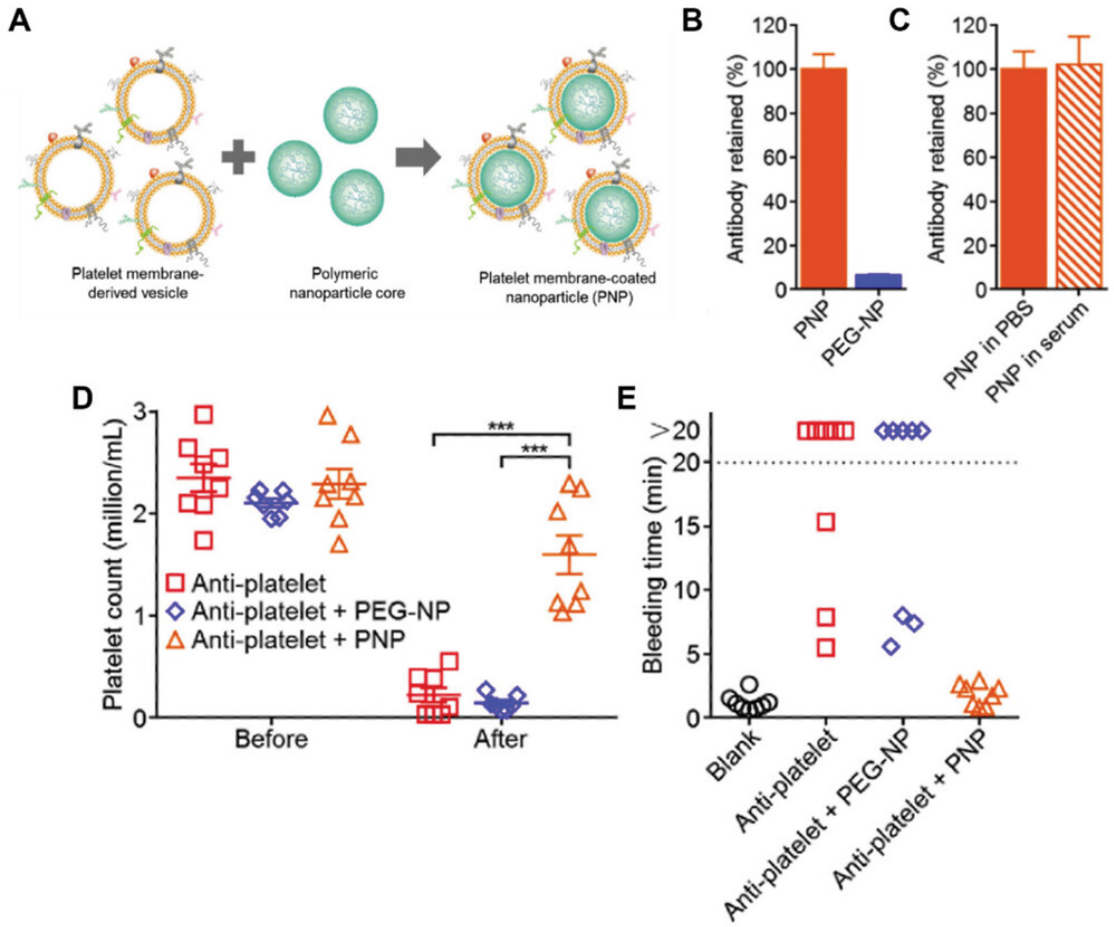

Figure 1.9 Platelet-membrane-coated nanoparticles (PNPs) for neutralizing anti-platelet antibodies for the treatment of immune thrombocytopenia. A) Preparation of PNPs. The platelet membrane was derived from fresh platelets using a repeated freeze–thaw process. Then the purified membrane is coated onto PLGA nanoparticles by sonication. B, C) In vitro binding of anti-platelet antibodies to PNPs. B) Relative binding of anti-platelet antibodies to either PNPs or PEG-NPs (n = 3; mean ± SD). C) Relative binding of anti-platelet antibodies to PNPs in either PBS or mouse serum. There is no significant difference between PBS and mouse serum environments (n = 3; mean ± SD). D, E) In vivo treatment of antibody-induced thrombocytopenia by PNPs. Mice were i.p. injected with anti-platelet antibodies. After 15 min, blank solution, PNPs, or PEG-NPs were injected intravenously via the tail vein. D) Platelet counts from blood collected before and 24 h after administration (n = 8; mean ± standard error of the mean (S.E.M.)). E) A bleeding time test was performed to test the hemostatic capacity. The tail tip was excised and then immersed into a warmed saline solution. The time of bleeding cessation was recorded. ***$p < 0.001$, Student's t-test. A–E) Reproduced with permission [91]. Copyright 2016, Elsevier.

Examples of using cellular nanosponges to neutralize pathological antibodies are summarized in **Table 1.4**. Overall, cellular nanosponges show promise in treating antibody-mediated autoimmune diseases, in which target antigens on susceptible cells can vary from patient

to patient. RBC and platelet nanosponges serve as valuable prototypes for selective antibody depletion while minimizing iatrogenic risks associated with many traditional drug-based therapies. Moreover, the applications of cellular nanosponges can be extended to other immune hypersensitivities driven by pathological antibodies targeting self-antigens, including pernicious anemia, Grave disease, and myasthenia gravis. Nanosponges can also be loaded with drugs or formulated with cores from different materials, such as metallic or inorganic nanoparticles, for multifunctional formulations [28]. Ultimately, cellular nanosponges represent a promising platform for the clearance of pathological antibodies, and further study towards translation is warranted.

Table 1.4. Summary of using cellular nanosponges to neutralize pathological antibodies.

Nanosponge platform [a)]	Antibody	Mechanism
RBC-NS	• Anti-RBC antibody [28]	• Specific binding of anti-RBC autoantibodies with surface antigens on RBC membrane
PNP	• Anti-platelet antibody [91]	• Specific binding of anti-platelet autoantibodies with surface antigens on platelet membrane

[a)] RBC-NS: RBC-membrane-coated PLGA nanoparticle; PNP: platelet-membrane-coated PLGA nanoparticle.

1.6 Neutralizing Viruses

Viruses bind with surface receptors on the host cell membranes through envelope or capsid proteins. These binding interactions enable viruses to fuse with the host cell membrane for cellular entry [9, 10]. Inspired by the critical role of virus-host cell binding in viral infectivity, researchers have developed nanoparticles cloaked with the host cell membrane as a countermeasure against viral infections. These nanoparticles inherit surface receptors of the source cells critical for viral binding. They act as decoys to intercept and neutralize viruses, thereby preventing viruses from

infecting the host cells. So far, cell-membrane-coated nanoparticles have been used to neutralize several different virus species, such as human immunodeficiency virus (HIV), severe acute respiratory syndrome coronavirus 2 (SARS-CoV-2), and Zika virus.

HIV attacks immune cells, particularly T lymphocytes, inducing immune cell depletion and leading to acquired immunodeficiency syndrome (AIDS) [97]. The cellular entry of HIV is initiated by binding of viral envelope glycoproteins, mainly gp120, with the cluster of differentiation 4 (CD4) receptor on T cells. HIV gp120 then binds to C-C chemokine receptor type 5 (CCR5) or C-X-C chemokine receptor type 4 (CXCR4) coreceptor on T cells [98]. Based on this mechanism, researchers cloaked PLGA nanoparticles with the membrane of CD4+ T cells (denoted "TNPs") for neutralizing HIV (**Figure 1.10A**) [30]. These nanosponges retained CD4, CCR5, and CXCR4 surface receptors and therefore bound to HIV gp120 in a dose-dependent manner and inhibited the gp120-induced apoptosis of bystander CD4+ T cells. Following pre-incubation with TNPs, the infectivity of HIV on peripheral mononuclear blood cells and human-monocyte-derived macrophages was reduced. Later, TNPs were shown to neutralize 125 different strains of HIV pseudoviruses, demonstrating the breadth and potency of the nanosponges in neutralizing viruses (**Figure 1.10B–D**) [31]. These two studies showed that TNPs suppressed both free and cell-associated viruses, providing a holistic approach to combating HIV infection.

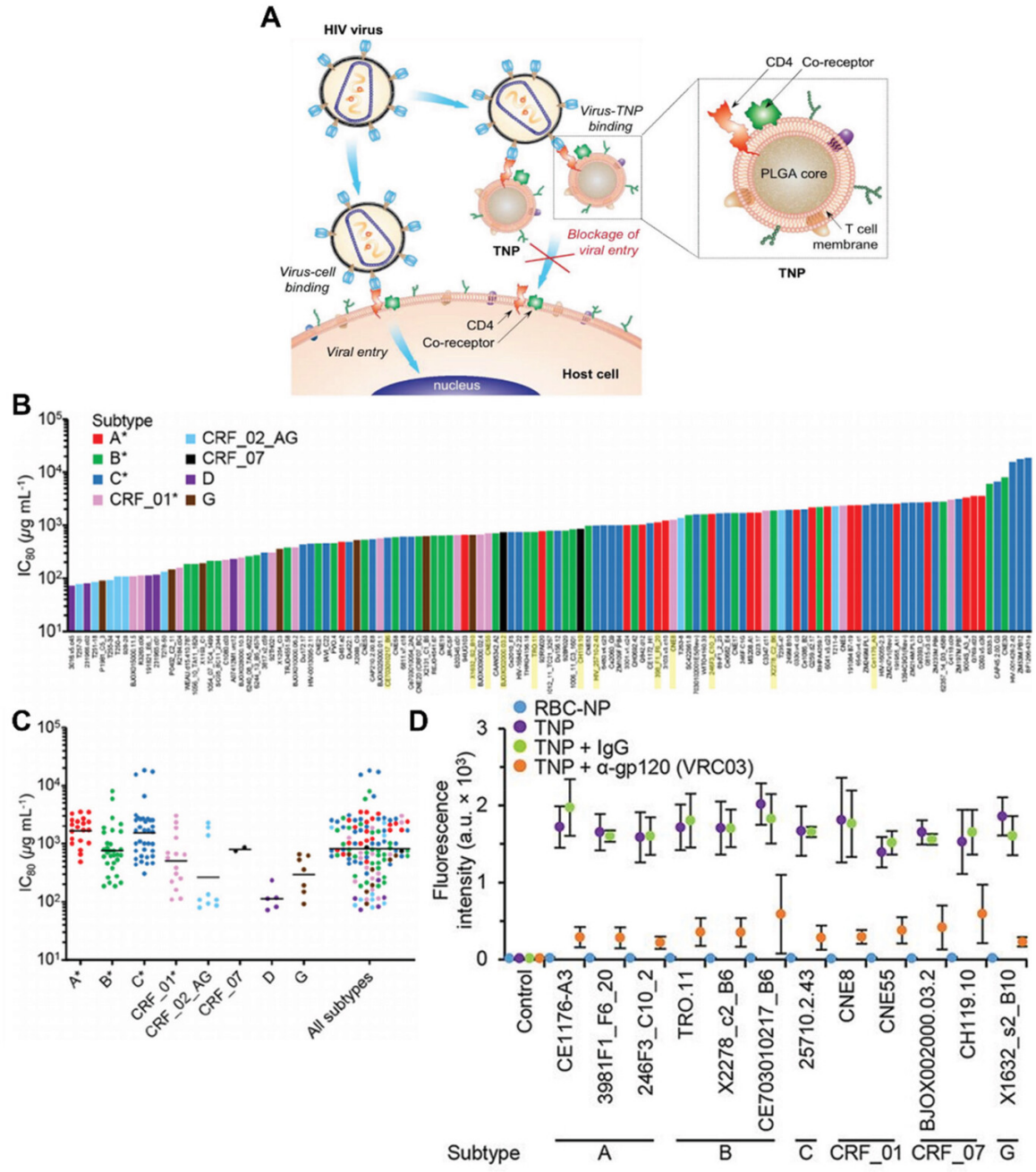

Figure 1.10 T-cell-membrane-coated PLGA nanoparticles (TNPs) for neutralizing HIV infectivity. A) Schematic illustration of the mechanism of HIV neutralization by TNPs. B) Neutralization potency (IC80) expressed as micrograms per milliliter of TNP against different HIV Env-pseudoviruses, as tested using the TZM-bl assays. C) Summary of neutralization potencies (IC80) for TNP against the multi-subtype pseudoviruses included in (B). Horizontal bars represent geomean IC80 values. D) The TNP readily bound to HEK 293 T/17 cells expressing a panel of HIV gp120, while coculture with the broadly neutralizing antibody VRC03 inhibited TNP-cell binding interactions. A) Reproduced with permission [30]. Copyright 2018, Wiley-VCH. B–D) Reproduced under the terms of the CC-BY Creative Commons Attribution 4.0 International license (https://creativecommons.org/licenses/by/4.0) [31]. Copyright 2020, The Authors, published by American Society of Microbiology.

Unlike HIV, SARS-CoV-2 enters the human host primarily via the respiratory tract and infects various airway and alveolar cells, leading to severe respiratory syndromes, organ injuries, and potential mortality [99]. The cellular entry of SARS-CoV-2 is mainly mediated by the binding of the viral spike glycoprotein (S protein) with angiotensin-converting enzyme 2 (ACE2) and cluster of differentiation 147 (CD147) receptors on the host cells [100, 101]. Based on this mechanism, researchers made two types of cellular nanosponges by cloaking PLGA nanoparticles with the membrane of human lung epithelial type II cells (Epithelial-NS) or of human macrophages (MΦ-NS, **Figure 1.11**) [32]. These nanosponges retained the critical receptors for SARS-CoV-2 binding, including ACE2 and CD147. Following pre-incubation with the nanosponges, the infectivity of SARSCoV-2 on monkey epithelial Vero E6 cells was reduced. These two nanosponges showed similar dose-dependent inhibitions of SARS-CoV-2 infectivity: the dose required to neutralize 50% of viral infectivity (IC50) was 827.1 μg mL^{-1} for Epithelial-NS and 882.7 μg mL^{-1} for MΦ-NS. In contrast, RBC-NS, which lacked SARS-CoV-2-specific surface receptors, were ineffective in neutralizing the viruses. Notably, some patients with COVID-19 infection progress to severe pneumonia, septic shock, or multiple organ failure due to cytokine storm [102]. Besides neutralizing the causative viruses, MΦ-NPs can also neutralize the associated cytokines and thus manage the downstream hyperinflammatory response.

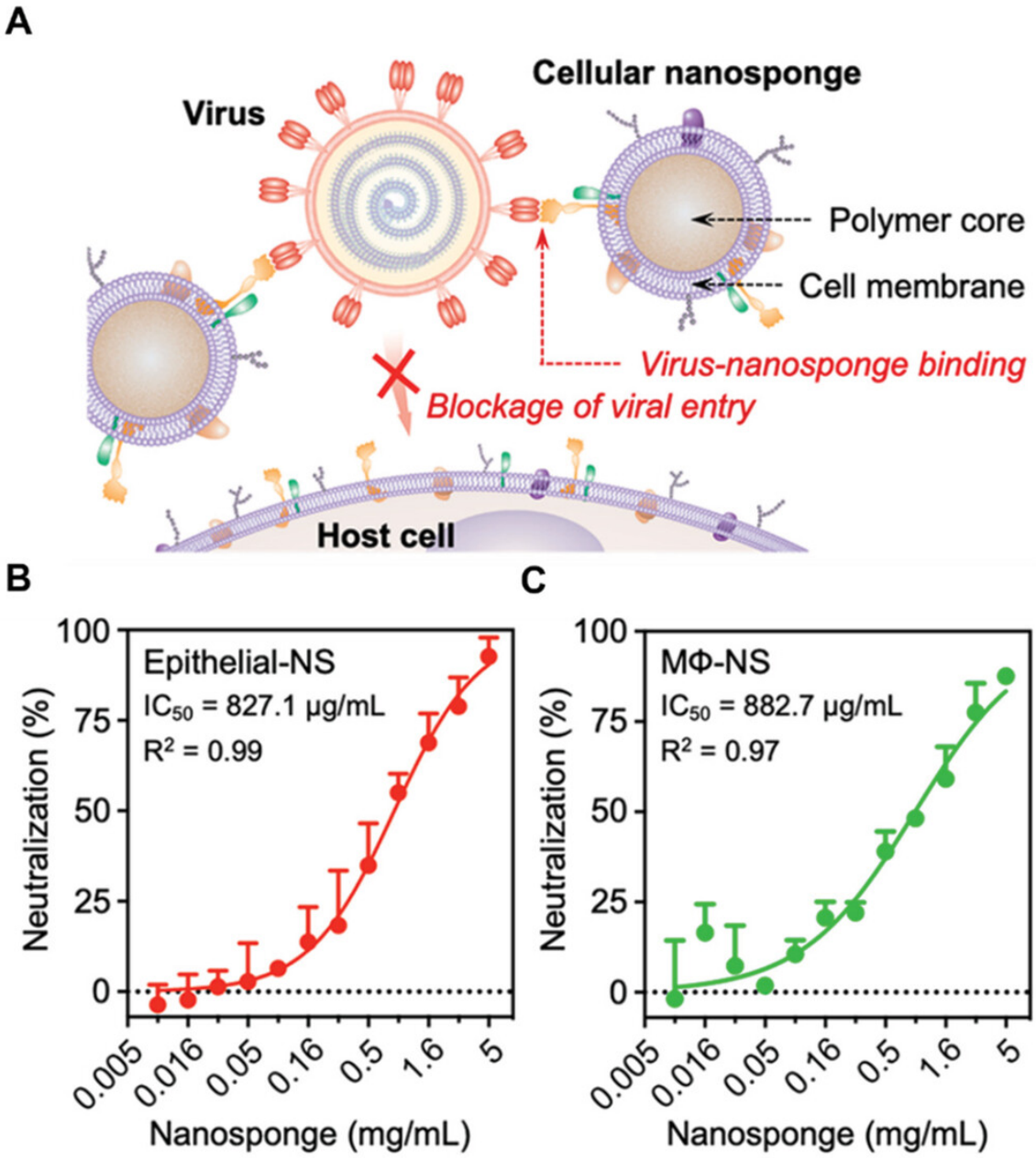

Figure 1.11 Cellular nanosponges for neutralizing SARS-CoV-2 infectivity. A) Schematic illustration of the mechanism of SARS-CoV-2 neutralization by cellular nanosponges. The nanosponges were constructed by wrapping polymeric nanoparticle cores with plasma membranes of lung epithelial cells and macrophages (MΦs). The resulting nanosponges (denoted "Epithelial-NS" and "MΦ-NS," respectively) inherited the surface antigen profiles of the source cells and served as decoys to bind with SARS-CoV-2. Such binding interaction blocks viral entry into the host cells and inhibits viral infectivity. B, C) Neutralization against SARS-CoV-2 infection by Epithelial-NS (B) and MΦ-NS (C) was tested using live SARS-CoV-2 viruses on Vero E6 cells. The IC50 values for Epithelial-NS and MΦ-NS were found to be 827.1 and 882.7 μg mL−1 (based on membrane protein concentration), respectively. In all data sets, n = 3. Data are presented as mean + SD. The horizontal dashed lines mark the zero levels. IC50 values were derived from the variable slope model using Graphpad Prism 8. A–C) Reproduced with permission [32]. Copyright 2020, American Chemical Society.

Zika virus is a mosquito-borne virus transmitted to human hosts through mosquito bites, leading to neurological disorders and congenital disabilities such as fetal microcephaly [103, 104]. As a natural host for Zika virus, mosquito cells have a high binding affinity for the virus. The binding interaction is possibly mediated by the viral envelope protein E and yet unidentified receptors on the mosquito cell membrane [105, 106]. Based on this mechanism, researchers coated gelatin nanoparticles with the membrane of mosquito Aedes albopictus C6/36 cells for neutralizing Zika virus [107]. These nanosponges inherited membrane proteins from the source cells and were able to bind the Zika virus. They inhibited the infectivity of the Zika virus on Vero cells, leading to reduced intracellular and extracellular viral titers. In mice infected with Zika virus, the nanosponges reduced the viral load in major organs, including the brain, and prolonged animal survival. Additionally, these nanosponges inhibited the spread of the virus across the placental blood barrier in pregnant mice and reduced the severity of fetal microcephaly.

The use of cellular nanosponges to neutralize viruses is summarized in **Table 1.5**. Overall, cellular nanosponges have been demonstrated to be a unique approach to neutralizing different virus species. Unlike conventional antiviral therapies, this neutralization strategy is potentially agnostic to viral mutations. As long as the identified host cells remain the viral targets, cellular nanosponges can recognize and neutralize the virus regardless of viral mutations [32]. Besides, this strategy does not directly suppress viral replication. Therefore, it does not impose high selective pressure for resistance development. Additionally, cellular nanosponges such as macrophage nanosponges have shown broad-spectrum neutralization of not only viruses but also proinflammatory cytokines [77]. They can provide more holistic treatment for viral infections, driven, in part, by overstimulated host immune responses [108]. For future clinical translation, the efficacy of these cellular nanosponges against viral infections needs to be further validated in

appropriate animal models. With continuous development, cellular nanosponges may make a significant contribution to combating viral infections.

Table 1.5. Summary of using cellular nanosponges to neutralize viruses.

Nanosponge platform [a)]	Virus [b)]	Mechanism [b, c)]
TNP	• HIV [30, 31]	• Specific binding of HIV glycoprotein gp120 with CD4 and other co-receptors on $CD4^+$ T cell membrane
Epithelial-NS	• SARS-CoV-2 [32]	• Specific binding of SARS-CoV-2 S protein with ACE2 receptor on epithelial cell membrane
MΦ-NS	• SARS-CoV-2 [32]	• Specific binding of SARS-CoV-2 S protein with ACE2 or CD147 receptors on macrophage cell membrane
Nanosponge made with mosquito cell membrane	• Zika virus [107]	• Specific bind of Zika envelope protein E with unidentified receptors on mosquito cell membrane.

[a)] TNP: CD4+ T-cell-membrane-coated PLGA nanoparticle; Epithelial-NS: human lung epithelial cell membrane-coated nanosponge; MΦ-NS: human macrophage cell membrane coated nanosponge; [b)] HIV: human immunodeficiency virus; SARSCoV-2: severe acute respiratory syndrome coronavirus 2; [c)] CD4: cluster of differentiation 4; S protein: spike protein; ACE2: angiotensin-converting enzyme 2; CD147: differentiation 147.

1.7 Summary

The hallmark of cellular nanosponges is their faithful mimicry of source cells, which allows them to neutralize a myriad of harmful molecules or infectious pathogens while bypassing the enormous diversity and complexity of these pathological agents. By leveraging the natural protein receptors on the cell membranes, cellular nanosponges have been demonstrated to effectively neutralize numerous biological and chemical agents, including bacterial toxins, chemical toxicants, inflammatory cytokines, autoantibodies, and viruses. Upon binding to the cellular nanosponges, the biological agents are expected to complex with the nanosponges, which can thus neutralize the

virulence and biological function of the agents. Such complexes are subsequently taken up by the immune cells such as macrophages for metabolic processing or cleared by the mononuclear phagocytic system (MRS). A number of cell membranes from cells such as RBC, platelet, macrophage, T cell, or bacterium have been used to fabricate corresponding cellular nanosponges towards a wide range of biological neutralization applications. In addition, different nanomaterials have been used to fabricate nanoparticle cores of the cellular nanosponges, which provide the nanosponges with additional functionality. As a function-driven and broad-spectrum neutralization therapeutic modality, the cellular nanosponges have some unique features as compared to the conventional chemical-based or antibody-based antidots. Instead of targeting specific harmful agents, the cellular nanosponges function as surrogates of the host cells to capture and neutralize harmful biological agents that target the host cells. Therefore, nanosponge therapy is well-positioned to treat complicated medical conditions that involve multiple pathogenesis mechanisms such as sepsis, which involves pathogen infection and inflammatory cytokine disorder. The nanosponge therapy is also expected to be agnostic to the mutations of the target agents such as viruses; as long as the host cell remains the viral target, the cellular nanosponges will be able to neutralize the virus regardless of viral mutation variants.

Despite the great promise, challenges exist toward further development and application of cellular nanosponges. For example, the density of protein receptors on wild-type cell membranes may limit the neutralization capacity of the nanosponges. To overcome this potential limitation, using metabolic or genetic engineering to enhance the expression level of the receptor offers a solution [61, 109, 110]. Alternatively, replacing stoichiometric binding with enzyme-based degradation may also overcome the limitation [80]. Cellular nanosponges also face the challenge of adapting various disease settings for broader biological neutralization applications. In this

regard, non-spherical substrates, such as nanofibers or planer substrates, can be coated with cell membranes for neutralization while providing additional functionalities desirable for applications such as tissue engineering or biosensing [60, 111, 112]. Toward future translation, cellular nanosponges need to be manufactured with maximum immune compatibility. For this purpose, the cell membranes can be derived from the patient's own cells, resulting in "personalized" neutralization therapy. The membranes can also be derived from genetically engineered "universal" cells to fabricate nanosponges that can be applied to all humans [113]. Nanosponge manufacturing also needs to consider a few key processes. For example, large-scale cell expansion is needed to ensure membrane material supply. In this perspective, biomanufacturing technologies based on 3D-bioreactors for large and ultra-large scale-up of cell production are beneficial [114, 115]. In addition, processes for large-scale cell membrane derivation, efficient nanoparticle coating, and reliable quality control methods are also required. Overall, with continuous research and development, we expect the cellular nanosponge technology will reveal and demonstrate more unique strengths towards biological neutralization applications, which will benefit various patient populations.

1.8 Reference

[1] C.J. Ruhm, Drug poisoning deaths in the United States, 1999-2012: a statistical adjustment analysis, Popul Health Metr 14 (2016).

[2] P. Masson, Evolution of and perspectives on therapeutic approaches to nerve agent poisoning, Toxicol Lett 206(1) (2011) 5-13.

[3] K.D.F. Bordon, C.T. Cologna, E.C. Fornari-Baldo, E.L. Pinheiro, F.A. Cerni, F.G. Amorim, F.A.P. Anjolette, F.A. Cordeiro, G.A. Wiezel, I.A. Cardoso, I.G. Ferreira, I.S. de Oliveira, J. Boldrini-Franca, M.B. Pucca, M.A. Baldo, E.C. Arantes, From Animal Poisons and Venoms to Medicines: Achievements, Challenges and Perspectives in Drug Discovery, Front Pharmacol 11 (2020).

[4] R.S. Hotchkiss, D.W. Nicholson, Apoptosis and caspases regulate death and inflammation in sepsis, Nat Rev Immunol 6(11) (2006) 813-822.

[5] A.K. Shrivastava, A. Pandey, Inflammation and rheumatoid arthritis, J Physiol Biochem 69(2) (2013) 335-347.

[6] M. Pallardy, R. Bechara, Chemical or Drug Hypersensitivity: Is the Immune System Clearing the Danger?, Toxicol Sci 158(1) (2017) 14-22.

[7] J.K. Rudkin, R.M. McLoughlin, A. Preston, R.C. Massey, Bacterial toxins: Offensive, defensive, or something else altogether?, Plos Pathog 13(9) (2017).

[8] D. Lobato-Marquez, R. Diaz-Orejas, F. Garcia-del Portillo, Toxin-antitoxins and bacterial virulence, Fems Microbiol Rev 40(5) (2016) 592-609.

[9] D.S. Dimitrov, Virus entry: Molecular mechanisms and biomedical applications, Nat Rev Microbiol 2(2) (2004) 109-122.

[10] M.A. Barocchi, V. Masignani, R. Rappuoli, Opinion: Cell entry machines: a common theme in nature?, Nat Rev Microbiol 3(4) (2005) 349-58.

[11] L.F. Zhang, J.C. Leroux, Current and forthcoming approaches for systemic detoxification Preface, Adv Drug Deliver Rev 90 (2015) 1-2.

[12] J.C. Leroux, Injectable nanocarriers for biodetoxification, Nat Nanotechnol 2(11) (2007) 679-684.

[13] Q.Z. Zhang, H. Gong, W.W. Gao, L.F. Zhang, Recent Progress in Capturing and Neutralizing Inflammatory Cytokines, Ccs Chem 2(3) (2020) 376-389.

[14] I. Tabas, C.K. Glass, Anti-Inflammatory Therapy in Chronic Disease: Challenges and Opportunities, Science 339(6116) (2013) 166-172.

[15] D.G. Beghini, S. Hernandez-Oliveira, L. Rodrigues-Simioni, J.C. Novello, S. Hyslop, S. Marangoni, Anti-sera raised in rabbits against crotoxin and phospholipase A2 from Crotalus durissus cascavella venom neutralize the neurotoxicity of the venom and crotoxin, Toxicon 44(2) (2004) 141-8.

[16] Z.C. Chen, M. Moayeri, H.Y. Zhao, D. Crown, S.H. Leppla, R.H. Purcell, Potent neutralization of anthrax edema toxin by a humanized monoclonal antibody that competes with calmodulin for edema factor binding, P Natl Acad Sci USA 106(32) (2009) 13487-13492.

[17] C.C. McCormick, A.R. Caballero, C.L. Balzli, A.H. Tang, R.J. O'Callaghan, Chemical Inhibition of Alpha-Toxin, a Key Corneal Virulence Factor of Staphylococcus aureus, Invest Ophth Vis Sci 50(6) (2009) 2848-2854.

[18] D.T. Hung, E.A. Shakhnovich, E. Pierson, J.J. Mekalanos, Small-molecule inhibitor of Vibrio cholerae virulence and intestinal colonization, Science 310(5748) (2005) 670-674.

[19] Y. Hoshino, H. Koide, K. Furuya, W.W. Haberaecker, S.H. Lee, T. Kodama, H. Kanazawa, N. Oku, K.J. Shea, The rational design of a synthetic polymer nanoparticle that neutralizes a toxic peptide in vivo, P Natl Acad Sci USA 109(1) (2012) 33-38.

[20] S. Iwata, Y. Tanaka, Progress in understanding the safety and efficacy of Janus kinase inhibitors for treatment of rheumatoid arthritis, Expert Rev Clin Immu 12(10) (2016) 1047-1057.

[21] R.J. Gilbert, Pore-forming toxins, Cell Mol Life Sci 59(5) (2002) 832-44.

[22] F. Hayes, L. Van Melderen, Toxins-antitoxins: diversity, evolution and function, Crit Rev Biochem Mol 46(5) (2011) 386-408.

[23] E. Bekerman, S. Einav, Infectious disease. Combating emerging viral threats, Science 348(6232) (2015) 282-3.

[24] R.H. Fang, A.V. Kroll, W.W. Gao, L.F. Zhang, Cell Membrane Coating Nanotechnology, Adv Mater 30(23) (2018) 1706759.

[25] C.M.J. Hu, L. Zhang, S. Aryal, C. Cheung, R.H. Fang, L.F. Zhang, Erythrocyte membrane-camouflaged polymeric nanoparticles as a biomimetic delivery platform, P Natl Acad Sci USA 108(27) (2011) 10980-10985.

[26] C.M.J. Hu, R.H. Fang, J. Copp, B.T. Luk, L.F. Zhang, A biomimetic nanosponge that absorbs pore-forming toxins, Nat Nanotechnol 8(5) (2013) 336-340.

[27] Y.J. Chen, M.C. Chen, Y. Zhang, J.H. Lee, T. Escajadillo, H. Gong, R.H. Fang, W.W. Gao, V. Nizet, L.F. Zhang, Broad-Spectrum Neutralization of Pore-Forming Toxins with Human Erythrocyte Membrane-Coated Nanosponges, Adv Healthc Mater 7(13) (2018).

[28] J.A. Copp, R.H. Fang, B.T. Luk, C.M.J. Hu, W.W. Gao, K. Zhang, L.F. Zhang, Clearance of pathological antibodies using biomimetic nanoparticles, P Natl Acad Sci USA 111(37) (2014) 13481-13486.

[29] Z.Q. Pang, C.M.J. Hu, R.H. Fang, B.T. Luk, W.W. Gao, F. Wang, E. Chuluun, P. Angsantikul, S. Thamphiwatana, W.Y. Lu, X.G. Jiang, L.F. Zhang, Detoxification of Organophosphate Poisoning Using Nanoparticle Bioscavengers, Acs Nano 9(6) (2015) 6450-6458.

[30] X.L. Wei, G. Zhang, D.N. Ran, N. Krishnan, R.H. Fang, W.W. Gao, S.A. Spector, L.F. Zhang, T-Cell-Mimicking Nanoparticles Can Neutralize HIV Infectivity, Adv Mater 30(45) (2018).

[31] G. Zhang, G.R. Campbell, Q.Z. Zhang, E. Maule, J. Hanna, W.W. Gao, L.F. Zhang, S.A. Spector, CD4(+) T Cell-Mimicking Nanoparticles Broadly Neutralize HIV-1 and Suppress Viral Replication through Autophagy, Mbio 11(5) (2020).

[32] Q.Z. Zhang, A. Honko, J.R. Zhou, H. Gong, S.N. Downs, J.H. Vasquez, R.H. Fang, W.W. Gao, A. Griffiths, L.F. Zhang, Cellular Nanosponges Inhibit SARS-CoV-2 Infectivity, Nano Lett 20(7) (2020) 5570-5574.

[33] W.W. Gao, Y.J. Chen, Y. Zhang, Q.Z. Zhang, L.F. Zhang, Nanoparticle-based local antimicrobial drug delivery, Adv Drug Deliver Rev 127 (2018) 46-57.

[34] S.Y. Wang, Y.O. Duan, Q.Z. Zhang, A. Komarla, H. Gong, W.W. Gao, L.F. Zhang, Drug Targeting via Platelet Membrane-Coated Nanoparticles, Small Struct 1(1) (2020).

[35] A. Verma, M.M. Ngundi, G.A. Price, K. Takeda, J. Yu, D.L. Burns, Role of the Antigen Capture Pathway in the Induction of a Neutralizing Antibody Response to Anthrax Protective Antigen, Mbio 9(1) (2018).

[36] M. Paul, L. Leibovici, Combination Antimicrobial Treatment Versus Monotherapy: The Contribution of Meta-analyses, Infect Dis Clin N Am 23(2) (2009) 277-+.

[37] M.J. McConnell, Where are we with monoclonal antibodies for multidrug-resistant infections?, Drug Discov Today 24(5) (2019) 1132-1138.

[38] F.C.O. Los, T.M. Randis, R.V. Aroian, A.J. Ratner, Role of Pore-Forming Toxins in Bacterial Infectious Diseases, Microbiol Mol Biol R 77(2) (2013) 173-207.

[39] Y.W. He, R.X. Li, H.C. Li, S.Y. Zhang, W.T. Dai, Q. Wu, L.X. Jiang, Z.C. Zheng, S. Shen, X. Chen, Y.F. Zhu, J.X. Wang, Z.Q. Pang, Erythroliposomes: Integrated Hybrid Nanovesicles Composed of Erythrocyte Membranes and Artificial Lipid Membranes for Pore-Forming Toxin Clearance, Acs Nano 13(4) (2019) 4148-4159.

[40] V. Chhabria, S. Beeton, Development of nanosponges from erythrocyte ghosts for removal of streptolysin-O from mammalian blood, Nanomedicine-Uk 11(21) (2016) 2797-2807.

[41] T. Escajadillo, J. Olson, B.T. Luk, L. Zhang, V. Nizet, A Red Blood Cell Membrane-Camouflaged Nanoparticle Counteracts Streptolysin O-Mediated Virulence Phenotypes of Invasive Group A Streptococcus, Front Pharmacol 8 (2017) 477.

[42] J. Xie, Q. Shen, K.X. Huang, T.Y. Zheng, L.T. Cheng, Z. Zhang, Y. Yu, G.J. Liao, X.Y. Wang, C. Li, Oriented Assembly of Cell-Mimicking Nanoparticles via a Molecular Affinity Strategy for Targeted Drug Delivery, Acs Nano 13(5) (2019) 5268-5277.

[43] A.L. LaGrow, P.S. Coburn, F.C. Miller, C. Land, S.M. Parkunan, B.T. Luk, W.W. Gao, L.F. Zhang, M.C. Callegan, A Novel Biomimetic Nanosponge Protects the Retina from the Enterococcus faecalis Cytolysin, Msphere 2(6) (2017).

[44] Y.J. Chen, Y. Zhang, M.C. Chen, J. Zhuang, R.H. Fang, W.W. Gao, L.F. Zhang, Biomimetic Nanosponges Suppress In Vivo Lethality Induced by the Whole Secreted Proteins of Pathogenic Bacteria, Small 15(6) (2019).

[45] B. Chen, F.F. Li, X.K. Zhu, W. Xie, X. Hu, M.H. Zan, X.K. Li, Q.Y. Li, S.S. Guo, X.Z. Zhao, Y.A. Jiang, Z.J. Cao, W. Liu, Highly biocompatible and recyclable biomimetic nanoparticles for antibiotic-resistant bacteria infection, Biomater Sci-Uk 9(3) (2021) 826-834.

[46] F. Wang, W.W. Gao, S. Thamphiwatana, B.T. Luk, P. Angsantikul, Q.Z. Zhang, C.M.J. Hu, R.H. Fang, J.A. Copp, D. Pornpattananangkul, W.Y. Lu, L.F. Zhang, Hydrogel Retaining Toxin-Absorbing Nanosponges for Local Treatment of Methicillin-Resistant Staphylococcus aureus Infection, Adv Mater 27(22) (2015) 3437-3443.

[47] Y. Zhang, J.H. Zhang, W.S. Chen, P. Angsantikul, K.A. Spiekermann, R.H. Fang, W.W. Gao, L.F. Zhang, Erythrocyte membrane-coated nanogel for combinatorial antivirulence and responsive antimicrobial delivery against Staphylococcus aureus infection, J Control Release 263 (2017) 185-191.

[48] E. Ben-Akiva, R.A. Meyer, H.Z. Yu, J.T. Smith, D.M. Pardoll, J.J. Green, Biomimetic anisotropic polymeric nanoparticles coated with red blood cell membranes for enhanced circulation and toxin removal, Sci Adv 6(16) (2020).

[49] Z.G. Wu, T.L. Li, W. Gao, T.L. Xu, B. Jurado-Sanchez, J.X. Li, W.W. Gao, Q. He, L.F. Zhang, J. Wang, Cell-Membrane-Coated Synthetic Nanomotors for Effective Biodetoxification, Adv Funct Mater 25(25) (2015) 3881-3887.

[50] O. Shannon, Platelet interaction with bacterial toxins and secreted products, Platelets 26(4) (2015) 302-308.

[51] J.X. Li, P. Angsantikul, W.J. Liu, B.E.F. de Avila, X.C. Chang, E. Sandraz, Y.Y. Liang, S.Y. Zhu, Y. Zhang, C.R. Chen, W.W. Gao, L.F. Zhang, J. Wang, Biomimetic Platelet-Camouflaged Nanorobots for Binding and Isolation of Biological Threats, Adv Mater 30(2) (2018).

[52] Y. Zhang, Y.J. Chen, C. Lo, J. Zhuang, P. Angsantikul, Q.Z. Zhang, X.L. Wei, Z.D. Zhou, M. Obonyo, R.H. Fang, W.W. Gao, L.F. Zhang, Inhibition of Pathogen Adhesion by Bacterial Outer Membrane-Coated Nanoparticles, Angew Chem Int Edit 58(33) (2019) 11404-11408.

[53] X.L. Wei, D.N. Ran, A. Campeau, C. Xiao, J.R. Zhou, D. Dehaini, Y. Jiang, A.V. Kroll, Q.Z. Zhang, W.W. Gao, D.J. Gonzalez, R.H. Fang, L.F. Zhang, Multiantigenic Nanotoxoids for Antivirulence Vaccination against Antibiotic-Resistant Gram-Negative Bacteria, Nano Lett 19(7) (2019) 4760-4769.

[54] J.D. Lapek, R.H. Fang, X.L. Wei, P.Y. Li, B. Wang, L.F. Zhang, D.J. Gonzalez, Biomimetic Virulomics for Capture and Identification of Cell-Type Specific Effector Proteins, Acs Nano 11(12) (2017) 11831-11838.

[55] U. Distler, S. Tenzer, Tools for Pathogen Proteomics: Fishing with Biomimetic Nanosponges, Acs Nano 11(12) (2017) 11768-11772.

[56] F. Worek, M. Koller, H. Thiermann, L. Szinicz, Diagnostic aspects of organophosphate poisoning, Toxicology 214(3) (2005) 182-189.

[57] S. Costanzi, J.H. Machado, M. Mitchell, Nerve Agents: What They Are, How They Work, How to Counter Them, Acs Chem Neurosci 9(5) (2018) 873-885.

[58] Y.J. Chen, Z. Jia, J. Zhuang, J.H. Lee, L.C. Wang, R.H. Fang, W.W. Gao, L.F. Zhang, Cell-Membrane-Cloaked Oil Nanosponges Enable Dual-Modal Detoxification, Acs Nano 13(6) (2019) 7209-7215.

[59] T.D.T. Nguyen, A. Pitchaimani, M.B. Koirala, F. Muhammad, S. Aryal, Engineered biomimetic nanoabsorbent for cellular detoxification of chemotherapeutics, Rsc Adv 6(39) (2016) 33003-33008.

[60] H. Gong, Q.Z. Zhang, A. Komarla, S.Y. Wang, Y. Duan, Z.D. Zhou, F. Chen, R.H. Fang, S. Xu, W.W. Gao, L.F. Zhang, Nanomaterial Biointerfacing via Mitochondrial Membrane Coating for Targeted Detoxification and Molecular Detection, Nano Lett 21(6) (2021) 2603-2609.

[61] X.Z. Ai, S.Y. Wang, Y.O. Duan, Q.Z. Zhang, M.S. Chen, W.W. Gao, L.F. Zhang, Emerging Approaches to Functionalizing Cell Membrane-Coated Nanoparticles, Biochemistry-Us 60(13) (2021) 941-955.

[62] P. Zhang, E.J. Liu, C. Tsao, S.A. Kasten, M.V. Boeri, T.L. Dao, S.J. Debus, C.L. Cadieux, C.A. Baker, T.C. Otto, D.M. Cerasoli, Y.T. Chen, P. Jain, F. Sun, W.C. Li, H.C. Hung, Z.F. Yuan, J.R. Ma, A.N. Bigley, F.M. Raushel, S.Y. Jiang, Nanoscavenger provides long-term prophylactic protection against nerve agents in rodents, Sci Transl Med 11(473) (2019).

[63] Y. Liu, J.J. Du, M. Yan, M.Y. Lau, J. Hu, H. Han, O.O. Yang, S. Liang, W. Wei, H. Wang, J.M. Li, X.Y. Zhu, L.Q. Shi, W. Chen, C. Ji, Y.F. Lu, Biomimetic enzyme nanocomplexes and their use as antidotes and preventive measures for alcohol intoxication, Nat Nanotechnol 8(3) (2013) 187-192.

[64] T. Hanada, A. Yoshimura, Regulation of cytokine signaling and inflammation, Cytokine Growth F R 13(4-5) (2002) 413-421.

[65] B.G. Chousterman, F.K. Swirski, G.F. Weber, Cytokine storm and sepsis disease pathogenesis, Semin Immunopathol 39(5) (2017) 517-528.

[66] J.M. Cavaillon, M. Adib-Conquy, C. Fitting, C. Adrie, D. Payen, Cytokine cascade in sepsis, Scand J Infect Dis 35(9) (2003) 535-544.

[67] G.R. Burmester, E. Feist, T. Doerner, Emerging cell and cytokine targets in rheumatoid arthritis, Nat Rev Rheumatol 10(2) (2014) 77-88.

[68] M. Noack, P. Miossec, Selected cytokine pathways in rheumatoid arthritis, Semin Immunopathol 39(4) (2017) 365-383.

[69] M.F. Neurath, Cytokines in inflammatory bowel disease, Nat Rev Immunol 14(5) (2014) 329-342.

[70] F. Sanchez-Munoz, A. Dominguez-Lopez, J.K. Yamamoto-Furusho, Role of cytokines in inflammatory bowel disease, World J Gastroentero 14(27) (2008) 4280-4288.

[71] D. Tousoulis, E. Oikonomou, E.K. Economou, F. Crea, J.C. Kaski, Inflammatory cytokines in atherosclerosis: current therapeutic approaches, Eur Heart J 37(22) (2016) 1723-+.

[72] H. Ait-Oufella, S. Taleb, Z. Mallat, A. Tedgui, Recent Advances on the Role of Cytokines in Atherosclerosis, Arterioscl Throm Vas 31(5) (2011) 969-979.

[73] A.S. Rosenberg, M. Puig, K. Nagaraju, E.P. Hoffman, S.A. Villalta, V.A. Rao, L.M. Wakefield, J. Woodcock, Immune-mediated pathology in Duchenne muscular dystrophy, Sci Transl Med 7(299) (2015).

[74] M. Feldmann, R.O. Williams, E. Paleolog, What have we learnt from targeted anti-TNF therapy?, Ann Rheum Dis 69 (2010) 97-99.

[75] E.H.S. Choy, G.S. Panayi, Mechanisms of disease: Cytokine pathways and joint inflammation in rheumatoid arthritis., New Engl J Med 344(12) (2001) 907-916.

[76] K. Peters, R.E. Unger, J. Brunner, C.J. Kirkpatrick, Molecular basis of endothelial dysfunction in sepsis, Cardiovasc Res 60(1) (2003) 49-57.

[77] S. Thamphiwatana, P. Angsantikul, T. Escajadillo, Q.Z. Zhang, J. Olson, B.T. Luk, S. Zhang, R.H. Fang, W.W. Gao, V. Nizet, L.F. Zhang, Macrophage-like nanoparticles concurrently absorbing endotoxins and proinflammatory cytokines for sepsis management, P Natl Acad Sci USA 114(43) (2017) 11488-11493.

[78] S. Shen, F. Han, A.R. Yuan, L. Wu, J. Cao, J. Qian, X.Y. Qi, Y.S. Yan, Y.R. Ge, Engineered nanoparticles disguised as macrophages for trapping lipopolysaccharide and preventing endotoxemia, Biomaterials 189 (2019) 60-68.

[79] M.S. Shi, K.L. Shen, B. Yang, P. Zhang, K.L. Lv, H.N. Qi, Y.X. Wang, M. Li, Q. Yuan, Y.F. Zhang, An electroporation strategy to synthesize the membrane-coated nanoparticles for enhanced anti-inflammation therapy in bone infection, Theranostics 11(5) (2021) 2349-2363.

[80] J. Zhuang, Y. Duan, Q.Z. Zhang, W.W. Gao, S.L. Li, R.H. Fang, L.F. Zhang, Multimodal Enzyme Delivery and Therapy Enabled by Cell Membrane-Coated Metal-Organic Framework Nanoparticles, Nano Lett 20(5) (2020) 4051-4058.

[81] Z.B. Ou, H. Zhong, L. Zhang, M.H. Deng, W.F. Zhang, J.Y. Wang, H.G. Feng, J.P. Gong, C.M. Miao, Z.J. Yi, Macrophage Membrane-Coated Nanoparticles Alleviate Hepatic Ischemia-Reperfusion Injury Caused by Orthotopic Liver Transplantation by Neutralizing Endotoxin, Int J Nanomed 15 (2020) 4125-4138.

[82] C.C. Yin, Q. Zhao, W. Li, Z.F. Zhao, J.Y. Wang, T. Deng, P. Zhang, K.L. Shen, Z.B. Li, Y.F. Zhang, Biomimetic anti-inflammatory nano-capsule serves as a cytokine blocker and M2 polarization inducer for bone tissue repair, Acta Biomater 102 (2020) 416-426.

[83] C. Gao, Q.X. Huang, C.H. Liu, C.H.T. Kwong, L.D. Yue, J.B. Wan, S.M.Y. Lee, R.B. Wang, Treatment of atherosclerosis by macrophage-biomimetic nanoparticles via targeted pharmacotherapy and sequestration of proinflammatory cytokines, Nat Commun 11(1) (2020).

[84] Q.Z. Zhang, D. Dehaini, Y. Zhang, J.L. Zhou, X.Y. Chen, L.F. Zhang, R.H. Fang, W.W. Gao, L.F. Zhang, Neutrophil membrane-coated nanoparticles inhibit synovial inflammation and alleviate joint damage in inflammatory arthritis, Nat Nanotechnol 13(12) (2018) 1182-+.

[85] S.Y. Li, Q. Wang, Y.Q. Shen, M. Hassan, J.Z. Shen, W. Jiang, Y.T. Su, J. Chen, L. Bai, W.C. Zhou, Y.C. Wang, Pseudoneutrophil Cytokine Sponges Disrupt Myeloid Expansion and Tumor Trafficking to Improve Cancer Immunotherapy, Nano Lett 20(1) (2020) 242-251.

[86] K. Lechner, U. Jager, How I treat autoimmune hemolytic anemias in adults, Blood 116(11) (2010) 1831-1838.

[87] D.M. Arnold, N.M. Heddle, J. Carruthers, D.J. Cook, M.A. Crowther, R.M. Meyer, Y. Liu, R.J. Cook, A. McLeod, J.A. MacEachern, J. Mangel, D. Anderson, L. Vickars, A. Tinmouth, A.C. Schuh, J.G. Kelton, A pilot randomized trial of adjuvant rituximab or placebo for nonsplenectomized patients with immune thrombocytopenia, Blood 119(6) (2012) 1356-1362.

[88] A. Shander, M.D. Cappellini, L.T. Goodnough, Iron overload and toxicity: the hidden risk of multiple blood transfusions, Vox Sang 97(3) (2009) 185-197.

[89] A. Salama, H. Berghofer, C. Mueller-Eckhardt, Red blood cell transfusion in warm-type autoimmune haemolytic anaemia, Lancet 340(8834-8835) (1992) 1515-7.

[90] N. Ahrens, A. Pruss, A. Kahne, H. Kiesewetter, A. Salama, Coexistence of autoantibodies and alloantibodies to red blood cells due to blood transfusion, Transfusion 47(5) (2007) 813-816.

[91] X.L. Wei, J. Gao, R.H. Fang, B.T. Luk, A.V. Kroll, D. Dehaini, J.R. Zhou, H.W. Kim, W.W. Gao, W.Y. Lu, L.F. Zhang, Nanoparticles camouflaged in platelet membrane coating as an antibody decoy for the treatment of immune thrombocytopenia, Biomaterials 111 (2016) 116-123.

[92] F. Rodeghiero, R. Stasi, T. Gernsheimer, M. Michel, D. Provan, D.M. Arnold, J.B. Bussel, D.B. Cines, B.H. Chong, N. Cooper, B. Godeau, K. Lechner, M.G. Mazzucconi, R. McMillan, M.A. Sanz, P. Imbach, V. Blanchette, T. Kuhne, M. Ruggeri, J.N. George, Standardization of

terminology, definitions and outcome criteria in immune thrombocytopenic purpura of adults and children: report from an international working group, Blood 113(11) (2009) 2386-2393.

[93] D. Provan, R. Stasi, A.C. Newland, V.S. Blanchette, P. Bolton-Maggs, J.B. Bussel, B.H. Chong, D.B. Cines, T.B. Gernsheimer, B. Godeau, J. Grainger, I. Greer, B.J. Hunt, P.A. Imbach, G. Lyons, R. McMillan, F. Rodeghiero, M.A. Sanz, M. Tarantino, S. Watson, J. Young, D.J. Kuter, International consensus report on the investigation and management of primary immune thrombocytopenia, Blood 115(2) (2010) 168-186.

[94] J.B. Segal, N.R. Powe, Prevalence of immune thrombocytopenia: analyses of administrative data, J Thromb Haemost 4(11) (2006) 2377-2383.

[95] K. Kojouri, S.K. Vesely, D.R. Terrell, J.N. George, Splenectomy for adult patients with idiopathic thrombocytopenic purpura: a systematic review to assess long-term platelet count responses, prediction of response, and surgical complications, Blood 104(9) (2004) 2623-2634.

[96] W. Ghanima, B. Godeau, D.B. Cines, J.B. Bussel, How I treat immune thrombocytopenia: the choice between splenectomy or a medical therapy as a second-line treatment, Blood 120(5) (2012) 960-969.

[97] L.J. Picker, D.I. Watkins, HIV pathogenesis: The first cut is the deepest, Nat Immunol 6(5) (2005) 430-432.

[98] C.B. Wilen, J.C. Tilton, R.W. Doms, HIV: Cell Binding and Entry, Csh Perspect Med 2(8) (2012).

[99] A.G. Harrison, T. Lin, P.H. Wang, Mechanisms of SARS-CoV-2 Transmission and Pathogenesis, Trends Immunol 41(12) (2020) 1100-1115.

[100] R.H. Yan, Y.Y. Zhang, Y.N. Li, L. Xia, Y.Y. Guo, Q. Zhou, Structural basis for the recognition of SARS-CoV-2 by full-length human ACE2, Science 367(6485) (2020) 1444-+.

[101] K. Wang, W. Chen, Z. Zhang, Y.Q. Deng, J.Q. Lian, P. Du, D. Wei, Y. Zhang, X.X. Sun, L. Gong, X. Yang, L. He, L. Zhang, Z.W. Yang, J.J. Geng, R. Chen, H. Zhang, B. Wang, Y.M. Zhu, G. Nan, J.L. Jiang, L. Li, J. Wu, P. Lin, W. Huang, L.Z. Xie, Z.H. Zheng, K. Zhang, J.L. Miao, H.Y. Cui, M. Huang, J. Zhang, L. Fu, X.M. Yang, Z.P. Zhao, S.H. Sun, H.J. Gu, Z. Wang, C.F. Wang, Y.C. Lu, Y.Y. Liu, Q.Y. Wang, H.J. Bian, P. Zhu, Z.N. Chen, CD147-spike protein is a novel route for SARS-CoV-2 infection to host cells, Signal Transduct Tar 5(1) (2020).

[102] J.B. Moore, C.H. June, Cytokine release syndrome in severe COVID-19, Science 368(6490) (2020) 473-474.

[103] I. Lee, S. Bos, G. Li, S.S. Wang, G. Gadea, P. Despres, R.Y. Zhao, Probing Molecular Insights into Zika Virus-Host Interactions, Viruses-Basel 10(5) (2018).

[104] J.K. Lee, O.S. Shin, Advances in Zika Virus-Host Cell Interaction: Current Knowledge and Future Perspectives, Int J Mol Sci 20(5) (2019).

[105] M.I. Giraldo, H.J. Xia, L. Aguilera-Aguirre, A. Hage, S. van Tol, C. Shan, X.P. Xie, G.L. Sturdevant, S.J. Robertson, K.L. McNally, K. Meade-White, S.R. Azar, S.L. Rossi, W. Maury, M. Woodson, H. Ramage, J.R. Johnson, N.J. Krogan, M.C. Morais, S.M. Best, P.Y. Shi, R. Rajsbaum, Envelope protein ubiquitination drives entry and pathogenesis of Zika virus, Nature 585(7825) (2020) 414-+.

[106] R.J. Gestuveo, J. Royle, C.L. Donald, D.J. Lamont, E.C. Hutchinson, A. Merits, A. Kohl, M. Varjak, Analysis of Zika virus capsid-Aedes aegypti mosquito interactome reveals pro-viral host factors critical for establishing infection, Nat Commun 12(1) (2021).

[107] L. Rao, W.B. Wang, Q.F. Meng, M.F. Tian, B. Cai, Y.C. Wang, A.X. Li, M.H. Zan, F. Xiao, L.L. Bu, G. Li, A. Li, Y.L. Liu, S.S. Guo, X.Z. Zhao, T.H. Wang, W. Liu, J.G. Wu, A Biomimetic Nanodecoy Traps Zika Virus To Prevent Viral Infection and Fetal Microcephaly Development, Nano Lett 19(4) (2019) 2215-2222.

[108] M.Z. Tay, C.M. Poh, L. Renia, P.A. MacAry, L.F.P. Ng, The trinity of COVID-19: immunity, inflammation and intervention, Nat Rev Immunol 20(6) (2020) 363-374.

[109] H.Z. Yan, D. Shao, Y.H. Lao, M.Q. Li, H.Z. Hu, K.W. Leong, Engineering Cell Membrane-Based Nanotherapeutics to Target Inflammation, Adv Sci 6(15) (2019).

[110] Y. Jiang, N. Krishnan, J.R. Zhou, S. Chekuri, X.L. Wei, A.V. Kroll, C.L. Yu, Y.O. Duan, W.W. Gao, R.N.H. Fang, L.F. Zhang, Engineered Cell-Membrane-Coated Nanoparticles Directly Present Tumor Antigens to Promote Anticancer Immunity, Adv Mater 32(30) (2020).

[111] W.S. Chen, Q.Z. Zhang, B.T. Luk, R.H. Fang, Y.N. Liu, W.W. Gao, L.F. Zhang, Coating nanofiber scaffolds with beta cell membrane to promote cell proliferation and function, Nanoscale 8(19) (2016) 10364-10370.

[112] H. Gong, F. Chen, Z.L. Huang, Y. Gu, Q.Z. Zhang, Y.J. Chen, Y. Zhang, J. Zhuang, Y.K. Cho, R.N.H. Fang, W.W. Gao, S. Xu, L.F. Zhang, Biomembrane-Modified Field Effect Transistors for Sensitive and Quantitative Detection of Biological Toxins and Pathogens, Acs Nano 13(3) (2019) 3714-3722.

[113] R. Lanza, D.W. Russell, A. Nagy, Engineering universal cells that evade immune detection, Nat Rev Immunol 19(12) (2019) 723-733.

[114] S.C. Nath, L. Harper, D.E. Rancourt, Cell-Based Therapy Manufacturing in Stirred Suspension Bioreactor: Thoughts for cGMP Compliance, Front Bioeng Biotech 8 (2020).

[115] J.M. Cha, M.Y. Lee, J. Hong, Bioreactor systems are essentially required for stem cell bioprocessing, Precis Future Med 3(1) (2019) 19-23.

Chapter 1, in full, is a reprint of the material as it appears in *Advanced Materials*, 2022 by Shuyan Wang, Dan Wang, Yaou Duan, Zhidong Zhou, Weiwei Gao, and Liangfang Zhang. The dissertation author was a major contributor and co-author of this paper.

Chapter 2

Multimodal Enzyme Delivery and Therapy Enabled by Cell Membrane-Coated Metal-Organic Framework Nanoparticles

2.1 Introduction

Enzymes are biocatalysts that help to carry out reactions essential to the normal functioning of all living organisms. The lack of critical enzymes or the loss of their functions could lead to the deleterious accumulation of biomolecule substrates, disrupting metabolic activities with potentially life-threatening consequences [1, 2]. Defective enzyme production commonly occurs as a result of inherited genetic disorders. Examples include Gaucher disease and Fabry disease [3, 4], both of which are lysosomal storage disorders caused by mutations in important housekeeping hydrolase genes [5, 6]. The evolutionary loss of certain genes is another cause of enzyme deficiency that can lead to some disease states [7]. For instance, uricase, the enzyme responsible for uric acid conversion into allantoin, is not encoded in the human genome, which can result in gouty arthritis when urate crystals are deposited in the joints [8, 9]. Enzyme replacement therapy has become the current standard of care for patients with enzyme deficiency, where exogenous proteins are intravenously infused into the bloodstream [10, 11]. Despite their application in the clinic, enzymes in free form usually suffer from protease susceptibility and short-acting pharmacokinetics, both of which can severely compromise bioavailability [12, 13]. In order to attain a therapeutic benefit, frequent administration is oftentimes mandatory for these therapies [14, 15], leading to high costs and negatively impacting patient compliance [16].

The use of nanoparticulate systems is an emerging strategy to address some of the shortcomings associated with the administration of free enzymes [17, 18]. Ideally, functional enzymes can be encased into a nanoscale network that allows their catalytic activities to be maintained, enabling substrate molecules to access the enzyme while preventing unwanted proteolytic degradation by the surrounding environment [19, 20]. Among the various nanomaterials, metal–organic frameworks (MOFs) have shown great promise for enzyme delivery

applications [21, 22]. MOFs can be fabricated with porous structures that facilitate high-yield enzyme loading and allow size-selective exposure to the targeted substrate [23, 24]. Despite these favorable characteristics, MOF-based platforms exhibit biocompatibility issues and run the risk of inducing immune reactions [25, 26], which would impede their translation into the clinic.

The use of cell membrane coatings to camouflage synthetic nanomaterials is an effective method for nanoparticle functionalization [27]. The membrane-coated nanoparticles fabricated using this platform technology exhibit cell-mimicking properties that enable them to excel at *in vivo* applications [28]. For example, red blood cell (RBC) membrane coatings can greatly prolong circulation within the bloodstream [29, 30], whereas platelet membrane coatings enable targeted delivery to bacteria, cancer, and damaged vasculature [31, 32]. It was also demonstrated that nanoparticles functionalized with white blood cell membrane can be used as nanoscale decoys to absorb and neutralize inflammatory cytokines, with potential applications for autoimmune disorders and sepsis treatment [33, 34]. Overall, cell membrane coatings can be derived from any type of cell, enabling researchers a wide range of options for adding functionality and creating synergies with nanoparticle-based therapeutics [27, 28, 35]. Notably, it was recently demonstrated that this approach could be applied to MOF nanoparticles loaded with siRNA for anticancer applications [36].

Here, we report on the fabrication of cell membrane-coated MOF nanoparticles for effective enzyme delivery (**Figure 2.1**). Taking uricase as the model enzyme, we successfully loaded the enzyme into a zeolitic imidazolate framework-8 MOF nanoparticle by a facile formulation process with precise input control [37]. The uricase-loaded MOF (MOF-uricase) nanoparticles were then coated with the membrane from either RBCs or macrophages (MΦs), each of which provided application-specific benefits. In particular, RBC membrane-coated MOF-uricase (RBC-MOF-uricase) were systemically administered to catalyze the efficient degradation

of serum uric acid in hyperuricemic mice. MΦ membrane-coated MOF-uricase (MΦ-MOF-uricase) were locally administered into the joints of mice with gout, where the cytokine-neutralizing property of the MΦ membrane synergized with the uricase the alleviate disease symptoms. By changing the enzyme payload and membrane coating, we envision that the reported hybrid delivery platform could be used to improve therapeutic outcomes for a wide range of conditions requiring enzyme therapy.

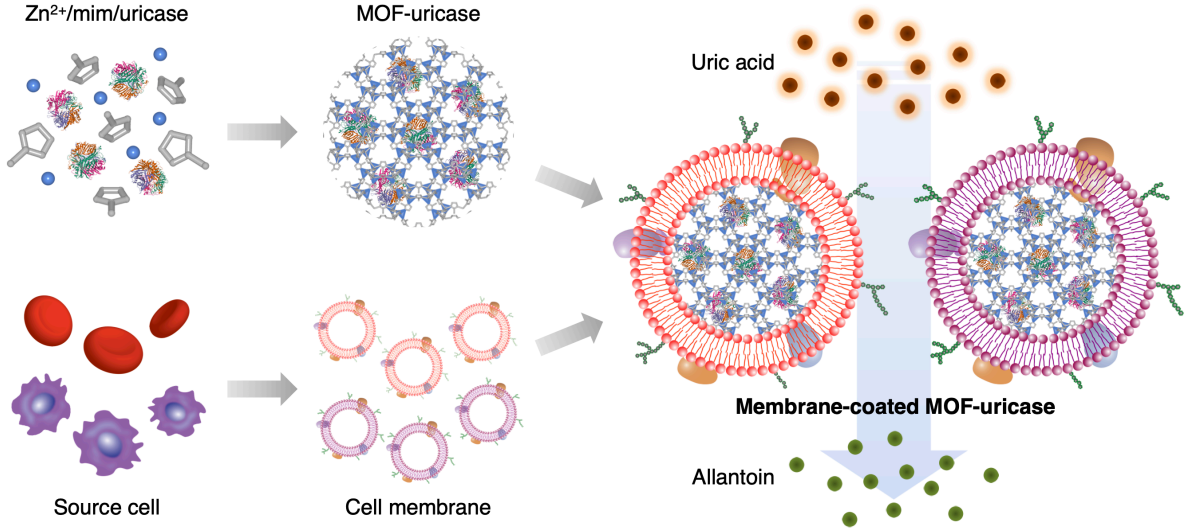

Figure 2.1 Cell membrane-coated uricase-loaded MOF nanoparticles for the enzymatic degradation of uric acid. To fabricate the formulation, MOF-uricase cores are generated by mixing the enzyme payload with Zn^{2+} and 2-methylimidazole (mim), followed by coating with natural cell membrane derived from source cells such as RBCs or MΦs. The resulting membrane-coated MOF-uricase nanoparticles effectively convert uric acid into allantoin, which can help to manage conditions such hyperuricemia and gout.

2.2 Results and Discussion

In the study, recombinant uricase was encapsulated within the MOF nanoparticles using a one-pot synthesis approach [36]. The enzyme was first premixed with 2-methylimidazole and added to a zinc ion-containing solution to start a process of self-assembly, which yielded bare MOF-uricase nanoparticles after several hours. To coat MOF-uricase with cell membrane, the freshly formed nanoparticles were physically extruded together with purified mouse RBC

membrane through porous polycarbonate membranes. The final RBC-MOF-uricase nanoparticles were isolated by centrifugation. To quantify loading efficiency, the uricase was fluorescently labeled, and then RBC-MOF-uricase were fabricated using different input amounts of the enzyme (**Figure 2.2A**). Across the inputs that were evaluated, the encapsulation efficiency was consistently around 90% up to 0.25 U of uricase. It should be noted that formulations fabricated with higher uricase inputs were unstable. The size of the RBC-MOF-uricase was highly dependent on uricase input (**Figure 2.2B**). RBC membrane-coated MOF (RBC-MOF) nanoparticles without any uricase were approximately 130 nm in size, whereas the size of RBC-MOF-uricase grew to near 270 nm at the highest input of 0.25 U. To prevent premature splenic clearance *in vivo* after intravenous administration [38], sub-200 nm RBC-MOF-uricase fabricated using a 0.1 U uricase input were used for further study.

Compared with bare MOF, the size of MOF-uricase increased by approximately 70 nm, and coating with the RBC membrane further increased the size of the nanoparticles by about 25 nm (**Figure 2.2C**). The surface zeta potential of the MOF dropped from 30 mV to 18 mV after uricase encapsulation, while the final RBC-MOF-uricase formulation displayed a negative surface potential of -30 mV (**Figure 2.2D**). The near identical surfaces charges between the RBC-MOF-uricase and the purified RBC membrane suggested good coating coverage. To visualize the physical structure of RBC-MOF-uricase, the nanoparticles were negatively stained with uranyl acetate and examined under transmission electron microscopy (**Figure 2.2E**). The imaging confirmed a characteristic core–shell structure, which is consistent with similar cell membrane-coated nanoparticle platforms, including those employing MOF cores [36, 39, 40].

The stability of the RBC-MOF-uricase formulation in physiological condition was evaluated by measuring size in phosphate buffered saline (PBS) over the course of 8 days

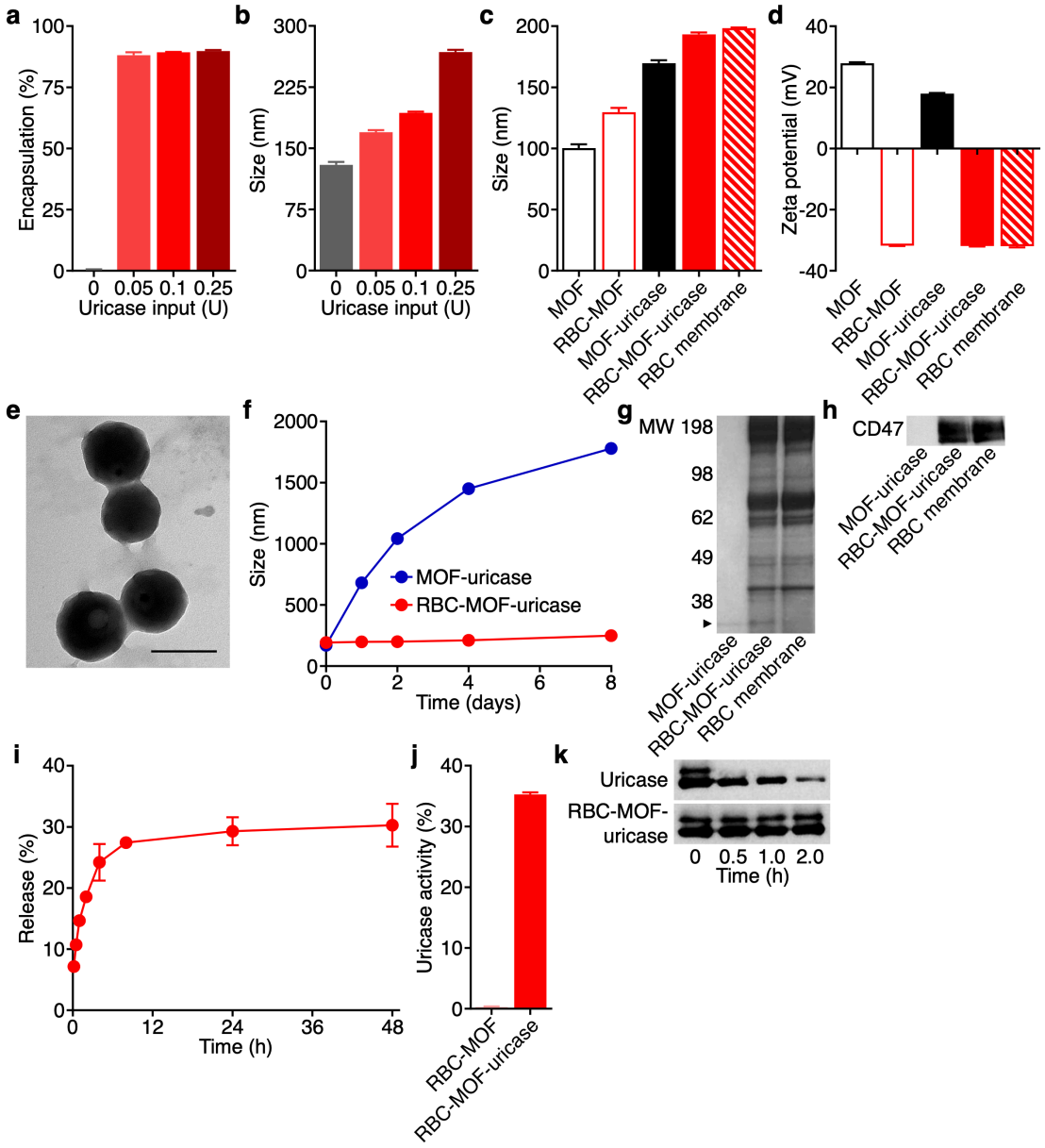

Figure 2.2 Synthesis and characterization of RBC-MOF-uricase. (a) Encapsulation efficiency of uricase in RBC-MOF-uricase at different uricase inputs (n = 3, mean + SD). (b) Diameter of RBC-MOF-uricase at different uricase inputs (n = 3, mean + SD). (c) Diameter of pristine MOF, RBC-MOF, MOF-uricase, RBC-MOF-uricase, and RBC membrane vesicles after fabrications (n = 3, mean + SD). (d) Zeta potential of pristine MOF, RBC-MOF, MOF-uricase, RBC-MOF-uricase, and RBC membrane vesicles after fabrication (n = 3, mean + SD). (e) Transmission electron microscopy image of RBC-MOF-uricase stained with uranyl acetate. Scale bar: 200 nm. (f) Stability of RBC-MOF-uricase over the course of 8 days (n = 3, mean ± SD). (g) Protein profiles of MOF-uricase, RBC-MOF-uricase, and RBC membrane. MW, molecular weight (kDa); arrow indicates uricase band. (h) Western blot for RBC surface marker CD47 (50 kDa) on MOF-uricase, RBC-MOF-uricase, and RBC membrane. (i) Uricase release from RBC-MOF-uricase at pH 7.4 in PBS over time (n = 3, mean ± SD). (j) *In vitro* uric acid conversion by RBC-MOF or RBC-MOF-uricase normalized to free uricase activity (n = 3, mean + SD). (k) Degradation of uricase (35 kDa), either in free form or in RBC-MOF-uricase, when exposed to trypsin for increasing amounts of time.

(**Figure 2.2F**). Whereas the uncoated MOF-uricase quickly grew in size to over 1 μm, the RBC membrane-coated nanoparticles exhibited a minimal size increase. This highlighted the role of the cell membrane in enhancing the colloidal stability of MOF-based systems. Next, we sought to characterize the protein content of RBC-MOF-uricase as an additional means on confirming membrane coating. The overall protein profile of the nanoformulation was near identical to that of purified RBC membrane, indicating successful translocation of the membrane proteins (**Figure 2.2G**). The RBC-MOF-uricase sample had an additional band at approximately 35 kDa, indicating the presence of uricase; this band was present on the protein profile for the uncoated MOF-uricase sample, but not for the purified RBC membrane. Western blotting analysis was used to confirm the presence of CD47 (**Figure 2.2H**), a key membrane protein found on RBCs that helps to reduce immune clearance by acting as a 'marker-of-self' [41].

The release of the uricase payload from the RBC-MOF-uricase formulation was profiled over time in PBS (**Figure 2.2I**). A quick burst was observed in the first 4 h, after which the release plateaued near 30%. Over the course of 2 days, more than 70% of the loaded uricase was retained, suggesting that the nanocomplex was highly stable and could be used to achieve prolonged delivery of the enzyme payload. The catalytic activity of RBC-MOF-uricase against uric acid as a substrate was evaluated *in vitro* (**Figure 2.2J**). From the results, it was observed that unloaded RBC-MOF nanoparticles had no catalytic activity, whereas the RBC-MOF-uricase retained approximately 35% of the activity of the inputted uricase. The decrease in catalytic activity may be partly explained by the fact that not all of the uricase is immediately available to participate in reactions when loaded inside the MOF matrix. To highlight the benefit of encapsulation into RBC-MOF for protecting the enzyme payload, both free uricase and RBC-MOF-uricase were incubated with trypsin (**Figure 2.2K**). From western blot analysis, it was observed that free uricase was

quickly degraded, while the integrity of the uricase inside the nanoformulation was maintained over the course of 2 h. This confirmed that the MOF matrix and membrane coating could provide a barrier to prevent unwanted contact of the encapsulated enzyme with degradative proteases, thus better preserving enzymatic activity over time.

After completing the *in vitro* characterizations, we next sought to characterize the performance of the RBC-MOF-uricase formulation *in vivo*. First, the biodistribution was studied 24 h after administration of RBC-MOF-uricase fluorescently labeled with a far-red dye (**Figure 2.3A**). The majority were found in the liver, which is the main organ mainly responsible for nanoparticle clearance [30]. Notably, approximately 15% of the total fluorescent signal was found in the blood at 24 h, attesting to the long-circulating properties provided by the RBC membrane coating. To assess the *in vivo* activity of the uricase payload, the nanoformulation was used to treat a murine model of hyperuricemia, where elevated uric acid levels are observed in the blood (**Figure 2.3B**). Without any uricase, the serum concentration of uric acid slowly increased over time, whereas intravenous administration of RBC-MOF-uricase resulted in a rapid reduction back to basal levels. In comparison, administration of free uricase only resulted in a transient drop in uric acid levels, which reelevated after 2 h. The modest efficacy observed in mice receiving free uricase could likely be attributed to poor bioavailability, highlighting the need for nanodelivery systems capable of extending blood residence while protecting the enzyme from degradation. To evaluate the biocompatibility of the RBC-MOF-uricase formulation, major blood cell populations, including white blood cells, RBCs, and platelets, were enumerated 24 h after nanoparticle administration (**Figure 2.3C**). No significant difference was observed compared with samples obtained from mice treated with PBS. At the same timepoint, the major organs, including the heart, liver, spleen, lungs, and kidneys, were histologically sectioned and stained with hematoxylin and

eosin (H&E) for analysis (**Figure 2.3D**). The overall structure, integrity, and immune infiltrate in all of these tissues were near identical to those from mice administered with PBS, demonstrating no signs of acute toxicity and further supporting the safety of RBC-MOF-uricase.

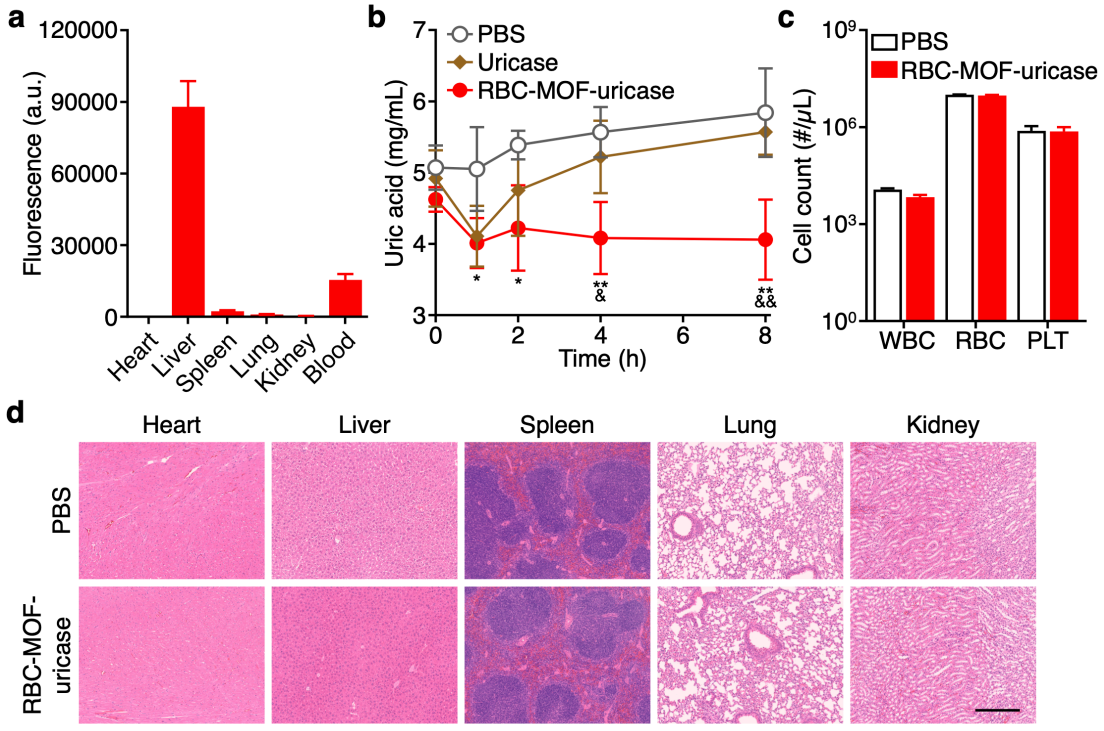

Figure 2.3 ***In vivo*** **hyperuricemia management and safety**. (a) Biodistribution of dye-labeled RBC-MOF-uricase in major organs, including the heart, liver, spleen, lungs, kidneys, and blood, 24 h after intravenous administration (n = 3, mean + SD). (b) Serum uric acid levels over time of hyperuricemic mice after intravenous treatment with PBS, free uricase, or RBC-MOF-uricase (n = 4, mean ± SD). *$p < 0.05$, **$p < 0.01$ (PBS compared with RBC-MOF-uricase); &$p < 0.05$, &&$p < 0.01$ (free uricase compared with RBC-MOF-uricase); one-way ANOVA. (c) Counts of various blood cells 24 h after intravenous administration of PBS or RBC-MOF-uricase (n = 3, geometric mean + SD). WBC: white blood cells, RBC: red blood cells, PLT: platelets. (d) H&E-stained histological sections from major organs 24 h after intravenous administration of PBS or RBC-MOF-uricase into healthy mice. Scale bar: 250 μm.

A major advantage of using cell membrane coatings to functionalize synthetic nanoparticle cores is the ability to custom-tailor the final formulation for different applications by changing the membrane source [27]. To this end, we developed a second MOF-uricase formulation using MΦ membrane, which excels at cytokine neutralization [34], aiming to address gout. The condition is

characterized by the local deposit of uric acid crystals, which can lead to excessive joint inflammation mediated by a number of proinflammatory cytokines [9]. MΦ-MOF-uricase nanoparticles were fabricated similarly to the RBC-based formulation. Because nanoparticles administered locally are not subjected to the same strict size requirements as those for systemic injection, we elected to employ MOF-uricase cores inputted with 0.25 U of uricase to maximize loading, which led to a formulation approximately 270 nm in size (**Figure 2.4A**). The zeta potential of MΦ-MOF-uricase was also negative, matching closely with that of purified MΦ membrane (**Figure 2.4B**). Whereas unloaded MΦ membrane-coated MOF (MΦ-MOF) nanoparticles did not exhibit any uricase activity, MΦ-MOF-uricase retained 38% of the initial activity of the inputted uricase (**Figure 2.4C**).

Proinflammatory cytokines such as interleukin-1β (IL1β), tumor necrosis factor-α (TNFα), and IL6 have been confirmed to play prominent roles in the progression of gout,[42] and MΦ membrane is known to possess their cognate receptors [34]. Accordingly, western blot analysis was used to verify the presence of IL1 receptor type I (IL1R1), IL1R2, TNF receptor-1 (TNFR1), TNFR2, IL6 receptor α-chain (IL6Rα), and glycoprotein 130 (gp130) (Figure 4d). As expected, none of these receptors were found on RBC membrane or RBC-MOF-uricase, whereas every marker was present on both MΦ membrane and MΦ-MOF-uricase. Next, we sought to test if the presence of these receptors on the MΦ-MOF-uricase formulation could be leveraged for the neutralization of the proinflammatory cytokines often implicated in joint inflammation [33]. Recombinant mouse IL1β, mouse TNFα, or mouse IL6 at a final concentration of 8 ng/mL was incubated with the nanoparticles at varying concentrations, and the percentage of bound cytokines was quantified (**Figure 2.4E-G**). Under these experimental conditions, the data indicated that MΦ-MOF-uricase exhibited half maximal inhibitory concentration values of 380 μg/mL for IL1β, 282

μg/mL for TNFα, and 425 μg/mL for IL6. In contrast, RBC-MOF-uricase did not effectively bind to any of the tested cytokines.

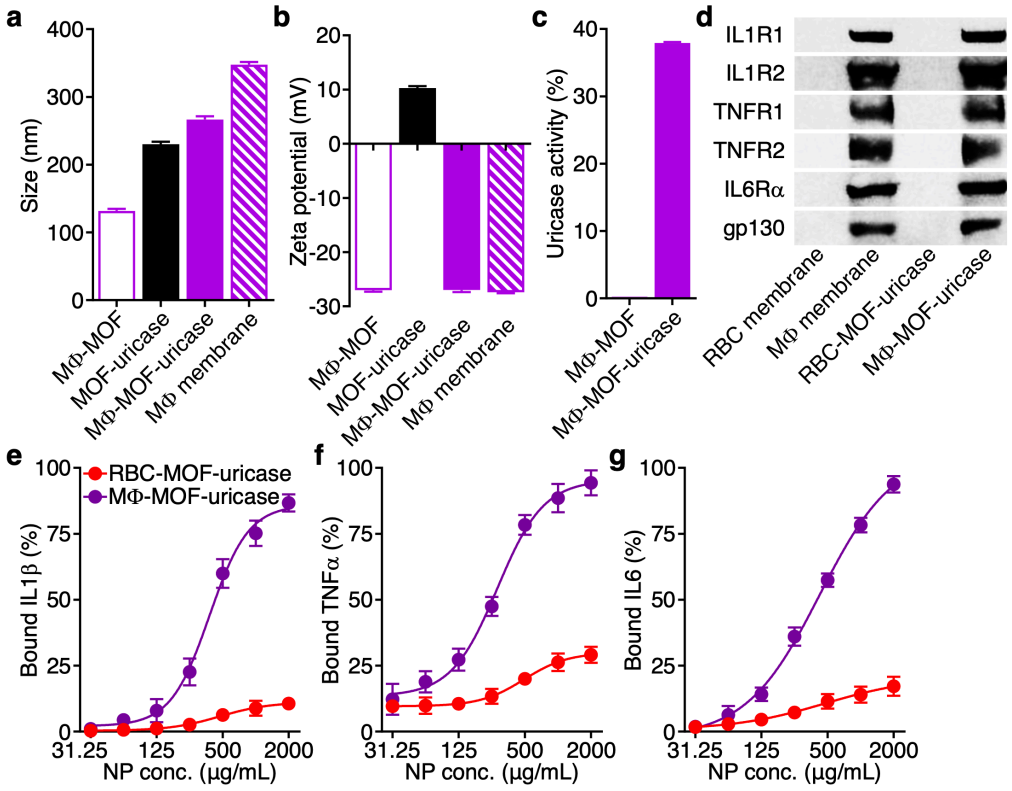

Figure 2.4 Synthesis and characterization of MΦ-MOF-uricase. (a) Diameter of MΦ-MOF, MOF-uricase, MΦ-MOF-uricase, and MΦ membrane vesicles after fabrication (n = 3, mean + SD). (b) Zeta potential of MΦ-MOF, MOF-uricase, MΦ-MOF-uricase, and MΦ membrane vesicles after fabrication (n = 3, mean + SD). (c) *In vitro* uric acid conversion by MΦ-MOF or MΦ-MOF-uricase normalized to free uricase activity (n = 3, mean + SD). (d) Western blot for cytokine receptors, including IL1R1 (80 kDa), IL1R2 (45 kDa), TNFR1 (55 kDa), TNFR2 (75 kDa), IL6Rα (80 kDa), and gp130 (130 kDa), on RBC membrane, MΦ membrane, RBC-MOF-uricase, and MΦ-MOF-uricase. (e-g) *In vitro* neutralization of cytokines, including IL1β (e), TNFα (f), and IL6 (g), by RBC-MOF-uricase and MΦ-MOF-uricase at various nanoparticle concentrations (n = 3, mean ± SD; four-parameter logistic regression).

After confirming its activity *in vitro*, the therapeutic efficacy of the MΦ-MOF-uricase formulation was evaluated *in vivo* using a murine gout model induced by the intraarticular injection of monosodium urate crystals into the ankle joints. At 24 h after induction, when all mice had developed significant inflammation at the injection site, various treatments were administered by intraarticular injection, and the degree of ankle swelling was monitored over time (**Figure 2.5A**).

Compared to the PBS control, free uricase and unloaded MΦ-MOF had a modest therapeutic effect, while MΦ-MOF-uricase showed the best efficacy and near completely alleviated the ankle swelling 48 h after treatment. With its cytokine neutralization capabilities, the MΦ membrane-coated formulation outperformed RBC-MOF-uricase, which also demonstrated considerable efficacy, likely due to its ability to enhance retention of the enzyme at the inflammation site. The uric acid remaining in the ankle tissues was quantified 48 h post-treatment, and it was shown that MΦ-MOF-uricase significantly reduced levels of the substrate molecule (**Figure 2.5B**). The effect was vastly improved compared with unloaded MΦ-MOF, where 80% of the deposited uric acid still remained within the tissues. Similarly, the proinflammatory cytokines present within the ankle tissues were evaluated at the same timepoint, and MΦ-MOF-uricase treatment was able to bring

levels back down to near baseline (**Figure 2.5C-E**). This was significantly better than other treatments, including free uricase, unloaded MΦ-MOF, and RBC-MOF-uricase, all of which

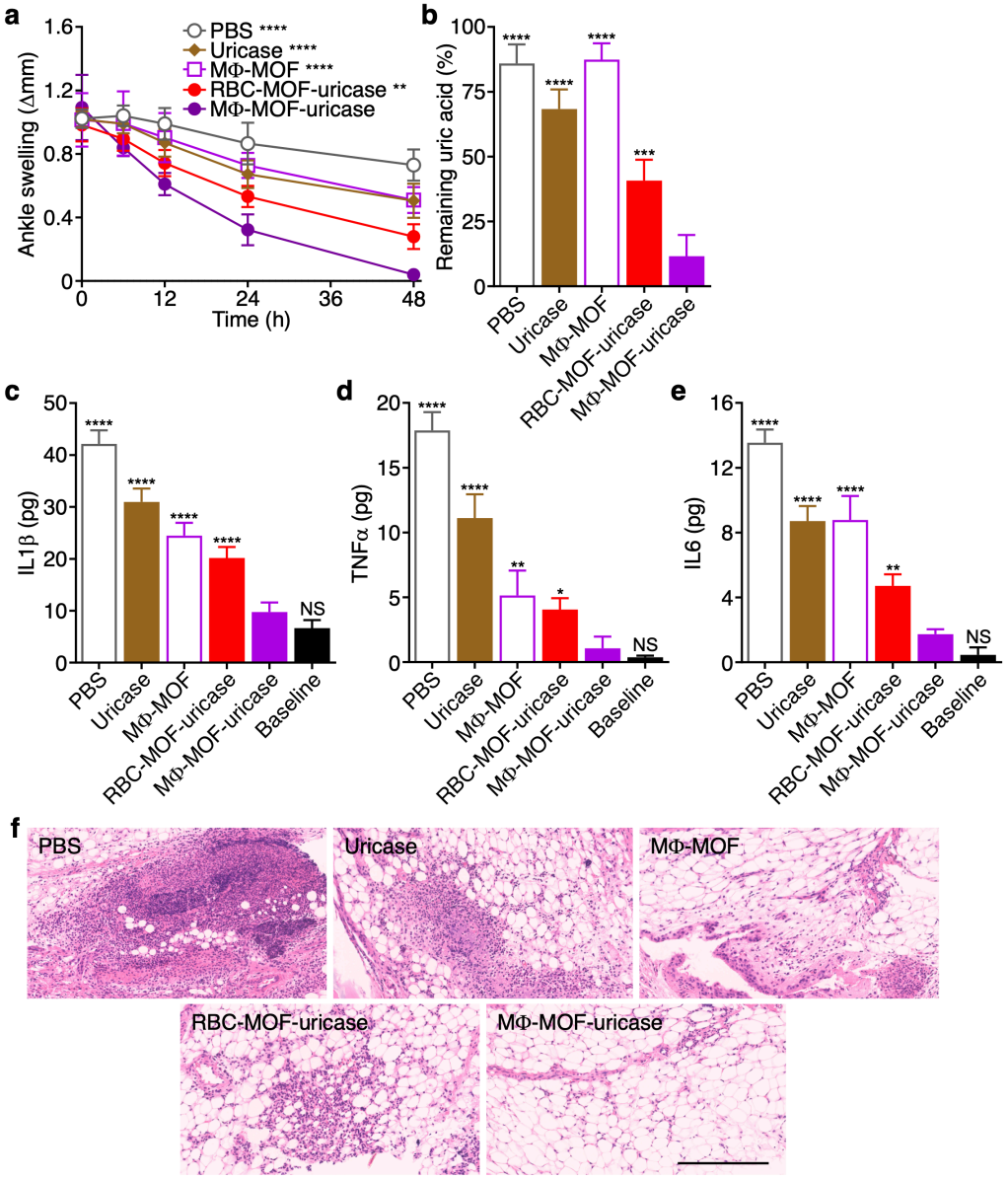

Figure 2.5 ***In vivo*** **gout management and safety**. (a) Change in ankle joint diameter of mice with gout after intraarticular treatment with PBS, free uricase, MΦ-MOF, RBC-MOF-uricase, or MΦ-MOF-uricase (n = 4, mean ± SD). $^{**}p < 0.01$, $^{****}p < 0.0001$ (compared with MΦ-MOF-uricase at 48 h); one-way ANOVA. (b) Remaining uric acid in the ankle joints of the mice in (a) after 48 h (n = 4, mean + SD). $^{***}p < 0.001$, $^{****}p < 0.0001$ (compared with MΦ-MOF-uricase); one-way ANOVA. (c-e) Levels of cytokines, including IL1β (c), TNFα (d), and IL6 (e), in the ankle joints of the mice in (a) after 48 h (n = 4, mean + SD). NS: not significant, $^{*}p < 0.05$, $^{**}p < 0.01$, $^{****}p < 0.0001$ (compared with MΦ-MOF-uricase); one-way ANOVA. (f) H&E-stained histological sections of ankle joints of the mice in (a) after 48 h. Scale bar: 250 μm.

reduced cytokine levels to varying degrees. Lastly, histological examination revealed that the immune cell infiltrate within the periarticular ankle tissue was markedly reduced in mice treated with MΦ-MOF-uricase, indicating only a slight amount of ongoing inflammation within the region (**Figure 2.5F**). Overall, when comparing the effects of MΦ-MOF-uricase with those achieved by MΦ-MOF or RBC-MOF-uricase, the data highlights the therapeutic benefits of combining MΦ membrane-mediated cytokine neutralization with locally delivered enzyme therapy for addressing gout.

2.3 Conclusion

In conclusion, we have successfully fabricated a cell membrane-coated MOF platform for enhancing the activity of enzyme therapies. Using uricase as a model enzyme, it was demonstrated that high encapsulation efficiency of the enzyme could be achieved, and membrane coating further improved colloidal stability in physiological buffer. Importantly, a significant amount of enzymatic activity was retained, and incorporation of uricase within the membrane-coated MOF matrix also protected it from proteolytic degradation. To demonstrate the versatility of this approach, two separate systems were developed using membrane sourced from either RBCs or MΦs. The RBC membrane-coated MOF-uricase formulation was used for the systemic treatment of hyperuricemia, rapidly reducing serum uric levels. On the other hand, the MΦ membrane, with its ability to neutralize a wide range of proinflammatory cytokines, synergized with the uricase to effectively treat localized joint inflammation caused by insoluble uric acid deposits. In the clinic, the administration of uricase, which is not a naturally occurring human enzyme, carries major immunogenicity concerns and runs the risk of triggering anaphylaxis [43, 44]. As we demonstrated here, cell membrane-coated nanodelivery systems are biocompatible and can be used to effectively

shield enzyme payloads from the surrounding environment; the effect of this on long-term immune responses against the enzyme payload will need to be evaluated in future studies. It is envisioned that this strategy can be applied across a wide range of enzyme payloads, and different membrane coatings could be employed to generate synergies based on their unique biointerfacing characteristics. Membrane material can be derived from autologous sources, facilitating the fabrication of personalized therapies [45]. The shape of the MOF core could also be varied to enhance nanoparticle–cell interactions, which would be particularly beneficial for targeted delivery applications [46]. Overall further development along these lines could lead to novel formulations with the potential for transforming the clinical landscape of enzyme therapies.

2.4 Experimental Methods

2.4.1 Nanoparticle preparation.

To prepare the MOF nanoparticles, 0.2 mL solutions of zinc nitrate hexahydrate at 1 mg/mL (Sigma-Aldrich) and 2-methylimidazole at 20 mg/mL (Sigma-Aldrich) were added together. The mixture was vortexed for 30 s and left undisturbed for 3 h. Loading of the uricase (*Candida* sp., 5.3 U/mg; Sigma-Aldrich) was achieved by premixing an appropriate amount of the enzyme with the 2-methylimidazole solution to achieve uricase inputs ranging from 0.05 to 0.25 U. For nanoparticle coating, mouse RBC membrane or MΦ membrane was respectively derived from CD-1 mouse blood (BioreclamationIVT) [30] or murine J774 MΦs (TIB-67; American Type Culture Collection)[34] using previously reported protocols and suspended at 1 mg/mL in water. The membrane solution was then added to an equal volume of MOF or MOF-uricase nanoparticles for 30 min, followed by sequential extrusion through polycarbonate porous membranes (Whatman) using an Avanti mini extruder. The resulting nanoparticles were isolated by centrifugation at 10,000 *g* for 5 min and then resuspended in water for further use. Unless otherwise stated, studies

were conducted with formulations made using uricase inputs of 0.1 U for RBC-MOF-uricase and 0.25 U for MΦ-MOF-uricase. RBC membrane vesicles and MΦ membrane vesicles were prepared by extruding purified cell membrane through the same set of porous membranes. All nanoparticle concentrations are expressed as membrane protein mass per unit volume.

2.4.2 Nanoparticle characterization.

Size and zeta potential were measured by dynamic light scattering (DLS) using a Malvern Zetasizer Nano ZS. To visualize nanoparticle morphology, the nanoparticle sample was adsorbed onto a carbon-coated 400-mesh copper grid (Electron Microscopy Sciences) and stained with 1 wt% uranyl acetate (Electron Microscopy Sciences), followed by imaging on a JEOL 1200 EX II transmission electron microscope. For the stability study, nanoparticle samples were stored in PBS at room temperature, and size was measured periodically by DLS over the course of 8 days.

2.4.3 Quantification of uricase loading, release, and activity.

For loading quantification, uricase was prelabeled with NHS-fluorescein (excitation/emission = 494/518 nm; Thermo Scientific), and the fluorescence of the supernatant after centrifugation of the extruded nanoparticles was measured using a BioTek Synergy Mx microplate reader. To quantify uricase release, at predetermined timepoints, aliquots of nanoparticles in PBS were centrifuged to pellet the nanoparticles, and the fluorescence of fluorescein in the supernatant was measured using a BioTek Synergy Mx microplate reader. The *in vitro* activity of RBC-MOF-uricase was quantified by an Amplex Red uric acid/uricase assay kit (Invitrogen), with uric acid as the substrate and free uricase as the standard. To study the *in vitro* activity of MΦ-MOF-uricase, monosodium urate was synthesized from uric acid (Sigma-

Aldrich) according to literature [47] and used as the substrate for quantification using an Amplex Red uric acid/uricase assay kit.

2.4.4 Protein characterization.

Samples at 1 mg/mL protein content or an equivalent amount of MOF-uricase were prepared in NuPAGE Novex lithium dodecyl sulfate (LDS) sample loading buffer (Invitrogen) and run on 12-well Bolt 4%-12% Bis-Tris minigels (Invitrogen) in MOPS running buffer (Invitrogen). To visualize the overall protein profile, the gel was incubated in InstantBlue Protein Stain (Expedeon) for 1 h and imaged under a Bio-Rad Gel Doc XR system. To assess the presence of specific markers, proteins were transferred to 0.45 μm nitrocellulose membranes (Pierce) in Bolt transfer buffer (Novex) at 10 V for 60 min. The membranes were then blocked with 2% bovine serum albumin (Sigma-Aldrich) in PBS with 0.05% Tween 20 (National Scientific). Blots were probed with primary antibodies specific for mouse CD47 (miap301; Biolegend), IL1R1 (H-8, Santa Cruz Biotechnology), IL1R2 (3H4H4, Proteintech), TNFR1 (H-5, Santa Cruz Biotechnology), TNFR2 (TR75-89, Santa Cruz Biotechnology), IL6Rα (D-8, Santa Cruz Biotechnology), or gp130 (E-8, Santa Cruz Biotechnology), followed by the appropriate horse radish peroxidase (HRP)-conjugated secondary antibodies (Biolegend). Development was done using ECL western blotting substrate (Pierce) in a Mini-Medical/90 developer (ImageWorks).

2.4.5 Uricase degradation study.

All animal experiments were performed in accordance with NIH guidelines and approved by the Institutional Animal Care and Use Committee of the University of California San Diego. Uricase-specific murine polyclonal antibodies were generated by immunizing a male CD-1 mouse

(Envigo) with 0.1 mg uricase in Imject alum adjuvant (Thermo Scientific). Two boosters were given before collecting blood to obtain antibody-containing serum. For the study, 5 μL of 0.25% trypsin-EDTA (Gibco) was added into 100 μL aliquots containing 0.05 U of uricase in free form or encapsulated within RBC-MOF, and the mixtures were incubated at 37 ºC for increasing amounts of time. Uricase degradation profiling achieved by western blot analysis as described above using the polyclonal anti-mouse uricase as the primary immunostain, followed by an HRP-conjugated anti-mouse IgG secondary antibody (Biolegend).

2.4.6 *In vitro* cytokine binding.

To study the *in vitro* binding of proinflammatory cytokines, recombinant mouse IL1β (Biolegend), TNFα (Biolegend), or IL6 (Biolegend) at a final concentration of 8 ng/mL was mixed with nanoparticles at final concentrations ranging from 0 to 2 mg/mL. The mixtures were incubated for 2 h at 37 °C and then centrifuged at 16,100 *g* for 10 min to remove the nanoparticles. Cytokine concentrations in the supernatant were quantified by mouse IL1β, TNFα, or IL6 enzyme-linked immunosorbent assay (ELISA) kits (Biolegend) per the manufacturer's instructions.

2.4.7 *In vivo* biodistribution and safety.

RBC-MOF-uricase was fluorescently labeled using 1,1'-dioctadecyl-3,3,3',3'-tetramethylindodicarbocyanine (excitation/emission = 644/665 nm; Invitrogen), and 400 μg of the nanoparticles was administered intravenously into adult C57BL/6 mice (Charles River Laboratories). Mice were euthanized at 24 h after nanoparticle administration for sample collection. For the biodistribution study, the major organs, including the liver, spleen, heart, lungs, kidneys, and blood, were collected. The organs were homogenized in 1 mL of PBS using a Biospec Mini-

Beadbeater-16. Fluorescence was read using a Tecan Infinite M200 plate reader. To calculate the signal in the blood, total volume was estimated as 6% of mouse body weight. To obtain blood cell counts, whole blood was collected into potassium–EDTA collection tubes (Sarstedt), and analysis was performed by the UC San Diego Animal Care Program Diagnostic Services Laboratory. To perform the histological analysis, the major organs were sectioned and stained with H&E (Leica Biosystems), followed by imaging using a Hamamatsu Nanozoomer 2.0-HT slide scanning system.

2.4.8 *In vivo* treatment efficacy studies.

Hyperuricemia in mice was induced based on a previously reported procedure [48]. Food and water were withheld overnight prior to the study. Briefly, to increase the serum uric acid levels, adult C57BL/6 mice were injected intraperitoneally with 4 mg of allantoxanamide (BOC Sciences) suspended in 0.2 mL of 0.5% carboxymethylcellulose sodium (Grainger). After 2 h, the mice were intravenously administered with 0.2 mL of PBS, RBC-MOF-uricase at 2 mg/mL, or free uricase at an equivalent concentration. Blood samples were collected at predetermined timepoints and allowed to clot for 30 min at room temperature. After centrifugation to obtain the serum, the uric acid content was assayed using an Amplex Red uric acid/uricase assay kit.

Gout was induced according to a previously reported procedure [49]. Briefly, adult C57BL/6 mice were placed under anesthesia with a cocktail of ketamine (Pfizer) at 100 mg/kg and xylazine (Lloyd Laboratories) at 20 mg/kg. This was followed by intraarticular injection with 0.5 mg of monosodium urate in 25 μL of PBS into the ankle joint. After 24 h, the ankle joints were intraarticularly injected with 25 μL of PBS, MΦ-MOF at 2 mg/mL, RBC-MOF-uricase (inputted with 0.25 U of uricase) at 2 mg/mL, MΦ-MOF-uricase at 2 mg/mL, or free uricase at an equivalent concentration with the mice under anesthesia. Ankle joint swelling was measured with an

electronic caliper at the indicated timepoints. To assess the remaining uric acid content and local proinflammatory cytokine (IL1β, TNFα, IL6) concentrations, mice were euthanized 48 h after treatment, and the periarticular tissues were collected. The tissues were homogenized in PBS containing a protease inhibitor cocktail (Sigma-Aldrich). After centrifugation, the supernatant was assayed for uric acid content using an Amplex Red uric acid/uricase assay kit and for cytokine concentrations by the appropriate ELISA kits per the manufacturer's instructions. To perform the histological analysis, the periarticular tissues were collected 48 h after treatment. The collected tissues were fixed with phosphate buffered formalin (Fisher Scientific), decalcified with 10% EDTA (Corning), and stained with H&E. Images were obtained using a Hamamatsu NanoZoomer 2.0-HT slide scanning system.

2.5 References

[1] J.M. Matés, C. Pérez-Gómez, I.N. De Castro, Antioxidant Enzymes and Human Diseases, Clin. Biochem. 32(8) (1999) 595-603.

[2] C. López-Otín, J.S. Bond, Proteases: Multifunctional Enzymes in Life and Disease, J. Biol. Chem. 283(45) (2008) 30433-30437.

[3] N.W. Barton, R.O. Brady, J.M. Dambrosia, A.M. Di Bisceglie, S.H. Doppelt, S.C. Hill, H.J. Mankin, G.J. Murray, R.I. Parker, C.E. Argoff, R.P. Grewal, K.-T. Yu, Replacement Therapy for Inherited Enzyme Deficiency — Macrophage-Targeted Glucocerebrosidase for Gaucher's Disease, N. Engl. J. Med. 324(21) (1991) 1464-1470.

[4] R.J. Desnick, R. Brady, J. Barranger, A.J. Collins, D.P. Germain, M. Goldman, G. Grabowski, S. Packman, W.R. Wilcox, Fabry Disease, an Under-Recognized Multisystemic Disorder: Expert Recommendations for Diagnosis, Management, and Enzyme Replacement Therapy, Ann. Intern. Med. 138(4) (2003) 338-346.

[5] A.H. Futerman, G. van Meer, The Cell Biology of Lysosomal Storage Disorders, Nat. Rev. Mol. Cell Biol. 5(7) (2004) 554-565.

[6] F.M. Platt, B. Boland, A.C. van der Spoel, Lysosomal Storage Disorders: The Cellular Impact of Lysosomal Dysfunction, J. Cell Biol. 199(5) (2012) 723-734.

[7] O. Khersonsky, D.S. Tawfik, Enzyme Promiscuity: A Mechanistic and Evolutionary Perspective, Annu. Rev. Biochem. 79(1) (2010) 471-505.

[8] H.K. Choi, D.B. Mount, A.M. Reginato, Pathogenesis of Gout, Ann. Intern. Med. 143(7) (2005) 499-516.

[9] N. Dalbeth, T.R. Merriman, L.K. Stamp, Gout, Lancet 388(10055) (2016) 2039-2052.

[10] R.J. Desnick, E.H. Schuchman, Enzyme Replacement and Enhancement Therapies: Lessons from Lysosomal Disorders, Nat. Rev. Genet. 3(12) (2002) 954-966.

[11] R.O. Brady, Enzyme Replacement for Lysosomal Diseases, Annu. Rev. Med. 57(1) (2006) 283-296.

[12] R.J. Desnick, E.H. Schuchman, Enzyme Replacement Therapy for Lysosomal Diseases: Lessons from 20 Years of Experience and Remaining Challenges, Annu. Rev. Genomics Hum. Genet. 13(1) (2012) 307-335.

[13] A. Fieker, J. Philpott, M. Armand, Enzyme Replacement Therapy for Pancreatic Insufficiency: Present and Future, Clin. Exp. Gastroenterol. 4 (2011) 55-73.

[14] R. Schiffmann, J.B. Kopp, H.A. Austin III, S. Sabnis, D.F. Moore, T. Weibel, J.E. Balow, R.O. Brady, Enzyme Replacement Therapy in Fabry Disease: A Randomized Controlled Trial, JAMA 285(21) (2001) 2743-2749.

[15] E.D. Kakkis, J. Muenzer, G.E. Tiller, L. Waber, J. Belmont, M. Passage, B. Izykowski, J. Phillips, R. Doroshow, I. Walot, R. Hoft, K.T. Yu, S. Okazaki, D. Lewis, R. Lachman, J.N. Thompson, E.F. Neufeld, Enzyme-Replacement Therapy in Mucopolysaccharidosis I, N. Engl. J. Med. 344(3) (2001) 182-188.

[16] M. Rohrbach, J.T.R. Clarke, Treatment of Lysosomal Storage Disorders, Drugs 67(18) (2007) 2697-2716.

[17] J. Kim, J.W. Grate, P. Wang, Nanostructures for Enzyme Stabilization, Chem. Eng. Sci. 61(3) (2006) 1017-1026.

[18] S.N. Dean, K.B. Turner, I.L. Medintz, S.A. Walper, Targeting and Delivery of Therapeutic Enzymes, Ther. Deliv. 8(7) (2017) 577-595.

[19] J. Zhuang, A.P. Young, C.-K. Tsung, Integration of Biomolecules with Metal–Organic Frameworks, Small 13(32) (2017) 1700880.

[20] S. Muro, C. Garnacho, J.A. Champion, J. Leferovich, C. Gajewski, E.H. Schuchman, S. Mitragotri, V.R. Muzykantov, Control of Endothelial Targeting and Intracellular Delivery of Therapeutic Enzymes by Modulating the Size and Shape of ICAM-1-Targeted Carriers, Mol. Ther. 16(8) (2008) 1450-1458.

[21] X. Lian, Y. Fang, E. Joseph, Q. Wang, J. Li, S. Banerjee, C. Lollar, X. Wang, H.-C. Zhou, Enzyme–MOF (Metal–Organic Framework) Composites, Chem. Soc. Rev. 46(11) (2017) 3386-3401.

[22] J. Mehta, N. Bhardwaj, S.K. Bhardwaj, K.-H. Kim, A. Deep, Recent Advances in Enzyme Immobilization Techniques: Metal-Organic Frameworks as Novel Substrates, Coord. Chem. Rev. 322 (2016) 30-40.

[23] F.-K. Shieh, S.-C. Wang, C.-I. Yen, C.-C. Wu, S. Dutta, L.-Y. Chou, J.V. Morabito, P. Hu, M.-H. Hsu, K.C.W. Wu, C.-K. Tsung, Imparting Functionality to Biocatalysts *via* Embedding Enzymes into Nanoporous Materials by a *De Novo* Approach: Size-Selective Sheltering of Catalase in Metal–Organic Framework Microcrystals, J. Am. Chem. Soc. 137(13) (2015) 4276-4279.

[24] F.-S. Liao, W.-S. Lo, Y.-S. Hsu, C.-C. Wu, S.-C. Wang, F.-K. Shieh, J.V. Morabito, L.-Y. Chou, K.C.W. Wu, C.-K. Tsung, Shielding against Unfolding by Embedding Enzymes in Metal–Organic Frameworks *via* a *De Novo* Approach, J. Am. Chem. Soc. 139(19) (2017) 6530-6533.

[25] M. Giménez-Marqués, T. Hidalgo, C. Serre, P. Horcajada, Nanostructured Metal–Organic Frameworks and Their Bio-Related Applications, Coord. Chem. Rev. 307 (2016) 342-360.

[26] T. Simon-Yarza, A. Mielcarek, P. Couvreur, C. Serre, Nanoparticles of Metal-Organic Frameworks: On the Road to In Vivo Efficacy in Biomedicine, Adv. Mater. 30(37) (2018) 1707365.

[27] R.H. Fang, A.V. Kroll, W. Gao, L. Zhang, Cell Membrane Coating Nanotechnology, Adv. Mater. 30(23) (2018) 1706759.

[28] A.V. Kroll, R.H. Fang, L. Zhang, Biointerfacing and Applications of Cell Membrane-Coated Nanoparticles, Bioconjug. Chem. 28(1) (2017) 23-32.

[29] B.T. Luk, R.H. Fang, C.M. Hu, J.A. Copp, S. Thamphiwatana, D. Dehaini, W. Gao, K. Zhang, S. Li, L. Zhang, Safe and Immunocompatible Nanocarriers Cloaked in RBC Membranes for Drug Delivery to Treat Solid Tumors, Theranostics 6(7) (2016) 1004-1011.

[30] C.-M.J. Hu, L. Zhang, S. Aryal, C. Cheung, R.H. Fang, L. Zhang, Erythrocyte Membrane-Camouflaged Polymeric Nanoparticles as a Biomimetic Delivery Platform, Proc. Natl. Acad. Sci. U. S. A. 108(27) (2011) 10980-10985.

[31] C.M. Hu, R.H. Fang, K.C. Wang, B.T. Luk, S. Thamphiwatana, D. Dehaini, P. Nguyen, P. Angsantikul, C.H. Wen, A.V. Kroll, C. Carpenter, M. Ramesh, V. Qu, S.H. Patel, J. Zhu, W. Shi, F.M. Hofman, T.C. Chen, W. Gao, K. Zhang, S. Chien, L. Zhang, Nanoparticle Biointerfacing by Platelet Membrane Cloaking, Nature 526(7571) (2015) 118-121.

[32] Q. Hu, W. Sun, C. Qian, C. Wang, H.N. Bomba, Z. Gu, Anticancer Platelet-Mimicking Nanovehicles, Adv. Mater. 27(44) (2015) 7043-7050.

[33] Q. Zhang, D. Dehaini, Y. Zhang, J. Zhou, X. Chen, L. Zhang, R.H. Fang, W. Gao, L. Zhang, Neutrophil Membrane-Coated Nanoparticles Inhibit Synovial Inflammation and Alleviate Joint Damage in Inflammatory Arthritis, Nat. Nanotechnol. 13(12) (2018) 1182-1190.

[34] S. Thamphiwatana, P. Angsantikul, T. Escajadillo, Q. Zhang, J. Olson, B.T. Luk, S. Zhang, R.H. Fang, W. Gao, V. Nizet, L. Zhang, Macrophage-Like Nanoparticles Concurrently Absorbing Endotoxins and Proinflammatory Cytokines for Sepsis Management, Proc. Natl. Acad. Sci. U. S. A. 114(43) (2017) 11488-11493.

[35] D. Dehaini, R.H. Fang, L. Zhang, Biomimetic Strategies for Targeted Nanoparticle Delivery, Bioeng. Transl. Med. 1(1) (2016) 30-46.

[36] J. Zhuang, H. Gong, J. Zhou, Q. Zhang, W. Gao, R.H. Fang, L. Zhang, Targeted Gene Silencing *In Vivo* by Platelet Membrane–Coated Metal-Organic Framework Nanoparticles, Sci. Adv. 6(13) (2020) eaaz6108.

[37] K. Liang, R. Ricco, C.M. Doherty, M.J. Styles, S. Bell, N. Kirby, S. Mudie, D. Haylock, A.J. Hill, C.J. Doonan, P. Falcaro, Biomimetic Mineralization of Metal-Organic Frameworks as Protective Coatings for Biomacromolecules, Nat. Comm. 6(1) (2015) 7240.

[38] E. Blanco, H. Shen, M. Ferrari, Principles of Nanoparticle Design for Overcoming Biological Barriers to Drug Delivery, Nat. Biotechnol. 33(9) (2015) 941-951.

[39] M.Z. Zou, W.L. Liu, C.X. Li, D.W. Zheng, J.Y. Zeng, F. Gao, J.J. Ye, X.Z. Zhang, A Multifunctional Biomimetic Nanoplatform for Relieving Hypoxia to Enhance Chemotherapy and Inhibit the PD-1/PD-L1 Axis, Small 14(28) (2018) 1801120.

[40] L. Zhang, Z.Z. Wang, Y. Zhang, F.F. Cao, K. Dong, J.S. Ren, X.G. Qu, Erythrocyte Membrane Cloaked Metal-Organic Framework Nanoparticle as Biomimetic Nanoreactor for Starvation-Activated Colon Cancer Therapy, ACS Nano 12(10) (2018) 10201-10211.

[41] P.-A. Oldenborg, A. Zheleznyak, Y.-F. Fang, C.F. Lagenaur, H.D. Gresham, F.P. Lindberg, Role of CD47 as a Marker of Self on Red Blood Cells, Science 288(5473) (2000) 2051-2054.

[42] A.K. So, F. Martinon, Inflammation in Gout: Mechanisms and Therapeutic Targets, Nat. Rev. Rheumatol. 13(11) (2017) 639-647.

[43] J.S. Sundy, H.S. Baraf, R.A. Yood, N.L. Edwards, S.R. Gutierrez-Urena, E.L. Treadwell, J. Vazquez-Mellado, W.B. White, P.E. Lipsky, Z. Horowitz, W. Huang, A.N. Maroli, R.W. Waltrip, 2nd, S.A. Hamburger, M.A. Becker, Efficacy and Tolerability of Pegloticase for the Treatment of Chronic Gout in Patients Refractory to Conventional Treatment: Two Randomized Controlled Trials, JAMA 306(7) (2011) 711-720.

[44] J.D. Bieber, R.A. Terkeltaub, Gout: On the Brink of Novel Therapeutic Options for an Ancient Disease, Arthritis Rheum. 50(8) (2004) 2400-2414.

[45] C. Sevencan, R.S.A. McCoy, P. Ravisankar, M. Liu, S. Govindarajan, J.Y. Zhu, B.H. Bay, D.T. Leong, Cell Membrane Nanotherapeutics: From Synthesis to Applications Emerging Tools for Personalized Cancer Therapy, Adv. Ther. 3(3) (2020) 1900201.

[46] J. Zhu, C. Sevencan, M. Zhang, R.S.A. McCoy, X. Ding, J. Ye, J. Xie, K. Ariga, J. Feng, B.H. Bay, D.T. Leong, Increasing the Potential Interacting Area of Nanomedicine Enhances Its Homotypic Cancer Targeting Efficacy, ACS Nano 14(3) (2020) 3259-3271.

[47] L. Liu, Y. Xue, Y. Zhu, D. Xuan, X. Yang, M. Liang, J. Wang, X. Zhu, J. Zhang, H. Zou, Interleukin 37 Limits Monosodium Urate Crystal-Induced Innate Immune Responses in Human and Murine Models of Gout, Arthritis Res. Ther. 18(1) (2016) 268.

[48] J.-M. Lü, Q. Yao, C. Chen, 3,4-Dihydroxy-5-Nitrobenzaldehyde (DHNB) Is A Potent Inhibitor of Xanthine Oxidase: A Potential Therapeutic Agent for Treatment of Hyperuricemia and Gout, Biochem. Pharmacol. 86(9) (2013) 1328-1337.

[49] Q. Yang, Q. Zhang, Y. Qing, L. Zhou, Q. Mi, J. Zhou, miR-155 Is Dispensable in Monosodium Urate-Induced Gouty Inflammation in Mice, Arthritis Res. Ther. 20(1) (2018) 144.

Chapter 2, in full, is a reprint of the material as it appears in *Nano Letters*, 2020 by Jia Zhuang, Yaou Duan, Qiangzhe Zhang, Weiwei Gao, Shulin Li, Ronnie H. Fang, and Liangfang Zhang. The dissertation author was the co-primary investigator and co-author of this paper.

Chapter 3

Macrophage Membrane Coated Nanosponges for the Treatment of Gastrointestinal Diseases

3.1 Capsulated Cellular Nanosponges for the Treatment of Experimental Inflammatory Bowel Disease

3.1.1 Introduction

Inflammatory bowel disease (IBD) refers to chronic relapsing disorders of gastrointestinal (GI) tract, including Crohn's disease and ulcerative colitis. These conditions are characterized by intestinal inflammation [1], intestinal epithelial barrier injury [2, 3], and gut microbiome dysbiosis [4, 5]. IBD reduces life quality of patients and places a substantial burden on healthcare systems [6, 7]. Current treatments include small-molecule immunosuppressive agents and kinase inhibitors, which can manage symptoms but fail to repair gut mucosal barrier damage or restore intestinal microbiome imbalance [8]. Prolonged use of these nonspecific agents may also lead to severe toxicity and increase the risk of opportunistic infections [9, 10]. Alternatively, biologics such as antibodies targeting tumor necrosis factor (TNF)-α or $\alpha_4\beta_7$ integrin offer promising treatment options for IBD by blocking inflammatory signals. However, these biologics may carry risks of immunogenicity, poor circulation stability, high cost, and antibody resistance upon repetitive administration [11, 12]. Therefore, developing new and effective therapeutics for IBD is highly desirable.

Recently, nanoparticles have gained considerable attention as potential solutions to the unmet needs in IBD treatment. Nanoparticle delivery systems exhibit attractive characteristics such as target-specificity, stability, biocompatibility, and non-toxicity to the GI system [13]. Various nanoparticle carriers have emerged for the delivery of small-molecular agents, antibodies, and siRNAs to the colon for IBD treatment [14, 15]. Some nanoparticles possess pH-responsive [16, 17], ROS-responsive [18-20], or receptor-mediated targeting properties, which can enhance their specificity and efficacy. In addition to serving as drug carriers, nanoparticles made with

macrophage modulatory and reactive oxygen species (ROS)-scavenging materials, such as hyaluronic acid and polydopamine, have been developed as therapeutics for IBD with promising outcomes [13, 21-23].

In the past few years, nanoparticles coated with natural cell membranes have become a compelling anti-inflammatory nanomedicine platform. This platform has been named ‘cellular nanosponge’ because of its unique ability to absorb and neutralize harmful molecules such as toxins and inflammatory cytokines. Among the various types of cellular nanosponges, white blood cell (WBC) nanosponges are made with WBC membranes, which replicate the antigenic profile of the source cell and act as host cell decoys to adsorb inflammatory molecules. WBC nanosponges can effectively bind to different types of cytokines through the corresponding cytokine receptors on the cell membranes. Cytokine neutralization can inhibit the downstream macrophage activation and halt the propagation of the immune cascade, thereby reducing inflammation. WBC nanosponges stand out among other anti-inflammatory agents due to their broad-spectrum biological neutralization ability, which is effective against various modes of action of these agents [24]. For example, the use of macrophage membrane-coated nanoparticles (MΦ-NPs) has shown promise in managing sepsis and reducing inflammation in various diseases. These nanoparticles scavenge endotoxins, diverting them away from endogenous macrophages, while also neutralizing inflammatory cytokines such as interleukin (IL)-6, IL-1β, and TNF-α. Studies have also demonstrated the efficacy of MΦ-NPs in treating acute pancreatitis and rheumatoid arthritis by inhibiting inflammation and reducing disease severity [25-27]. Following a similar principle, neutrophil nanosponges have also been used to alleviate joint damage in inflammatory arthritis by inhibiting synovial inflammation [28].

The promise of cellular nanosponges in treating inflammatory disorders has motivated our efforts to investigate their potential use for the treatment of IBD. Here, we report the development of a capsulated oral formulation of MΦ-NPs (denoted 'cp-MΦ-NPs') as an effective, safe, and convenient option for IBD treatment. The selection of macrophage membrane over other types of cell membranes is due to the predominant roles of macrophages in IBD pathogenesis [29]. The polymeric core in the MΦ-NP formulation provides a solid support of the cell membrane to prevent membrane fusion and maintain nanoparticle stability. A stable MΦ-NP formulation is crucial for accumulation in inflamed colonic epithelium, penetration into the gastrointestinal mucus, and binding with targeted molecules [21, 30, 31]. We first fabricate MΦ-NPs by coating mouse macrophage membrane onto synthetic cores made from poly(lactic-co-glycolic acid) (PLGA). These nanoparticles are then lyophilized and loaded into protective gelatin capsules. The capsules are further dip-coated with pH-responsive enteric polymer coating Eudragit S-100 (**Figure 3.1.1A**). The Eudragit S-100 coated capsules protect cp-MΦ-NPs from the harsh acidic and proteolytic gastric environment and ensure colonic delivery of the nanoparticles. In vitro, we show that cp-MΦ-NPs can effectively neutralize the inflammatory cytokines associated with IBD. In vivo, we administer cp-MΦ-NPs orally into a mouse model of dextran sulfate sodium (DSS)-induced colitis. Upon release from the capsule in the colon, the released MΦ-NPs mimic endogenous macrophages and bind to pro-inflammatory cytokines that would otherwise target macrophages. As a result, the cp-MΦ-NP treatment restores intestinal barrier functions and ameliorates IBD symptoms in both prophylactic and delayed treatment regimes. Overall, our results suggest that cp-MΦ-NPs are a promising biomimetic nanomedicine platform for the treatment of IBD.

3.1.2 Results and Discussion

In the study, we formulated cp-MΦ-NPs through a three-step process. First, we fabricated MΦ-NPs through a process including macrophage membrane derivation, PLGA core fabrication, and membrane coating. Second, we suspended the freshly made nanoparticles in 10% sucrose, lyophilized them into dry powder, and loaded the dry powder into gelatin capsules. The loading was achieved with a special filing funnel provided by the vendor, and the loading efficiency was 90.8 ± 2.4%. A similar lyophilization process showed to maintain nanosponge

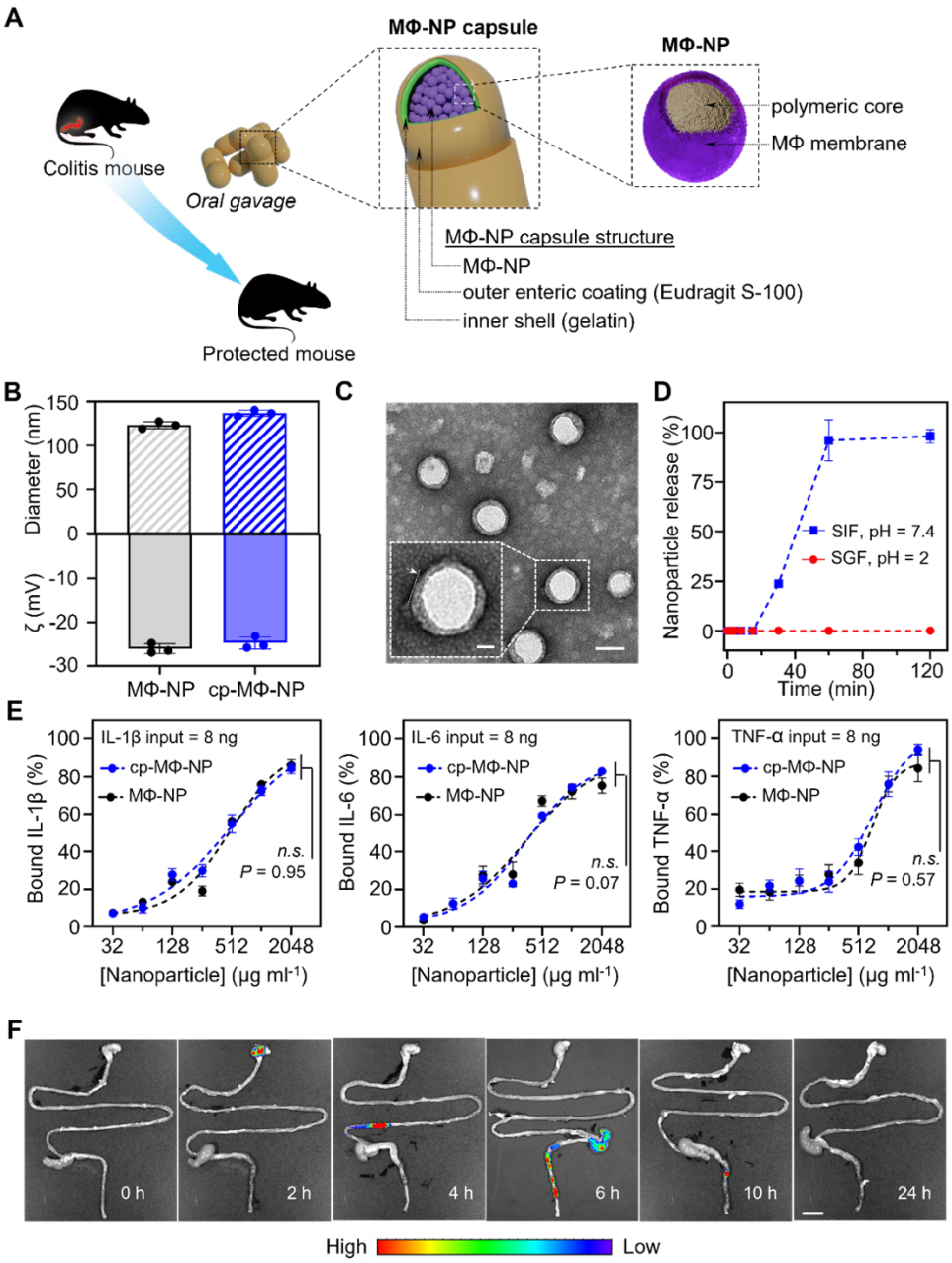

Figure 3.1.1 Preparation and characterization of cp-MΦ-NPs. (A) Schematic illustration of cp-MΦ-NPs and their use to manage IBD. MΦ-NP capsules are fabricated by coating MΦ membrane onto polymeric cores, followed by lyophilization, capsule loading, and enteric coating of capsules. (B) The average diameter and surface zeta potential of MΦ-NPs and cp-MΦ-NPs measured with dynamic light scattering (DLS). (C) Transmission electron microscopic (TEM) images of resuspended cp-MΦ-NPs negatively stained with uranyl acetate. Scale bar = 100 nm (inset scale bar = 30 nm). (D) MΦ-NP release profile from Eudragit S100-coated capsules in simulated gastric fluid (SGF, pH = 2, red) or simulated intestinal fluid (SIF, pH = 7.4, blue). (E) Binding kinetic profiles of MΦ-NPs and cp-MΦ-NPs against IL-1β, IL-6, and TNF-α. (F) Representative GI tract images of mice after oral administration of fluorescence-labeled cp-MΦ-NPs. Scale bar = 1 cm. In all datasets, n = 3; data are presented as mean ± s.d.; *n.s.* = not significant.

size and stability [32]. Third, the capsules were coated with Eudragit S100, a pH-responsive enteric polymer, to ensure colon-specific payload release [33]. Dynamic light scattering (DLS) measurements revealed that resuspended cp-MΦ-NPs and freshly prepared MΦ-NPs had a comparable hydrodynamic diameter (137.0 nm and 123.7 nm, respectively) and surface zeta potential (-24.8 mV and -26.1 mV, respectively), suggesting that the lyophilization and encapsulation procedures had negligible impact on the nanoparticle structures (**Figure 3.1.1B**). In addition, cp-MΦ-NPs revealed a characteristic core−shell morphology under transmission electron microscopy (TEM). The morphology is comparable to freshly prepared MΦ-NPs, confirming the preservation of nanoparticle structure during the formulation process (**Figure 3.1.1C**) [34].

To test pH-responsive nanosponge release from the capsules, we labeled cp-MΦ-NPs with a fluorescent dye and put the capsules in a simulated gastric fluid (SGF, pH = 2). Negligible amount of MΦ-NPs was released from the capsules into the fluid in 2 h. In contrast, when put in a simulated intestinal fluid (SIF, pH = 7.4), the capsules released about 90% of the loaded MΦ-NPs within 60 min. This test confirmed a pH-responsive MΦ-NP release from the capsules (**Figure 3.1.1D**). When suspended in SIF (pH = 7.4), the hydrodynamic size of cp-MΦ-NPs remained stable for 7 days, indicating excellent colloidal stability. We also incubated cp-MΦ-NPs released from the capsules with IL-1β, IL-6, and TNF-α, three representative pro-inflammatory cytokines in IBD [35, 36]. Nanoparticle binding with these cytokines showed a clear dose dependence binding kinetics (**Figure 3.1.1E**). In fact, cp-MΦ-NPs and freshly prepared MΦ-NPs showed comparable cytokine binding kinetics and capacity, implying that the cp-MΦ-NP formulation preserved the cytokine binding bioactivity of MΦ-NPs. A western blot analysis further verified the preservation of key MΦ surface antigens on cp-MΦ-NPs. Moreover, cp-MΦ-NPs were also able to ameliorate the cytokine-induced inflammatory effect on macrophages and reactive oxygen species (ROS)

effect on colon epithelial cells in vitro. Lastly, when tested on MC38 cells, a colon tumor cell line derived from colon epithelial cells, cp-MΦ-NPs showed the absence of cytotoxicity.

To study the specificity of cp-MΦ-NPs for colon delivery, we administered fluorescence-labeled cp-MΦ-NPs orally into C57BL/6 mice and observed their colonic distribution at predetermined time points (**Figure 3.1.1F**). At 2 h and 4 h after the oral administration, most cp-MΦ-NPs were at the stomach and the ileum, respectively. The fluorescent signal was confined within a narrow region during this period, suggesting an intact capsule structure. At 6 h, the fluorescence predominantly localized at the colon, and its distribution became broader, suggesting the dissolution of the capsule and the release of cp-MΦ-NPs. At 10 h, nanoparticle fluorescent intensity diminished significantly and became undetectable at 24 h. These results verified that the capsules were able to deliver cp-MΦ-NPs specifically to the colon after oral administration.

Next, we investigated the efficacy of cp-MΦ-NPs to ameliorate IBD in a prophylactic regimen using a mouse model of DSS-induced colitis. Specifically, we provided C57BL/6 mice with drinking water containing 3% DSS for 6 days while administrating cp-MΦ-NPs (3 mg MΦ-NPs per capsule; 1 capsule per day for 9 days) via oral gavage (**Figure 3.1.2A**) [36]. The control groups included healthy mice and mice treated with DSS only, DSS with capsulated red blood cell membraned-coated nanoparticles (denoted as 'cp-RBC-NPs'), or DSS with empty capsules. We first monitored mouse body weight change among different groups as an efficacy indication [37]. Compared to the healthy controls, administration of DDS alone led to rapid weight loss in the treated mice (**Figure 3.1.2B**). A maximum weight loss was observed on day 10, which amounted to a decrease to 86% of the original weight (14% loss). This confirmed the establishment of the disease model (**Figure 3.1.2C**). Throughout the study, mice treated with cp-MΦ-NPs showed the smallest body weight loss (retaining over 95% of the original body weight on day 10), indicating

effective amelioration of the colitis symptoms. Notably, mice treated with cp-RBC-NPs or empty capsules showed comparable weight loss as that of the DDS only group (no treatment), of which the body weight reduced to 88% and 84% of the original body weight, respectively.

The colon length of mice with DSS-induced colitis correlates with the disease severity, as more severe colitis corresponds to a shorter colon length [21, 36]. Therefore, we used colon length as another indication to evaluate the efficacy of cp-MΦ-NP treatment. Compared to the colon of healthy mice, the colon of mice with colitis shortened significantly (**Figure 3.1.2D**). In contrast, the colon length of mice treated with cp-MΦ-NPs is comparable to that of the healthy controls. Neither cp-RBC-NPs nor empty capsules showed efficacy. Quantitative colon length measurements further confirmed the above observation. The average colon length of healthy mice was 9.4 ± 0.2 cm. DSS challenge shortened the colon length to an average of 6.5 ± 0.5 cm. On the contrary, cp-MΦ-NP treatment restored the colon length to 8.8 ± 0.5 cm, comparable tothat of healthy mice, and significantly longer than that in either cp-RBC-NP or empty capsules treatment groups (7.3 ± 0.2 cm and 6.5 ± 0.8 cm, respectively) (**Figure 3.1.2E**). In the study, we also monitored the disease activityindex (DAI), a summation of weight loss scores, stool consistency scores, and rectal bleeding scores [21, 36]. As shown in **Figure 3.1.2F**, cp-MΦ-NP treatment

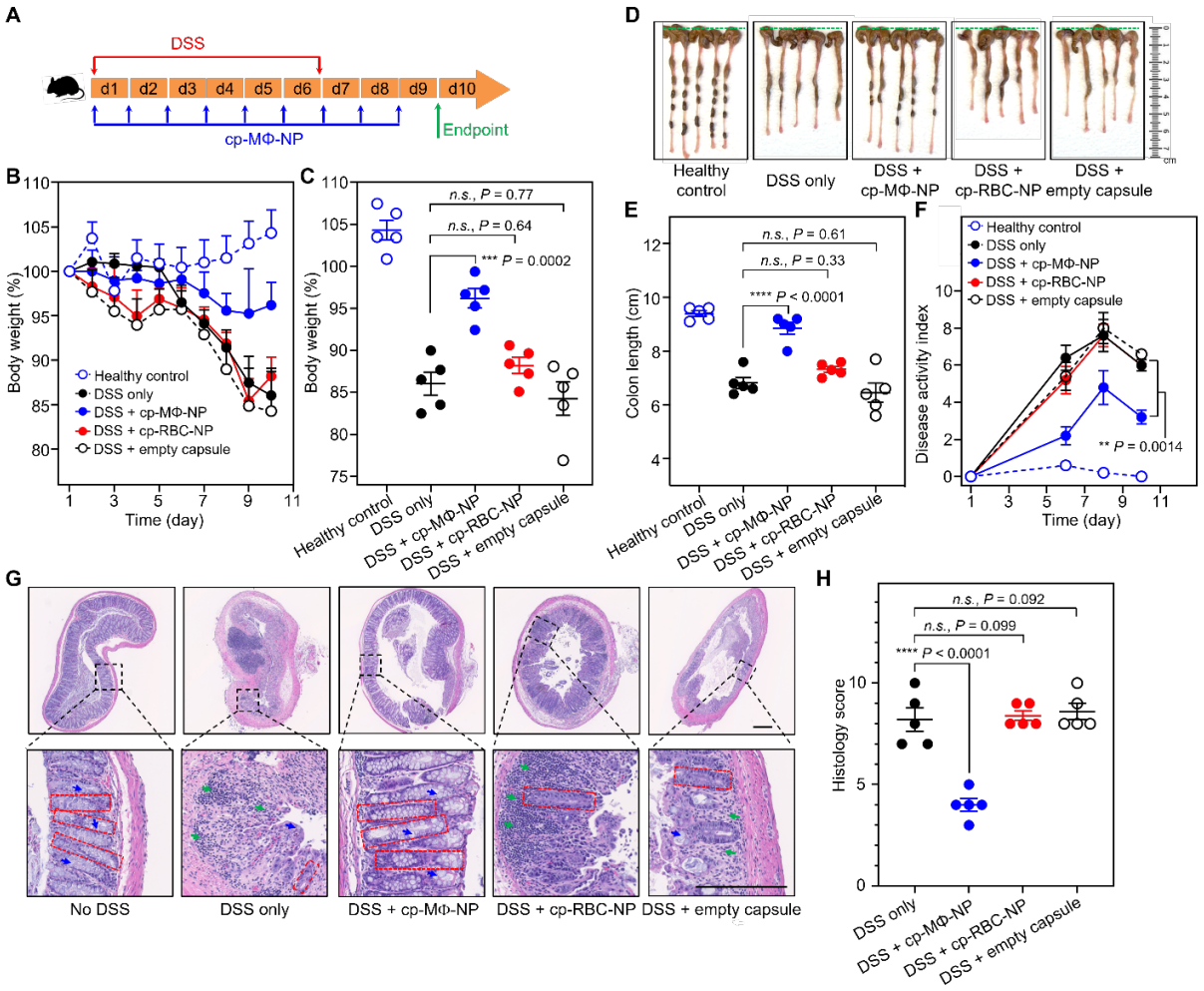

Figure 3.1.2 *In vivo* efficacy of cp-MΦ-NPs for DSS-induced colitis in a prophylactic regimen. (A) The prophylactic study protocol. Seven-week-old male C57BL/6 mice were provided with either water or 3% DSS-containing water for 6 days. Meanwhile, the mice were administrated daily with PBS, an empty capsule, cp-RBC-NPs or cp-MΦ-NPs (3 mg of MΦ-NPs per capsule, 1 capsule per day) via oral gavage for 9 days. (B, C) Daily body weight plotted as the daily value (B) or values at the end of the treatment (C). (D) Mouse colon tissues from different experimental groups were collected and imaged on day 10. (E) Quantification of colon length in (D). (F) The disease activity index (DAI) calculated based on stool consistency (0–4), rectal bleeding (0–4), and weight loss (0–4). (G) Representative H&E staining images of mouse colon tissues from different experimental groups on day 10, scale bar = 1 mm (red dotted box: the crypt, blue arrow: the goblet cell, green arrow: infiltrating immune cells, scale bar in magnified image = 250 μm). (H) Histomorphological evaluation of the colonic damage based on inflammatory cell infiltrate (0–3), epithelial architecture (0–3), muscle thickening (0-3), goblet cell depletion (0-1), and crypt abscess (0-1) as scoring criteria. In all datasets, n = 5; data are presented as mean ± s.d.; *n.s.* = not significant; ***$p < 0.001$ and ****$p < 0.0001$. Statistical analysis was performed with one-way ANOVA.

significantly decreased the DAI throughout the study as compared to DSS-challenged mice and mice treated with cp-RBC-NPs or the empty capsules. We then performed a histological analysis

of the colon tissues to investigate the cp-MΦ-NP efficacy at a tissue level. Colon tissue from healthy mice showed well-defined fingerlike crypt structures, goblet cells, and the absence of infiltrating immune cells (**Figure 3.1.2G**). Without treatment (DSS only), the colon tissue of the mice with IBD showed heavy crypt distortion, severe goblet cell loss, and noticeable infiltrating immune cells, comparable to previously reported histological analysis [21]. Colon tissue from mice treated with cp-MΦ-NPs showed similar histological features to those of the healthy controls, including regular crypt structures, minimal loss of goblet cells, and a low level of infiltrating immune cells. Meanwhile, colon tissues of mice treated with cp-RBCs-NPs or empty capsules showed distinctive histological features as those in the no-treatment group. We calculated the histology scores summarizing the key colonic damage features [38]. As shown in **Figure 3.1.2H**, cp-MΦ-NP treatment significantly reduced the scores to a level close to that of the healthy controls. In contrast, all other treatments scored highest, demonstrating cp-MΦ-NP protection against pathological damage in colonic epithelium.

To evaluate the in vivo cp-MΦ-NP efficacy at a cellular level, we examined the colonic epithelial cell function and barrier integrity at the end of the indicated treatments. Tissue cross-sections from the healthy mice stained for zonula occludens protein-1 (ZO-1) and occludin, two signature tight junction-associated proteins, showed strong fluorescence with orderly patterns on the colonic lumen, indicating an intact intestinal barrier (**Figure 3.1.3A**) [21]. However, the fluorescence diminished on the cross-sections of the tissue from mice with colitis but received no treatment, suggesting the disruptions of the colon epithelial and mucosal barriers. The cp-MΦ-NP treatment restored the tissue damage, preserving colonic epithelial cell function and barrier integrity. Notably, ZO-1 and occludin expressions on samples of mice treated with cp-RBC-NPs and empty capsules appeared similar to the DSS group without treatment, indicating the absence

of efficacy. To gain a quantitative comparison, we evaluated ZO-1 messenger RNA (mRNA) expression in intestinal epithelial cells (**Figure 3.1.3B**). Consistent with the protein immunofluorescence analysis, cp-MΦ-NP treatment kept the expression of ZO-1 mRNA at a level comparable to that of the healthy controls. All other treatment groups showed a significant reduction in ZO-1 mRNA expression. We also found similar results when analyzing occludin mRNA expression, where mice treated with cp-MΦ-NPs showed a similar expression level as the healthy mice (**Figure 3.1.3C**). We further evaluated intestinal epithelial cell function via a terminal deoxynucleotidyl transferase dUTP nick end labeling (TUNEL) assay (**Figure 3.1.3D**) [39]. Compared to the healthy controls, the TUNEL assay found colonic epithelium apoptosis in large areas of the crypts from mice with DSS-induced colitis. Treatment with cp-MΦ-NPs reduced the apoptosis to a level comparable to that of the healthy controls. Groups treated with cp-RBC-NPs or empty capsules showed apoptosis levels comparable to that of the disease group. Further quantification of TUNEL-positive cells is consistent with the observation, confirming the efficacy of cp-MΦ-NPs (**Figure 3.1.3E**). We hypothesize that the observed anti-inflammatory efficacy was due to the capability of cp-MΦ-NPs to neutralize pro-inflammatory cytokines. To test this hypothesis, we measured colonic concentrations of representative pro-inflammatory cytokines, including IL-6, TNF-α, and IL-1β. As shown in **Figure 3.1.3F**, mice pretreated with DSS exhibited a significant

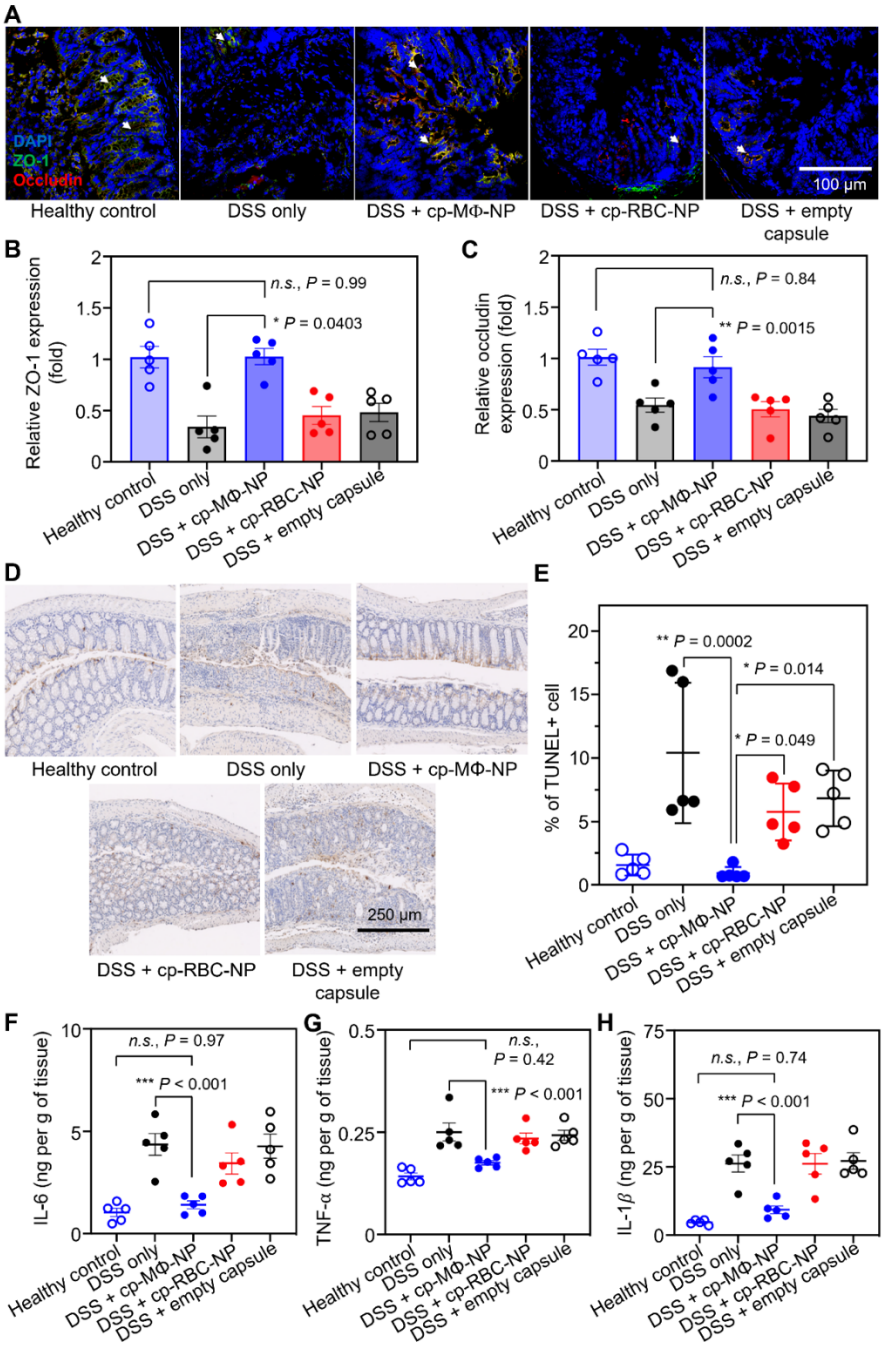

Figure 3.1.3 Cellular and molecular studies of cp-MΦ-NPs protecting colonic epithelium. (A) Representative immunofluorescence images of colon sections collected on day 10 after the indicated treatments for analysis of the tight junction ZO-1 and occludin expressions. (B, C) Quantitative mRNA expression levels of ZO-1 (B) and occludin (C) via RT-PCR. (D) Representative TUNEL staining of colon sections collected on day 10 after the indicated treatments. (E) Quantification of TUNEL positivity based on (D). (F-H) Quantitative analysis of the pro-inflammatory cytokine levels, including IL-6 (F), TNF-α (G), and IL-1β (H) on day 10 after the indicated treatment. In all datasets (E-H), n = 5; data are presented as mean ± s.d.; *n.s.* = not significant; $*p < 0.05$, $**p < 0.01$, and $***p < 0.001$; statistical analysis was performed with one-way ANOVA.

increase in colonic IL-6 levels compared to the healthy controls, consistent with previous studies [21, 36]. In contrast, the local IL-6 level in mice treated with cp-MΦ-NPs decreased to a comparable level as the healthy controls. Similar results were also observed for TNF-α and IL-1β, confirming the pro-inflammatory cytokine neutralization capability of cp-MΦ-NPs (**Figure 3.1.3G, H**).

To fully evaluate the treatment benefit of cp-MΦ-NPs for IBD, we examined the in vivo efficacy in a delayed treatment regimen, where cp-MΦ-NPs were administered after establishing the colitis (**Figure 3.1.4A**). In the study, administration of DDS alone led to significant body weight loss with time. Without treatment, mice with DSS-induced colitis showed a continuous body weight loss with 75.5% of the original body weight on day 13 (**Figure 3.1.4B**). Within the same period, mice treated with cp-MΦ-NPs showed significant bodyweight recovery, reaching 90% of the original body weights on day 13, indicating a preclinical treatment benefit of cp-MΦ-NPs. Colitis mice treated with cp-RBC-NPs or empty capsules showed similar weight loss as the DSS-only group, confirming the treatment efficacy of cp-MΦ-NPs (**Figure 3.1.4C**). At the study endpoint, the mice were sacrificed and examined the colon length. The cp-MΦ-NP treatment preserved the colon length comparable to the healthy controls (**Figure 3.1.4D**). Neither cp-RBC-NP nor empty capsules showed efficacy. Quantitative measurements of the colon length further confirmed the efficacy observed from cp-MΦ-NPs (**Figure 3.1.4E**). Meanwhile, the DAI values of the mice treated

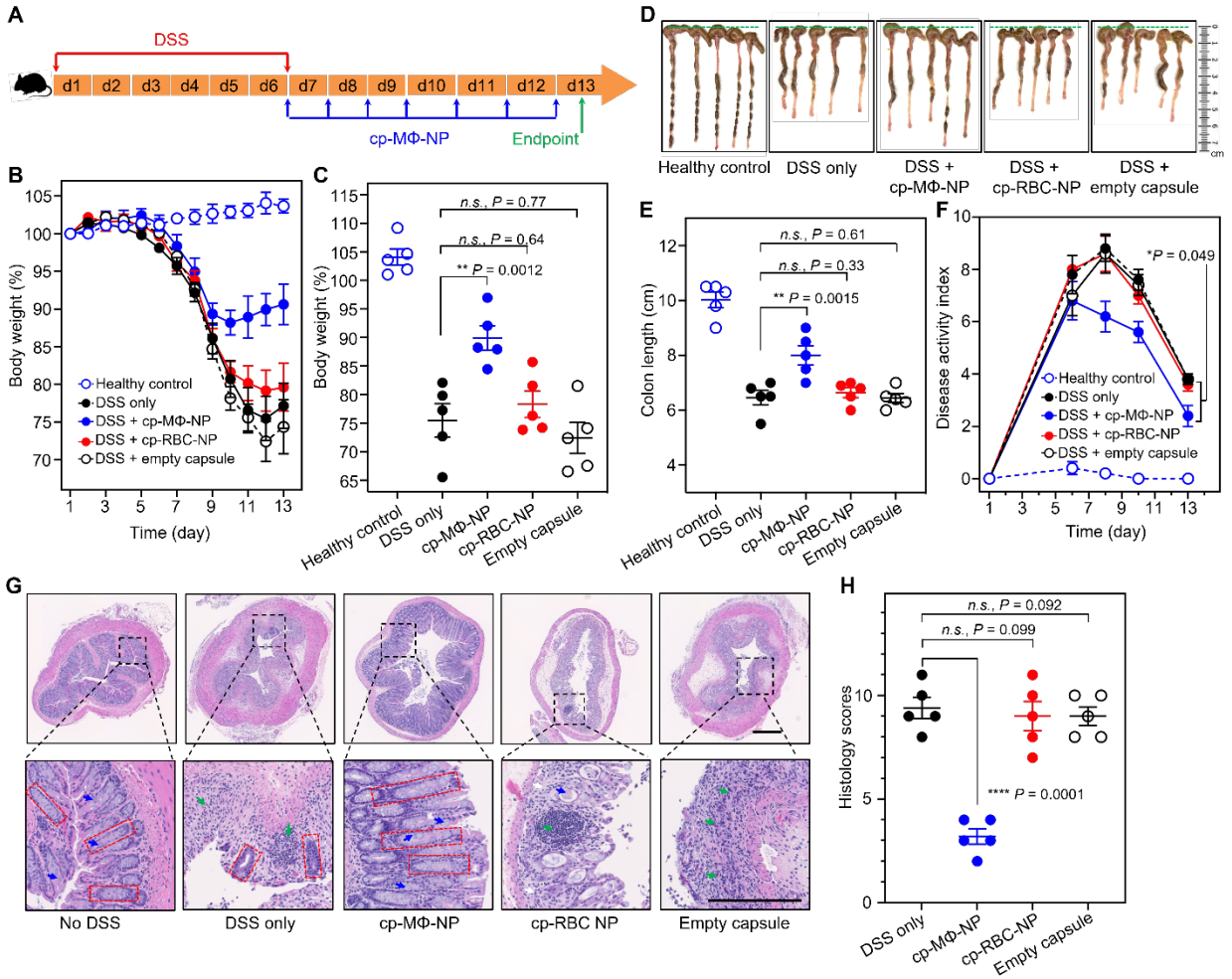

Figure 3.1.4 *In vivo* efficacy of cp-MΦ-NPs for DSS-induced colitis in a delayed treatment regimen. (A) The delayed treatment study protocol. Seven-week-old male C57BL/6 mice were provided with either water or 3% DSS-containing water for 6 days. Then the mice were administrated daily with PBS, an empty capsule, cp-RBC-NPs, or cp-MΦ-NPs (3 mg of MΦ-NPs per capsule; 1 capsule per day) via oral gavage from day 7 to day 13. (B, C) Daily body weight plotted as the daily value (B) or values at the end of the treatment (C). (D) Mouse colon tissues from different experimental groups were collected and imaged on day 13. (E) Quantification of colon length in (D). (F) The disease activity index (DAI) calculated based on stool consistency (0–4), rectal bleeding (0–4), and weight loss (0–4). (G) Representative H&E staining images of mouse colon tissues from different experimental groups on day 13, scale bar = 1 mm (red dotted box: the crypt, blue arrow: the goblet cell, green arrow: infiltrating immune cells, scale bar in magnified image = 250 μm). (H) Histomorphological evaluation of the colonic damage based on inflammatory cell infiltrate (0–3), epithelial architecture (0–3), muscle thickening (0-3), goblet cell depletion (0-1), and crypt abscess (0-1) as scoring criteria. In all datasets, n = 5; data are presented as mean ± s.d.; *n.s.* = not significant; *$p < 0.05$, **$p < 0.01$, and ****$p < 0.0001$; statistical analysis was performed with one-way ANOVA.

with cp-MΦ-NPs decreased once the treatment started (**Figure 3.1.4F**), but the DAI values of mice in other groups remained high. Histological analysis showed that the colon tissues from healthy mice

displayed well-defined fingerlike crypt structures, goblet cells, and no infiltrating immune cells, indicating intact colonic epithelial barriers (**Figure 3.1.4G**). However, the DSS challenge impaired the colonic epithelial barriers, indicated by severe crypt distortion, severe goblet cell loss, and heavy infiltration of immune cells. Colon tissues from mice treated with cp-MΦ-NPs showed similar histological features as those of the healthy controls. In contrast, tissues from mice treated with cp-RBC-NPs or empty capsules exhibited histological features like the DSS-only group. We also scored the severity of colonic epithelial barrier damage and found mice treated with cp-MΦ-NPs were scored similarly to the healthy controls (**Figure 3.1.4H**). Their scores were significantly lower than that of other treatment groups. Collectively, these results confirmed that cp-MΦ-NPs effectively ameliorated DSS-induced colitis damage in a delayed treatment regimen.

Finally, we evaluated the acute toxicity of cp-MΦ-NPs after their oral administration into healthy C57BL/6 mice. Each mouse received one capsule per day (3 mg cp-MΦ-NPs per capsule) from day 1 to day 7. Mice administrated with PBS or empty capsules served as controls. We monitored body weight changes daily but found no significant weight loss in all groups (**Figure 3.1.5A**). On day 8, we collected blood, feces, and colons from the mice and performed comprehensive biomarker analyses. Serum metabolic panel analysis showed no significant changes in biomarkers associated with liver or kidney functions in mice treated with cp-MΦ-NPs (**Figure 3.1.5B**). Moreover, the WBCs, RBCs, and platelets remained at comparable levels among all groups (**Figure 3.1.5C**).

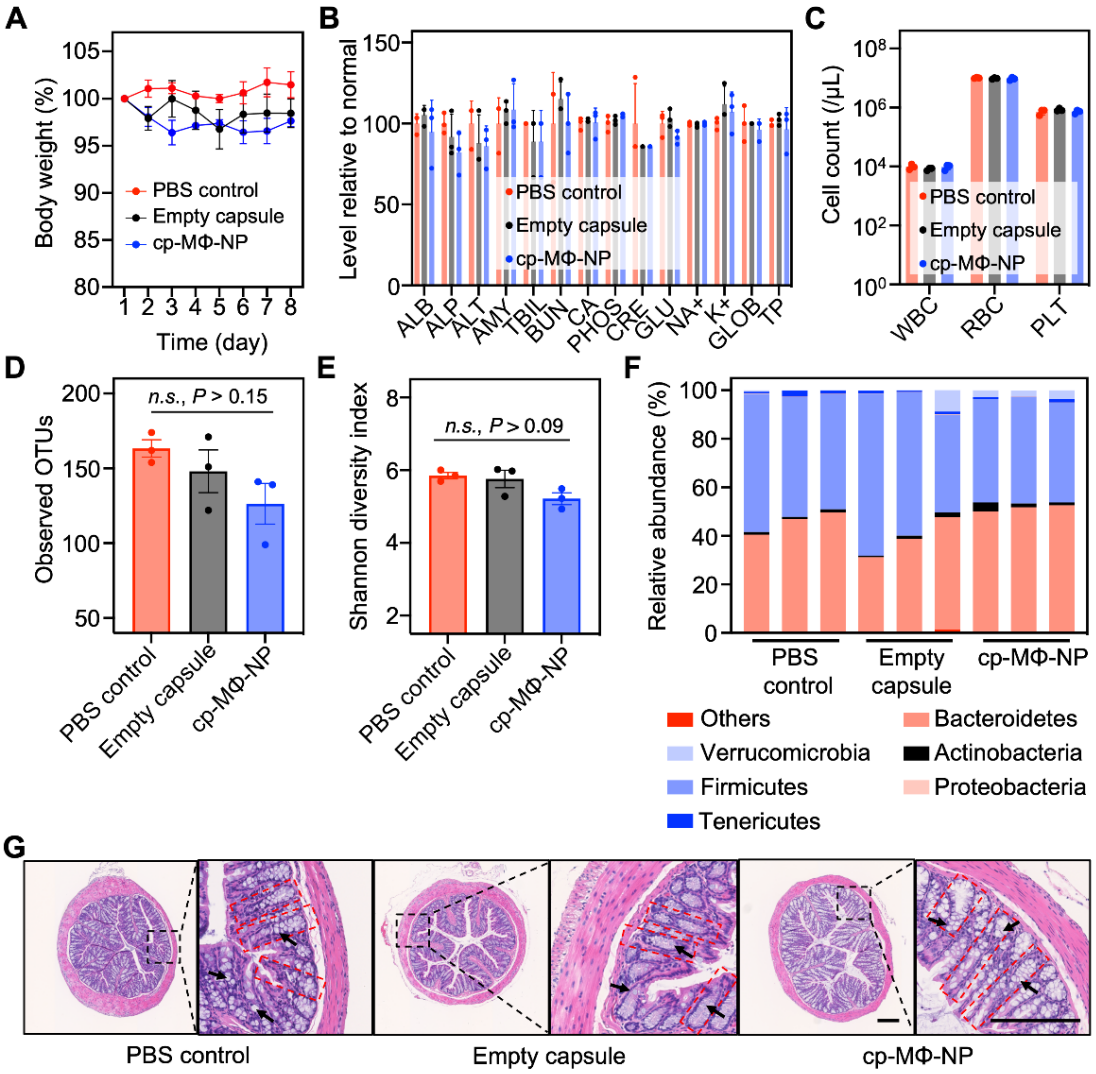

Figure 3.1.5 ***In vivo*** **biosafety of cp-MΦ-NPs**. Seven-week-old male C57BL/6 mice were administrated daily with PBS, an empty capsule, or cp-MΦ-NPs (3 mg of MΦ-NPs per capsule; 1 capsule per day) via oral gavage for 7 days. (A) Daily body weight during the study. (B, C) Comprehensive serum chemistry panel (B) and blood cell count (C) performed at the end of the 7-day treatments. ALB, albumin; ALP, alkaline phosphatase; ALT, alanine aminotransferase; AMY, amylase; TBIL, bilirubin; BUN, urea nitrogen; CA, calcium; PHOS, phosphorus; CRE, creatinine; GLU, glucose; NA+, sodium; K+, potassium; GLOB, globulin (calculated); TP, total protein. (D, E) Gut microbiome analysis based on quantification of microbial community observed OTU richness (D) and quantification of α-diversity (Shannon index, E). (F) Relative abundance of gut microbiome at phylum-level taxa presented as a percentage of total sequences. (G) H&E-stained histological sections from colonic tissues collected at the end of the 7-day treatments. Red dotted boxes indicate the crypts, and black arrows indicate the goblet cells. Scale bar = 250 μm. In all datasets, n = 3; data are presented as mean ± s.d.; *n.s.* = not significant.

Analysis of fecal samples via 16S rRNA sequencing in the V3 and V4 regions also demonstrated that daily administration of cp-MΦ-NPs induced an insignificant impact on the operational taxonomic unit (OTU) richness representing intestinal flora abundance (**Figure 3.1.5D**). Measurements of the Shannon α-diversity index also showed a negligible impact of cp-MΦ-NP treatment on the microbiota richness and distribution evenness (**Figure 3.1.5E**). Examination of the relative abundance of flora at the phylum level exhibited a similar microbiome composition among all experimental groups (**Figure 3.1.5F**). Furthermore, we collected the colonic tissues and stained the sections with hematoxylin and eosin (H&E) for histopathological analysis (**Figure 3.1.5G**). We found that the overall structure, integrity, and immune infiltration of tissues in mice treated with cp-MΦ- NPs or empty capsules were similar to those of the PBS control group. Together, these results indicate that cp-MΦ-NPs have a high biosafety profile.

3.1.3 Conclusion

In summary, we have successfully developed a capsulated MΦ-NP formulation that showed great promise as an anti-inflammatory strategy for managing IBD. The resulting cp-MΦ-NPs were able to withstand the harsh gastric environment and deliver the medication directly to the inflamed colon without being denatured. Once at the disease site, the MΦ-NPs were released from the capsules and present the same antigenic profiles as the endogenous macrophages, acting as decoys to neutralize pro-inflammatory cytokines. Unlike conventional anti-cytokine biologics that inhibit specific and limited targets, cp-MΦ-NPs represent a broad-spectrum approach the provides a disease-relevant inhibition of the inflammation cascade in IBD. In a DSS-induced murine IBD model, oral administration of cp-MΦ-NPs in both prophylactic and delayed treatment regimens significantly reduced colonic pro-inflammatory cytokine levels. The treatment resulted

in bodyweight recovery, preservation of colon length, and colon tissue protection. Importantly, cp-MΦ-NPs showed no acute toxicity.

In previous studies, cellular nanosponges have shown efficacy in treating various inflammatory diseases [40, 41]. The characteristics of these diseases play a crucial role in determining the design of nanosponge formulations. Factors such as the membrane type, route of administration, and membrane functionalization are typically tailored accordingly. In this work, the development of cp-MΦ-NPs exemplifies the underlying principle of biological neutralization shared by various types of cellular nanosponges. However, the cp-MΦ-NP formulation illustrates the importance of customized design features including freeze-drying, capsule encapsulation, colon targeting, and oral delivery. The success of this approach has greatly expanded the application potential of the cellular nanosponge platform.

Toward future translation of cp-MΦ-NPs, several critical aspects should be considered. Firstly, optimizing the physicochemical properties of the nanosponges may further enhance the disease-targeting ability and treatment efficacy of cp-MΦ-NPs. For instance, modifying the surface chemistry of the nanosponges can reduce absorption by healthy tissue while enabling deeper penetration into inflamed tissue, thereby enhancing their anti-inflammatory activity [42]. Tuning the size and size distribution of the nanosponges may also improve nanoparticle diffusion and retention, leading to better treatment efficacy. Additionally, robust evidence in mouse models suggests that an altered intestinal microbial flora may contribute to IBD development and progression [43, 44]. Thus, modulating nanosponge interactions with microbiota and infiltrated immune cells could be beneficial. Nanosponge surface functionalization approaches such as lipid insertion, membrane hybridization, metabolic synthesis, and genetic engineering can help achieve this goal. Furthermore, it is crucial to establish a large-scale manufacturing process, along with

adequate quality control and quality assurance measures, to ensure an adequate supply of cp-MΦ-NPs for preclinical and clinical tests. These challenges and opportunities remain to be explored in the future.

3.1.4 Experimental Methods

3.1.4.1 Macrophage Membrane Derivation

Cell membrane of J774 cells, a mouse macrophage cell line, was collected according to a previously established protocol [25]. Briefly, frozen cell stocks were thawed and washed with 1X phosphate-buffered saline (PBS, Corning) three times. Cells were then suspended in a hypotonic lysing buffer containing 30 mM Tris-HCl (pH 7.5), 225 mM D-mannitol, 75 mM sucrose, 0.2 mM ethylene glycol-bis(β-aminoethyl ether)-*N*,*N*,*N*′,*N*′-tetraacetic acid) (EGTA, all from Millipore-Sigma), and a protease and phosphatase inhibitor cocktail (Thermo Fisher Scientific). After 15 min of incubation at room temperature, cells were disrupted using a Dounce homogenizer with a tight-fitting pestle (20 passes). The homogenized solution was centrifuged at 10,000 ×g for 25 min at 4°C. The pellets were discarded, and the supernatant was centrifuged again at 150,000 ×g for 35 min at 4°C to pellet the membrane. Following the centrifugation, the membrane was washed once by being resuspended in ethylenediaminetetraacetic acid (EDTA, 37 ml, 0.2 mM, Millipore-Sigma) and collected with centrifugation at 150,000 ×g for 35 min at 4°C. Finally, the membrane was resuspended in 1 ml 0.2 mM EDTA. The membrane protein concentration was measured by using a BCA kit (Pierce Thermo Scientific). The membrane suspension was stored at -80°C for subsequent uses.

3.1.4.2 Red blood cell (RBC) membrane derivation

Human RBC membrane derivation was performed using a published protocol [45, 46]. Briefly, packed human RBCs (ZenBio Inc.) were washed with ice-cold 1X PBS and lysed with a hypotonic solution containing 0.25X PBS for 20 min. After the cell lysing process, the lysed cells were pelleted by centrifugation at 800 ×g for 5 min, followed by removing the supernatant containing hemoglobin. Such hypotonic-based cell lysing steps were repeated three times. The RBC membrane was resuspended in water at a protein concentration of 10 mg ml^{-1} and stored at -80 °C for subsequent studies.

3.1.4.3 Preparation of cell membrane-coated nanoparticles

Nanoparticles coated with J774 mouse macrophage membrane (denoted "MΦ-NPs") were synthesized using a previously published procedure [25]. Briefly, 1 ml of poly(dl-lactic-co-glycolic acid) (PLGA, 50:50, 0.67 dl g^{-1}, Lactel Absorbable Polymers) in acetone (20 mg ml^{-1}, Millipore-Sigma) was added dropwise into 4 ml water. The mixture was vacuumed under an aspirator for 2 h to evaporate the acetone completely. For fluorescence imaging, 1,1'-Dioctadecyl-3,3,3',3'-Tetramethylindotricarbocyanine Iodide (DiR, excitation/emission = 748/780 nm, Thermo Fisher Scientific) was added to the PLGA solution before the mixture was added into the water. The dye concentration was 0.1 wt% of PLGA polymer. The macrophage membrane was mixed with the PLGA core for cell membrane coating at a polymer-to-membrane protein weight ratio of 1:1. The mixture was then sonicated with a bath sonicator (Fisher Scientific FS30D) for 3 min. RBC membrane-coated nanoparticles (denoted "RBC-NPs") were fabricated following the same process.

3.1.4.4 Preparation of nanoparticle-loaded capsules

For MΦ-NP encapsulation, MΦ-NPs were first lyophilized in 10% sucrose for 48 h using FreeZone 4.5 lyophilizer (Labconco). Following the lyophilization, 3 mg of MΦ-NP powder was loaded into a mouse-specific, size M gel capsule using a capsule loading kit (all from Braintree Scientific). After the encapsulation, capsules were coated with the commercial enteric coating polymer Eudragit S100 (Evonik Operations) for protection from the gastric environment. In brief, the Eudragit S100 polymer was dissolved in 95% ethanol (Koptec) with 2.5% triethyl citrate (Millipore-Sigma) to a final concentration of 6 w/v%. The polymer solution was then stirred overnight in a closed container at room temperature. The capsules were dipped into the Eudragit S100 coating solution for coating, followed by 25 min of air-dry. The dip-coating process was repeated three times. Loading RBC-NP into the capsules was performed by following the same procedure.

3.1.4.5 Nanoparticle physicochemical characterization

The size (diameter, nm) and surface zeta potential (mV) of the nanoparticles were measured using dynamic light scattering (DLS, Malvern Zetasizer Nano ZS). For studying morphology, the nanoparticle samples were adsorbed onto carbon-coated copper grids (400-mesh, Electron Microscopy Sciences) and stained with 0.2 wt% uranyl acetate (Electron Microscopy Sciences). The grids were imaged on a JEOL 1200 EX II transmission electron microscope. For evaluating the colloidal stability, the samples were incubated in SIF at 37°C, and the nanoparticle size was measured daily with DLS for 7 days. For evaluating the protective effect of the capsule against the gastric environment, DiD-labeled MΦ-NPs were lyophilized and loaded into the Eudragit S100-coated capsules. Then the capsules were incubated in a simulated gastric fluid (SGF, pH = 2) or simulated intestinal fluid (SIF, pH = 7.4, both from RICCA Chemical). The fluid

samples were stirred at room temperature. The release of DiD-labeled MΦ-NPs was quantified by measuring DiD fluorescence signal (excitation/emission = 644/665 nm) in the fluid samples using a Tecan Infinite M200 plate reader (Tecan).

3.1.4.6 *In vitro* cytokine binding study

Recombinant mouse TNF-α (2 ng ml^{-1}), IL-1β (8 ng ml^{-1}), or IL-6 (8 ng ml^{-1}, all from Biolegend) was mixed with MΦ-NPs at final concentrations ranging from 0 to 2 mg ml^{-1}. The mixtures were incubated for 2 h at 37°C, and the MΦ-NPs were removed by centrifugation at 16,100 ×g for 10 min. The concentrations of unbound cytokines remaining in the supernatant were quantified using mouse TNF-α, IL-1β, and IL-6 enzyme-linked immunosorbent assay (ELISA, kits purchased from Biolegend). The measurements were carried out in 1X PBS (pH = 7.4). The bound cytokine levels were calculated by subtracting the concentration of unbound cytokine from the initial cytokine input. Nonlinear curve fitting was performed in GraphPad Prism 9.

3.1.4.7 Animals

All mice used in this study were housed in an animal facility at the University of California San Diego (UCSD) under federal, state, local, and National Institutes of Health (NIH) guidelines. 6-week-old male C57BL/6 mice were purchased from Jackson Laboratory and were maintained under standard housing with 12 h light - 12 h dark cycle, ambient temperature, and average humidity. All animal experiments were performed in accordance with NIH guidelines and approved by the Institutional Animal Care and Use Committee (IACUC) of UCSD.

3.1.4.8 Pharmacokinetics and biodistribution studies

Capsules loaded with DiR-labeled MΦ-NPs (3 mg per capsule) were orally administrated to 7-week-old male C57BL/6 mice using a capsule dosing syringe (Braintree Scientific). At 2, 4, 6, 10, and 24 h after the oral gavage, three mice were euthanized at each time point, and the entire gastrointestinal (GI) tract was collected. The GI tracks were rinsed with 1X PBS three times for biodistribution analysis and imaged using a Xenogen IVIS 200 system. The collected GI tracks were weighed and homogenized for quantitative analysis in 1 ml 1X PBS. The fluorescent signals were quantified using a Tecan Infinite M200 plate reader (Tecan, excitation/emission = 748/780 nm).

3.1.4.9 Dextran sulfate sodium (DSS)-induced mouse colitis model

Six-week-old male C57BL/6 mice were divided into groups of five mice per cage and acclimatized for 1 week before the in vivo experiments. In all studies, nanosponge dosage was limited to a single capsule per day with its maximum nanosponge loading capacity. In a prophylactic regimen, the treatment started from day 1 and ended on day 9. Specifically, mice were administered with 3% DSS supplemented in drinking water for 6 days, followed by regular water. Mice fed with regular drinking water only were used as a control group. During the treatment period, PBS, empty capsules, capsules loaded with RBC-NPs (denoted 'cp-RBC-NPs', 3 mg RBC-NPs per capsule), and capsules loaded with MΦ-NPs (denoted 'cp-MΦ-NPs', 3 mg MΦ-NPs per capsule) were orally administrated into mice using a capsule dosing syringe one capsule per day for 9 days. For the delayed treatment regimen, mice were administrated with 3% DSS supplemented in drinking water for 6 days, followed by regular drinking water. At the end of day 6, mice were orally administered with PBS, empty capsules, RBC-NP capsules (3 mg RBC-NPs

per capsule), and MΦ-NP capsules (3 mg MΦ-NPs per capsule) at a dosage of one capsule per day until day 13.

3.1.4.10 Disease severity evaluation

In all studies, changes in the body weight of all mice were recorded daily throughout the experimental period. In addition, fecal samples were collected on predetermined time points used to calculate the disease activity index (DAI) based on stool consistency (0-4), rectal bleeding (0-4), and weight loss (0-4) [47]. Specifically, (a) stool consistency: 0 = normal, 1 = soft stool, 2 = loose stool, and 4 = diarrhea; (b) rectal bleeding: 0 = no blood, 1 = Hemoccult positive, 2 = Hemoccult positive and visual pellet bleeding, and 4 = gross bleeding with blood around anus; (c) weight loss: 0 = no loss, 1 = 1-5% loss, 2 = 5-10% loss, 3 = 10-20%, and 4 ≥ 20% loss. At the study endpoints, mice were euthanized. The entire colon was extracted, and the length was measured. Then, a piece of colonic tissue (0.5 cm in length, n = 5) was excised from the distal section and cut into three sections. The three sections were used for histological analysis, immunofluorescence staining, and mRNA quantification, respectively. The remaining colonic tissue was weighed and homogenized in 0.5 ml of 1X PBS for the quantification of pro-inflammatory cytokines concentration. In the quantification, homogenized samples were centrifuged for 10 min at 10,000 ×g at 4°C. The concentration of TNF-α, IL-1β, and IL-6 in the supernatant were quantified using an ELISA kit (BioLegend).

3.1.4.11 Histological analysis of colonic tissues

Colon samples collected from the above study were also used for H&E and TUNEL staining (n = 5, UCSD Histology Core). To quantify TUNEL positivity, five random areas were

selected from each group. Within each area, the total number of cells and the number of TUNEL-positive cells were counted. TUNEL positivity was determined by calculating the ratio of TUNEL-positive cells to the total cells. For evaluating the disease severity, the histological samples were scored for the presence of neutrophilic and mononuclear infiltrates (0-3), epithelial architecture damage (0–3), muscle thickening (0-3), goblet cell depletion (0-1), and crypt abscess (0-1) [48]. The colonic histological damage scores were summed, resulting in a final score between 0 and 11.

3.1.4.12 Immunofluorescence analysis of colonic tissues

For immunofluorescence analysis of ZO-1 and occludin-1 expressions on mouse colonic tissues, 0.5 cm of colonic tissues were fixed in Tissue-Tek O.C.T. Compound at -80°C (Sakura Finetek). After cryo-section, the colonic tissue samples were permeabilized with 0.25% Trition-100X and blocked with 2% bovine serum albumin (BSA) in 1X PBS for 1 h. The sections were then stained with 5 μg ml^{-1} mouse anti-ZO-1 antibodies conjugated with AlexaFluor-488 (ThermoFisher) and 1 μg ml^{-1} mouse anti-occludin antibodies conjugated with AlexaFluor-594 (ThermoFisher) overnight at 4°C. Meanwhile, Hoechst 33342 (1 μg ml^{-1}, ThermoFisher) was used for nuclei staining. Finally, the immunofluorescence signals were observed by using a confocal microscope (Leica SP8).

3.1.4.13 Quantitative reverse transcription PCR (qRT-PCR)

According to the manufacturer's protocol, RNA was extracted from mouse colonic tissues using a Direct-zol RNA Miniprep kit (Zymo Research). The RNA was reverse transcribed into cDNA using the ProtoScript First Strand cDNA Synthesis kit (New England BioLabs), followed by qPCR using LUNA Universal qPCR Master Mix (New England BioLabs). The cycling

condition was 95°C for 1 min and then 40 cycles of 95°C for 15 s and 60°C for 45 s. The relative expression of target genes was calculated using β-actin as a reference gene. The primers used for amplifications include the following: ZO-1 forward (CTTCTCTTGCTGGCCCTAAAC), ZO-1 reverse (TGGCTTCACTTGAGGTTTCTG), Occludin forward (CACACTTGCTTGGGACAGAG), Occludin reverse (TAGCCATAGCCTCCATAGCC), β-actin forward (AAGTGTGACGTTGACATCCG), and β-actin reverse (GATCCACATCTGCTGGAAGG). All sequences refer to 5' to 3'.

3.1.4.14 In vivo biosafety study

For in vivo biosafety study, six-week-old male C57BL/6 mice were divided into groups of three mice per cage and acclimatized for 1 week before the in vivo experiments. During the study period, PBS (100 μl), empty capsules, and MΦ-NP capsules (3 mg MΦ-NPs per capsule) were orally administrated into mice using a capsule dosing syringe at a dosage of one capsule per day for 7 days. Throughout the study, mouse weight changes were recorded daily, and the mice were euthanized at the endpoint for sample collection. For blood chemistry analysis and blood cell counts, mouse whole blood was collected into potassium–EDTA collection tubes (Sarstedt). The analysis was performed by the UCSD Animal Care Program Diagnostic Services Laboratory. For the histological analysis, the colons were sectioned and stained with H&E (Leica Biosystems), followed by imaging with a Nanozoomer 2.0-HT slide scanning system (Hamamatsu).

3.1.4.15 Microbiome analysis

200 mg of feces were collected from each mouse on day 8 of the in vivo biosafety study. The fecal samples were properly packed and shipped to Zymo Research Corporation for

microbiome analysis. In brief, microbiome DNA was extracted from the mouse feces using ZymoBIOMICS®-96 MagBead DNA Kit. The isolated DNA was then used to generate 16S rRNA libraries via the Quick-16S™ NGS Library Prep Kit (all from Zymo Research). 16S rRNA sequencing was performed on Illumina® MiSeq™ with a primer set specific to the V3 and V4 regions, and the analysis was conducted using Qiime v.1.9.1. and LEfSe analysis package.

3.1.5 References

[1] S.C. Ng, H.Y. Shi, N. Hamidi, F.E. Underwood, W. Tang, E.I. Benchimol, R. Panaccione, S. Ghosh, J.C.Y. Wu, F.K.L. Chan, J.J.Y. Sung, G.G. Kaplan, Worldwide incidence and prevalence of inflammatory bowel disease in the 21st century: a systematic review of population-based studies, Lancet 390(10114) (2017) 2769-2778.

[2] J.R. Turner, Intestinal mucosal barrier function in health and disease, Nat. Rev. Immunol. 9(11) (2009) 799-809.

[3] S. Mehandru, J.F. Colombel, The intestinal barrier, an arbitrator turned provocateur in IBD, Nat. Rev. Gastro. Hepat. 18(2) (2021) 83-84.

[4] J. Halfvarson, C.J. Brislawn, R. Lamendella, Y. Vazquez-Baeza, W.A. Walters, L.M. Bramer, M. D'Amato, F. Bonfiglio, D. McDonald, A. Gonzalez, E.E. McClure, M.F. Dunklebarger, R. Knight, J.K. Jansson, Dynamics of the human gut microbiome in inflammatory bowel disease, Nat. Microbiol. 2(5) (2017) 17004.

[5] E.A. Franzosa, A. Sirota-Madi, J. Avila-Pacheco, N. Fornelos, H.J. Haiser, S. Reinker, T. Vatanen, A.B. Hall, H. Mallick, L.J. McIver, J.S. Sauk, R.G. Wilson, B.W. Stevens, J.M. Scott, K. Pierce, A.A. Deik, K. Bullock, F. Imhann, J.A. Porter, A. Zhernakova, J.Y. Fu, R.K. Weersma, C. Wijmenga, C.B. Clish, H. Vlamakis, C. Huttenhower, R.J. Xavier, Gut microbiome structure and metabolic activity in inflammatory bowel disease, Nat. Microbiol. 4(5) (2019) 898-898.

[6] S. Alatab, S.G. Sepanlou, K. Ikuta, H. Vahedi, C. Bisignano, S. Safiri, A. Sadeghi, M.R. Nixon, A. Abdoli, H. Abolhassani, V. Alipour, M.A.H. Almadi, A. Almasi-Hashiani, A. Anushiravani, J. Arabloo, S. Atique, A. Awasthi, A. Badawi, A.A.A. Baig, N. Bhala, A. Bijani, A. Biondi, A.M. Borzi, K.E. Burke, F. Carvalho, A. Daryani, M. Dubey, A. Eftekhari, E. Fernandes, J.C. Fernandes, F. Fischer, A. Haj-Mirzaian, A. Haj-Mirzaian, A. Hasanzadeh, M. Hashemian, S.I. Hay, C.L. Hoang, M. Househ, O.S. Ilesanmi, N.J. Balalami, S.L. James, A.P. Kengne, M.M. Malekzadeh, S. Merat, T.J. Meretoja, T. Mestrovic, E.M. Mirrakhimov, H. Mirzaei, K.A. Mohammad, A.H. Mokdad, L. Monasta, I. Negoi, T.H. Nguyen, C.T. Nguyen, A. Pourshams, H. Poustchi, M. Rabiee, N. Rabiee, K. Ramezanzadeh, D.L. Rawaf, S. Rawaf, N. Rezaei, S.R. Robinson, L. Ronfani, S. Saxena, M. Sepehrimanesh, M.A. Shaikh, Z. Sharafi, M. Sharif, S. Siabani, A.R. Sima, J.A. Singh,

A. Soheili, R. Sotoudehmanesh, H.A.R. Suleria, B.E. Tesfay, B. Tran, D. Tsoi, M. Vacante, A.B. Wondmieneh, A. Zarghi, Z.J. Zhang, M. Dirac, R. Malekzadeh, M. Naghavi, G.B.D.I.B.D. Co, The global, regional, and national burden of inflammatory bowel disease in 195 countries and territories, 1990-2017: a systematic analysis for the Global Burden of Disease Study 2017, Lancet Gastroenterol. 5(1) (2020) 17-30.

[7] J.A. Beard, D.L. Franco, B.H. Click, The burden of cost in inflammatory bowel disease: a medical economic perspective and the future of value-based care, Current Gastroenterology Reports 22(2) (2020) 6.

[8] J. Zhou, M.Y. Li, Q.F. Chen, X.J. Li, L.F. Chen, Z.L. Dong, W.J. Zhu, Y. Yang, Z. Liu, Q. Chen, Programmable probiotics modulate inflammation and gut microbiota for inflammatory bowel disease treatment after effective oral delivery, Nat. Commun. 13(1) (2022) 3432.

[9] C.N. Bernstein, M. Fried, J.H. Krabshuis, H. Cohen, R. Eliakim, S. Fedail, R. Gearry, K.L. Goh, S. Hamid, A.G. Khan, A.W. LeMair, Malfertheiner, O.Y. Qin, J.F. Rey, A. Sood, F. Steinwurz, O.O. Thomsen, A. Thomson, G. Watermeyer, World gastroenterology organization practice guidelines for the diagnosis and management of IBD in 2010, Inflamm. Bowel Dis. 16(1) (2010) 112-124.

[10] B. Bressler, J.K. Marshall, C.N. Bernstein, A. Bitton, J. Jones, G.I. Leontiadis, R. Panaccione, A.H. Steinhart, F. Tse, B. Feagan, T.U. Colitis, Clinical practice guidelines for the medical management of nonhospitalized ulcerative colitis: The Toronto Consensus, Gastroenterology 148(5) (2015) 1035-1529.

[11] T.T. Hansel, H. Kropshofer, T. Singer, J.A. Mitchell, A.J.T. George, The safety and side effects of monoclonal antibodies, Nat. Rev. Drug Discov. 9(4) (2010) 325-338.

[12] J.G. Sathish, S. Sethu, M.C. Bielsky, L. de Haan, N.S. French, K. Govindappa, J. Green, C.E.M. Griffiths, S. Holgate, D. Jones, I. Kimber, J. Moggs, D.J. Naisbitt, M. Pirmohamed, G. Reichmann, J. Sims, M. Subramanyam, M.D. Todd, J.W. Van der Laan, R.J. Weaver, B.K. Park, Challenges and approaches for the development of safer immunomodulatory biologics, Nat. Rev. Drug Discov. 12(4) (2013) 306-324.

[13] D.F. Li, M.F. Yang, H.M. Xu, M.Z. Zhu, Y. Zhang, C.M. Tian, Y.Q. Nie, J.Y. Wang, Y.J. Liang, J. Yao, L.S. Wang, Nanoparticles for oral delivery: targeted therapy for inflammatory bowel disease, J. Mater. Chem. B 10(31) (2022) 5853-5872.

[14] B. Xiao, H. Laroui, E. Viennois, S. Ayyadurai, M.A. Charania, Y.C. Zhang, Z. Zhang, M.T. Baker, B.Y. Zhang, A.T. Gewirtz, D. Merlin, Nanoparticles with surface antibody against CD98 and carrying CD98 small interfering RNA reduce colitis in mice, Gastroenterology 146(5) (2014) 1289-1300.

[15] B. Xiao, H. Laroui, S. Ayyadurai, E. Viennois, M.A. Charania, Y.C. Zhang, D. Merlin, Mannosylated bioreducible nanoparticle-mediated macrophage-specific TNF-alpha RNA interference for IBD therapy, Biomaterials 34(30) (2013) 7471-7482.

[16] S.Q. Gou, Y.M. Huang, Y. Wan, Y. Ma, X. Zhou, X.L. Tong, J. Huang, Y.J. Kang, G.Q. Pan, F.Y. Dai, B. Xiao, Multi-bioresponsive silk fibroin-based nanoparticles with on-demand cytoplasmic drug release capacity for CD44-targeted alleviation of ulcerative colitis, Biomaterials 212 (2019) 39-54.

[17] H. Ali, B. Weigmann, M.F. Neurath, E.M. Collnot, M. Windbergs, C.M. Lehr, Budesonide loaded nanoparticles with pH-sensitive coating for improved mucosal targeting in mouse models of inflammatory bowel diseases, J. Control. Release. 183 (2014) 167-177.

[18] D.S. Wilson, G. Dalmasso, L.X. Wang, S.V. Sitaraman, D. Merlin, N. Murthy, Orally delivered thioketal nanoparticles loaded with TNF-alpha-siRNA target inflammation and inhibit gene expression in the intestines, Nat. Mater. 9(11) (2010) 923-928.

[19] X.J. Yan, Q. Pan, H.H. Xin, Y.X. Chen, Y. Ping, Genome-editing prodrug: Targeted delivery and conditional stabilization of CRISPR-Cas9 for precision therapy of inflammatory disease, Sci. Adv. 7(50) (2021) eabj0624.

[20] X.Y. Wang, J.J. Yan, L.Z. Wang, D.H. Pan, Y.P. Xu, F. Wang, J. Sheng, X.N. Li, M. Yang, Oral delivery of anti-TNF antibody shielded by natural polyphenol-mediated supramolecular assembly for inflammatory bowel disease therapy, Theranostics 10(23) (2020) 10808-10822.

[21] Y. Lee, K. Sugihara, M.G. Gillilland, S. Jon, N. Kamada, J.J. Moon, Hyaluronic acid-bilirubin nanomedicine for targeted modulation of dysregulated intestinal barrier, microbiome and immune responses in colitis, Nat. Mater. 19(1) (2020) 118-126.

[22] H. Liu, Z.W. Cai, F. Wang, L.W. Hong, L.F. Deng, J. Zhong, Z.T. Wang, W.G. Cui, Colon-targeted adhesive hydrogel microsphere for regulation of gut immunity and flora, Adv. Sci. 8(18) (2021) 2101619.

[23] Y.F. Liu, Y. Cheng, H. Zhang, M. Zhou, Y.J. Yu, S.C. Lin, B. Jiang, X.Z. Zhao, L.Y. Miao, C.W. Wei, Q.Y. Liu, Y.W. Lin, Y. Du, C.J. Butch, H. Wei, Integrated cascade nanozyme catalyzes in vivo ROS scavenging for anti-inflammatory therapy, Sci. Adv. 6(29) (2020) eabb2695.

[24] D. Wang, S.Y. Wang, Z.D. Zhou, D. Bai, Q.Z. Zhang, X.Z. Ai, W. Gao, L. Zhang, White Blood Cell Membrane-Coated Nanoparticles: Recent Development and Medical Applications, Adv. Healthc. Mater. 11(7) (2022) 2101349.

[25] S. Thamphiwatana, P. Angsantikul, T. Escajadillo, Q.Z. Zhang, J. Olson, B.T. Luk, S. Zhang, R.H. Fang, W. Gao, V. Nizet, L. Zhang, Macrophage-like nanoparticles concurrently absorbing endotoxins and proinflammatory cytokines for sepsis management, Proc. Natl. Acad. Sci. U.S.A. 114(43) (2017) 11488-11493.

[26] Q.Z. Zhang, J.L. Zhou, J.R. Zhou, R.H. Fang, W. Gao, L. Zhang, Lure-and-kill macrophage nanoparticles alleviate the severity of experimental acute pancreatitis, Nat. Commun. 12(1) (2021) 4136.

[27] M.Y. Hou, Y.S. Wei, Z.Y. Zhao, W.Q. Han, R.X. Zhou, Y. Zhou, Y.R. Zheng, L.C. Yin, Immuno-engineered nanodecoys for the multi-target anti-inflammatory treatment of autoimmune diseases, Adv. Mater. 34(12) (2022) 2108817.

[28] X.L. Wei, G. Zhang, D.N. Ran, N. Krishnan, R.H. Fang, W. Gao, S.A. Spector, L. Zhang, T-cell-mimicking nanoparticles can neutralize HIV infectivity, Adv. Mater. 30(45) (2018) 1802233.

[29] Y.R. Na, M. Stakenborg, S.H. Seok, G. Matteoli, Macrophages in intestinal inflammation and resolution: a potential therapeutic target in IBD, Nat. Rev. Gastro. Hepat. 16(9) (2019) 531-543.

[30] S.P. Bandi, Y.S. Kumbhar, V.V.K. Venuganti, Effect of particle size and surface charge of nanoparticles in penetration through intestinal mucus barrier, J. Nanoparticle Res. 22(3) (2020) 62.

[31] C.M.J. Hu, R.H. Fang, J. Copp, B.T. Luk, L. Zhang, A biomimetic nanosponge that absorbs pore-forming toxins, Nat. Nanotechnol. 8(5) (2013) 336-340.

[32] C.M.J. Hu, R.H. Fang, K.C. Wang, B.T. Luk, S. Thamphiwatana, D. Dehaini, P. Nguyen, P. Angsantikul, C.H. Wen, A.V. Kroll, C. Carpenter, M. Ramesh, V. Qu, S.H. Patel, J. Zhu, W. Shi, F.M. Hofman, T.C. Chen, W. Gao, K. Zhang, S. Chien, L. Zhang, Nanoparticle biointerfacing by platelet membrane cloaking, Nature 526(7571) (2015) 118-121.

[33] E. El-Maghawry, M.I. Tadros, S.A. Elkheshen, A. Abd-Elbary, Eudragit (R)-S100 Coated PLGA Nanoparticles for Colon Targeting of Etoricoxib: Optimization and Pharmacokinetic Assessments in Healthy Human Volunteers, Int. J. Nanomedicine 15 (2020) 3965-3980.

[34] Q.Z. Zhang, A. Honko, J.R. Zhou, H. Gong, S.N. Downs, J.H. Vasquez, R.H. Fang, W. Gao, A. Griffiths, L. Zhang, Cellular nanosponges inhibit SARS-CoV-2 infectivity, Nano Lett. 20(7) (2020) 5570-5574.

[35] M.F. Neurath, Cytokines in inflammatory bowel disease, Nat. Rev. Immunol. 14(5) (2014) 329-342.

[36] L. Swanson, G.D. Katkar, J. Tam, R.F. Pranadinata, Y. Chareddy, J. Coates, M.S. Anandachar, V. Castillo, J. Olson, V. Nizet, I. Kufareva, S. Das, P. Ghosh, TLR4 signaling and macrophage inflammatory responses are dampened by GIV/Girdin, Proc. Natl. Acad. Sci. U.S.A. 117(43) (2020) 26895-26906.

[37] D.D. Eichele, K.K. Kharbanda, Dextran sodium sulfate colitis murine model: An indispensable tool for advancing our understanding of inflammatory bowel diseases pathogenesis, World J. Gastroentero. 23(33) (2017) 6016-6029.

[38] P. Arda-Pirincci, G. Aykol-Celik, Galectin-1 reduces the severity of dextran sulfate sodium (DSS)-induced ulcerative colitis by suppressing inflammatory and oxidative stress response, Bosn. J. Basic Med. Sci. 20(3) (2020) 319-328.

[39] Y. Araki, T. Bamba, K.I. Mukaisho, O. Kanauchi, H. Ban, S. Bamba, A. Andoh, Y. Fujiyama, T. Hattori, H. Sugihara, Dextran sulfate sodium administered orally is depolymerized in the stomach and induces cell cycle arrest plus apoptosis in the colon in early mouse colitis, Oncol. Rep. 28(5) (2012) 1597-1605.

[40] R.H. Fang, A.V. Kroll, W. Gao, L. Zhang, Cell membrane coating nanotechnology, Adv. Mater. 30(23) (2018) 1706759.

[41] S.Y. Wang, D. Wang, Y.O. Duan, Z.D. Zhou, W.W. Gao, L.F. Zhang, Cellular Nanosponges for Biological Neutralization, Adv. Mater. 34(13) (2022).

[42] A. Lamprecht, IBD Selective nanoparticle adhesion can enhance colitis therapy, Nat. Rev. Gastro. Hepat. 7(6) (2010) 311-312.

[43] Y.C. Zhang, X.M. Si, L. Yang, H. Wang, Y. Sun, N. Liu, Association between intestinal microbiota and inflammatory bowel disease, Animal Model Exp. Med. 5(4) (2022) 311-322.

[44] J. Ni, G.D. Wu, L. Albenberg, V.T. Tomov, Gut microbiota and IBD: causation or correlation?, Nat. Rev. Gastro. Hepat. 14(10) (2017) 573-584.

[45] Q. Zhang, R. Fang, W. Gao, L. Zhang, A biomimetic nanoparticle to 'lure and kill' phospholipase A2, Angew. Chem. Int. Edit. 59 (2020) 10461-10465.

[46] Y. Chen, Y. Zhang, J. Zhuang, J.H. Lee, L. Wang, R. Fang, W. Gao, L. Zhang, Cell membrane-cloaked oil nanosponges enable dual-modal detoxification, ACS Nano 13 (2019) 7209-7215.

[47] J.J. Kim, M.S. Shajib, M.M. Manocha, W.I. Khan, Investigating Intestinal Inflammation in DSS-induced Model of IBD, J. Vis. Exp. (60) (2012) 1-6.

[48] S. Das, A. Sarkar, S.S. Choudhury, K.A. Owen, V.L. Derr-Castillo, S. Fox, L. Eckmann, M.R. Elliott, J.E. Casanova, P.B. Ernst, Engulfment and cell motility protein 1 (ELMO1) has an essential role in the internalization of Salmonella typhimurium into enteric macrophages that impact disease outcome, Cell Mol. Gastroenter. 1(3) (2015) 311-324.

The first portion of Chapter 3, in full, is a reprint of the material as it appears in *ACS Nano*, 2023 by Yaou Duan, Edward Zhang, Ronnie H. Fang, Weiwei Gao, and Liangfang Zhang. The dissertation author was the primary investigator and author of this paper.

3.2 Gastrointestinal tract drug delivery using algae motors embedded in a degradable capsule

3.2.1 Introduction

Oral delivery to the gastrointestinal (GI) tract has been one of the most widely used approaches for drug administration due to its high patient compliance, non-invasiveness, simplicity, and low cost [1, 2]. Despite their potential advantages, oral drug formulations face several barriers within the GI tract, including poor stability in gastric fluid, limited drug interaction with the intestinal lining, and low solubility [3]. Several engineered systems, based on microinjectors and microneedles, have been described recently for improving the oral delivery of large biological macromolecules via mechanical penetration mechanisms [4, 5]. Other platforms, including bioadhesive patches, responsive hydrogels, mucus-penetrating particles, ionic liquids, and microgrippers, have been reported for enhancing GI delivery via improved tissue adhesion, prolonged retention, and improved drug localization [6-10]. The use of micromotors is another promising and effective approach for the active transport of therapeutic agents to specific sites of interest [1, 11-14]. A variety of synthetic micromotors, capable of propelling to hard-to-reach locations within the body, have been developed for active drug delivery, as well as for other biomedical applications including biosensing or microsurgery [15-19]. Early in vivo studies using micromotors focused primarily on the GI tract, which can provide a favorable environment for movement [19, 20]. Such pioneering studies employed chemically powered micromotors based on magnesium or zinc microengines for the enhanced delivery of antibiotics, vaccines, and micronutrients [19-22]. These self-propelled micromotors hold particular promise for the local delivery of drug payloads towards the treatment of GI diseases and disorders [19]. Although these active platforms substantially enhanced delivery efficacy compared to corresponding static

microcarriers, they suffer from short lifetimes of operation up to approximately 15 minutes once in contact with GI fluid. This decreases the potential of these synthetic micromotors to interact with GI mucosa and limits their overall retention, thus leading to decreased drug bioavailability. To address this limitation, active micromotor-based GI drug delivery systems with improved characteristics need to be developed.

Here, we report an algae motor-loaded capsule system that combines the efficient long-lasting movement of natural algae in the small intestine with the protective capabilities of oral capsules, thus enabling prolonged retention within the intestinal mucosa towards greatly improved GI delivery. Microorganisms, such as bacteria, sperm, and microalgae have evolved over millions of years to develop robust actuation systems that enable autonomous motion [23]. The natural cellular systems have recently emerged as attractive cargo carriers that are capable of transporting therapeutics to hard-to-reach body locations [24, 25]. Combining these motile microorganisms with synthetic materials results in biohybrid systems capable of performing multiple tasks [26-28]. Whereas sperm and bacteria have been used for over a decade in diverse biomedical applications, ranging from cancer therapy to assisted fertilization [29-31], microalgae swimmers have rarely been explored as robotic actuators [32]. Microalgae are eukaryotic swimmers that are facile to culture, and they offer attractive properties for biomedical applications, including efficient propulsion (>100 μm/s), autofluorescence, and phototactic guidance capabilities.

We chose *Chlamydomonas reinhardtii* as a model microalgal swimmer for active payload delivery in the GI tract due to its many attractive properties, including cytocompatibility, cost-effective scalable production, good adaptability and motility in diverse aqueous environments, abundance of reactive surface groups for functionalization, and autofluorescence for ease of tracking in vivo [27, 32-34]. *C. reinhardtii* swims by beating its two flagella synchronously with

a frequency of 50 Hz [35], reaching high speeds up to approximately 200 μm/s [32, 36]. We demonstrate that *C. reinhardtii* display substantially longer propulsion in intestinal fluid compared to synthetic chemically powered magnesium (Mg) micromotors, which are the only type of self-propelled microrobot swimmers that have been reported for in vivo operation in the GI tract [19-22]. To protect the algae motors from the harsh gastric environment, they were embedded inside a protective capsule (**Figure 3.2.1A-C**), which was prepared with an inner hydrophobic coating to entrap aqueous solution for maintaining algae viability along with an outer pH-responsive enteric polymer coating. Upon release from the capsule, the algae display constant motility in intestinal fluid (**Figure 3.2.1D**). Compared to the short lifetime of commonly used Mg micromotors, the algae motors remain motile for more than 12 h at body temperature. In vivo, this prolonged movement leads to notably improved intestinal distribution (**Figure 3.2.1E**), resulting in enhanced retention of a model chemotherapeutic doxorubicin (Dox) conjugated to the algae motors. Overall, our findings indicate that natural algae-based active carriers hold great promise for oral drug delivery to enhance the treatment of GI diseases.

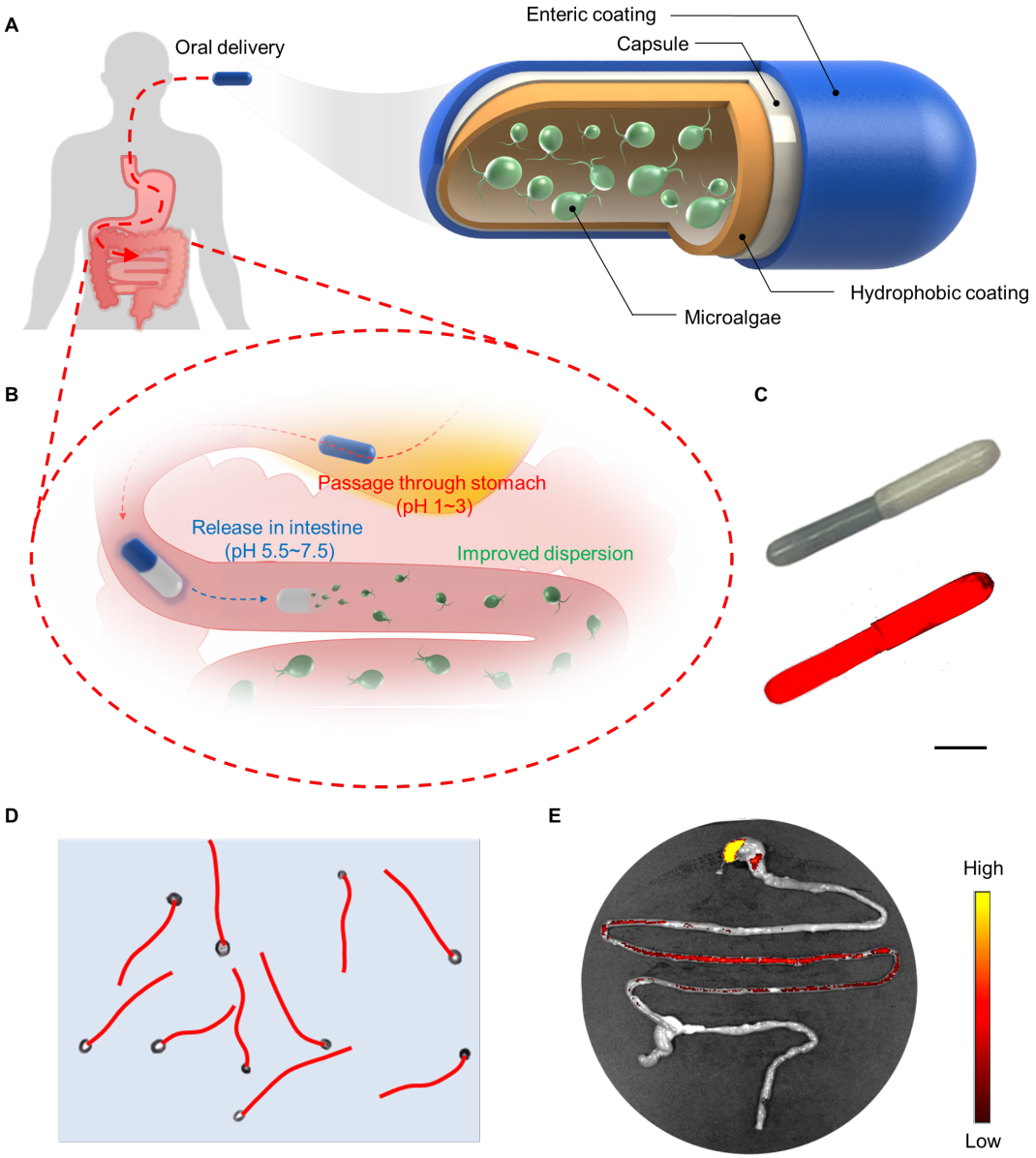

Figure 3.2.1 Schematic of algae motors in a capsule for gastrointestinal tract delivery. (A) Algae motors loaded within protective capsules containing an inner hydrophobic coating layer and an outer enteric coating layer can be used for oral delivery applications. **(B)** The algae motor-loaded capsule first enters the stomach, where the enteric coating protects it from degradation at acidic gastric pH. Upon entering the intestines, the enteric coating is dissolved in the nearly neutral pH and the capsule is degraded, leading to complete release of the algae motors. **(C)** Brightfield (upper) and fluorescent (lower) images of an algae motor-loaded capsule. Scale bar, 2 mm. **(D)** Representative tracking trajectories demonstrating the autonomous movement of algae motors in simulated intestinal fluid. **(E)** Representative biodistribution of fluorescently labeled algae motors in the GI tract 5 h after administration in a capsule by oral gavage.

3.2.2 Results and Discussion

Movement of algae-based micromotors in simulated intestinal fluid

We first studied the motion properties of *C. reinhardtii*, which are commonly utilised as a model algal species [37], and compared them with that of Mg micromotors (**Figure 3.2.2A**). The artificial intestinal fluid (SIF) mainly, composed of potassium dihydrogen phosphate at pH 6.8, was used to test the movement of algae and Mg micromotors. In SIF, the natural algae motors exhibited a stable speed profile of approximately 120 μm/s that lasted for a minimum of 12 h. This consistent motile behavior is ascribed to the coordinated, self-sustained beating of algae flagella [38] even in suboptimal survival conditions such as SIF. In contrast, the speed of Mg micromotors in SIF dramatically decreased from an initial 180 μm/s to 80 μm/s after 15 min before reaching 0 μm/s after another 15 min. This sharp drop in speed reflects the rapid dissolution and depletion of the Mg engine during propulsion. The percentage of motile Mg motors also dropped to 20% after 15 min of propulsion, whereas the 89% of the algae motors remained moving after 12 h (**Figure 3.2.2B**). In tracing their motion, the movement patterns of algae tracked over 2 s intervals appeared consistent over the course of 12 h (**Figure 3.2.2C**), whereas no movement was observed for Mg motors after 30 min (**Figure 3.2.2D**). These data illustrated that the algae motors could self-propel efficiently in SIF and maintain consistently fast motility over long periods of time, thereby supporting potential for active GI delivery applications.

To demonstrate their potential for drug delivery, the algae motors were modified with two different cargos: a fluorescent dye and polymeric nanoparticles. The green dye fluorescein (excitation/emission = 494 nm/518 nm) was first chemically conjugated to the surface of the algae [39]. After dye conjugation, the algae could be fluorescently tracked (**Figure 3.2.2G-H**), and the median speed calculated from 100 individual algae was near identical to that of unmodified algae (**Figure 3.2.2E-F**) and consistent with previously reported values [32, 36]. Similarly, red blood

cell (RBC) membrane-coated poly(lactic-*co*-glycolic acid) (PLGA) nanoparticles [40] (denoted "NP") were linked to the algae via click chemistry. To visualize the NP on the algae, the fluorescent dye 1,1′-dioctadecyl-3,3,3′,3′-tetramethylindocarbocyanine (DiI, excitation/emission = 550 nm/567 nm) was encapsulated inside the PLGA core during the fabrication process. The NP-modified algae motors (denoted "algae-NP motors") exhibited a similar swimming pattern and speed distribution profile in SIF compared to unmodified algae motors (**Figure 3.2.2I-J**). In addition, the intrinsic phototaxis of the algae was not compromised after the NP functionalization. The data here confirmed that different payloads, ranging from molecules to nanoparticles, can be successfully loaded onto algae motors without affecting their propulsion characteristics, further highlighting the active GI delivery potential of algae-based motor systems.

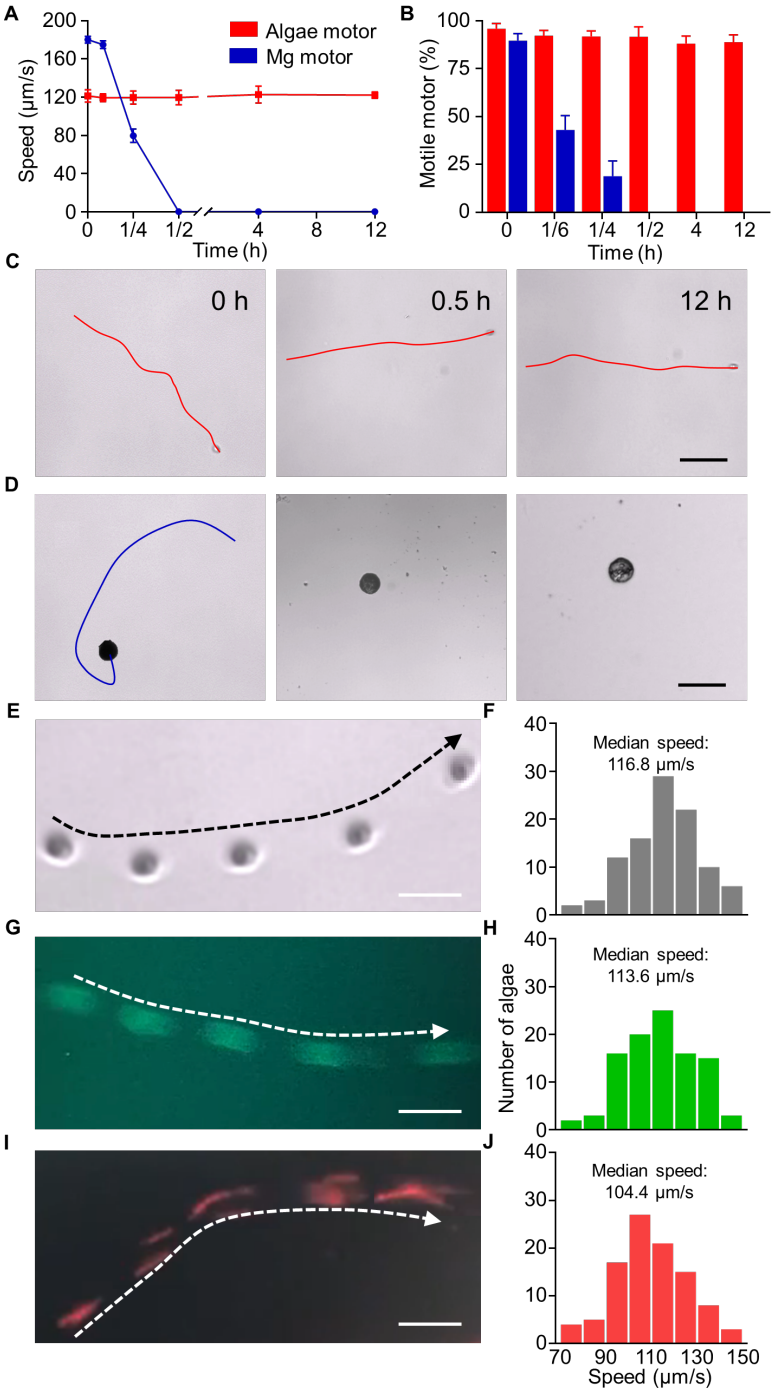

Figure 3.2.2 Motility of algae motors and magnesium motors in simulated intestinal fluid (SIF) at room temperature. **(A)** Speed of algae motors and Mg motors in SIF during 12 h of operation (n = 5, mean ± SD). **(B)** The percentage of motile motors in SIF during 12 h period (n = 5, mean + SD). **(C, D)** Time-lapse snapshots and trajectories of algae motors (C) and Mg motors (D) over a span of 2 s at different timepoints during operation. Scale bars, 50 μm. (**E-J**) Time-lapse images showing trajectories over a span of 1 s and corresponding speed distributions of unmodified algae (E, F), fluorescein-labeled algae motors (G, H), and algae motors carrying DiI-loaded RBC membrane-coated nanoparticles (I, J) (n = 100). Scale bars, 20 μm.

Formulation of algae motors into protective capsules

In order to effectively use algae motors for delivery to the GI tract in vivo, it is necessary to overcome the harsh acidic environment of the stomach, which can degrade the algae prior to reaching the small intestines. To address this, we modified a commercial capsule to encapsulate viable algae in an internal aqueous medium for safe passage through the stomach. First, an organosilicon solution, consisting of 4% octadecyltrimethoxysilane (OTMS) [41], was prepared to create a thin hydrophobic coating on the inside of the capsule via a thermal evaporation technique. To test the stability of a capsule with this internal coating, an aqueous solution containing rhodamine dye was encapsulated. Visually, the capsule remained unchanged, whereas significant deformation was observed for a control uncoated capsule. By changing the number of coating layers, the degradation of the capsules, which is reflected by the release of the dye, could be modulated, with 10 layers of coating offering the longest delay in release in SIF. Secondly, the exterior surface of the capsule was coated with Eudragit L100-55, a pH-responsive polymer commonly used for protecting oral medication from harsh gastric acid conditions; previous studies have demonstrated the utility of Eudragit L100-55 as enteric coating for enhancing the delivery of micromotors to the intestines [42]. To imitate physiological conditions in the stomach, simulated gastric fluid (SGF) at pH 1.5, containing sodium chloride and hydrochloric acid, was utilized. In our case, three layers of coating using a 7% (w/v) polymer solution offered full protection of the encapsulated cargo from SGF. Upon changing from SGF to SIF, burst cargo release was observed within 10 min due to dissolution of the enteric coating at higher pH values. These results confirmed that it was possible to load cargo in aqueous solutions using suitably coated capsules for the GI delivery of algae motors.

Next, we investigated the encapsulation of live algae into the modified capsules and their

release in vitro. Algae were suspended in tris-acetate-phosphate (TAP) medium and loaded into capsules with 10 inner OTMS layers and 3 outer enteric coating layers. For visualization, the OTMS and enteric coating layers were labeled with 3',3'-dioctadecyloxacarbocyanine (DiO, excitation/emission = 484 nm/501 nm) and Pacific Blue (excitation/emission = 410 nm/455 nm), respectively. Under fluorescence microscopy, a strong signal was observed for both coating layers along with the autofluorescence of the algae (excitation/emission = 647 nm/680 nm), confirming successful encapsulation of algae motors into the fabricated capsule platform (**Figure 3.2.3A**). In SGF, it was demonstrated that there was no release of algae from the capsules, whereas the algae motors could be released over time in SIF (**Figure 3.2.3B**). The release in SIF was gradual for approximately 30 minutes, after which the majority of the algae was released by 45 min from the start of the experiment. The total number of released algae reached 9.15×10^5 after 45 min (**Figure 3.2.3C-D**). Motion tracking of algae motors within the capsule and algae motors released from the capsule revealed similar patterns of movement (**Figure 3.2.3E**). The median speed calculated from 100 individual algae also remained unchanged throughout the fabrication process, as well as after release from the capsules (**Figure 3.2.3F-G**). These data indicated that the algae motors could be effectively encapsulated and then released from the modified capsule with negligible effect on their swimming performance.

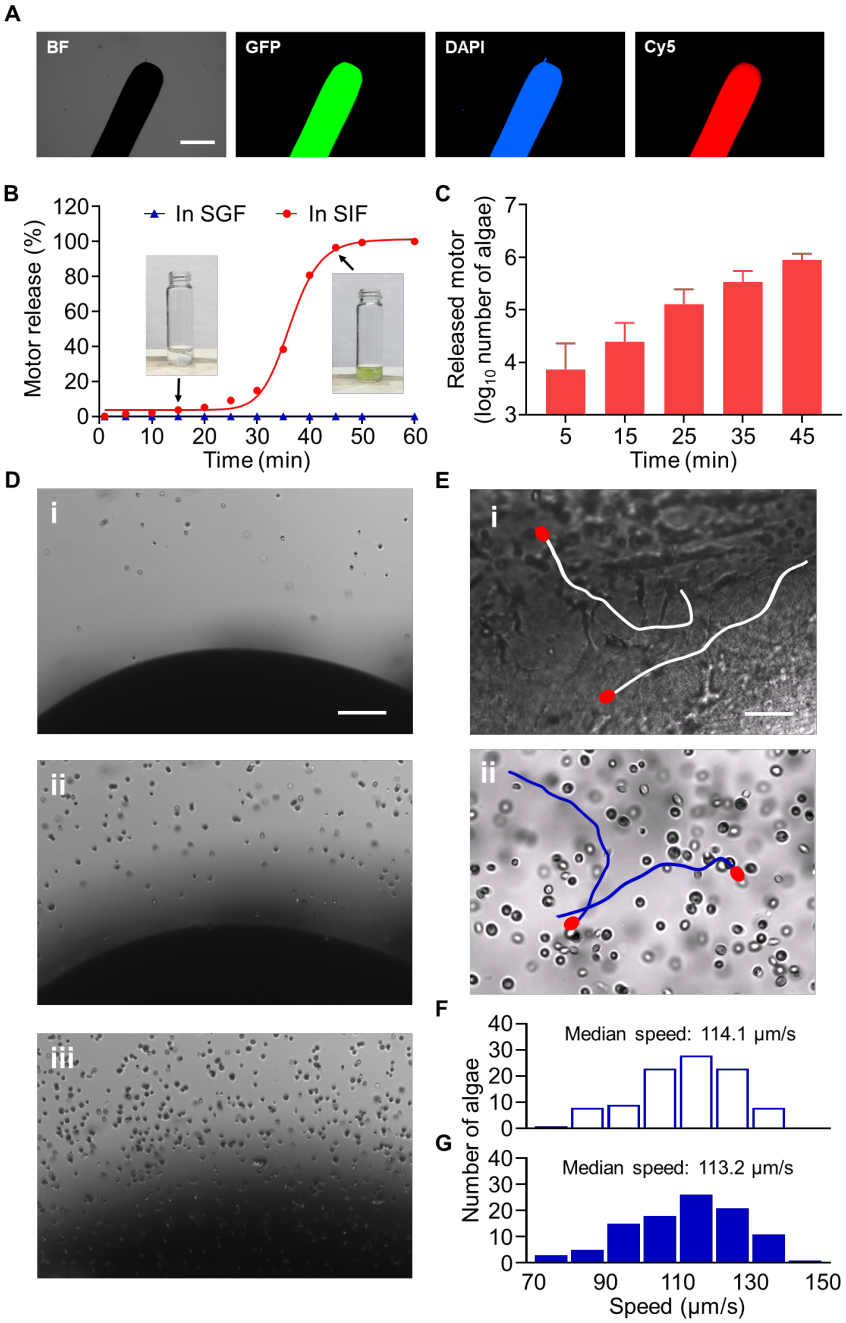

Figure 3.2.3 Loading and release of algae motors in a capsule *in vitro*. (A) Brightfield and fluorescence microscopy images of autofluorescence of algae motors (red) in a capsule formulation fabricated with a DiO-labeled octadecyltrimethoxysilane (OTMS) inner coating (green) and a Pacific Blue-labeled enteric outer coating (blue). Scale bar, 1 mm. **(B)** Release profile of algae motors from a capsule in simulated gastric fluid (SGF) (blue line) and simulated intestinal fluid (SIF) (red line). Inset images correspond to t = 15 min (left) and t = 45 min (right). **(C)** Quantification of algae release from capsules over time in SIF (n = 3, mean + SD). **(D)** Time-lapse images (t = 15 min, 30 min, and 45 min) showing the release of algae motors from a capsule in SIF. Scale bar, 100 μm. **(E)** Representative tracking lines of encapsulated algae motors in TAP medium and released algae motors in SIF. Scale bar, 50 μm. **(F, G)** Speed distribution of the encapsulated algae motors (F) and released algae motors (G) from (E) (n = 100).

After evaluating the release of algae motors from the capsules under in vitro conditions, we investigated the delivery capabilities of the platform within the GI tract. First, mimicking the physiological conditions of the intestines, the motion behavior of algae motors and Mg motors was evaluated in SIF at 37 °C in vitro (**Figure 3.2.4A-B**). The speed of the algae motors was affected by the elevated temperature, decreasing from 113 μm/s to 83 μm/s within 15 min of self-propulsion, and further dropping to 40 μm/s after 12 h. At the experimental endpoint, approximately 70% of the algae remained motile, indicating that they could survive for prolonged periods of time even in unfavorable conditions. In comparison, the conventional Mg motors rapidly lost their movement, with only 33% still propelling at a high speed of 180 μm/s after 5 min. After another 10 min, only 8% remained motile with an average speed of 80 μm/s. This fast drop in speed and the fraction of motors displaying active motion reflected the rapid depletion of the Mg engine. The algae motors also exhibited the ability to swim in viscous simulated mucus [43] over an extended period of time, whereas the Mg motors did not. These findings illustrated the greatly improved behavior of the algae motors compared to their Mg-based counterparts for applications requiring prolonged propulsion.

In vivo biodistribution of algae motors after oral delivery

Following the in vitro tests, a study was carried out to assess the in vivo biodistribution and retention of the algae motors when delivered orally in capsule form. To facilitate imaging and quantification in biological tissue, both the algae motors and Mg motors were labeled with the same fluorescent dye. The algae motors were directly conjugated with fluorescein, whereas the Mg motors were first coated with poly-l-lysine [44] followed by conjugation with fluorescein. As a result, both motors could be easily visualized under fluorescence microscopy and displayed near-

identical signals that did not diminish after 6 h in SIF at 37 °C. Next, the algae motors and Mg motors were embedded in the protective capsules and administered by oral gavage into mice. At 5 h after administration, the mice were euthanized and their GI tracts were imaged ex vivo (**Figure 3.2.4C**). Whereas a narrow distribution was observed from the fluorescent signal of the Mg motors, the signal for the algae motors was more evenly distributed through the intestines. Quantification of the total radiant efficiency within the small intestines corroborated the improved retention of the algae motors compared with the Mg motors (**Figure 3.2.4D**). The observed differences in biodistribution suggested that algae, with their long-lasting movement properties, could be effective at delivering drug payloads locally within the GI tract.

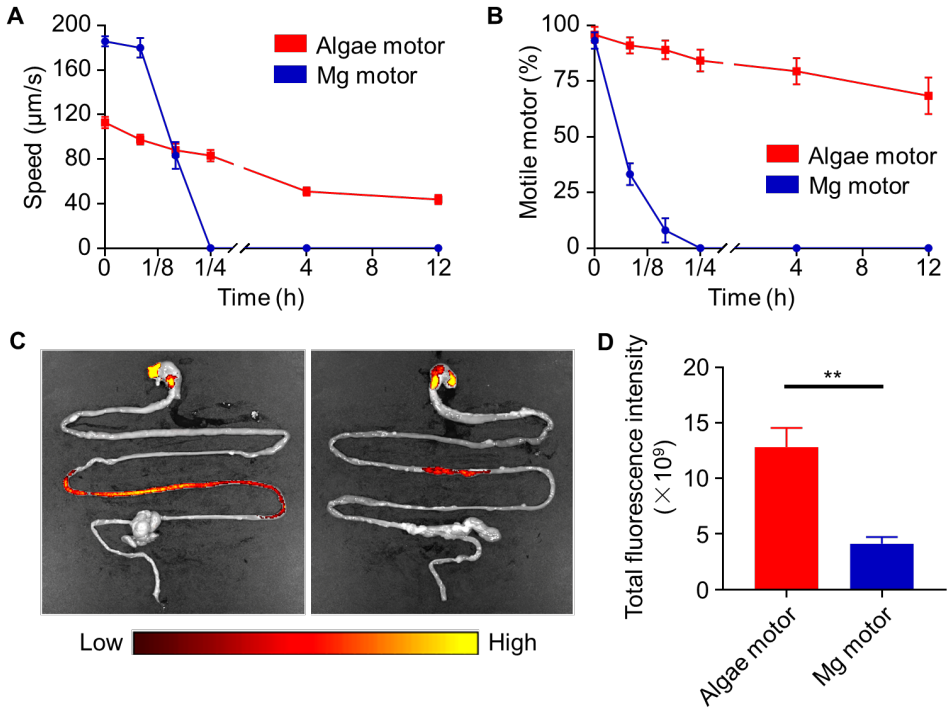

Figure 3.2.4 Comparison of the distribution of algae motors and magnesium motors in the gastrointestinal tract. (A) Speed of algae motors and Mg motors at 37 °C in SIF during 12 h of operation (n = 5, mean ± SD). **(B)** Percentage of motile algae motors (red line) and Mg motors (blue line) at 37 °C in SIF during 12 h of operation (n = 5, mean ± SD). **(C)** Representative images of the GI tract of mice 5 h after oral administration of fluorescein-labeled algae motors in a capsule (left) or Mg motors in a capsule (right). **(D)** Quantitative analysis of total fluorescence intensity within the small intestine from the images in (C) (n = 3, mean + SD). Student's two-tailed *t*-test, $^{**}p < 0.01$.

In vivo delivery of therapeutic drugs using algae motor capsules

To better understand the mechanism behind the improved biodistribution and retention of algae motors within the small intestine, we compared our algae motor capsule formulation with different control groups, including TAP medium only (negative control), free algae without a capsule, and static algae in a capsule. To prepare the static algae control, live algae were deflagellated using acetic acid and resuspended in phosphate buffer saline (PBS) for encapsulation. Optical visualization and scanning electron microscopy (SEM) images confirmed successful deflagellation and that the resulting static algae lost their motion capabilities in SIF at 37 °C. The intrinsic fluorescence of chlorophyll a in algal chloroplasts allows for noninvasive fluorescence imaging of algae without the need for chemical modification [45]. We then proceeded to perform ex vivo fluorescence imaging on the GI tract of mice receiving the various formulations with equivalent fluorescence in order to determine the influence of active movement and capsule protection on biodistribution (**Figure 3.2.5A**). At 5 h after oral administration, algae motors delivered inside capsules were more broadly distributed across the intestines compared with static algae that were also encapsulated. This result highlighted the importance of self-propulsion, which likely helped to increase the interaction of the algae with the intestinal wall, thus leading to enhanced retention. Additionally, there was almost no signal observed in the intestines after administration of free algae, demonstrating the necessity of using the capsules to protect from the harsh stomach acid. Quantification of the fluorescent signal from each sample further supported the imaging results, as the fluorescence from the encapsulated algae motor group was 3.5-fold greater than the encapsulated static algae group (**Figure 3.2.5B**). To control for the background signal from food contaminants within the stomach [42, 46], capsules loaded with dye-labeled algae motors were delivered orally, and it was confirmed that the majority of the algae were distributed

within the intestine.

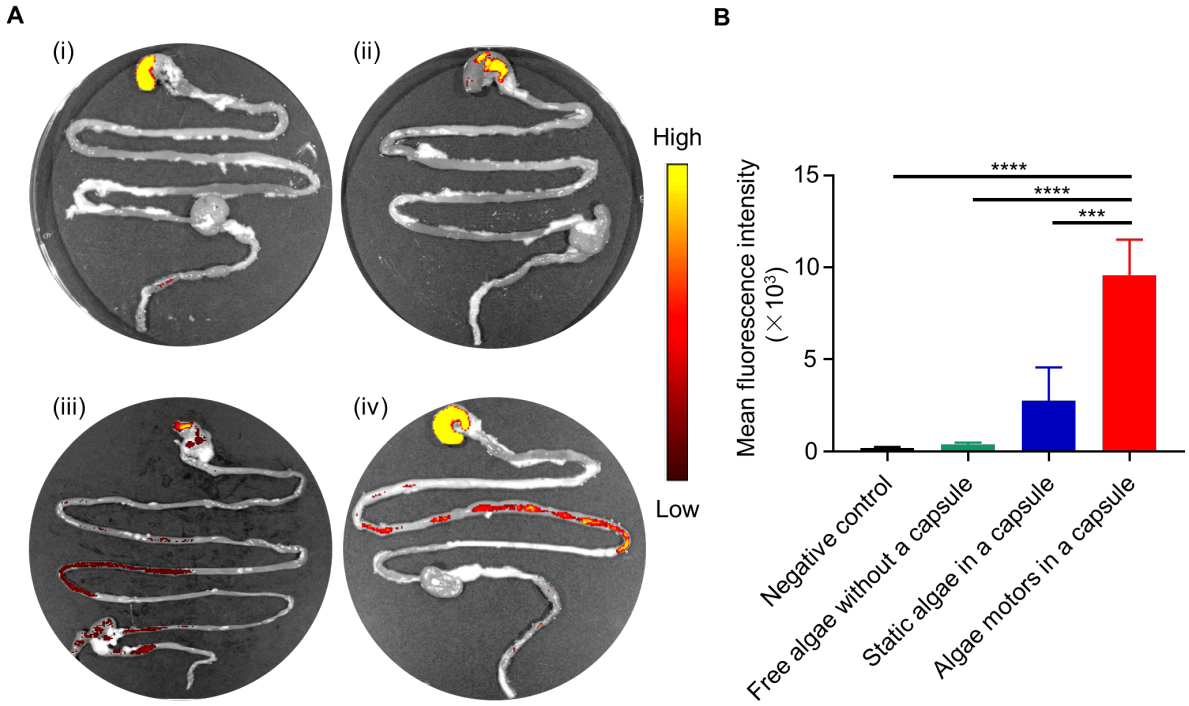

Figure 3.2.5 Gastrointestinal tract delivery of algae motors in comparison with other algae controls. **(A)** Representative ex vivo fluorescence images of GI tissues of mice 5 h after oral administration with TAP medium as negative control, free algae without capsule, static algae in a capsule, and algae motors in a capsule. **(B)** Quantitative analysis of the mean fluorescence from the experiment in (A) (n = 3, mean + SD). One-way ANOVA, ***$p < 0.001$, ****$p < 0.0001$.

We next explored the feasibility of using algae motors for delivering therapeutic drugs to the GI tract. Doxorubicin (Dox), a commonly used frontline chemotherapeutic agent [47], was selected as a model drug payload. First, RBC membrane-coated NP was loaded with Dox (denoted "NP(Dox)") via a double emulsion solvent evaporation technique [48, 49]. Transmission electron microscopy (TEM) imaging confirmed the core–shell structure of the NP. Fluorescence imaging showed colocalization of the Dox-loaded PLGA cores and the DiO-labeled RBC membrane coating, verifying successful drug loading. Next, NP(Dox) was linked to the algae (denoted "algae-NP(Dox)") by click chemistry (**Figure 3.2.6A**). Fluorescence and SEM imaging confirmed the effective binding of NP(Dox) to the algae (**Figure 3.2.6B-C**). To test the Dox loading onto the

algae, we incubated 1×10^6 algae with different concentrations of NP(Dox). The Dox loading yield onto the algae was measured at different NP(Dox) inputs and the maximum loading amount (15 μg) was obtained with 50 μg input of Dox, corresponding to a 30% loading efficiency per 10^6 cells (**Figure 3.2.6D**). It was also confirmed that Dox, either in free form or nanoparticulate form, did not have an influence on the viability of the algae. The mean and median speed of algae-NP(Dox) measured from 100 individual algae motors were 108.69 μm/s and 108.78 μm/s, respectively, and these values were comparable to those of the bare algae (**Figure 3.2.6E-F**). Furthermore, it was demonstrated that the drug release profile of NP(Dox) was not affected by binding to the algae motors (**Figure 3.2.6G**). After loading onto algae motors, the NP(Dox) payload retained its cytotoxic activity, as it was demonstrated that algae-NP(Dox) could inhibit the growth of B16F10 melanoma cell lines in vitro (**Figure 3.2.6H**). Algae-NP(Dox) and NP(Dox), both loaded into protective capsules, were then administered at the same drug dosage, followed by extraction of the intestines to quantify Dox concentration (**Figure 3.2.6I).** Compared with the tissue homogenates of mice administered with NP(Dox), the samples from mice receiving algae-NP(Dox) exhibited significantly higher drug levels at all of the timepoints (3 h, 6 h, and 9 h) that were tested. These data further supported the benefits of using algae motors with prolonged active self-propulsion to enhance the delivery and retention of therapeutic payloads in the small intestinal tissues. Future studies will focus on evaluating the potential of algae motors for drug delivery to treat diseases in suitable animal models, e.g. inflammatory bowel disease (IBD) and bacterial gastroenteritis.

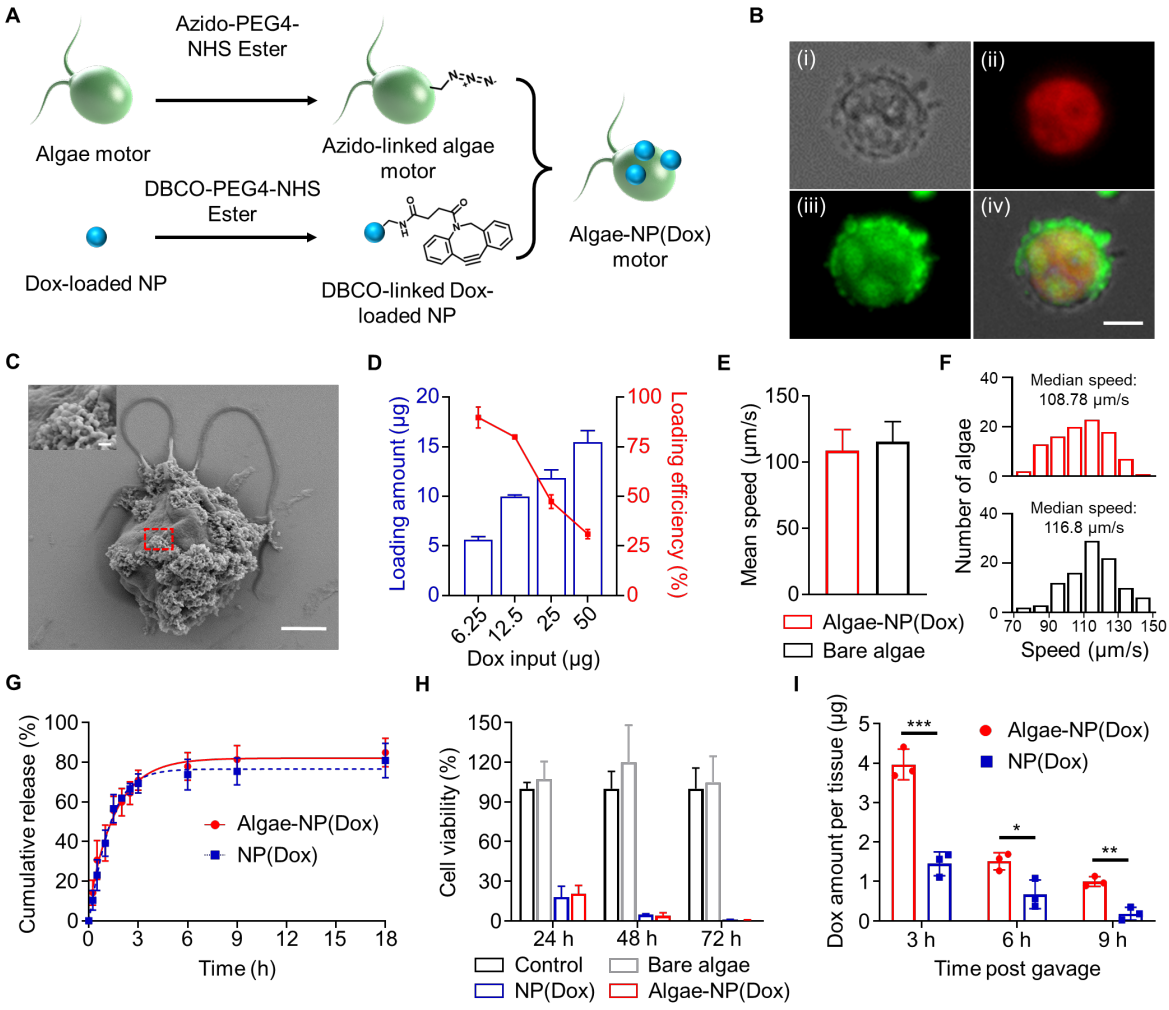

Figure 3.2.6 Characterization of drug-loaded algae motors. (A) Schematic illustration of the fabrication process for algae-NP(Dox) motor. **(B)** Brightfield, autofluorescence of algae chloroplast (red), DiO-labeled RBC membrane (green), and merged microscopy images showing the loading of Dox-loaded NP with dye-labeled RBC membrane onto an algae motor. Scale bar: 5 μm. **(C)** SEM image of an algae motor loaded with NP(Dox). Scale bar, 2.5 μm. Inset shows a zoomed in view corresponding to the dashed red box. Scale bar, 200 nm. **(D)** Quantification of drug loading amount and loading efficiency of 1×10^6 algae-NP(Dox) at different Dox inputs (n = 3, mean ± SD). **(E, F)** Mean (E) and median (F) speed of algae-NP(Dox) motor and bare algae. The speed was measured from 100 individual alga. **(G)** The cumulative drug release profiles from algae-NP(Dox) motor and NP(Dox) (n = 3, mean ± SD). **(H)** Viability of B16-F10 cancer cell lines after 24 h, 48 h and 72 h of incubation with blank solution, bare algae, NP(Dox), and algae-NP(Dox) motor (n = 3, mean ± SD). **(I)** Quantification of the total Dox content per small intestine at different times after administration of algae-NP(Dox) motor and NP(Dox) in a capsule (n = 3, mean ± SD). Student's multiple *t*-test, *$p < 0.05$, **$p < 0.01$, ***$p < 0.001$.

In vivo toxicity evaluation of algae motor capsules

Finally, we evaluated the in vivo safety profile of the algae motor capsule platform

following oral administration. A comprehensive blood chemistry panel and blood cell count were conducted 24 h after administration (**Figure 3.2.7A-B**). Compared to untreated control mice, the level of all serum biochemistry markers and number of blood cells (red blood cells, white blood cells, and platelets) in the mice receiving algae motor capsule treatment remained at normal levels. A longer-term safety study in which mice were administered with one algae motor capsule every other day on days 0, 2, 4, and 6 also yielded the same result, whereby negligible toxicity, indicated by the minor changes of metabolic biomarkers and blood cell counting, to the mice was observed. Histological analysis of GI tract tissue sections from algae motor-treated mice stained with hematoxylin and eosin (H&E) revealed that structural integrity was preserved and that there was no immune cell infiltration into the mucosa or submucosa, indicating the lack of an inflammatory response (**Figure 3.2.7C**). There was also no observable inflammation or pathological changes on H&E-stained sections from other major organs such as the heart, lungs, liver, kidneys, and spleen (**Figure 3.2.7D**). Overall, these results suggested that the algae motor capsule platform is safe to use for oral drug administration.

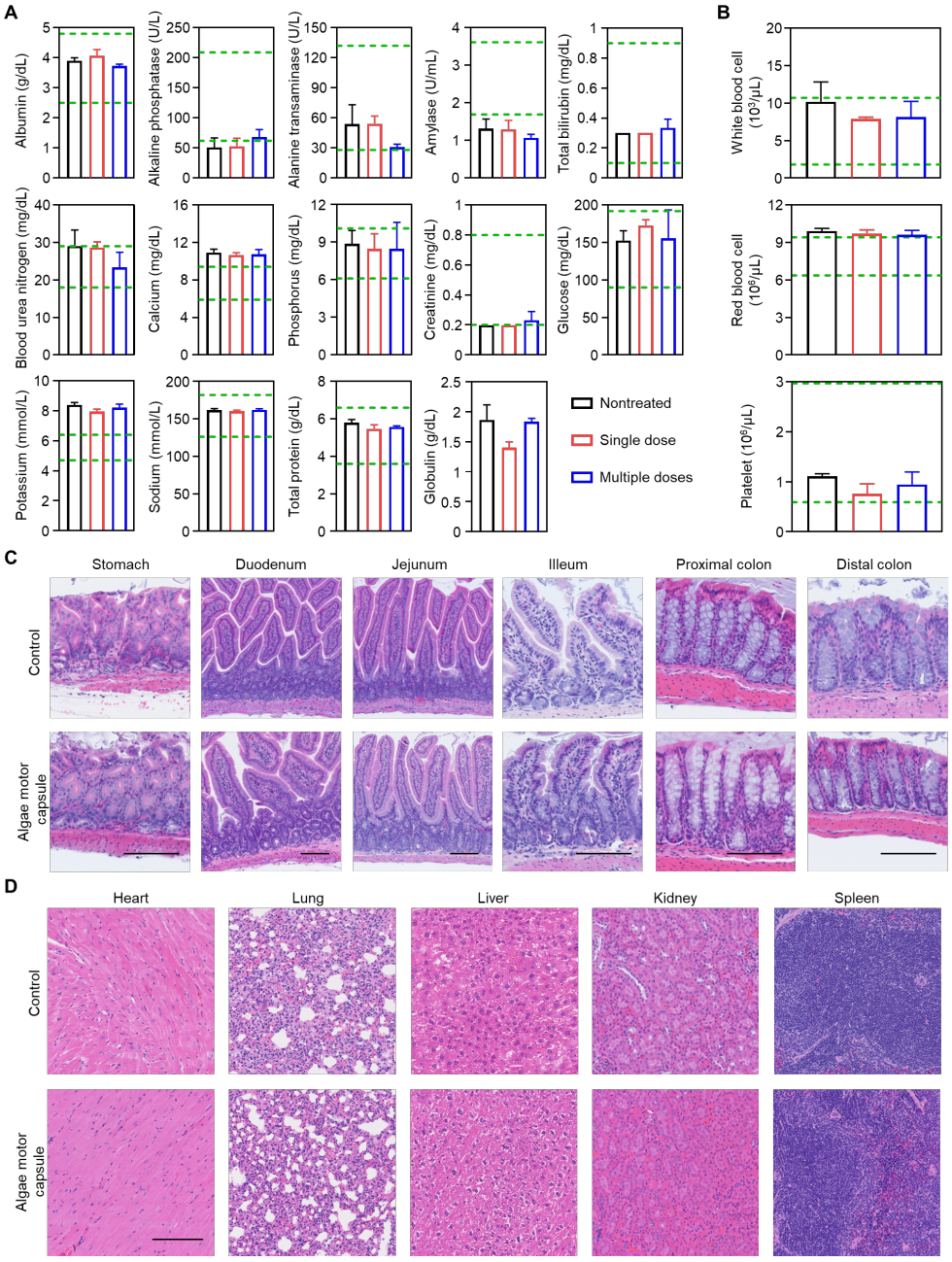

Figure 3.2.7 ***In vivo*** **safety analysis of algae motors following oral administration. (A, B)** Comprehensive blood chemistry panel (A) and blood cell counting (B) taken from nontreated mice, mice with single dose treatment, and mice with multiple dose treatment (n = 3, mean + SD). For single dose evaluation, mice were orally administrated with one algae motor capsule at day 0, and blood samples were collected at day 1. For multiple doses evaluation mice were orally administrated with one algae motor capsule every other day on days 0, 2, 4, and 6. Blood samples were collected at day 7. The green dashed lines indicate mouse reference ranges of each analyte. **(C)** Representative H&E-stained histological sections from different sections of the GI tract from nontreated mice and mice treated with the algae motors in a capsule 24 h after oral administration. Scale bar, 100 μm. **(D)** H&E-stained histological sections of major organs, including the heart, lungs, liver, kidneys, and spleen, from nontreated mice and mice treated with the algae motors in a capsule 24 h after oral administration. Scale bar, 250 μm.

3.2.3 Conclusion

The development of microorganism-based micromotors for addressing key healthcare issues is still in its infancy [25]. Although various in vitro studies have illustrated the use of bacteria-based drug delivery systems, there are major risks associated with their in vivo use when considering factors such as pathogenicity or immunogenicity [24]. As an alternative cell type, microalgae are nonpathogenic and have been explored in the development of biohybrid systems [36, 50]. Microalgal swimmers recently have been employed as biomedical robotic actuators, primarily under in vitro settings [32]. Early in vivo studies have mainly focused on the therapeutic delivery of algae-derived compounds [51]. More recently, a few studies have reported the use of algae as drug carriers for in vivo operation [45, 52]. For example, the spiral structure of *Spirulina platensis* was leveraged to passively prolong retention of curcumin in the intestines for the improved treatment of colon cancer and colitis [45]. Additionally, a magnetic nanoparticle-loaded microalgae biohybrid imaging system was reported recently, and a swarm of these microswimmers could be externally controlled by a magnetic field and tracked using magnetic resonance imaging [50]. Despite these advances, there have been no studies exploiting the intrinsic self-propulsion of algae for enhanced GI delivery.

In the present study, several key points have been considered in order to tackle the challenges facing the algae-based active GI delivery: protection from the harsh acid environment of the stomach enroute to the intestines, selection of suitable algal strain with long-lasting self-propulsion in intestinal fluid, and cargo/drug loading capability. By addressing these issues, we demonstrated here an algae motor capsule system for effective intestinal targeting and prolonged tissue retention. Compared to the short lifetime of current Mg-based micromotors, the algae motors displayed prolonged propulsion in GI fluid towards enhanced local delivery for the treatment of

potential GI diseases and disorders. To achieve intestinal delivery, an enteric-coated capsule modified with an inner hydrophobic organosilicon layer was fabricated to effectively protect encapsulated algae from the harsh gastric fluid while maintaining their viability. The capsule fabrication, encapsulation, and release processes had a negligible effect on the viability of the algae motors. Modifying capsules in the manner described here provides an effective approach for delivering motile living organisms in aqueous media to the GI tract. To demonstrate the distinct advantages of the platform for in vivo intestinal delivery, algae motor capsules were administered orally, and their biodistribution and retention properties were compared to various controls. The algae motors displayed broader distribution and stronger retention in the GI tract compared to synthetic Mg motors. This was likely mediated by the prolonged motion of the live algae, as it was shown that static algae that were incapable of propulsion exhibited considerably less retention in the intestines. Importantly, we also demonstrated that the the ability of the algae motor capsule system could also be utilised for the delivery of a model anticancer drug to the GI tract. Moreover, the platform displayed a favorable biosafety profile following oral administration.

The characteristics of the algae motor in a capsule formulation, particularly its long-lasting self-propulsion, can be leveraged for microrobotic biomedical applications beyond the treatment of GI diseases and disorders, ranging from GI detoxication to imaging and sensing. There are several approaches in which algae motors could be improved in order to enhance their utility for GI delivery applications. For example, the incorporation of imaging agents could enable direct visualization of algae movement as they operate within the intestines. A recent report described a photoacoustic computed tomography-guided microrobotic system for realizing real-time navigation and monitoring of synthetic Mg motors in the intestines in vivo [53]. In another example, positron emission tomography combined with computed tomography was used to evaluate the

swarm behavior of enzyme-powered nanomotors in the bladder [17]. By conjugating magnetic microparticles to the algae surface [32], an external magnetic navigation system could be used to precisely guide and track algae motors to the target sites. Whereas the current work focused on demonstrating the potential of algae motor capsules for enhancing intestinal delivery, future work will be required to confirm the therapeutic advantages of the platform in clinically relevant disease models, such as those for bacterial GI infection, irritable bowel disease, or colon cancer. Microalgae can also be engineered to express biologic payloads that can be produced in situ after oral administration [54, 55]. It should be noted that the properties of the capsules can also be tuned in order to more precisely target specific regions of the GI tract [42]. Overall, functionalized algae motors, loaded within a protective capsule, represent an attractive biohybrid motor system that can be applied across a wide range of biomedical applications.

3.2.4 Experimental methods

3.2.4.1 Algae culture

The green algae *Chlamydomonas reinhardtii* (strain CC-125 wild-type mt+) were obtained from the *Chlamydomonas* Resource Center. The algae were transferred from the agar plate to tris-acetate-phosphate (TAP) medium (Thermo Fisher Scientific) and cultured at room temperature, under cycles of 12 h sunlight and 12 h dark.

3.2.4.2 Preparation of Mg micromotors

Mg micromotors were fabricated using 20 ± 5 μm commercial Mg microparticles (FMW20, TangShan Weihao Magnesium Powder Co.) as the core. The Mg microparticles were washed 2 times with acetone and dried under N_2 current to remove impurities. Then, ~10 mg of Mg

microparticles were dispersed onto glass slides, which were previously coated with 100 µl of 0.5% polyvinylpyrrolidone ethanolic solution (Spectrum Chemical). A coating of TiO_2 was deposited onto the Mg microparticles by atomic layer deposition at 100 °C for 3000 cycles utilizing a Beneq TFS 200 System, leaving a small opening at the contact point between the Mg particles and the glass slide. Finally, the Mg micromotors were released by gentle scratching from the glass slide. For surface modification with a fluorescent dye, 0.5 mg of Mg micromotors were first mixed with 0.1% poly-l-lysine (Sigma Aldrich) aqueous solution for 30 min. Then, 2 µg of 5/6-carboxyfluorescein succinimidyl ester (NHS-fluorescein; Thermo Fisher Scientific) was mixed with the motors in PBS buffer for 1 h. The resulting fluorescein-labeled Mg micromotors were centrifuged at 3000*g* for 3 min, washed with ultrapure water, and dried for further use.

3.2.4.3 Preparation of fluorescent dye-labeled algae

Green algae were washed 3 times with ultrapure water to remove TAP medium and suspended in 4-(2-hydroxyethyl)-1-piperazineethanesulfonic acid buffer (HEPES, Thermo Fisher Scientific). Then, a 2 µg of NHS-fluorescein was added to 1 ml of algae at 2×10^6 per ml, followed by incubation for 1 h at room temperature. After dye conjugation, the modified algae were washed 3 times with TAP medium to remove free dye, and then they were suspended in TAP medium for further use. Near infrared dye-labeled algae was prepared with a similar method by replacing NHS-fluorescein with NHS-Cyanine7 (NHS-Cy7, λex/λem = 750 nm/773 nm; Lumiprobe).

3.2.4.4 Synthesis of Doxorubicin-loaded polymeric nanoparticles

Dox-loaded polymeric nanoparticles were synthesized following a published method with slight modification [49]. First, 50 µl of 25 mg/ml doxorubicin-HCl (Sigma Aldrich) solution was

emulsified in a 500 μl of chloroform solution containing 50 mg/ml PLGA (50:50, 0.66 dl/g, Lactel Absorbable Polymers) using a Fisher Scientific FS30D ultrasonic probe sonicator operating at a power of 10 W. The process lasted for 2 min with alternating cycles of 2 s power on and 2 s power off in an ice bath. Then, the emulsion was transferred to 5 ml of Tris-HCl (Teknova) aqueous solution and sonicated for another 2 min. The emulsion was stirred for 3 h to completely remove the chloroform. The nanoparticles were centrifuged at 16,100*g* for 5 min, washed 3 times with ultrapure water, and lyophilized for future use. Nanoparticles loaded with DiI (Thermo Fisher Scientific) were prepared using a similar procedure by replacing Dox with the dye.

3.2.4.5 Synthesis of cell membrane-coated nanoparticles

RBC membrane-coated nanoparticles (NP) were synthesized by a membrane cloaking technique [40]. RBC membrane was mixed with PLGA cores at a 1:1 membrane protein to polymer weight ratio. The mixture was sonicated in a Fisher Scientific FS30D ultrasonic bath sonicator for 3 min. The NP were isolated by centrifugation for 5 min at 16,100*g* and washed 3 times with ultrapure water. To characterize NP morphology, samples were deposited onto a carbon-coated 400-mesh copper grid and stained with 1 wt% uranyl acetate (Electron Microscopy Sciences), followed by imaging on a JEOL 1200 EX II transmission electron microscope.

3.2.4.6 Preparation of algae-NP motors

To attach NP onto algae, 1×10^7 green algae were washed 3 times with ultrapure water and treated with 20 μM of dibenzocyclooctyne-(polyethylene glycol)$_4$-*N*-hydroxysuccinimidyl ester (DBCO-PEG$_4$-NHS; Click Chemistry Tools) for 1 h at room temperature. The NP were incubated with 20 μM of azide-PEG$_4$-NHS for 1 h at room temperature. Both the algae and NP were washed

5 times with ultrapure water to remove the unreacted NHS ester. Then, the modified algae and NP were mixed together and vortexed for 3 h to complete the click chemistry reaction. After conjugation, the resulting algae-NP were separated by centrifugation for 3 min at 500*g*, washed 3 times with TAP medium, and resuspended in TAP medium for further use. NP(Dox) conjugation onto the algae followed a similar method by replacing NP with NP(Dox). To evaluate the NP(Dox) loading efficiency, algae motors at 1×10^6/ml were conjugated to NP(Dox) with Dox content at different concentrations (6.25, 12.5, 25, and 50 μg/ml). After fabrication of algae-NP(Dox) motor, Dox content in unbound NP(Dox) was measured for the absorbance at 480 nm by the UV-Vis spectrometer. The Dox loading amount to algae motor was calculated by subtracting the unbound Dox from Dox input.

3.2.4.7 Phototaxis of algae-NP motors

Phototaxis studies were conducted in 3D-printed microfluidic channels with a 5 mm × 4 mm × 2 mm chamber. Before testing, the channel was prefilled with 50 μl TAP medium. Then, the algae-NP motors were added to one side of the channel, while the other side was illuminated using an LED white light for 500 s. As a control, algae motors were added to one side without a light source on the other side. Timelapse videos were recorded at 10 s per frame using an Invitrogen EVOS FL fluorescence microscope with a 2× objective.

3.2.4.8 Influence of Doxorubicin on algae viability

To evaluate the influence of free drug, algae motors at 1×10^6/ml were suspended into solutions containing different concentrations (0, 5, 10, and 25 μg/ml) of free Dox. After 24 h of incubation, each sample was collected, washed 3 times with ultrapure water to remove free drug,

and resuspended into ultrapure water. Next, the samples were stained in 5 μM SYTOX fluorescent probe (Thermo Fisher) to measure algae viability. A similar method was used to test the viability of algae after conjugation of NP(Dox).

3.2.4.9 In vitro anticancer activity of algae-NP(Dox) motors

B16-F10 mouse melanoma cell lines (CRL-6475, American Type Culture Collection) were seeded into a 96-well plate at 5×10^4 per well and further incubated with free Dulbecco's Modified Eagle's Medium (DMEM), free Dox, free algae, and algae-NP(Dox) motors for 24 h, 48 h, and 72 h. All drug-containing wells used the same Dox concentration of 50 μg/ml. An MTS assay (Promega) was used to evaluate the cell viability per the manufacturer's protocol.

3.2.4.10 Algae motility analysis

To evaluate their motion, unmodified algae motors, fluorescein-conjugated algae motors, and algae-NP motors were suspended in SIF (RICCA Chemical). Then, the algae were observed at 0 min, 5 min, 15 min, 30 min, 4 h, and 12 h at room temperature (22 °C). In a separate experiment, algae were observed at 0 min, 5 min, 10 min, 15 min, 4 h, and 12 h at body temperature (37 °C). For Mg micromotor motion analysis, the motors were uniformly dispersed on a glass slide, followed by addition of SIF solution. Motion was evaluated at the same timepoints as above, and SIF was continuously supplemented to prevent the motors from drying. To test the influence of NP(Dox) on motility, the motion of algae-NP(Dox) motors was measured in SIF. To evaluate the operation of algae motors in a mucus-rich environment, their motion behavior was analyzed in a simulated porcine small intestinal mucus containing 20 mg/ml of mucin (Alfa Aesar) [43]. Brightfield movies were captured by a Nikon Eclipse Ti-S/L100 inverted optical microscope

coupled with different objectives (10×, and 20×) and a Hamamatsu digital camera C11440. Meanwhile, fluorescent movies were captured using a Sony RX100 V camera on an Invitrogen EVOS FL fluorescence microscope with different objectives (20× and 40×) in two fluorescence channels, GFP and RFP, corresponding to fluorescein and DiI. An NIS Element tracking module was used to measure the speed of the motors in SIF.

3.2.4.11 Characterization of algae-NP motors

To confirm NP binding on the surface of the algae motors, the RBC membrane on NP was labeled beforehand with DiO (Thermo Fisher Scientific). Fluorescence microscopy images were captured by using an Invitrogen EVOS FL microscope in two fluorescence channels, Cy5 and GFP, corresponding to the autofluorescence of algae and DiO. To further confirm the structure of algae-NP motors, SEM was performed to visualize their morphology. The algae-NP motors were first fixed with a 2.5% glutaraldehyde solution (Sigma Aldrich) overnight at 4 °C and then washed 3 times with ultrapure water. The samples were sputtered with palladium for imaging on a Zeiss Sigma 500 SEM instrument using an acceleration voltage of 3 kV.

3.2.4.12 Fabrication of algae motor capsules

Mouse-specific size M gel capsules were supplied by Torpac. To perform the hydrophobic inner coating, 4% (w/w) of OTMS (Tokyo Chemical Industry) solution was prepared in pure ethanol and stirred at room temperature for 2 h. An insulin syringe was used to fill the capsule with ~4 μl of the OTMS solution, following a curing process at 120 °C for 1 h to completely evaporate the solvent. This process was repeated for up to 10 times to add more coating layers, and the capsules were stored at room temperature. For algae motor encapsulation, 4 μl of algae at a

concentration of 2.5×10^5 per µl in TAP medium was slowly injected into the capsule using a primed syringe pump. After algae encapsulation, the commercial enteric coating polymer Eudragit L100-55 (Evonik Industries) was selected to coat the capsule for protection from gastric acid. First, the enteric coating polymer was dissolved at 7% (w/v) in ethanol solution by stirring at room temperature overnight. The capsules were then immersed into the enteric coating solution with a dip-coating approach followed by solvent evaporation for a total of 3 times. After enteric coating, the capsules were stored at room temperature. To evaluate the release of algae motors from the capsule formulation, the loaded capsules were immersed into either SGF at pH 1.5 comprising 0.2% (w/w) sodium chloride and 0.31% (w/w) hydrochloric acid or SIF at pH 6.8 containing 0.68% (w/w) potassium dihydrogen phosphate and 0.15% (w/w) sodium hydroxide under stirring at 700 rpm. For biodistribution studies, the static algae control (1×10^6), fluorescein-conjugated algae (2×10^6), fluorescein-labeled Mg motors (0.5 mg), and algae-NP(Dox) motors (5 µg of Dox) were encapsulated following a similar process. To generate the static algae control, live algae were rapidly treated with 0.5 M of acetic acid to remove their flagella. To quantify the autofluorescence ($\lambda ex/\lambda em$ = 647 nm/680 nm) of algae motor and static algae samples, a Tecan Infinite M200 plate reader was used.

3.2.4.13 Animal care.

Mice were housed in an animal facility at the University of California San Diego (UCSD) under federal, state, local, and National Institutes of Health (NIH) guidelines. Six-week-old CD-1 male mice were purchased from Charles River Labs. Mice were maintained in standard housing with cycles of 12 h light and 12 h dark, ambient temperature, and normal humidity. All animal experiments were performed in accordance with NIH guidelines and approved by the Institutional

Animal Care and Use Committee (IACUC) of UCSD.

3.2.4.14 Pharmacokinetics and biodistribution studies

To characterize the biodistribution of algae motors, male CD-1 mice were fed an alfalfa-free diet (Labdiet, St. Louis, MO, USA) starting 1 week prior to the experiments. To compare the biodistribution between fluorescein-labeled algae motors (2×10^6) and Mg-based motors (0.5 mg), mice were administered the corresponding capsules containing the motors labeled with equal amounts of dye. To evaluate the influence of active propulsion and capsule protection, mice were administered with encapsulated active algae (1×10^6), encapsulated static algae (1×10^6), unencapsulated active algae (1×10^6), or PBS by oral gavage. The mice were euthanized at 5 h after administration. The entire GI tracts were then collected, rinsed with PBS, and imaged using a Xenogen IVIS 200 system. For quantitative fluorescent measurements, the collected tissues were weighed and then homogenized in PBS. The fluorescent signals were quantified using a Tecan Infinite M200 plate reader. To evaluate drug retention, male CD-1 mice were administered with algae-NP(Dox) motor capsules (5 μg of Dox), NP(Dox) capsules (5 μg of Dox), and PBS via oral gavage. At 3, 6, and 9 h after oral administration, the GI tracts were then collected, weighed, and then homogenized in PBS. The amount of Dox was quantified using a Tecan Infinite M200 plate reader based on absorbance readings at 480 nm.

3.2.4.15 In vivo safety studies

Mice were euthanized at 24 h after oral administration of TAP medium or encapsulated algae motors (1×10^6). For the comprehensive metabolic panel, aliquots of blood were allowed to coagulate, and the serum was collected by centrifugation. To obtain blood cell counts, whole blood

was collected into potassium EDTA collection tubes (Sarstedt). For long-term safety, mice were administered algae motors in a capsule on days 0, 2, 4, and 6, and they were euthanized for analysis on day 7. Lab tests were performed by the UCSD Animal Care Program Diagnostic Services Laboratory. To perform the histological analysis, different sections of GI tract and major organs were sectioned and stained with H&E (Leica Biosystems), followed by imaging using a Hamamatsu Nanozoomer 2.0-HT slide scanning system.

3.2.4.16 Statistical analysis

All experiments were repeated as independent experiments several times as shown by the figure captions. The results are reported as mean ± s.d. A two-tailed, Student's t-test was used for testing the significance between two groups. A one-way analysis of variance (ANOVA) with Dunnett's test was performed to test the significance for multiple comparison. Statistical significance is indicated as $*p < 0.05$, $**p < 0.01$, $***p < 0.001$ and $****p < 0.0001$. No data were excluded from analysis. Samples were randomly allocated to different experimental groups. Organisms were cultured and maintained in the same environment and randomly allocated to each group. Investigators were not blinded to groups allocation during data collection and analysis.

3.2.5 References

[1] J.X. Li, B.E.F. de Avila, W. Gao, L.F. Zhang, J. Wang, Micro/nanorobots for biomedicine: Delivery, surgery, sensing, and detoxification, Sci Robot 2(4) (2017).

[2] S.S. Hua, Advances in Oral Drug Delivery for Regional Targeting in the Gastrointestinal Tract-Influence of Physiological, Pathophysiological and Pharmaceutical Factors, Front Pharmacol 11 (2020).

[3] L.M. Ensign, R. Cone, J. Hanes, Oral drug delivery with polymeric nanoparticles: The gastrointestinal mucus barriers, Adv Drug Deliver Rev 64(6) (2012) 557-570.

[4] A. Abramson, M.R. Frederiksen, A. Vegge, B. Jensen, M. Poulsen, B. Mouridsen, M.O.

Jespersen, R.K. Kirk, J. Windum, F. Hubalek, J.J. Water, J. Fels, S.B. Gunnarsson, A. Bohr, E.M. Straarup, M.W.H. Ley, X.Y. Lu, J. Wainer, J. Collins, S. Tamang, K. Ishida, A. Hayward, P. Herskind, S.T. Buckley, N. Roxhed, R. Langer, U. Rahbek, G. Traverso, Oral delivery of systemic monoclonal antibodies, peptides and small molecules using gastric auto-injectors, Nat Biotechnol 40(1) (2022) 103-+.

[5] A. Abramson, E. Caffarel-Salvador, V. Soares, D. Minahan, R.Y. Tian, X.Y. Lu, D. Dellal, Y. Gao, S. Kim, J. Wainer, J. Collins, S. Tamang, A. Hayward, T. Yoshitake, H.C. Lee, J. Fujimoto, J. Fels, M.R. Frederiksen, U. Rahbek, N. Roxhed, R. Langer, G. Traverso, A luminal unfolding microneedle injector for oral delivery of macromolecules, Nat Med 25(10) (2019) 1512-+.

[6] J.J. Wu, H. Yuk, T.L. Sarrafian, C.F. Guo, L.G. Griffiths, C.S. Nabzdyk, X.H. Zhao, An off-the-shelf bioadhesive patch for sutureless repair of gastrointestinal defects, Sci Transl Med 14(630) (2022).

[7] X.Y. Liu, C. Steiger, S.T. Lin, G.A. Parada, J. Liu, H.F. Chan, H. Yuk, N.V. Phan, J. Collins, S. Tamang, G. Traverso, X.H. Zhao, Ingestible hydrogel device, Nat Commun 10 (2019).

[8] N.G. Lamson, A. Berger, K.C. Fein, K.A. Whitehead, Anionic nanoparticles enable the oral delivery of proteins by enhancing intestinal permeability, Nat Biomed Eng 4(1) (2020) 84-96.

[9] P. Angsantikul, K.V. Peng, A.M. Curreri, Y. Chua, K.V.Z. Chen, J. Ehondor, S. Mitragotri, Ionic Liquids and Deep Eutectic Solvents for Enhanced Delivery of Antibodies in the Gastrointestinal Tract, Adv Funct Mater 31(44) (2021).

[10] A. Ghosh, L. Li, L.Y. Xu, R.P. Dash, N. Gupta, J. Lam, Q.R. Jin, V. Akshintala, G. Pahapale, W.Q. Liu, A. Sarkar, R. Rais, D.H. Gracias, F.M. Selaru, Gastrointestinal-resident, shape-changing microdevices extend drug release in vivo, Sci Adv 6(44) (2020).

[11] C.Y. Gao, Y. Wang, Z.H. Ye, Z.H. Lin, X. Ma, Q. He, Biomedical Micro-/Nanomotors: From Overcoming Biological Barriers to In Vivo Imaging, Adv Mater 33(6) (2021).

[12] C.K. Schmidt, M. Medina-Sanchez, R.J. Edmondson, O.G. Schmidt, Engineering microrobots for targeted cancer therapies from a medical perspective, Nat Commun 11(1) (2020).

[13] Z.G. Wu, Y. Chen, D. Mukasa, O.S. Pak, W. Gao, Medical micro/nanorobots in complex media, Chem Soc Rev 49(22) (2020) 8088-8112.

[14] B. Wang, K. Kostarelos, B.J. Nelson, L. Zhang, Trends in Micro-/Nanorobotics: Materials Development, Actuation, Localization, and System Integration for Biomedical Applications, Adv Mater 33(4) (2021).

[15] B. Wang, K.F. Chan, K. Yuan, Q.Q. Wang, X.F. Xia, L.D. Yang, H. Ko, Y.X.J. Wang, J.J.Y. Sung, P.W.Y. Chiu, L. Zhang, Endoscopy-assisted magnetic navigation of biohybrid soft microrobots with rapid endoluminal delivery and imaging, Sci Robot 6(52) (2021).

[16] H.Y. Zhang, Z.S. Li, C.Y. Gao, X.J. Fan, Y.X. Pang, T.L. Li, Z.G. Wu, H. Xie, Q. He, Dual-responsive biohybrid neutrobots for active target delivery, Sci Robot 6(52) (2021).

[17] A.C. Hortelao, C. Simo, M. Guix, S. Guallar-Garrido, E. Julian, D. Vilela, L. Rejc, P. Ramos-Cabrer, U. Cossio, V. Gomez-Vallejo, T. Patino, J. Llop, S. Sanchez, Swarming behavior and in vivo monitoring of enzymatic nanomotors within the bladder, Sci Robot 6(52) (2021).

[18] Z.G. Wu, J. Troll, H.H. Jeong, Q. Wei, M. Stang, F. Ziemssen, Z.G. Wang, M.D. Dong, S. Schnichels, T. Qiu, P. Fischer, A swarm of slippery micropropellers penetrates the vitreous body of the eye, Sci Adv 4(11) (2018).

[19] B.E.F. de Avila, P. Angsantikul, J.X. Li, M.A. Lopez-Ramirez, D.E. Ramirez-Herrera, S. Thamphiwatana, C.R. Chen, J. Delezuk, R. Samakapiruk, V. Ramez, M. Obonyo, L.F. Zhang, J. Wang, Micromotor-enabled active drug delivery for in vivo treatment of stomach infection (vol 8, 272, 2017), Nat Commun 8 (2017).

[20] X.L. Wei, M. Beltran-Gastelum, E. Karshalev, B.E.F. de Avila, J.R. Zhou, D.N. Ran, P. Angsantikul, R.H. Fang, J. Wang, L.F. Zhang, Biomimetic Micromotor Enables Active Delivery of Antigens for Oral Vaccination, Nano Lett 19(3) (2019) 1914-1921.

[21] L.J. Cai, C. Zhao, H.X. Chen, L. Fan, Y.J. Zhao, X.Y. Qian, R.J. Chai, Suction-Cup-Inspired Adhesive Micromotors for Drug Delivery, Adv Sci 9(1) (2022).

[22] E. Karshalev, Y. Zhang, B.E.F. de Avila, M. Beltran-Gastelum, Y.J. Chen, R. Mundaca-Uribe, F.Y. Zhang, B. Nguyen, Y. Tong, R.H. Fang, L.F. Zhang, J. Wang, Micromotors for Active Delivery of Minerals toward the Treatment of Iron Deficiency Anemia, Nano Lett 19(11) (2019) 7816-7826.

[23] J. Wang, Nanomachines: Fundamentals and applications (John Wiley & Sons, 2013).

[24] Z. Hosseinidoust, B. Mostaghaci, O. Yasa, B.W. Park, A.V. Singh, M. Sitti, Bioengineered and biohybrid bacteria-based systems for drug delivery, Adv Drug Deliver Rev 106 (2016) 27-44.

[25] L. Ricotti, B. Trimmer, A.W. Feinberg, R. Raman, K.K. Parker, R. Bashir, M. Sitti, S. Martel, P. Dario, A. Menciassi, Biohybrid actuators for robotics: A review of devices actuated by living cells, Sci Robot 2(12) (2017).

[26] V. Magdanz, S. Sanchez, O.G. Schmidt, Development of a Sperm-Flagella Driven Micro-Bio-Robot, Adv Mater 25(45) (2013) 6581-6588.

[27] F.Y. Zhang, Z.X. Li, L. Yin, Q.Z. Zhang, N. Askarinam, R. Mundaca-Uribe, F. Tehrani, E. Karshalev, W.W. Gao, L.F. Zhang, J. Wang, ACE2 Receptor-Modified Algae-Based Microrobot for Removal of SARS-CoV-2 in Wastewater, J Am Chem Soc 143(31) (2021) 12194-12201.

[28] O. Felfoul, M. Mohammadi, S. Taherkhani, D. de Lanauze, Y.Z. Xu, D. Loghin, S. Essa, S. Jancik, D. Houle, M. Lafleur, L. Gaboury, M. Tabrizian, N. Kaou, M. Atkin, T. Vuong, G. Batist, N. Beauchemin, D. Radzioch, S. Martel, Magneto-aerotactic bacteria deliver drug-containing

nanoliposomes to tumour hypoxic regions, Nat Nanotechnol 11(11) (2016) 941-947.

[29] H.F. Xu, M. Medina-Sanchez, V. Magdanz, L. Schwarz, F. Hebenstreit, O.G. Schmidt, Sperm-Hybrid Micromotor for Targeted Drug Delivery, Acs Nano 12(1) (2018) 327-337.

[30] M. Medina-Sanchez, L. Schwarz, A.K. Meyer, F. Hebenstreit, O.G. Schmidt, Cellular Cargo Delivery: Toward Assisted Fertilization by Sperm-Carrying Micromotors, Nano Lett 16(1) (2016) 555-561.

[31] S.Z. Xie, L. Zhao, X.J. Song, M.S. Tang, C.F. Mo, X.H. Li, Doxorubicin-conjugated Escherichia coli Nissle 1917 swimmers to achieve tumor targeting and responsive drug release, J Control Release 268 (2017) 390-399.

[32] O. Yasa, P. Erkoc, Y. Alapan, M. Sitti, Microalga-Powered Microswimmers toward Active Cargo Delivery, Adv Mater 30(45) (2018).

[33] M.B. Akolpoglu, N.O. Dogan, U. Bozuyuk, H. Ceylan, S. Kizilel, M. Sitti, High-Yield Production of Biohybrid Microalgae for On-Demand Cargo Delivery, Adv Sci 7(16) (2020).

[34] I.P. Kerschgens, K. Gademann, Antibiotic Algae by Chemical Surface Engineering, Chembiochem 19(5) (2018) 439-443.

[35] T.J. Boddeker, S. Karpitschka, C.T. Kreis, Q. Magdelaine, O. Baumchen, Dynamic force measurements on swimming Chlamydomonas cells using micropipette force sensors, J R Soc Interface 17(162) (2020).

[36] D.B. Weibel, P. Garstecki, D. Ryan, W.R. Diluzio, M. Mayer, J.E. Seto, G.M. Whitesides, Microoxen: Microorganisms to move microscale loads, P Natl Acad Sci USA 102(34) (2005) 11963-11967.

[37] B.P.H. Huang, Chlamydomonas-Reinhardtii - a Model System for the Genetic-Analysis of Flagellar Structure and Motility, Int Rev Cytol 99 (1986) 181-215.

[38] K.Y. Wan, R.E. Goldstein, Coordinated beating of algal flagella is mediated by basal coupling, P Natl Acad Sci USA 113(20) (2016) E2784-E2793.

[39] S. Kalkhof, A. Sinz, Chances and pitfalls of chemical cross-linking with amine-reactive N-hydroxysuccinimide esters, Anal Bioanal Chem 392(1-2) (2008) 305-312.

[40] C.M.J. Hu, L. Zhang, S. Aryal, C. Cheung, R.H. Fang, L.F. Zhang, Erythrocyte membrane-camouflaged polymeric nanoparticles as a biomimetic delivery platform, P Natl Acad Sci USA 108(27) (2011) 10980-10985.

[41] J.D. Cox, M.S. Curry, S.K. Skirboll, P.L. Gourley, D.Y. Sasaki, Surface passivation of a microfluidic device to glial cell adhesion: a comparison of hydrophobic and hydrophilic SAM coatings, Biomaterials 23(3) (2002) 929-935.

[42] J.X. Li, S. Thamphiwatana, W.J. Liu, B.E.F. de Avila, P. Angsantikul, E. Sandraz, J.X. Wang, T.L. Xu, F. Soto, V. Ramez, X.L. Wang, W.W. Gao, L.F. Zhang, J. Wang, Enteric Micromotor Can Selectively Position and Spontaneously Propel in the Gastrointestinal Tract, Acs Nano 10(10) (2016) 9536-9542.

[43] M. Boegh, H.M. Nielsen, Mucus as a Barrier to Drug Delivery - Understanding and Mimicking the Barrier Properties, Basic Clin Pharmacol 116(3) (2015) 179-186.

[44] F.Y. Zhang, R. Mundaca-Uribe, H. Gong, B.E.F. de Avila, M. Beltran-Gastelum, E. Karshalev, A. Nourhani, Y. Tong, B. Nguyen, M. Gallot, Y. Zhang, L.F. Zhang, J. Wang, A Macrophage-Magnesium Hybrid Biomotor: Fabrication and Characterization, Adv Mater 31(27) (2019).

[45] D.N. Zhong, D.X. Zhang, W. Chen, J. He, C.J. Ren, X.C. Zhang, N. Kong, W. Tao, M. Zhou, Orally deliverable strategy based on microalgal biomass for intestinal disease treatment, Sci Adv 7(48) (2021).

[46] Y. Inoue, K. Izawa, S. Kiryu, A. Tojo, K. Ohtomo, Diet and abdominal autofluorescence detected by in vivo fluorescence imaging of living mice, Mol Imaging 7(1) (2008) 21-27.

[47] O. Tacar, P. Sriamornsak, C.R. Dass, Doxorubicin: an update on anticancer molecular action, toxicity and novel drug delivery systems, J Pharm Pharmacol 65(2) (2013) 157-170.

[48] R.H. Fang, A.V. Kroll, W.W. Gao, L.F. Zhang, Cell Membrane Coating Nanotechnology, Adv Mater 30(23) (2018).

[49] N. Yang, Y.P. Ding, Y.L. Zhang, B. Wang, X. Zhao, K.M. Cheng, Y.X. Huang, M. Taleb, J. Zhao, W.F. Dong, L.R. Zhang, G.J. Nie, Surface Functionalization of Polymeric Nanoparticles with Umbilical Cord-Derived Mesenchymal Stem Cell Membrane for Tumor-Targeted Therapy, Acs Appl Mater Inter 10(27) (2018) 22963-22973.

[50] X.H. Yan, Q. Zhou, M. Vincent, Y. Deng, J.F. Yu, J.B. Xu, T.T. Xu, T. Tang, L.M. Bian, Y.X.J. Wang, K. Kostarelos, L. Zhang, Multifunctional biohybrid magnetite microrobots for imaging-guided therapy, Sci Robot 2(12) (2017).

[51] H.M.D. Wang, X.C. Li, D.J. Lee, J.S. Chang, Potential biomedical applications of marine algae, Bioresource Technol 244 (2017) 1407-1415.

[52] Y. Qiao, F. Yang, T.T. Xie, Z. Du, D.N. Zhong, Y.C. Qi, Y.Y. Li, W.L. Li, Z.M. Lu, J.H. Rao, Y. Sun, M. Zhou, Engineered algae: A novel oxygen-generating system for effective treatment of hypoxic cancer, Sci Adv 6(21) (2020).

[53] Z.G. Wu, L. Li, Y.R. Yang, P. Hu, Y. Li, S.Y.O. Yang, L.V. Wang, W. Gao, A microrobotic system guided by photoacoustic computed tomography for targeted navigation in intestines in vivo, Sci Robot 4(32) (2019).

[54] B.W. Jester, H. Zhao, M. Gewe, T. Adame, L. Perruzza, D.T. Bolick, J. Agosti, N. Khuong, R. Kuestner, C. Gamble, K. Cruickshank, J. Ferrara, R. Lim, T. Paddock, C. Brady, S. Ertel, M.H. Zhang, A. Pollock, J. Lee, J. Xiong, M. Tasch, T. Saveria, D. Doughty, J. Marshall, D. Carrieri, L. Goetsch, J.S. Dang, N. Sanjaya, D. Fletcher, A. Martinez, B. Kadis, K. Sigmar, E. Afreen, T. Nguyen, A. Randolph, A. Taber, A. Krzeszowski, B. Robinett, D.B. Volkin, F. Grassi, R. Guerrant, R. Takeuchi, B. Finrow, C. Behnke, J. Roberts, Development of spirulina for the manufacture and oral delivery of protein therapeutics (Mar, 10.1038/s41587-022-01249-7, 2022), Nat Biotechnol 40(6) (2022) 974-974.

[55] M.A. Scranton, J.T. Ostrand, F.J. Fields, S.P. Mayfield, Chlamydomonas as a model for biofuels and bio-products production, Plant J 82(3) (2015) 523-531.

The second portion of Chapter 3, in full, is a reprint of the material as it appears in *Science Robotics*, 2022 by Fangyu Zhang, Zhengxing Li, Yaou Duan, Amal Abbas, Rodolfo Mundaca-Uribe, Lu Yin, Hao Luan, Weiwei Gao, Ronnie H. Fang, Liangfang Zhang and Joseph Wang. The dissertation author was the co-primary investigator and co-author of this paper.

3.3 Extremophile-based biohybrid micromotors for biomedical operations in harsh acidic environments

3.3.1 Introduction

The operation and navigation of robots in extreme environments have been listed as one of the ten grand challenges facing robotics in the next decade [1]. Recent robotic research along these lines has focused primarily on developing macroscale robots for operation in challenging environments, such as deep oceans with high pressure [2], polar regions with low temperature [3], and deserts with high temperature [4]. Upon scaling to the microscale regime, robots face additional challenges associated with propulsion in a low Reynolds number medium. Over the past decade, various microrobotic platforms have been developed to meet the propulsion requirements for diverse biomedical and environmental applications using three motion mechanisms, including energy harvesting from external fields [5-9], reaction with fuels present in the local surroundings [10-15], or utilizing the intrinsic motility and natural taxis behavior of living biological organisms [16-20]. Microrobotic platforms can provide distinctive advantages for in vivo operations by leveraging their active propulsion to deliver therapeutics to specific sites within the body [21-26]. Notably, micromotors have recently emerged as powerful tools for effective oral drug delivery, helping to address several limitations of traditional oral drug formulations such as poor drug absorption, short retention, and low bioavailability [27, 28]. However, the extended operation of micromotors in the highly acidic gastric environment is still challenging and requires the

development of innovative solutions [29].

Although several studies have aimed at integrating self-actuating mechanical devices in millimeter-sized robotic pills for application in the harsh conditions of the GI tract [30-32], effective and long-term operation of micromotors in an extremely acidic medium (pH < 3) remains highly challenging owing to its ability to corrode or degrade various types of micromotor platforms. There are only few reports on the influence of extremely acidic conditions on the movement of micromotors. For example, coating magnetically powered microswimmers with Al_2O_3 films was reported to enhance their propulsion in acidic conditions [33]. Al/Pd spherical micromotors were shown to operate in a wide range of pH conditions [34]. Finally, the self-propulsion of zinc microrockets and magnesium-based Janus micromotors in the gastric environment has led to enhanced therapeutic GI delivery [35, 36]. Although synthetic micromotors have demonstrated utility for GI applications, their short lifetimes in acidic conditions limit their practical use to only short segments within the GI tract. Prolonged operation in the gastric and intestinal fluid can endow micromotors with the ability to actively drive therapeutic payloads to widely distributed areas over the entire GI tract and enhance the dispersion and retention of drugs for treating diseases and disorders. It is clear that realizing efficient and prolonged micromotor operation in a highly acidic medium remains an important unmet need, particularly for biomedical applications in the gastric environment.

In this work, we demonstrate an extremophile-based biohybrid micromotor capable of continuous and prolonged operation in extremely low pH environments. Many extremophiles, capable of surviving under extreme physical or chemical conditions, are found in some of the

harshest environments on earth [37]. Among them, acidophilic microalgae have been shown to support the ecosystems of extremely acidic environments scattered around the globe associated with sulfur springs, volcanic vents, and acid mine drainages [38]. Such acidophilic algae evolved from their respective neutrophilic ancestors to thrive at low pH by reducing their proton influx and increasing their proton pump efficiency [39, 40]. Here, we demonstrated the efficient and prolonged motion behavior of acidophilic algae in strong hydrochloric acid down to pH 1 and their tremendous potential for microrobotic gastrointestinal (GI) delivery applications. Specifically, we relied on *Chlamydomonas pitschmannii,* an acidophilic alga isolated from an acid mine drainage [41]. *C. pitschmannii* displayed a negligible change in speed over an extremely broad pH range, from pH 1 to 10, compared to the neutrophilic alga *Chlamydomonas reinhardtii*, which was incapable of swimming in acidic medium (pH < 4) and rapidly degraded (**Figure 3.3.1A, B**). Notably, the movement of *C. pitschmannii* in acidic medium was maintained over an extended period of at least 72 h (**Figure 3.3.1C**). We further evaluated the performance of the acidophilic biomotors in gastric fluid (pH 1.5) and intestinal fluid (pH 6.5) and tracked their *in vivo* biodistribution to establish their potential for biomedical applications involving GI tract delivery (**Figure 3.3.1D, E**). Multifunctional biohybrid algae motors were fabricated by decorating the acidophilic algae with polymeric nanoparticles, which were loaded with a green fluorescent dye for visualization purposes (**Figure 3.3.1F**). The binding between nanoparticles and *C. pitschmannii* algae was clearly observed by electron microscopy (**Figure 3.3.1G**). Finally, by tuning the surface properties of the cargo, selective targeting to the stomach or broad GI tract delivery could be achieved. The effective and long-term movement of cargo-loaded acidophilic

algae motors over a wide range of pH conditions, including harsh acidic media, along with their strong retention in the GI tract, suggests that the platform holds considerable promise for future biomedical applications in the GI tract. Further work on extremophile-based multifunctional biohybrid micromotors could lead to the development of novel microrobotic platforms capable of excelling in a variety of harsh environments.

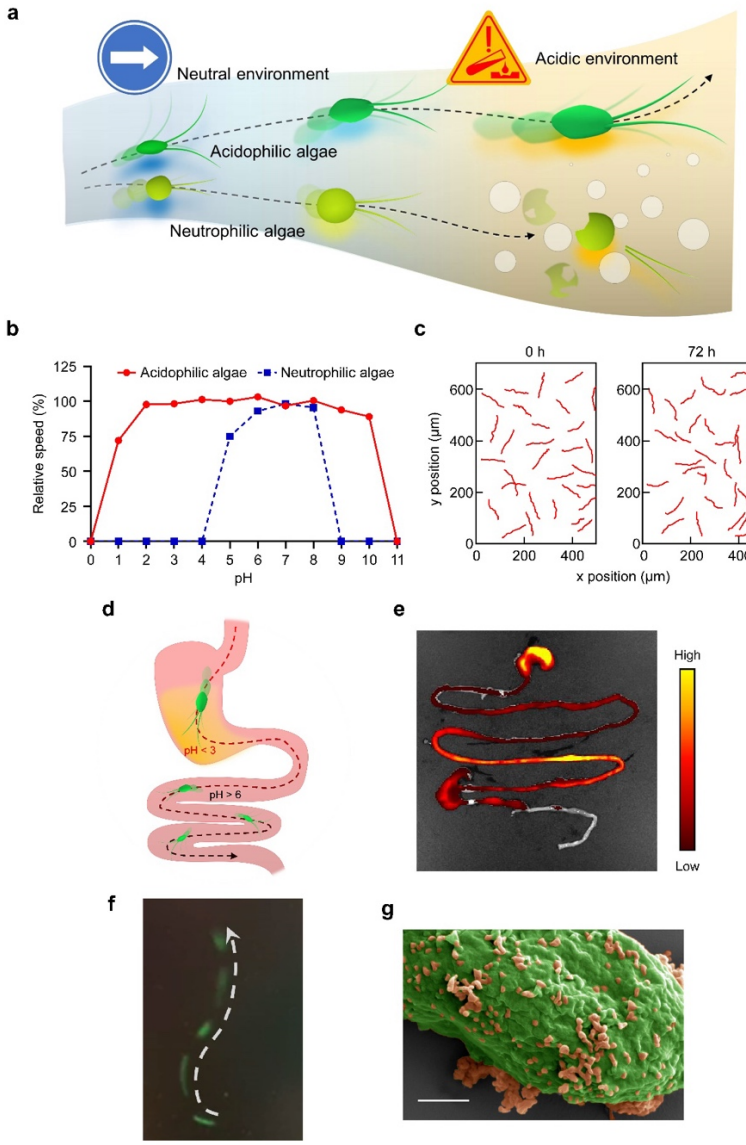

Figure 3.3.1 Schematics of acidophilic algae micromotors for various biomedical applications. a. Acidophilic algae motors are capable of prolonged motion in both neutral and acidic environments, whereas neutrophilic algae are incapable of operating in highly acidic environments. **b.** The relative speed of acidophilic algae and neutrophilic algae over a range of pH values compared to their speed in optimal culture conditions (modified acidic medium at pH 3.5 for acidophilic algae; TAP at pH 7 for neutrophilic algae). **c.** 2D motion trajectories of acidophilic algae motors over a period of 1 s before and 72 h after swimming in HCl at pH 1.5. **d.** Acidophilic algae motors can operate throughout the entire GI tract for in vivo delivery applications. **e.** Representative biodistribution of acidophilic algae motors in the GI tract at 2 h after administration by oral gavage. **f.** 1-second motion trajectory of acidophilic algae-based biohybrid motors carrying dye-labeled nanoparticles in HCl at pH ~1.5. Scale bar, 10 μm. **g.** Representative pseudocolored scanning electron microscopy image of a nanoparticle-functionalized acidophilic algae motor. Scale bar, 1 μm.

3.3.2 Results and Discussion

Motion behavior of acidophilic algae

C. pitschmannii CPCC 354 was selected as a model acidophilic algae strain, and its swimming behavior was characterized in extremely acidic conditions. To evaluate their movement, the algae were cultured in a modified acidic medium (MAM) [42] (pH 3.5) to a density of 1 × 10^6/ml, followed by transfer to hydrochloric acid for speed measurement. The algae exhibited constant swimming with a speed of 95-105 μm/s (corresponding to ~10 body length/s) in an extremely acidic environment at pH 1.5 (**Figure 3.3.2A**). Their movement was also tracked over a 5 s period under the same condition in order to visualize a representative trajectory (**Figure 3.3.2B**). When investigating the tolerance range of the algae to extreme acid, we found that they displayed a significant decrease in speed and loss of activity after 1 h of motion at pH 1 (**Figure 3.3.2C**). Furthermore, the effect of the anion was evaluated by immersing the algae in different common strong acids (HCl, H_2SO_4, and HNO_3) adjusted to pH 1.5 (**Figure 3.3.2D**). The detrimental effect of nitric acid on the algae motion could be explained by its strong oxidizing capacity compared to the other two acids.

Interestingly, we observed that the acidophilic algae could not only resist extreme acidic conditions (pH < 3), but they were also able to survive in neutral and alkaline environments (**Figure 3.3.2E**). After 30 min of adaptation, the acidophilic algae displayed efficient movement across a broad pH range from 1 to 10 (**Figure 3.3.2F**). In comparison, a model neutrophilic algae *C. reinhardtii*, which have been commonly used as microorganism-based micromotors for various environmental and biomedical applications [17, 20, 26, 43], were unable to tolerate extreme acidic

pH and could swim only over a narrow pH range between 5 to 8 (**Figure 3.3.2F**). The contrast between the two types of algae was further highlighted by visualizing their trajectories at pH 1.5, 4, and 7 after various periods of time (**Figure 3.3.2G, H**). Only slight speed differences were observed for the acidophilic algae at all pH values after 24 h, whereas the motility of neutrophilic algae rapidly diminished at pH 1.5 and 4

.

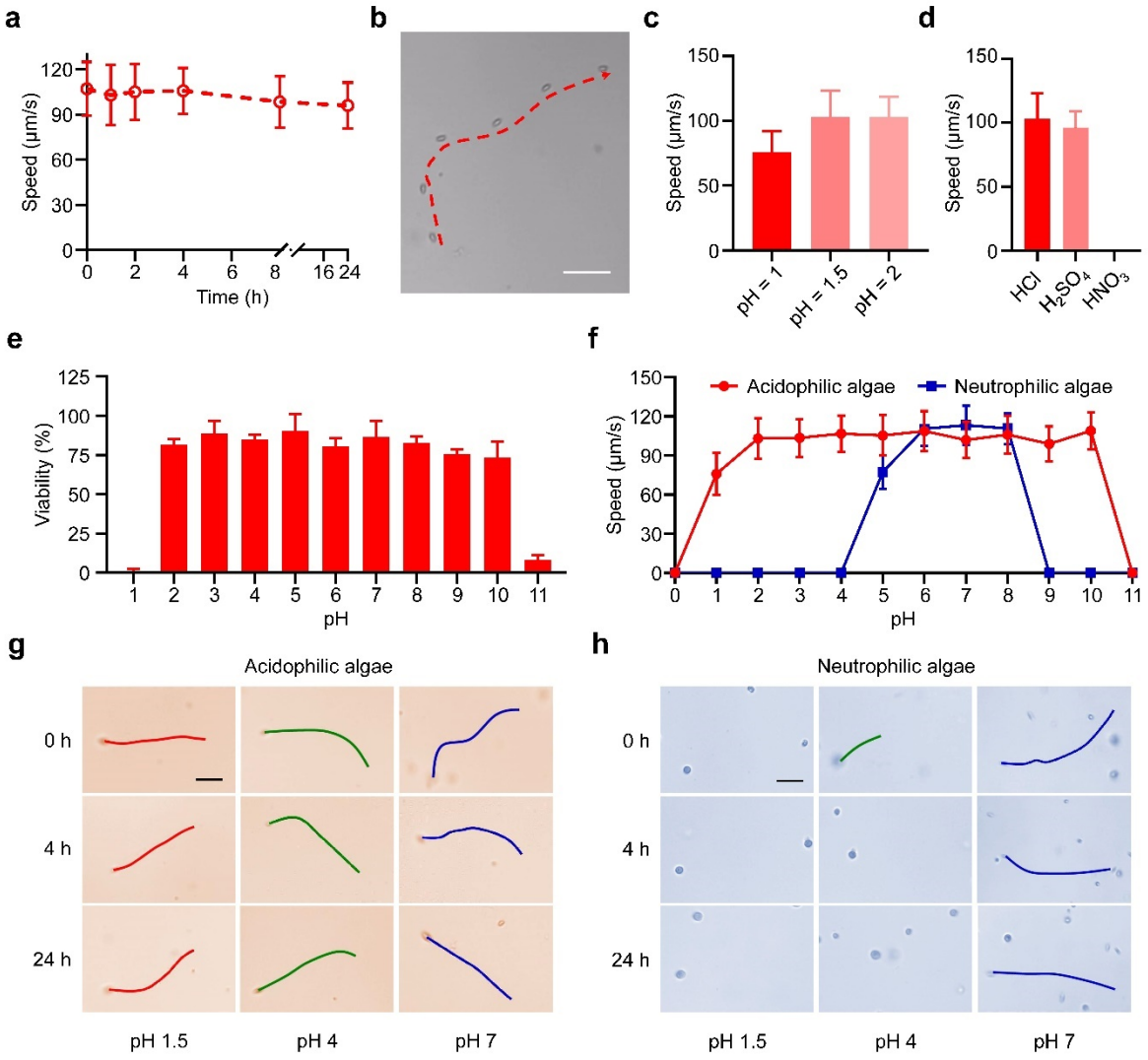

Figure 3.3.2 Motion behavior of acidophilic algae biomotors in extremely acidic conditions. a. Speed of acidophilic algae biomotors at different timepoints (0, 1, 2, 4, 8, and 24 h) in HCl at pH 1.5. **b.** The representative trajectory of an acidophilic alga biomotor over a period of 5 s in HCl at pH 1.5. Scale bar, 100 μm. **c.** Swimming speed of algae biomotors upon 1 h of exposure to HCl at pH 1, 1.5, and 2 (n = 100, mean + s.d.). **d.** Swimming speed of acidophilic algae biomotors in different acidic mediums (HCl, H_2SO_4, and HNO_3) at pH 1.5 (n = 100, mean + s.d.). **e.** Viability of acidophilic algae in different media at pH values from 1 to 11 (n = 3, mean + s.d.). **f.** Speed comparison of acidophilic algae with neutrophilic algae at pH between 0 to 11 (n = 100, mean ± s.d.). Speed was measured from 100 individual algae. **g, h.** Representative trajectories over a period of 2 s for acidophilic algae (g) and neutrophilic algae (h) after various durations (0 h, 4 h, and 24 h) of exposure to HCl at pH 1.5, 4, and 7. Scale bar, 50 μm.

Biodistribution and retention of acidophilic algae in the GI tract

The oral route of administration is the most common approach for drug delivery to treat GI disease [44]. A major challenge of GI delivery is overcoming the physiological barrier caused by the extreme acidity within the stomach. To investigate the potential of acidophilic algae biomotors for improved GI delivery, we first tested their motion ability and viability in vitro in simulated gastric (pH ~1.5) and intestinal (pH ~6.5) fluids. They exhibited good adaptation in both physiological fluids, and their self-propulsion (~100 μm/s) was unaffected after 8 h of constant movement, indicating great promise for in vivo GI operation. In comparison, the neutrophilic algae lost their motion ability rapidly upon transfer from the culture medium to gastric fluid at room temperature. We also observed for any changes in morphology using electron microscopy after incubation in strong gastric acid. The acidophilic algae displayed an intact structure after 2 h of motion, whereas the neutrophilic algae were structurally damaged after the same period of time. To further mimic the physiological conditions in the stomach [45], we assessed the speed and lifetime of acidophilic algae in simulated gastric fluid containing 1 mg/ml of pepsin at body temperature (37 °C) and found that the algae maintained speeds of 65 μm/s and 35 μm/s after 1 h and 2 h of incubation, respectively. These results supported the potential of the acidophilic algae for active transport throughout the GI tract, whereas the regular neutrophilic algae would be unable to traverse the harsh acidic medium in the stomach.

Next, we demonstrated the distinct advantages of acidophilic algae biomotors for GI delivery by examining their biodistribution and retention after oral administration using a murine model. Ex vivo fluorescence imaging was conducted to determine the influence of acid tolerance

on algae localization within the GI tract (**Figure 3.3.3A-C**). In order to visualize and track the algae, their surfaces were covalently bound with the near-infrared fluorescent dye Cy7 (λex/λem = 750 nm/773 nm) [46], which did not hinder their motion behavior in GI fluid. Before oral gavage, we confirmed that the dye-conjugated acidophilic algae, neutrophilic algae, and alkaline-treated static acidophilic algae were similar in number and fluorescence intensity. At various timepoints (0.5 h, 2 h, 5 h, 10 h, and 24 h) after oral administration, the mice were euthanized, and their GI tracts were isolated to visualize the location of algae. As shown in Fig. 3a, the acidophilic algae displayed a strong signal throughout the entire GI tract, showing sustained retention in the stomach as well as wide distribution in the lower GI tract within the first 5 h. In comparison, the signals from the neutrophilic algae (**Figure 3.3.3B**) and the static acidophilic algae (**Figure 3.3.3C**) diminished rapidly within 2 h after administration. These results emphasized the importance of the acid tolerance and self-propulsion properties of acidophilic algae, which enabled efficient operation in the stomach and effective distribution in the lower GI tract. The visual observations were further corroborated by quantifying the total radiant efficiency in the stomach (**Figure 3.3.3D**) or in the small intestine and colon (**Figure 3.3.3E**) at different timepoints.

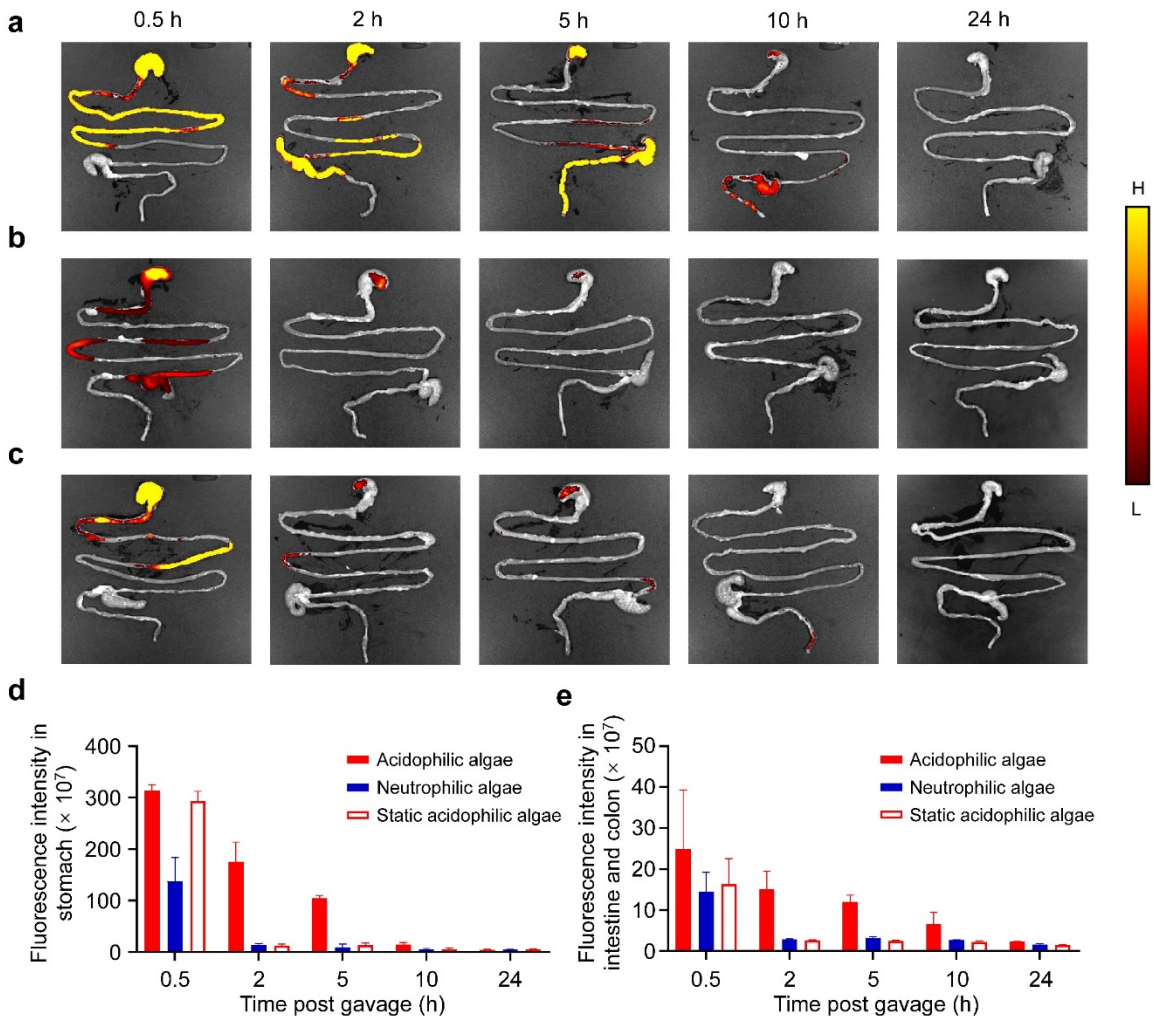

Figure 3.3.3 Biodistribution of acidophilic algae biomotors in the GI tract. a-c. Mice were orally gavaged with Cy7-labeled acidophilic algae (a), Cy7-labeled neutrophilic algae (b), or Cy7-labeled static acidophilic algae (c), and distribution in the GI tract was visualized over time. **d, e.** Measurement of the fluorescence intensity in the stomach (d) or small intestine and colon (e) at different timepoints (0.5 h, 2 h, 5 h, 10 h, and 24 h) after oral gavage (n = 3, mean + s.d.).

Biosafety of acidophilic algae in GI

To assess the safety of the acidophilic algae, we evaluated their toxicity profile both systemically and locally in the lower GI tract. A treatment dosage of 1×10^7 acidophilic algae was orally administered to mice, while untreated mice served as controls. A comprehensive blood

chemistry panel and blood cell count were conducted 24 h afterward (**Figure 3.3.4A, B**). There was no statistical difference between the untreated control and the algae treatment group in any of the 14 blood parameters and blood cell populations that were analyzed. Hematoxylin and eosin (H&E)-stained histological sections showed that the stomach and intestinal mucosa or submucosa maintained their integrity without any lymphocyte infiltration or signs of inflammation (**Figure 3.3.4C**). Finally, histological analysis of the major organs, including the heart, liver, spleen, lungs, and kidneys, was performed (**Figure 3.3.4D**). The appearance of all the organs was normal compared to healthy mice. Further studies will be required to comprehensively evaluate the impact of algae administration on other immune parameters, both local and systemic, across multiple timescales.

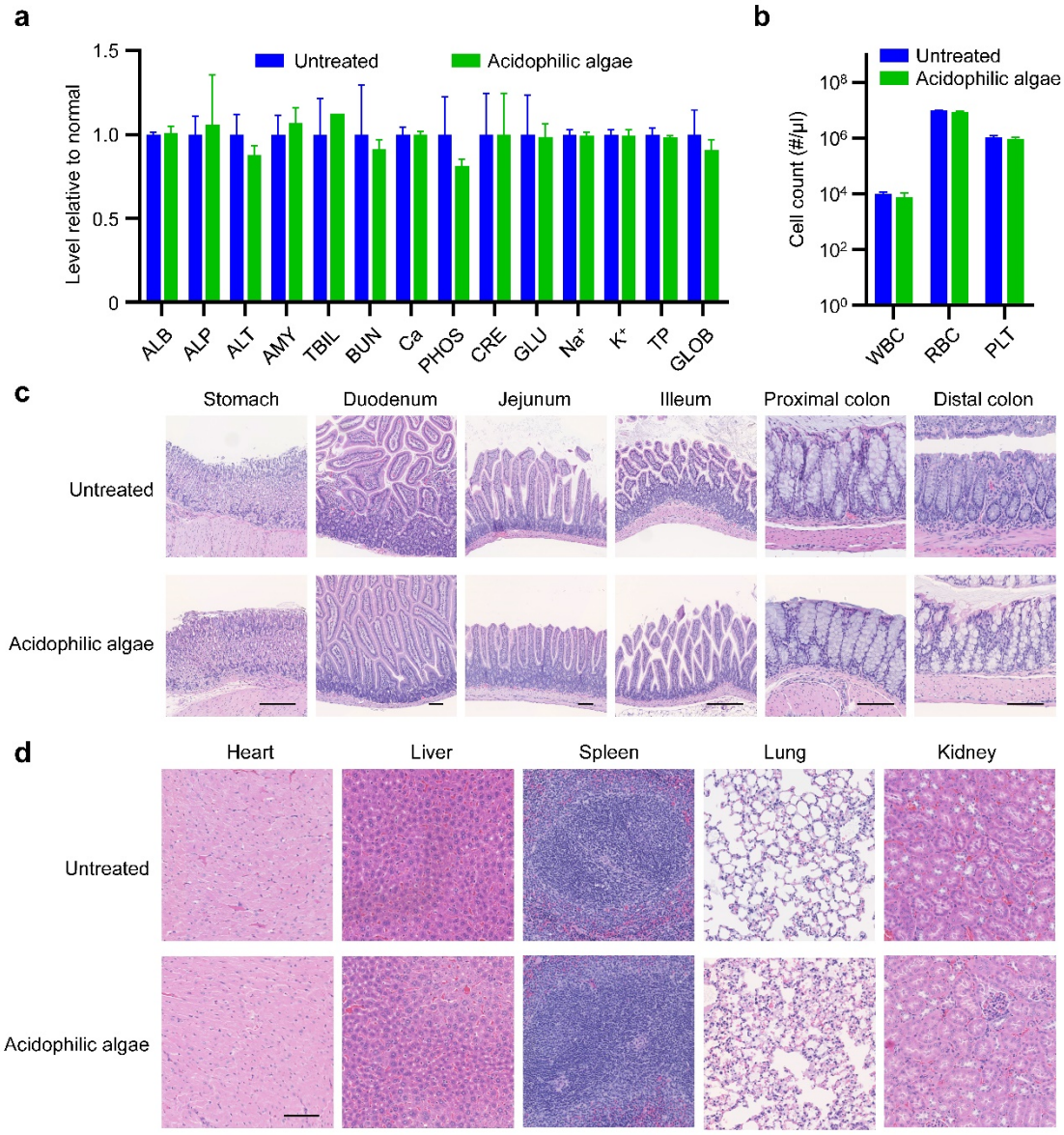

Figure 3.3.4 ***In vivo*** **safety evaluation of acidophilic algae. a.** Comprehensive blood chemistry panel for untreated mice or mice at 24 h after treatment with acidophilic algae micromotors (n = 3, mean + s.d.). Abbreviations: ALB, albumin; ALP, alkaline phosphatase; ALT, alanine transaminase; AMY, amylase; TBIL, total bilirubin; BUN, blood urea nitrogen; Ca, calcium; PHOS, phosphorus; CRE, creatinine; GLU, glucose; Na^+, sodium; K^+, potassium; TP, total protein; GLOB, globulin (calculated). **b.** Counts for various blood cells taken from untreated mice or mice at 24 h after treatment with acidophilic algae micromotors (n = 3, mean + s.d.). Abbreviations: WBC, white blood cells; RBC, red blood cells; PLT, platelets. **c.** Representative hematoxylin and eosin (H&E)-stained histology sections of different portions of the GI tract from untreated mice or mice at 24 h after treatment with acidophilic algae micromotors. Scale bar, 100 μm **d.** Representative H&E-stained histology sections of major organs from untreated mice or mice at 24 h after treatment with acidophilic algae micromotors. Scale bar, 100 μm

Stomach delivery with acidophilic algae motors

Upon confirming the biodistribution and safety of acidophilic algae for GI administration, we evaluated the feasibility of leveraging them for cargo delivery. Poly(lactic-*co*-glycolic acid) (PLGA) nanoparticles were chosen as the model payload since they are attractive for therapeutic delivery applications with properties such as controlled and sustained drug release, high drug loading yield, and low toxicity [47]. To fabricate the acidophilic algae biohybrid motors, positively charged poly-l-lysine (PLL)-coated PLGA nanoparticles (denoted 'PLLNP') were attached to the negatively charged acidophilic algae surface via electrostatic interaction, thus generating PLLNP-loaded acidophilic algae biohybrid motors (denoted 'acido-algae-PLLNP') (**Figure 3.3.5A**). The surface coating on the PLGA core was first optimized by tuning the incubation time between the nanoparticles and the PLL polyelectrolyte to yield PLLNP with a strong positive surface charge. The determination of zeta potential at different pH values is important for complexing two materials based on electrostatic interactions [48]. To this end, the surface charge of bare acidophilic algae and PLLNP was evaluated at pH values ranging from 1 to 11. It was found that the PLL coating could promote the effective binding of PLGA nanoparticles to algae at neutral pH, which was visualized by fluorescence microscopy (**Figure 3.3.5B**). The algae were uniformly surrounded by 3,3'-dioctadecyloxacarbocyanine perchlorate (DiO; λex/λem = 484 nm/501 nm)-loaded PLLNP. A pseudocolored scanning electron microscopy (SEM) image illustrated the attachment of the nanoparticles onto the algae cell surface (**Figure 3.3.5C**). The motion behavior of the acido-algae-PLLNP was characterized by measuring their speed under extreme acidic conditions at pH 1.5 (**Figure 3.3.5D**). The decreased speed of the acido-algae-PLLNP (~50 μm/s) compared to bare

acidophilic algae (~100 μm/s) could be attributed to the influence of the positively charged cargo on the flagella, as indicated by inconsistent (zigzag trajectory) movement patterns (**Figure 3.3.5E**).

Next, we evaluated the gastric cargo delivery ability of the acido-algae-PLLNP biohybrid motors. A near-infrared dye, 1,1'-dioctadecyl-3,3,3',3'-tetramethylindotricarbocyanine iodide (DiR, λex/λem = 748 nm/780 nm), was encapsulated into PLLNP as a model payload. Prior to the animal studies, an in vitro study was conducted to assess the stability of cargo loading on the biohybrid motors. In the acido-algae-PLLNP formulation, released dye or unbound nanoparticles were hardly detected even after 24 h of incubation in HCl (pH 2) or simulated gastric fluid (pH 1.5), indicating highly stable cargo binding to the algae via electrostatic interactions, hydrogen bonding between PLL and the diverse functional groups present on the algae surface, and physical entrapment of nanoparticles by the highly porous structure of the algae cell wall. Then, acido-algae-PLLNP and PLLNP control (without algae) were orally administered to mice to study their biodistribution and retention. After 2 h, 5 h, and 10 h, the mice were euthanized, and their GI tracts were isolated for ex vivo imaging (**Figure 3.3.5F**). Both acido-algae-PLLNP and PLLNP were mainly located in the stomach, which is attributed to the mucoadhesive property of the positively charged PLLNP [44]. However, the motion of the biohybrid motors enabled a higher chance of contact between the nanoparticles and the luminal lining, facilitating efficient cargo retention in the stomach. Such accumulation can be used to improve drug delivery and enhance tissue penetration, as was demonstrated previously using micromotors for oral vaccine delivery [49]. Quantification of the fluorescence intensity within the stomach supported the greatly improved retention of PLLNP when delivered by acido-algae-PLLNP biohybrid motors as opposed to in free form within the first

5 h after oral gavage (**Figure 3.3.5G**).

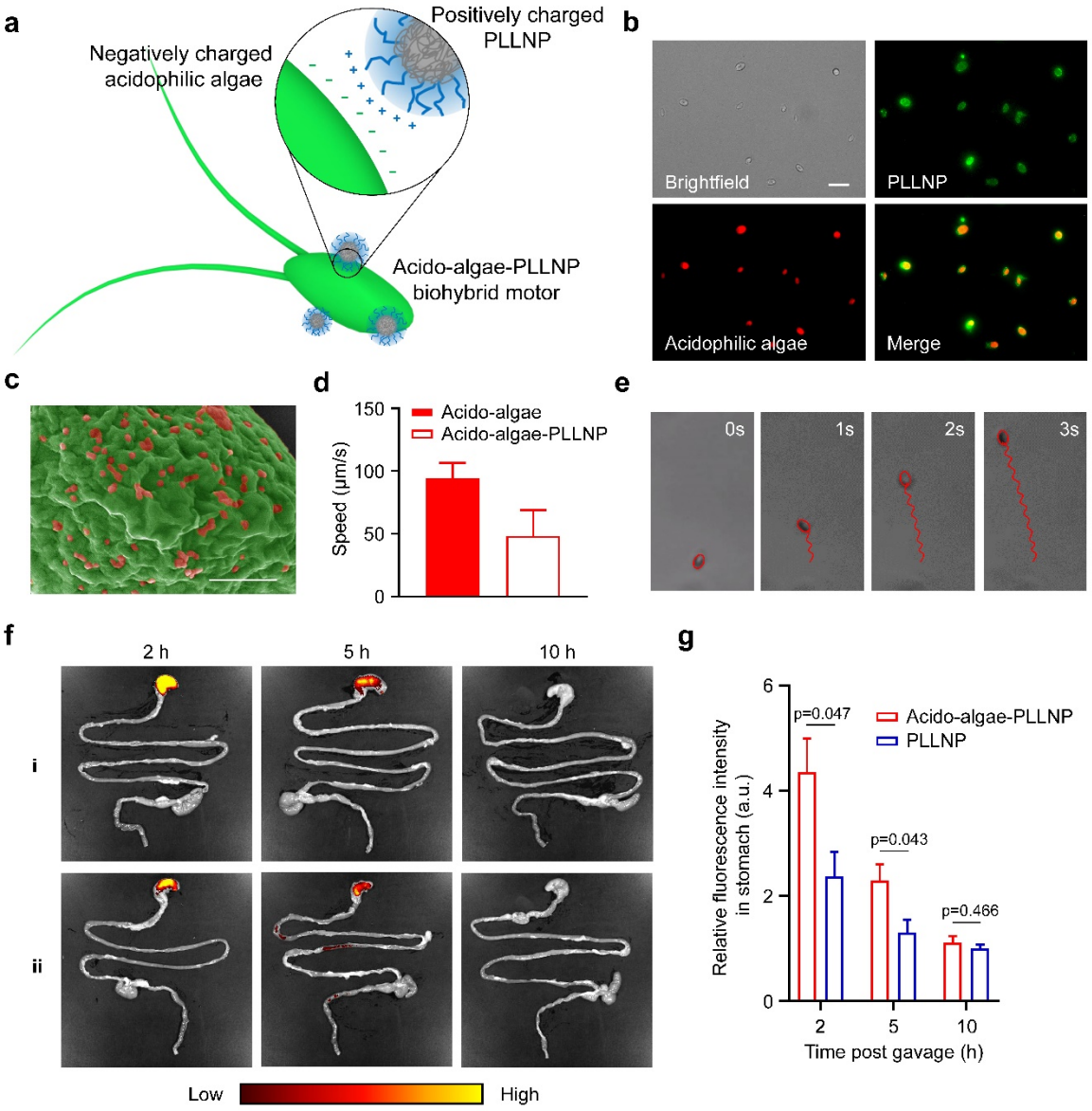

Figure 3.3.5 Acido-algae-PLLNP biohybrid motors for stomach delivery. a. Loading of PLLNP onto acidophilic algae motors by electrostatic interaction. **b.** Fluorescence microscopy images of acido-algae-PLLNP biohybrid motors. Red: acidophilic algae (chloroplast autofluorescence). Green: PLLNP (DiO). Scale bar, 20 μm. **c.** Pseudocolored SEM images of an acido-algae-PLLNP biohybrid motor. Scale bar, 1 μm. **d.** Speed comparison of acido-algae-PLLNP and bare acidophilic algae (denoted 'acido-algae' in the figure) at pH 1.5 (n = 20, mean + s.d.). **e.** Representative trajectories of the acido-algae-PLLNP biohybrid motor over a period of 3 s in HCl at pH 1.5. Scale bar, 10 μm. **f.** Ex vivo imaging of the GI tract at 2 h, 5 h, and 10 h after oral administration of acido-algae-PLLNP (i) or PLLNP (ii). **g.** Fluorescence intensity of DiR dye delivered by acido-algae-PLLNP or PLLNP in the stomach at 2 h, 5 h, and 10 h after oral gavage (n = 3, mean + s.d.).

Entire GI delivery with acidophilic algae motors

After confirming effective cargo delivery to the stomach by using mucoadhesive PLLNP attached to the surface of acidophilic algae motors, we sought to evaluate whether the acidophilic algae could be used to transport cargo throughout the entire GI tract given their effective distribution shown in Fig. 3. Instead of using positively charged PLLNP, we elected to employ PLGA cores with a cell membrane coating, which endows versatile surface functionality and biomimetic properties to nanocarriers [50]. Red blood cell membrane-coated PLGA nanoparticles (denoted 'RBCNP') were prepared based on a previously established protocol [51]. The hydrodynamic size and zeta potential of RBCNP were characterized by dynamic light scattering, indicating the slight increase in size and negative charge after membrane coating. The RBC membrane coating onto the PLGA surface was further verified by transmission electron microscopy (TEM), showing an intact core-shell structure. To achieve loading of RBCNP onto algae, a bioorthogonal conjugation approach using copper-free click chemistry was employed [52] (**Figure 3.3.6A**). Briefly, the algae and RBCNP were separately functionalized with dibenzocyclooctyne-(polyethylene glycol)$_4$-N-hydroxysuccinimidyl ester (DBCO-PEG$_4$-NHS) and azido-PEG$_4$-NHS ester, respectively. The two components were then conjugated together by leveraging these newly introduced functional groups. The attachment of RBCNP to acidophilic algae (denoted 'acido-algae-RBCNP') was validated by a pseudocolored SEM image (**Figure 3.3.6B**) and fluorescent imaging, confirming the effective binding between DiO dye-labeled RBCNP and the algal surface (**Figure 3.3.6C**). Importantly, the covalent binding of RBCNP had

minimal effects on the motion behavior (speed and tracking pattern) of the algae motors (**Figure 3.3.6D, E**). After 24 h of incubation in acidic fluid, 90% of the fluorescence intensity of DiR-loaded RBCNP onto the algae surface was preserved, indicating the high binding stability between acidophilic algae and RBCNP in a harsh acidic environment.

Next, we evaluated the feasibility of using acido-algae-RBCNP biohybrid motors for delivery throughout the GI tract. DiR was loaded into RBCNP as a model payload to track nanoparticle localization at different GI sites in vivo. At 2 h, 5 h, and 10 h after oral administration of acido-algae-RBCNP and free RBCNP (without algae) with a similar amount of DiR loading, the GI tract was excised for ex vivo fluorescence imaging (**Figure 3.3.6F**). Due to their acid tolerance and movement capabilities, the acido-algae-RBCNP motors were able to transport the RBCNP to the entire GI tract as opposed to only the stomach. The fluorescent signals from the active biohybrid motor group were more substantial in both the stomach and the small intestine at 2 h and remained stronger at 5 h and 10 h when compared with the free RBCNP group. Importantly, it should be noted that the 10 h cargo retention facilitated by the biohybrid motors was much longer than the gastric emptying time of a fluid meal [53]. A similar trend of improved GI payload retention by acido-algae-RBCNP was confirmed when quantifying the fluorescent signals, with 2-fold and 1.5-fold enhancement at 2 h and 5 h after oral gavage, respectively (**Figure 3.3.6G**). These results confirmed that controlling the surface properties of the nanoparticle payload could selectively position the biohybrid motors in different regions of the GI tract.

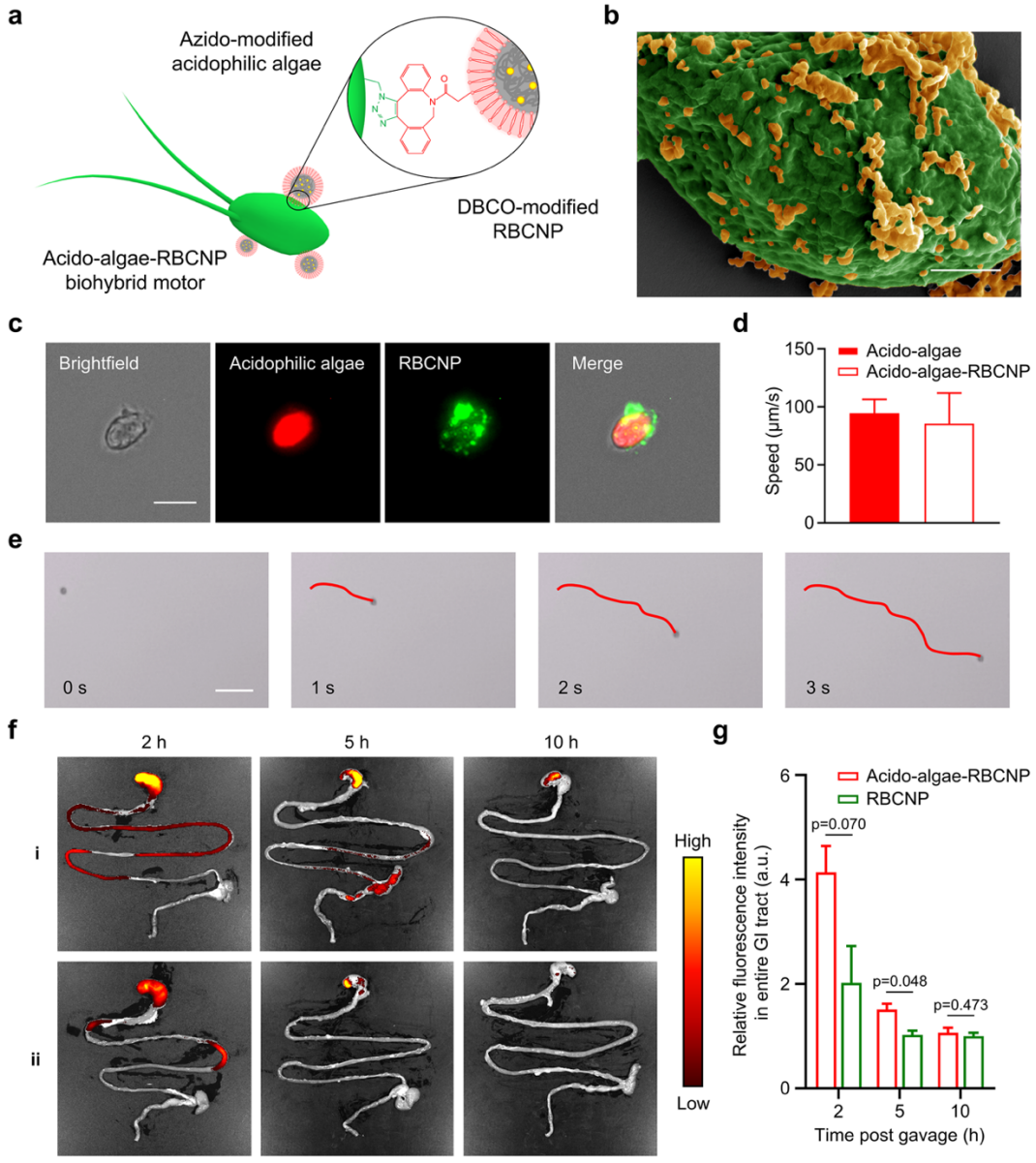

Figure 3.3.6 Acido-algae-RBCNP biohybrid motors for entire GI tract delivery. a. Loading of RBCNP onto acidophilic algae motors via click chemistry. **b.** Pseudocolored SEM image of an acido-algae-RBCNP biohybrid motor. Scale bar, 1 μm. **c.** Representative fluorescence microscopy images of an acido-algae-RBCNP biohybrid motor. Red: acidophilic algae (chloroplast autofluorescence). Green: RBCNP (DiO). Scale bar, 10 μm. **d.** Speed comparison of acido-algae-RBCNP and bare acidophilic algae (denoted 'acido-algae' in the figure) at pH 1.5 (n = 20, mean + s.d.). **e.** Representative trajectories of acido-algae-RBCNP biohybrid motor over a period of 3 s in HCl at pH 1.5. Scale bar, 50 μm. **f.** Ex vivo imaging of the GI tract at 2 h, 5 h, and 10 h after oral administration of acido-algae-RBCNP (i) or RBCNP (ii). **g.** Fluorescence intensity of DiR dye delivered by acido-algae-RBCNP or RBCNP in the entire GI at 2 h, 5 h, and 10 h after oral gavage (n = 3, mean + s.d.).

3.3.3 Conclusion

In summary, we have reported on the first extremophile-based algae biohybrid motor for application in harsh conditions such as acidic biological fluid. Acidophilic *C. pitschmannii* algae were chosen based on their ability to effectively swim in highly acidic conditions. The unique adaptability and long-lasting self-propulsion of the acidophilic algae over a wide pH range (1.5-10) provided the natural micromotor essential flexibility for efficient performance in both gastric and intestinal fluid. In a murine model, oral administration of the acidophilic algae resulted in improved GI distribution and retention compared to neutrophilic algae and static acidophilic algae controls. By functionalizing the algae with cargo-loaded PLGA nanoparticles via different conjugation approaches, the resulting multifunctional biohybrid micromotors were able to facilitate cargo delivery to the stomach or the entire GI tract in vivo. Once inside the GI tract, the PLGA nanoparticles provide controlled and sustained drug release through the hydrolytic cleavage of their polyester backbones [54]. While the current surface attachment strategies were effective for loading drug onto the algae motors, other approaches such as the incorporation of small-molecule drugs inside the algae could be explored [55]. In addition, various drug payloads, including chemotherapeutics and biologics, could be incorporated to improve their therapeutic activity for local GI diseases [56]. Long-term biosafety monitoring needs to be performed prior to the clinical studies of the biohybrid motors to verify their lack of immunogenicity and toxicity. Looking forward, we envision decoration of the acidophilic algae with multiple functional units, including therapeutics, contrast agents, targeting moieties, and magnetic particles to create multifunctional microrobotic platforms with accurate maneuverability for targeted GI drug

delivery. Overall, extremophile-based biohybrids offer considerable promise and open the door for diverse applications in harsh and inhospitable environments that are unsuitable for traditional microrobots.

3.3.4 Experimental Methods

3.3.4.1 Algae culture

The acidophilic algae *Chlamydomonas pitschmannii* (strain CPCC-354 wild-type) were obtained from the Canadian Phycological Culture Centre (CPCC). The algae were transferred from their original medium to modified acid medium (MAM, CPCC) and cultivated at room temperature under cycles of 12 h sunlight and 12 h darkness. The neutrophilic algae *Chlamydomonas reinhardtii* (strain CC-125 wild-type mt+) were obtained from the Chlamydomonas Resource Center. The algae were transferred from the agar plate to tris-acetate-phosphate (TAP) medium (Thermo Fisher Scientific) and cultured under the same conditions.

3.3.4.2 Preparation of dye-conjugated acidophilic algae

Acidophilic algae were transferred from the culture medium to 1× phosphate-buffered saline (PBS, Thermo Fisher Scientific) followed by 3 washes. Next, 10 μg/ml NHS-Cyanine7 (NHS-Cy7, Lumiprobe) was incubated with the algae at 1×10^7 per ml for 1 h at room temperature. After dye conjugation, the modified algae were washed with ultrapure water for the removal of the unreacted dye and resuspended in ultrapure water for further use. Static acidophilic algae were prepared through the dropwise addition of 1 M acetic acid (Sigma Aldrich) to active acidophilic

algae. After 20 seconds, the pH value of the mixture was quickly neutralized to 7 by the addition of 1 M sodium hydroxide (Sigma Aldrich), and the algae were transferred into PBS. Then, the Cy7 dye conjugation was performed following a similar method as above. Neutrophilic algae were suspended in 10 mM 4-(2-hydroxyethyl)-1-piperazineethanesulfonic acid buffer (HEPES, Thermo Fisher Scientific) to complete the Cy7 conjugation.

3.3.4.3 Synthesis of fluorescent dye-loaded nanoparticles

The synthesis of polymeric nanoparticles was based on a previously reported nanoprecipitation method[51]. Briefly, 0.67 dl/g carboxyl-terminated 50:50 poly(lactic-*co*-glycolic) acid (PLGA, LACTEL Absorbable Polymers) at 20 mg/ml in 1 ml of acetone was added into 1 ml of 10 mM Tris-buffer. To fluorescently label the nanoparticles, 0.1 wt% of 3,3'-dioctadecyloxacarbocyanine perchlorate (DiO, λex/λem = 484 nm/501 nm; Thermo Fisher Scientific) was encapsulated into the PLGA cores. After nanoprecipitation, the organic solvent was evaporated under a vacuum for 1 h. Near-infrared dye-loaded polymeric nanoparticles for in vivo studies were prepared following a similar method by replacing DiO with 1,1'-dioctadecyl-3,3,3',3'-tetramethylindotricarbocyanine iodide (DiR, λex/λem = 748 nm/780 nm; Thermo Fisher Scientific).

3.3.4.4 Preparation of membrane-coated nanoparticles

To prepare the PLGA nanoparticles coated with poly-l-lysine (PLL) (Sigma Aldrich), 10 mg/ml of preformed PLGA nanoparticles in ultrapure water were added dropwise into 1 ml of 0.05%

w/v PLL under 700 rpm stirring for 2 h. Next, 5 washes were used to remove any free polyelectrolyte, and the PLLNP were resuspended in ultrapure water for further use. To characterize the size and zeta potential of the PLGA cores and PLLNP, the samples were tested using a Zetasizer MAL 1267090 (Malvern Panalytical).

Red blood cell (RBC) membrane-coated nanoparticles (RBCNP) were prepared by a cell membrane cloaking technique [50, 51]. RBC membrane was mixed with PLGA cores at a 1:1 weight ratio of membrane protein to PLGA polymer. The mixture was then sonicated using a Fisher Scientific FS30D ultrasonic bath sonicator for 3 min. The RBCNP were isolated by centrifugation for 5 min at 16,100*g* and washed 3 times with ultrapure water. To characterize the size and surface zeta potential of RBCNP, the samples were tested using a Zetasizer MAL 1267090. To characterize the morphology, the samples were deposited onto a carbon-coated 400-mesh copper grid and stained with 1 wt% uranyl acetate (Electron Microscopy Sciences), followed by imaging on a JEOL 1200 EX II transmission electron microscope.

3.3.4.5 Preparation of biohybrid motors

To attach PLLNP, 1×10^7 acidophilic algae were first isolated from MAM and resuspended in ultrapure water. Then, the PLLNP were mixed with algae for 30 min. After nanoparticle attachment, the resulting acido-algae-PLLNP biohybrid motors were washed 3 times and resuspended in ultrapure water.

To conjugate RBCNP onto algae, the acidophilic algae and RBCNP were linked using click chemistry. First, 1×10^7 algae were treated with 20 μM of dibenzocyclooctyne-(polyethylene

glycol)$_4$-N-hydroxysuccinimidyl ester (DBCO-PEG$_4$-NHS, Click Chemistry Tools) for 1 h at room temperature. The RBCNP were incubated with 20 μM of azido-PEG$_4$-NHS (Click Chemistry Tools) for 1 h at room temperature. Both the algae and RBCNP were centrifuged and washed 3 times with ultrapure water to remove the unreacted NHS esters. Then, the modified algae and RBCNP were mixed and vortexed for 4 h to complete the click chemistry reaction. After conjugation, the resulting acido-algae-RBCNP biohybrid motors were separated by centrifugation at 800*g* for 3 min, followed by 3 washes.

3.3.4.6 Binding stability study

To test the binding stability between PLLNP and acidophilic algae after the formation of biohybrid motors, the acido-algae-PLLNP with DiR loading were incubated with two acidic conditions (simulated gastric fluid and HCl at pH 2) for 24 h. The detached PLLNP in the supernatant was removed by centrifugation at 800*g* for 3 min. Before and after incubation, the fluorescence intensity of PLLNP with DiR loading on the algae surface was measured by plate reader. The binding stability of acido-algae-RBCNP was evaluated following the same method.

3.3.4.7 Motion analysis

The speed of acidophilic algae, neutrophilic algae, fluorescein-conjugated algae motors, acido-algae-PLLNP biohybrid motors, and acido-algae-RBCNP biohybrid motors was analyzed in different media: modified acid medium (MAM, pH ~3.5), simulated gastric fluid (SGF, pH ~1.5, RICCA Chemical), simulated intestinal fluid (SIF, pH ~6.5, RICCA Chemical), 1× PBS (pH ~7.4),

ultrapure water, pH-adjusted aqueous solutions (pH from 0 to 11), sulfuric acid (pH ~1.5, Sigma Aldrich), and nitric acid (pH ~1.5, Fisher Scientific). The motion of the acidophilic algae motors was also observed in HCl solution (pH ~1.5, Sigma Aldrich) at 0 h, 1 h, 4 h, 8 h, 24 h, and 72 h at room temperature (22 °C). Movies were captured by a Nikon Eclipse Ti-S/L100 inverted optical brightfield microscope coupled with 10× or 20× objectives and a Hamamatsu digital camera C11440 or by a Sony RX100 V camera on an Invitrogen EVOS FL fluorescence microscope with 20× or 40× objectives. An NIS Element tracking module was used to measure the speed of the motors in different media. To mimic the conditions in the stomach of mice, simulated gastric fluid containing 1 mg/ml of pepsin (Sigma Aldrich) was used to test the influence of enzymes on the motility of acidophilic algae. Speed was measured after incubation for 0 h, 1 h, 2 h, 4 h, and 8 h at body temperature (37 °C).

3.3.4.8 Viability of biohybrid motors

To evaluate the viability of acidophilic algae in solutions with different pH, algae were transferred from MAM to aqueous solutions with pH from 0 to 11 and incubated for 2 h at room temperature (22 °C). After incubation, algae motors were resuspended into 5 μM SYTOX green fluorescent probe (Thermo Fisher Scientific) for 1 h at room temperature (22 °C). The viability of the algae was determined by counting the live/dead ratio using an Invitrogen EVOS FL fluorescence microscope.

3.3.4.9 Characterization of biohybrid motors

To visualize nanoparticle binding on the surface of the algae, PLGA cores were loaded beforehand with the fluorescent dye DiO. An Invitrogen EVOS FL microscope was used to capture the autofluorescence of algae chloroplasts in the Cy5 channel and DiO-encapsulated nanoparticles in the GFP channel. To further confirm the morphology of the acido-algae-PLLNP and acido-algae-RBCNP biohybrid motors, SEM imaging was performed. Briefly, the biohybrid motors were fixed with a 2.5% glutaraldehyde solution (Sigma Aldrich) overnight at 4 °C, followed by washing in ultrapure water. The samples were then sputtered with palladium for imaging on a Zeiss Sigma 500 SEM instrument with an accelerating voltage of 3 kV.

3.3.4.10 Animal care

Mice were housed in an animal facility at the University of California San Diego (UCSD) under federal, state, local, and National Institutes of Health (NIH) guidelines. Mice were maintained in standard housing with cycles of 12 h light and 12 h dark, ambient temperature, and normal humidity. All animal experiments were performed in accordance with NIH guidelines and approved by the Institutional Animal Care and Use Committee (IACUC) of UCSD.

3.3.4.11 Ex vivo GI tract retention study

To study GI tract distribution and retention, 8-week-old male CD-1 mice (Charles River Laboratories) were orally administered with Cy7-conjugated acidophilic algae, Cy7-conjugated static acidophilic algae, or Cy7-conjugated neutrophilic algae in 500 µl of PBS at a concentration of 1×10^7 per ml. At the predetermined time points (0.5 h, 2 h, 5 h, 10 h, and 24 h), the mice were

euthanized, and their GI tracts were excised for analysis. To evaluate the performance of the biohybrid motors in vivo, the mice were orally administered with acido-algae-PLLNP, PLLNP, acido-algae-RBCNP or RBCNP. At predetermined time points (2 h, 5 h, and 10 h), the mice were euthanized, and their GI tracts were excised for analysis. Fluorescent ex vivo GI images were obtained with the Xenogen IVIS 200 system.

3.3.4.12 In vivo safety studies

8-week-old male CD-1 mice were euthanized at 24 h after oral administration of algae motors in 500 μl of PBS at a concentration of 1×10^7 per ml. For the comprehensive chemistry panel, aliquots of blood were allowed to coagulate, and the serum was collected by centrifugation. To obtain blood cell counts, whole blood was collected into potassium EDTA collection tubes (Sarstedt). Analyses were conducted by the UCSD Animal Care Program Diagnostic Services Laboratory. To perform the histological analysis, different portions of the GI tract and major organs were sectioned and stained with H&E (Leica Biosystems), followed by imaging using a Hamamatsu Nanozoomer 2.0-HT slide scanning system.

3.3.5 References

[1] G.Z. Yang, J. Bellingham, P.E. Dupont, P. Fischer, L. Floridi, R. Full, N. Jacobstein, V. Kumar, M. McNutt, R. Merrifield, B.J. Nelson, B. Scassellati, M. Taddeo, R. Taylor, M. Veloso, Z.L. Wang, R. Wood, The grand challenges of Science Robotics, Sci Robot 3(14) (2018).

[2] K.L. Smith, A.D. Sherman, P.R. McGill, R.G. Henthorn, J. Ferreira, T.P. Connolly, C.L. Huffard, Abyssal Benthic Rover, an autonomous vehicle for long-term monitoring of deep-ocean processes, Sci Robot 6(60) (2021).

[3] H. Singh, T. Maksym, J. Wilkinson, G. Williams, Inexpensive, small AUVs for studying ice-covered polar environments, Sci Robot 2(7) (2017).

[4] J. Dupeyroux, J.R. Serres, S. Viollet, AntBot: A six-legged walking robot able to home like desert ants in outdoor environments, Sci Robot 4(27) (2019).

[5] A. Ghosh, P. Fischer, Controlled Propulsion of Artificial Magnetic Nanostructured Propellers, Nano Lett 9(6) (2009) 2243-2245.

[6] L. Zhang, J.J. Abbott, L.X. Dong, B.E. Kratochvil, D. Bell, B.J. Nelson, Artificial bacterial flagella: Fabrication and magnetic control, Appl Phys Lett 94(6) (2009).

[7] B.H. Dai, J.Z. Wang, Z. Xiong, X.J. Zhan, W. Dai, C.C. Li, S.P. Feng, J.Y. Tang, Programmable artificial phototactic microswimmer, Nat Nanotechnol 11(12) (2016) 1087-1092.

[8] M. Xuan, Z. Wu, J. Shao, L. Dai, T. Si, Q. He, Near Infrared Light-Powered Janus Mesoporous Silica Nanoparticle Motors, J Am Chem Soc 138(20) (2016) 6492-7.

[9] W. Wang, S.X. Li, L. Mair, S. Ahmed, T.J. Huang, T.E. Mallouk, Acoustic Propulsion of Nanorod Motors Inside Living Cells, Angew Chem Int Edit 53(12) (2014) 3201-3204.

[10] A.A. Solovev, Y.F. Mei, E.B. Urena, G.S. Huang, O.G. Schmidt, Catalytic Microtubular Jet Engines Self-Propelled by Accumulated Gas Bubbles, Small 5(14) (2009) 1688-1692.

[11] W.F. Paxton, K.C. Kistler, C.C. Olmeda, A. Sen, S.K. St Angelo, Y.Y. Cao, T.E. Mallouk, P.E. Lammert, V.H. Crespi, Catalytic nanomotors: Autonomous movement of striped nanorods, Journal of the American Chemical Society 126(41) (2004) 13424-13431.

[12] W. Gao, S. Sattayasamitsathit, J. Orozco, J. Wang, Highly Efficient Catalytic Microengines: Template Electrosynthesis of Polyaniline/Platinum Microtubes, Journal of the American Chemical Society 133(31) (2011) 11862-11864.

[13] X. Ma, A. Jannasch, U.R. Albrecht, K. Hahn, A. Miguel-Lopez, E. Schaffer, S. Sanchez, Enzyme-Powered Hollow Mesoporous Janus Nanomotors, Nano Lett 15(10) (2015) 7043-7050.

[14] W. Gao, A. Pei, J. Wang, Water-Driven Micromotors, Acs Nano 6(9) (2012) 8432-8438.

[15] J. Wang, Nanomachines: fundamentals and applications, (Wiley-VCH, Weinheim, 2013).

[16] M. Medina-Sanchez, L. Schwarz, A.K. Meyer, F. Hebenstreit, O.G. Schmidt, Cellular Cargo

Delivery: Toward Assisted Fertilization by Sperm-Carrying Micromotors, Nano Lett 16(1) (2016) 555-561.

[17] D.B. Weibel, P. Garstecki, D. Ryan, W.R. Diluzio, M. Mayer, J.E. Seto, G.M. Whitesides, Microoxen: Microorganisms to move microscale loads, P Natl Acad Sci USA 102(34) (2005) 11963-11967.

[18] Y. Alapan, O. Yasa, O. Schauer, J. Giltinan, A.F. Tabak, V. Sourjik, M. Sitti, Soft erythrocyte-based bacterial microswimmers for cargo delivery, Sci Robot 3(17) (2018).

[19] O. Felfoul, M. Mohammadi, S. Taherkhani, D. de Lanauze, Y.Z. Xu, D. Loghin, S. Essa, S. Jancik, D. Houle, M. Lafleur, L. Gaboury, M. Tabrizian, N. Kaou, M. Atkin, T. Vuong, G. Batist, N. Beauchemin, D. Radzioch, S. Martel, Magneto-aerotactic bacteria deliver drug-containing nanoliposomes to tumour hypoxic regions, Nat Nanotechnol 11(11) (2016) 941-947.

[20] F.Y. Zhang, Z.X. Li, L. Yin, Q.Z. Zhang, N. Askarinam, R. Mundaca-Uribe, F. Tehrani, E. Karshalev, W.W. Gao, L.F. Zhang, J. Wang, ACE2 Receptor-Modified Algae-Based Microrobot for Removal of SARS-CoV-2 in Wastewater, Journal of the American Chemical Society 143(31) (2021) 12194-12201.

[21] B.E.F. de Avila, P. Angsantikul, J.X. Li, W. Gao, L.F. Zhang, J. Wang, Micromotors Go In Vivo: From Test Tubes to Live Animals, Adv Funct Mater 28(25) (2018).

[22] Y. Alapan, U. Bozuyuk, P. Erkoc, A.C. Karacakol, M. Sitti, Multifunctional surface microrollers for targeted cargo delivery in physiological blood flow, Sci Robot 5(42) (2020).

[23] H.Y. Zhang, Z.S. Li, C.Y. Gao, X.J. Fan, Y.X. Pang, T.L. Li, Z.G. Wu, H. Xie, Q. He, Dual-responsive biohybrid neutrobots for active target delivery, Sci Robot 6(52) (2021).

[24] Z.G. Wu, J. Troll, H.H. Jeong, Q. Wei, M. Stang, F. Ziemssen, Z.G. Wang, M.D. Dong, S. Schnichels, T. Qiu, P. Fischer, A swarm of slippery micropropellers penetrates the vitreous body of the eye, Sci Adv 4(11) (2018).

[25] B. Wang, K.F. Chan, K. Yuan, Q.Q. Wang, X.F. Xia, L.D. Yang, H. Ko, Y.X.J. Wang, J.J.Y. Sung, P.W.Y. Chiu, L. Zhang, Endoscopy-assisted magnetic navigation of biohybrid soft microrobots with rapid endoluminal delivery and imaging, Sci Robot 6(52) (2021).

[26] F.Y. Zhang, J. Zhuang, Z.X. Li, H. Gong, B.E.F. de Avila, Y. Duan, Q.Z. Zhang, J.R. Zhou, L. Yin, E. Karshalev, W.W. Gao, V. Nizet, R.H. Fang, L.F. Zhang, J. Wang, Nanoparticle-modified microrobots for in vivo antibiotic delivery to treat acute bacterial pneumonia, Nat Mater 21(11) (2022) 1324-+.

[27] R. Mundaca-Uribe, E. Karshalev, B.E.F. de Avila, X.L. Wei, B. Nguyen, I. Litvan, R.H. Fang, L.F. Zhang, J. Wang, A Microstirring Pill Enhances Bioavailability of Orally Administered Drugs, Adv Sci 8(12) (2021).

[28] F.Y. Zhang, Z.X. Li, Y. Duan, A. Abbas, R. Mundaca-Uribe, L. Yin, H. Luan, W.W. Gao, R.H. Fang, L.F. Zhang, J. Wang, Gastrointestinal tract drug delivery using algae motors embedded in a degradable capsule, Sci Robot 7(70) (2022).

[29] J.N. Chu, G. Traverso, Foundations of gastrointestinal-based drug delivery and future developments, Nat Rev Gastro Hepat 19(4) (2022) 219-238.

[30] A.M. Bellinger, M. Jafari, T.M. Grant, S.Y. Zhang, H.C. Slater, E.A. Wenger, S. Mo, Y.A.L. Lee, H. Mazdiyasni, L. Kogan, R. Barman, C. Cleveland, L. Booth, T. Bensel, D. Minahan, H.M. Hurowitz, T. Tai, J. Daily, B. Nikolic, L. Wood, P.A. Eckhoff, R. Langer, G. Traverso, Oral, ultra-long-lasting drug delivery: Application toward malaria elimination goals, Sci Transl Med 8(365) (2016).

[31] A. Abramson, E. Caffarel-Salvador, M. Khang, D. Dellal, D. Silverstein, Y. Gao, M.R. Frederiksen, A. Vegge, F. Hubalek, J.J. Water, A.V. Friderichsen, J. Fels, R.K. Kirk, C. Cleveland, J. Collins, S. Tamang, A. Hayward, T. Landh, S.T. Buckley, N. Roxhed, U. Rahbek, R. Langer, G. Traverso, An ingestible self-orienting system for oral delivery of macromolecules, Science 363(6427) (2019) 611-+.

[32] A. Abramson, M.R. Frederiksen, A. Vegge, B. Jensen, M. Poulsen, B. Mouridsen, M.O. Jespersen, R.K. Kirk, J. Windum, F. Hubalek, J.J. Water, J. Fels, S.B. Gunnarsson, A. Bohr, E.M. Straarup, M.W.H. Ley, X.Y. Lu, J. Wainer, J. Collins, S. Tamang, K. Ishida, A. Hayward, P. Herskind, S.T. Buckley, N. Roxhed, R. Langer, U. Rahbek, G. Traverso, Oral delivery of systemic monoclonal antibodies, peptides and small molecules using gastric auto-injectors, Nat Biotechnol 40(1) (2022) 103-+.

[33] D. Walker, B.T. Kasdorf, H.H. Jeong, O. Lieleg, P. Fischer, Enzymatically active biomimetic micropropellers for the penetration of mucin gels, Sci Adv 1(11) (2015).

[34] W. Gao, M. D'Agostino, V. Garcia-Gradilla, J. Orozco, J. Wang, Multi-Fuel Driven Janus Micromotors, Small 9(3) (2013) 467-471.

[35] B.E.F. de Avila, P. Angsantikul, J.X. Li, M.A. Lopez-Ramirez, D.E. Ramirez-Herrera, S. Thamphiwatana, C.R. Chen, J. Delezuk, R. Samakapiruk, V. Ramez, M. Obonyo, L.F. Zhang, J. Wang, Micromotor-enabled active drug delivery for in vivo treatment of stomach infection (vol 8, 272, 2017), Nat Commun 8 (2017).

[36] W. Gao, R.F. Dong, S. Thamphiwatana, J.X. Li, W.W. Gao, L.F. Zhang, J. Wang, Artificial Micromotors in the Mouse's Stomach: A Step toward in Vivo Use of Synthetic Motors, Acs Nano 9(1) (2015) 117-123.

[37] N. Merino, H.S. Aronson, D.P. Bojanova, J. Feyhl-Buska, M.L. Wong, S. Zhang, D. Giovannelli, Living at the Extremes: Extremophiles and the Limits of Life in a Planetary Context (vol 10, pg 780, 2019), Front Microbiol 10 (2019).

[38] S. Hirooka, Y. Hirose, Y. Kanesaki, S. Higuchi, T. Fujiwara, R. Onuma, A. Era, R. Ohbayashi, A. Uzuka, H. Nozaki, H. Yoshikawa, S.Y. Miyagishima, Acidophilic green algal genome provides insights into adaptation to an acidic environment, P Natl Acad Sci USA 114(39) (2017) E8304-E8313.

[39] I. Nancucheo, D.B. Johnson, Acidophilic algae isolated from mine-impacted environments and their roles in sustaining heterotrophic acidophiles, Front Microbiol 3 (2012).

[40] W. Gross, Ecophysiology of algae living in highly acidic environments, Hydrobiologia 433(1-3) (2000) 31-37.

[41] A.P. Dean, A. Hartley, O.A. McIntosh, A. Smith, H.K. Feord, N.H. Holmberg, T. King, E. Yardley, K.N. White, J.K. Pittman, Metabolic adaptation of a Chlamydomonas acidophila strain isolated from acid mine drainage ponds with low eukaryotic diversity, Sci Total Environ 647 (2019) 75-87.

[42] M.M. Olaveson, P.M. Stokes, Responses of the Acidophilic Alga Euglena-Mutabilis (Euglenophyceae) to Carbon Enrichment at Ph 3, J Phycol 25(3) (1989) 529-539.

[43] O. Yasa, P. Erkoc, Y. Alapan, M. Sitti, Microalga-Powered Microswimmers toward Active Cargo Delivery, Adv Mater 30(45) (2018).

[44] L.M. Ensign, R. Cone, J. Hanes, Oral drug delivery with polymeric nanoparticles: The gastrointestinal mucus barriers, Adv Drug Deliver Rev 64(6) (2012) 557-570.

[45] A. Brodkorb, L. Egger, M. Alminger, P. Alvito, R. Assuncao, S. Ballance, T. Bohn, C. Bourlieu-Lacanal, R. Boutrou, F. Carriere, A. Clemente, M. Corredig, D. Dupont, C. Dufour, C. Edwards, M. Golding, S. Karakaya, B. Kirkhus, S. Le Feunteun, U. Lesmes, A. Macierzanka, A.R. Mackie, C. Martins, S. Marze, D.J. McClements, O. Menard, M. Minekus, R. Portmann, C.N. Santos, I. Souchon, R.P. Singh, G.E. Vegarud, M.S.J. Wickham, W. Weitschies, I. Recio, INFOGEST static in vitro simulation of gastrointestinal food digestion, Nat Protoc 14(4) (2019) 991-1014.

[46] Y. Inoue, K. Izawa, S. Kiryu, A. Tojo, K. Ohtomo, Diet and abdominal autofluorescence detected by in vivo fluorescence imaging of living mice, Mol Imaging 7(1) (2008) 21-27.

[47] N. Kamaly, Z.Y. Xiao, P.M. Valencia, A.F. Radovic-Moreno, O.C. Farokhzad, Targeted polymeric therapeutic nanoparticles: design, development and clinical translation, Chem Soc Rev 41(7) (2012) 2971-3010.

[48] S. Honary, F. Zahir, Effect of Zeta Potential on the Properties of Nano-Drug Delivery Systems - A Review (Part 1), Trop J Pharm Res 12(2) (2013) 255-264.

[49] X.L. Wei, M. Beltran-Gastelum, E. Karshalev, B.E.F. de Avila, J.R. Zhou, D.N. Ran, P. Angsantikul, R.H. Fang, J. Wang, L.F. Zhang, Biomimetic Micromotor Enables Active Delivery of Antigens for Oral Vaccination, Nano Lett 19(3) (2019) 1914-1921.

[50] R.H. Fang, A.V. Kroll, W.W. Gao, L.F. Zhang, Cell Membrane Coating Nanotechnology, Adv Mater 30(23) (2018).

[51] J.A. Copp, R.H. Fang, B.T. Luk, C.M.J. Hu, W.W. Gao, K. Zhang, L.F. Zhang, Clearance of pathological antibodies using biomimetic nanoparticles, P Natl Acad Sci USA 111(37) (2014) 13481-13486.

[52] Q.Y. Hu, W.J. Sun, J.Q. Wang, H.T. Ruan, X.D. Zhang, Y.Q. Ye, S. Shen, C. Wang, W.Y. Lu, K. Cheng, G. Dotti, J.F. Zeidner, J. Wang, Z. Gu, Conjugation of haematopoietic stem cells and platelets decorated with anti-PD-1 antibodies augments anti-leukaemia efficacy, Nat Biomed Eng 2(11) (2018) 831-840.

[53] S. Hellmig, F. Von Schoning, C. Gadow, S. Katsoulis, J. Hedderich, U.R. Folsch, E. Stuber, Gastric emptying time of fluids and solids in healthy subjects determined by 13C breath tests: influence of age, sex and body mass index, J Gastroenterol Hepatol 21(12) (2006) 1832-8.

[54] H.K. Makadia, S.J. Siegel, Poly Lactic-co-Glycolic Acid (PLGA) as Biodegradable Controlled Drug Delivery Carrier, Polymers-Basel 3(3) (2011) 1377-1397.

[55] J.M. Hyman, E.I. Geihe, B.M. Trantow, B. Parvin, P.A. Wender, A molecular method for the delivery of small molecules and proteins across the cell wall of algae using molecular transporters, P Natl Acad Sci USA 109(33) (2012) 13225-13230.

[56] C. Lautenschlager, C. Schmidt, D. Fischer, A. Stallmach, Drug delivery strategies in the therapy of inflammatory bowel disease, Adv Drug Deliver Rev 71 (2014) 58-76.

The third portion of Chapter 3, in full, is a reprint of the material as it appears in *Science Advances*, 2022 by Fangyu Zhang, Zhengxing Li, Yaou Duan, Hao Luan, Zhongyuan Guo, Chuanrui Chen, Mingyao Xu, Weiwei Gao, Ronnie H. Fang, Liangfang Zhang, and Joseph Wang. The dissertation author was the co-primary investigator and co-author of this paper.

Chapter 4

Extending the *In Vivo* Residence Time of Macrophage Membrane Coated Nanoparticles Through Genetic Modification

4.1 Introduction

In recent years, there has been a surge of interest in the development of cell membrane-based nanomaterials, especially cell membrane-coated nanoparticles, for biomedical applications due to their cell-mimicking properties [1, 2]. Initially, researchers began by using the membrane of red blood cells as a coating, but the approach has since expanded to include membranes from various cell types [3, 4]. Among these nanoparticles, those coated with macrophage membrane, referred to as "MΦ-NPs", have proven particularly versatile in treating a range of diseases [5]. Similar to macrophage cells, MΦ-NPs have the ability to simultaneously absorb endotoxins and proinflammatory cytokines, making them effective in managing sepsis caused by bacterial infection and orthotopic liver transplantation [6, 7]. MΦ-NPs also inherit the complex bioactivity of their source cells in conditions such as cancer, atherosclerosis, and infection, enabling them to deliver drug payloads to tumors, atheromatous plaques, and bacteria [8-10]. Like macrophages, MΦ-NPs can interact with inflammatory enzymes such as phospholipase A2. In a recent study, these nanoparticles acted as sacrificial targets for phospholipase A2 and reduced the severity of experimental pancreatitis [11]. Additionally, MΦ-NPs display the same receptors as the source cells that viruses such as SARS-CoV-2 rely on for cellular entry, allowing them to inhibit SARS-CoV-2 infectivity [12, 13]. Collectively, these findings illustrate the promising clinical potential of MΦ-NPs.

Although nanoparticles are often opsonized in the bloodstream and cleared quickly by the mononuclear phagocytic system [14, 15], cell membrane-coated nanoparticles have demonstrated considerable potential in extending systemic circulation lifetime because of the unique properties of natural cell membrane coating [3, 16]. Nonetheless, enhancing *in vivo* residence time is always desirable for certain applications such as biological neutralization and targeted drug delivery. Therefore, developing strategies to further increase the residence time of cell membrane-based

nanomaterials would be beneficial. In this work, we report on the use of a genetic engineering approach to modifying MΦ-NPs for prolonged *in vivo* residence time. To achieve this goal, we first engineer THP-1 cells, a human leukemia monocytic cell line, to express proline-alanine-serine (PAS) peptide sequences on the membrane through lentiviral transduction (**Figure 4.1**). PAS polypeptides are characterized by their high solubility and lack of charge, making them versatile biological polymers for cell membrane functionalization [17, 18]. Modifying cell membrane with PAS peptides has been demonstrated using HEK293 cells, leading to extended circulation times [19]. Additionally, PAS sequences exhibit high biodegradability, primarily accumulated in the liver, and demonstrate minimal toxicity and immunogenicity. While there are other approaches to functionalizing cell membrane, we focus on genetic modification because it allows for the expression of specific molecules on sensitive cells, which may be incompatible with harsh reaction conditions involved in other approaches. Moreover, genetic modification enables the generation of stable cell lines and avoids repetitive chemical modifications, leading to minimal variations. This is particularly attractive for large-scale production and future clinical translation of the technology.

After genetically modifying MΦ cell membrane with PAS peptides, we extracted their membrane and coat it onto polymeric cores made of poly(lactic-*co*-glycolic acid) (PLGA). The resulting nanoparticles (denoted as "PAS-MΦ-NPs") exhibited enhanced immune evading capabilities while retaining the natural scavenging ability of MΦ membrane against lipopolysaccharides (LPS). *In vitro* experiments demonstrated that PAS-MΦ-NPs significantly reduced protein adsorption and internalization by MΦ cells compared to wild-type MΦ membrane-coated nanoparticles (denoted as "WT-MΦ-NPs"). In mice, the anti-opsonization property of PAS-MΦ-NPs resulted in a notable increase in systemic circulation half-life and a decrease of alveolar MΦ uptake upon intratracheal administration. This prolonged residence time contributed to enhanced therapeutic efficacy of the nanoparticles. Notably, in mouse models of LPS-induced lung

inflammation and sublethal endotoxemia, PAS-MΦ-NPs exhibited the highest inhibition of LPS-induced inflammation. Overall, this study demonstrates the practicality of genetic modification of cell membranes as an approach to prolonging the *in vivo* residence time of MΦ-NP, leading to improved therapeutic outcomes.

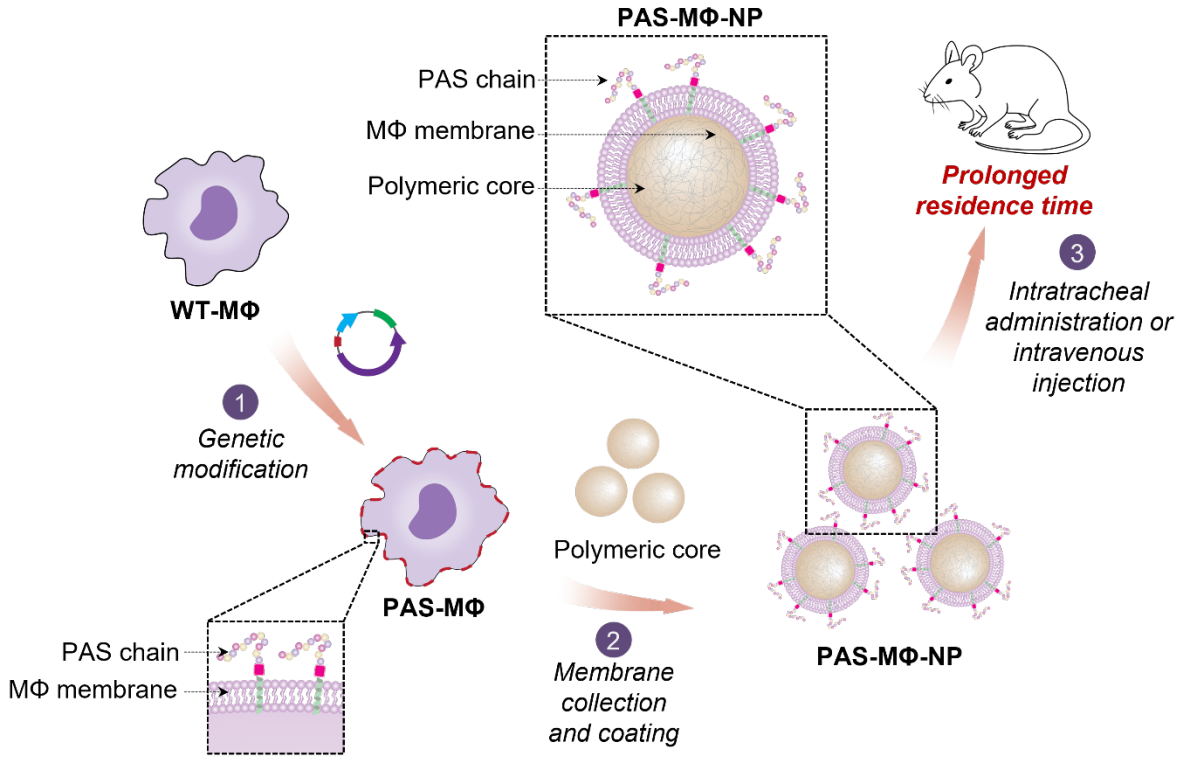

Figure 4.1 Schematic illustration of genetically modified macrophage membrane-coated nanoparticles. Wild-type macrophages (WT-MΦs) are genetically modified to express proline-alanine-serine (PAS) peptide chains on the cell membrane. The membrane of the PAS-expressed MΦs (PAS-MΦs) is then derived and coated onto polymeric nanoparticle cores, forming PAS-MΦ membrane-coated nanoparticles (PAS-MΦ-NPs). These nanoparticles show prolonged residence times when injected intravenously or administered intratracheally into mice.

4.2 Results and Discussion

In the study, we first constructed a fusion protein plasmid containing three components: *N*-terminal cell surface secretion signal Igk leader, PAS-mCherry, and a C-terminal transmembrane anchor domain from platelet-derived growth factor receptor protein (PDGFR) [19, 20]. Genetically expressing mCherry is widely used to label various cells, including macrophages, without

alternating their intrinsic properties [21-23]. We then used lentivirus to transduce THP-1 cells to express the PAS-mCherry fusion proteins on the cell surface [24, 25]. After the transduction and then puromycin selection, MΦ cells exhibited a prominent mCherry signal (**Figure 4.2A**). When observed under a fluorescence microscope, the mCherry signal was primarily on the cell peripheral, confirming a successful PAS expression on the cell surface. Flow cytometry analysis showed that mCherry expression on the transduced MΦ cells (PAS-MΦs) was 25-fold higher than that of the wild-type MΦs (WT-MΦs, **Figure 4.2B**). We also found that the PAS mRNA expression level in PAS-MΦs elevated significantly (**Figure 4.2C**). However, the PAS-MΦs showed similar levels of key MΦ surface biomarkers as the WT-MΦs, including CD14, CD284, CD126, CD130, CD120, and CD119. This clearly implies that the genetic modification had negligible impact on the native cell surface antigen profile. Notably, transfecting and expressing foreign proteins on macrophage membrane is generally a challenging task. Herein, we used the platelet-derived growth factor receptor (PDGFR) transmembrane anchoring domain to anchor PAS, which showed minimum interference with cellular functions and adequate expression efficiency.

After having established PAS-MΦs, we formulated PAS-MΦ-NPs through a three-step process, including (i) membrane derivation via cell lysis and differential centrifugation, (ii) poly(lactic-*co*-glycolic acid) (PLGA) nanoparticle fabrication by nanoprecipitation, and (iii) membrane coating by sonication [11]. Both PAS-MΦ-NPs and WT-MΦ-NPs showed an increase in hydrodynamic diameter as compared to the uncoated PLGA cores, and the sizes of the two nanoparticles were comparable (**Figure 4.2D**). Their surface zeta potential values were less negative than that of PLGA cores and were also comparable. A similar core-shell morphology was visualized when both nanoparticles were negatively stained with uranyl acetate and examined under transmission electron microscopy (TEM, **Figure 4.2E**). We also suspended PAS-MΦ-NPs and WT-MΦ-NPs in 10% sucrose or 1X PBS solution at 4°C and examined their colloidal stability.

Both nanoparticle formulations maintained their sizes during a 72-h period, indicating good stability when stored in the buffers (**Figure 4.2F**). Together, these characterizations showed that PAS-MΦ-NPs and WT-MΦ-NPs had comparable physicochemical properties.

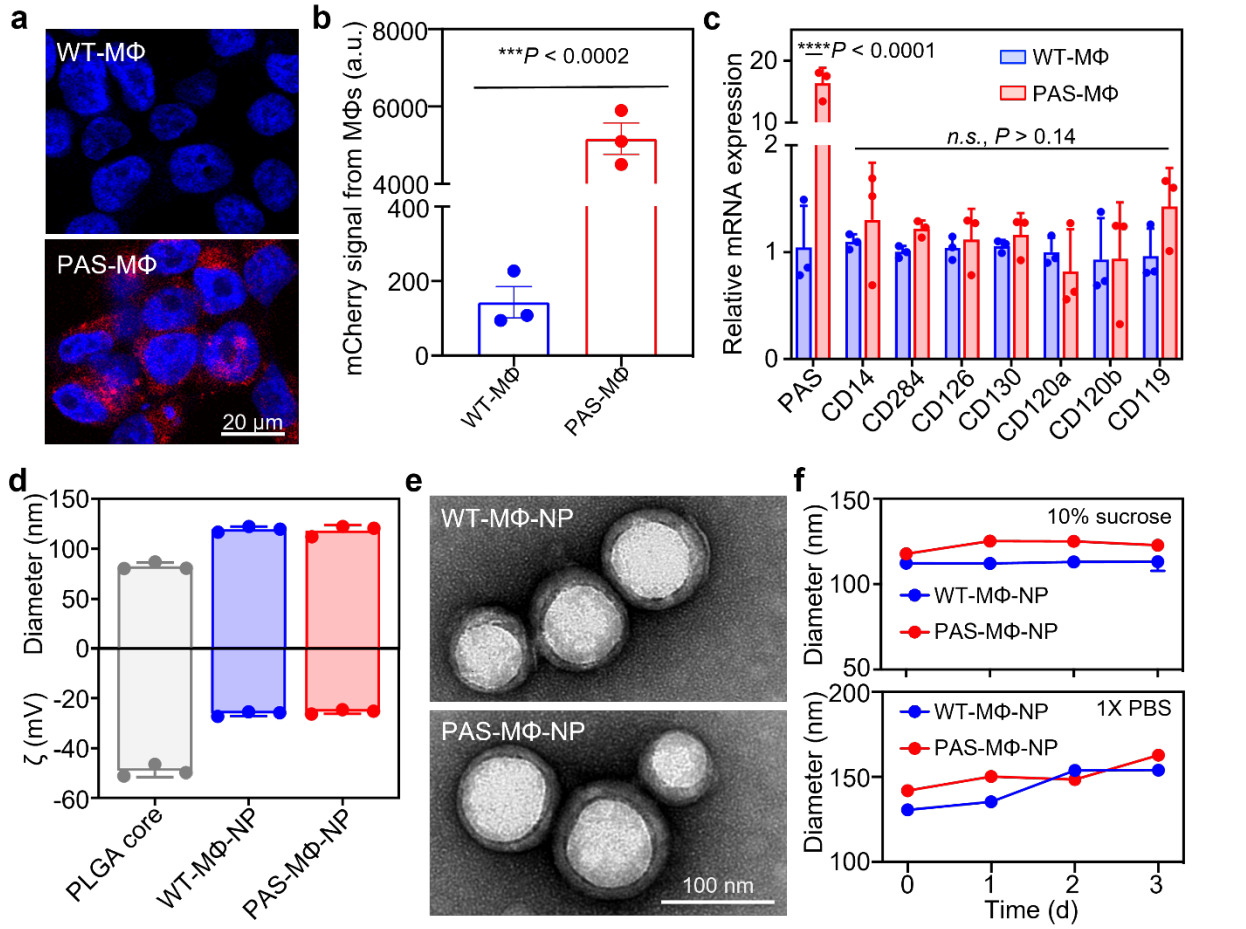

Figure 4.2 Fabrication and characterization of PAS-MΦ-NPs. a) Confocal images of MΦs before and after the transfection with lentivirus expressing PAS-mCherry fusion protein sequences. Nuclei: blue; PAS: red. b) Flow cytometry anaylsis of MΦs before and after the transfection. c) The mRNA expression of PAS-mCherry and other key MΦ markers. d) The average diameter and surface zeta potential of PLGA cores, WT-MΦ-NPs, and PAS-MΦ-NPs measured with dynamic light scattering (DLS). e) Transmission electron microscopy (TEM) images of WT-MΦ-NPs and PAS-MΦ-NPs negatively stained with uranyl acetate. Scale bar = 100 nm. f) The stability of WT-MΦ-NPs and PAS-MΦ-NPs examined over 72 h in 10% sucrose and 1X PBS, respectively. In c, d, and f, n = 3; data are presented as mean ± standard deviation; n.s. = not significant, ***p<0.001, and ****p<0.0001; statistical analysis was performed with unpaired two-tailed t-tests.

Next, we evaluated the effects of PAS modification on nanoparticle opsonization and immune cell uptake *in vitro*. To study protein adsorption, we incubated uncoated PLGA cores, WT-MΦ-NPs, or PAS-MΦ-NPs in a fluorescence-labeled bovine serum albumin (BSA) solution. After 1 h of incubation, we observed a high fluorescence intensity from uncoated PLGA cores, indicating rapid BSA adsorption (**Figure 4.3A**). In contrast, the fluorescence from WT-MΦ-NPs was significantly lower, demonstrating that the cell membrane coating effectively shielded the core and reduced protein adsorption. The fluorescence from PAS-MΦ-NPs was the lowest among the three samples, suggesting that PAS modification further inhibited BSA binding to the nanoparticle surface. To evaluate the effect of PAS modification on MΦ uptake of the nanoparticles, we labeled both PAS-MΦ-NPs and WT-MΦ-NPs with a fluorescent dye and incubated them with J774 cells, a mouse MΦ cell line. After 1 h of incubation, we observed that the signal from cells incubated with PAS-MΦ-NPs was significantly lower than that from the WT-MΦ-NP group (**Figure 4.3B**). We also examined the nanoparticle uptake kinetics by measuring cell fluorescence signals at various timepoints. As shown in **Figure 4.3C**, the fluorescence signal from cells incubated with PAS-MΦ-NPs was much lower than from those incubated with WT-MΦ-NPs at all tested timepoints. These results confirmed the effectiveness of PAS modification in reducing nanoparticle uptake by MΦ cells *in vitro*.

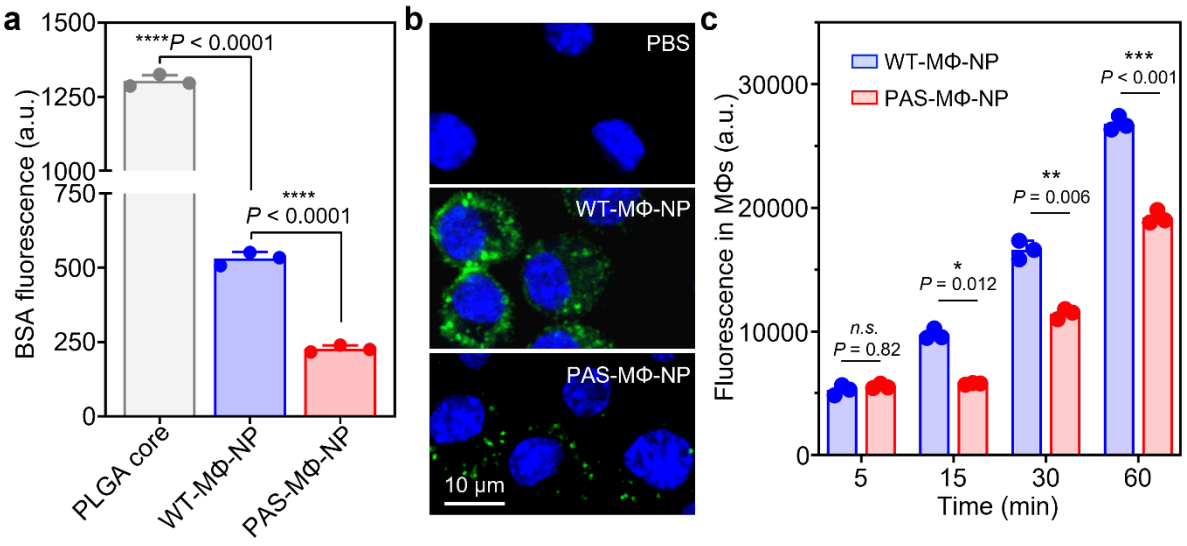

Figure 4.3 *In vitro* suppression of opsonization and MΦ uptake. a) Fluorescence intensity from adsorbed BSA-Alexa 647 on PLGA cores, WT-MΦ-NPs, and PAS-MΦ-NPs. b) Confocal fluorescence microscopic images of MΦs incubated with PBS, WT-MΦ-NPs, and PAS-MΦ-NPs, respectively. Scale bar = 40 μm. c) Mouse J774 uptake of DiO-labeled WT-MΦ-NPs and PAS-MΦ-NPs at various time points. In (a) and (c), n = 3; data are presented as mean ± standard deviation; n.s. = not significant; *p<0.05, **p<0.01, and ***p<0.001; statistical analysis was performed with one-way ANOVA in (a) and two-way ANOVA in (c).

The effect of PAS modification on nanoparticle uptake *in vivo* was also investigated in two settings. First, we administered the nanoparticles into the lungs and examined their uptake by alveolar MΦ cells. Specifically, we administered fluorescent dye-labeled PAS-MΦ-NPs or WT-MΦ-NPs to mice intratracheally. After 24 h, we extracted alveolar MΦ cells from mouse bronchoalveolar lavage fluid and quantified nanoparticle uptakes by measuring cell fluorescence. Under a fluorescence microscope, we observed a much lower fluorescence signal in alveolar MΦ cells of mice treated with PAS-MΦ-NPs than those treated with WT-MΦ-NPs (**Figure 4.4A**). We also quantified fluorescence intensity of alveolar MΦ cells at various timepoints within 24 h after the nanoparticle administration. As shown in **Figure 4.4B**, at 1 h timepoint approximately 35% of alveolar MΦ cells showed a detectable WT-MΦ-NP signal, while only 12% of alveolar MΦ cells showed a detectable PAS-MΦ-NP signal. As time progressed to 24 h, alveolar MΦ cells with a detectable WT-MΦ-NP signal increased to over 83%, while about 61% of the cells showed a detectable PAS-MΦ-NP signal.

Second, we injected fluorescent dye-labeled nanoparticles into the mice through tail veins and examined nanoparticle circulation lifetime in the blood. We collected blood samples at predetermined time points and measured their fluorescence intensity. Figure 4c shows that mice retained a higher level of PAS-MΦ-NPs than WT-MΦ-NPs in blood during the entire test period. At 24 and 48 h time points, we observed 22.3% and 11.2% of PAS-MΦ-NPs remained in the blood, respectively, in contrast to 7.5% and 2.2% of WT-MΦ-NPs. To further illustrate the difference in circulation time between PAS-MΦ-NPs and WT-MΦ-NPs, we fitted the pharmacokinetic data into a two-compartment model and calculated the elimination half-life through the slope of the semilog plot (**Figure 4.4C**, inset) [26, 27]. Consistent with the blood retention results, PAS-MΦ-NPs showed an elimination half-time of approximately 20.8 h, while the half-life of WT-MΦ-NP was about 12.3 h, which translated to 1.7-fold increase in elimination half-life after PAS modification. Notably, the *in vivo* circulation time of cell membrane-coated nanoparticles is much shorter than that of the parent source cells. This significant contrast in circulation duration is likely attributed to the pronounced physicochemical and biological differences between the passively diffusing inert nanoparticles and the actively swimming live cells. They differ greatly in their size, morphology, mechanical modulus, and biological activity. Besides the pharmacokinetic study, we further evaluated the tissue distribution of the nanoparticles at different timepoints post intravenous administration. In the study, the blood and major organs including heart, liver, spleen, lungs, and kidneys from the tested mice were collected at 30 min, 1 h, and 24 h post nanoparticle injection for fluorescence measurements. As shown in **Figure 4.4D**, when analyzing normalized nanoparticle content per gram of tissue, we observed that most nanoparticles were in the liver and spleen, two primary organs for the reticuloendothelial system. A strong fluorescence signal was also detected in the blood. At 24 h, the fluorescence signal in the blood significantly decreased, while the signal in the liver increased accordingly, confirming nanoparticle clearance by the reticuloendothelial system. Notably, the PAS-

MΦ-NP group showed higher blood retention and lower liver uptake throughout the study as compared to the WT-MΦ-NP group. Note that in these in vivo studies, we selected PAS-MΦ-NP and un-MΦ-NP as the two study groups due to the prominent distinction of PAS expression between them, enabling a fair and direct comparison to evaluate the contribution and superiority of PAS expression.

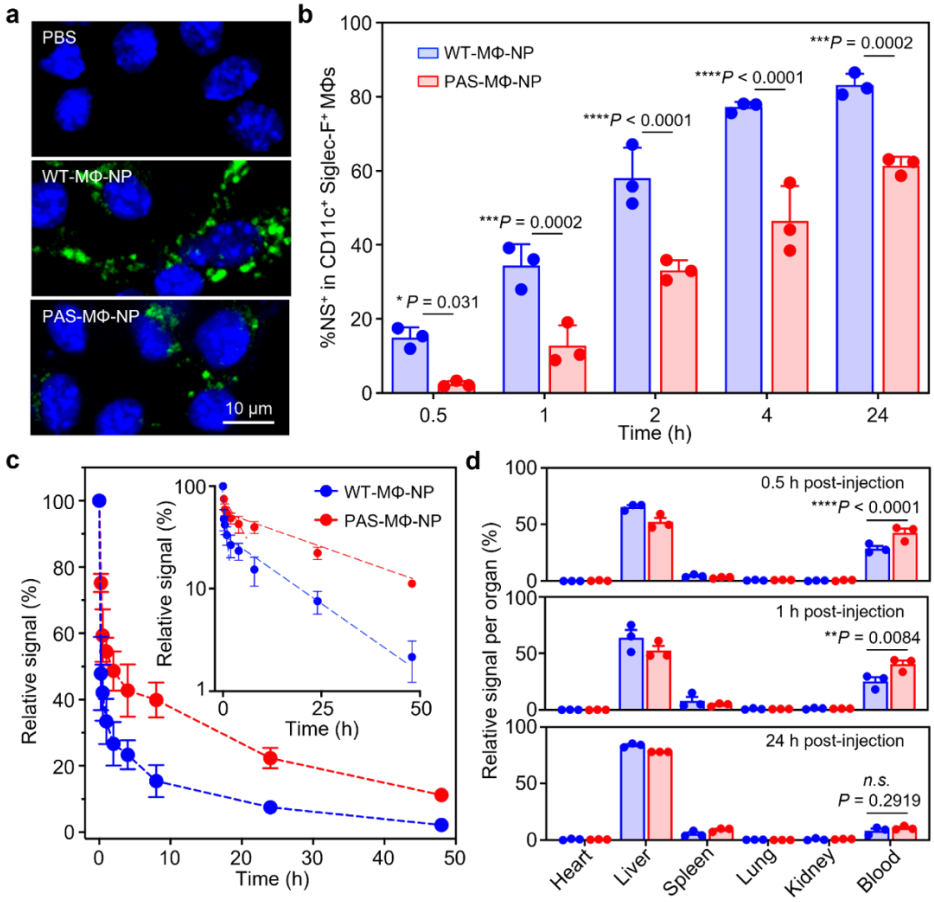

Figure 4.4 *In vivo* reduction of lung alveolar MΦ clearance, pharmacokinetics and biodistribution. a) Confocal fluorescence microscopic images of *in vivo* collected alveolar MΦ cells 24 h after intratracheal administration of the DiO-labeled WT-MΦ-NPs and PAS-MΦ-NPs. b) Flow cytometry quantification of the uptake of WT-MΦ-NPs and PAS-MΦ-NPs in CD11c+Siglec-F+ alveolar MΦs at various time points after intratracheal administration *in vivo* (n = 3; mean ± s.d.). c) *In vivo* circulation kinetics of WT-MΦ-NPs and PAS-MΦ-NPs. Nanoparticles were labeled with DiR and injected intravenously through the tail vein of mice. (n = 3; mean ± s.d.). (Inset) The semilog plot of fluorescence signals at various time points. d) Biodistribution of WT-MΦ-NPs and PAS-MΦ-NPs collected after injecting DiR-labeled nanoparticles intravenously into the mice. At 0.5, 1, and 24 h post-injection, the major organs were collected, weighed, and homogenized for fluorescence quantification (n = 3; mean ± s.d.). Data are presented as mean ± standard deviation; n.s. = not significant; *p<0.05, **p<0.01, ***p<0.001, and ****p<0.0001; statistical analysis was performed with two-way ANOVA in (b) and one-way ANOVA in (d).

After having demonstrated that PAS modification was able to effectively increase nanoparticle residence time *in vivo*, we further examined whether this property could help improve the therapeutic efficacy of PAS-MΦ-NPs. To this end, we first tested nanoparticle efficacy of neutralizing LPS in a mouse model of LPS-induced lung inflammation [6, 28]. In this model, LPS is identified as a pathogen-associated molecular pattern (PAMP) by sentinel immune cells such as monocytes and macrophages [29, 30]. Once inside the lung, MΦ-NPs mimic host cells and use toll-like receptor-4 (TLR-4) and pattern recognition receptor CD14 on the membrane to capture LPS. Such binding interactions prevent host defense reactions and adaptive immune activation [31, 32]. MΦ-NPs can also scavenge inflammatory cytokines through the corresponding cytokine receptors present on macrophage membrane, thereby, inhibiting the cytokine-induced inflammation cascades [6]. In the study, healthy BALB/c mice were administrated with PAS-MΦ-NPs, WT-MΦ-NPs, or PBS (30 μL, 10 mg/kg) intratracheally. One hour later, the mice were intratracheally administered with LPS (30 μL, 400 μg/kg) to induce lung inflammation (**Figure 4.5A**) [33]. After 5 h following LPS administration, we sacrificed the mice and quantified the levels of proinflammatory cytokines in the lung tissue. **Figure 4.5B** shows that comparing to LPS alone group, animals treated with either PAS-MΦ-NPs or WT-MΦ-NPs had significantly lower IL-6 levels, while PAS-MΦ-NP treatment was more effective than WT-MΦ-NP treatment. Similar results were observed for the levels of TNF-α (**Figure 4.5C**) and IL-12p40 (**Figure 4.5D**). Since we have already verified that PAS modification did not affect native membrane antigen profile, the enhanced efficacy of PAS-MΦ-NPs through intratracheal administration was likely attributable to their prolonged retention time in the lungs.

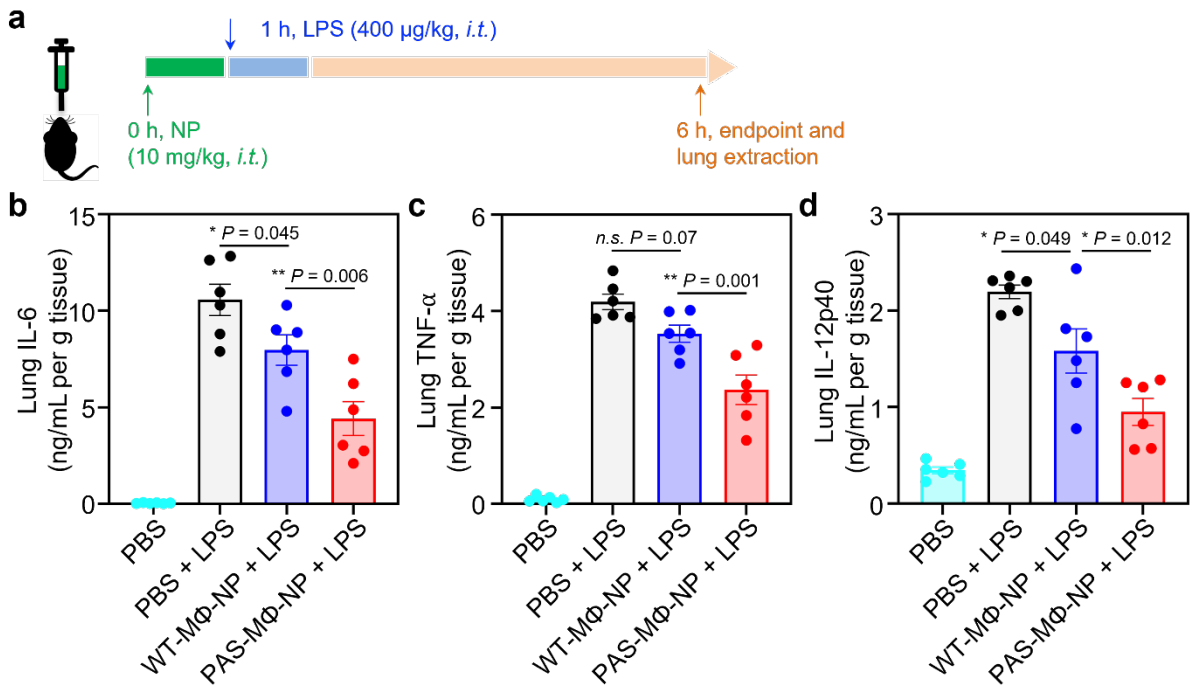

Figure 4.5 PAS-MΦ-NP enhancing local LPS neutralization efficacy in the lungs of an LPS-induced lung inflammation mouse model. a) The study protocol. (b-d) Quantification of inflammatory cytokines, including IL-6 (b), TNF-α (c), and IL-12p40 (d), in the lung tissue of mice intratracheally challenged with LPS alone or LPS with pretreatment of WT-MΦ-NPs or PAS-MΦ-NPs (n = 6; mean ± s.d.). Mice treated with 1X PBS were included as a control group. Data are presented as mean ± standard deviation; n.s. = not significant; *p<0.05, and **p<0.01; statistical analysis was performed with one-way ANOVA.

In another *in vivo* efficacy study, we used a mouse model of LPS-induced sublethal endotoxemia [34]. In the study, we first injected PBS, PAS-MΦ-NPs, or WT-MΦ-NPs (80 mg/kg) into BALB/c mice through tail veins (**Figure 4.6A**). After 0.5 h, the mice were challenged with LPS (5 μg/kg) through tail vein injection to induce sublethal endotoxemia [6]. Serum samples were collected from the mice at predetermined time points, and treatment efficacy was evaluated by quantifying serum levels of proinflammatory cytokines. As shown in **Figure 4.6B**, the LPS challenge in PBS-treated mice led to a rapid increase of serum IL-6 concentration, reaching a maximum at 3 h and then gradually decreasing. When treated with WT-MΦ-NPs, serum IL-6 levels decreased due to the nanoparticle's ability to absorb and neutralize LPS and inflammatory

cytokines. Compared to these two groups, IL-6 levels in mice treated with PAS-MΦ-NPs remained significantly lower throughout the study, indicating a better therapeutic efficacy. LPS challenge also elevated serum levels of TNF-α (**Figure 4.6C**) and IFN-γ (**Figure 4.6D**), reaching a peak at 1 h and 6 h, respectively. Effective treatment efficacy was observed in mice treated with PAS-MΦ-NPs or WT-MΦ-NPs, and PAS-MΦ-NP treatment was much more effective than WT-MΦ-NP treatment. In fact, the TNF-α and IFN-γ levels were near the baseline levels in mice treated with PAS-MΦ-NPs, highlighting the contribution of PAS modification to improving the treatment efficacy. In terms of the *in vivo* fate of LPS-bound and/or cytokine-bound MΦ-NPs, it's likely that they accumulated in the liver and were digested there following the biodistribution pattern observed in Figure 4d. These nanoparticles could also be opsonized during the circulation and thus were taken up and cleared by circulating immune cells.

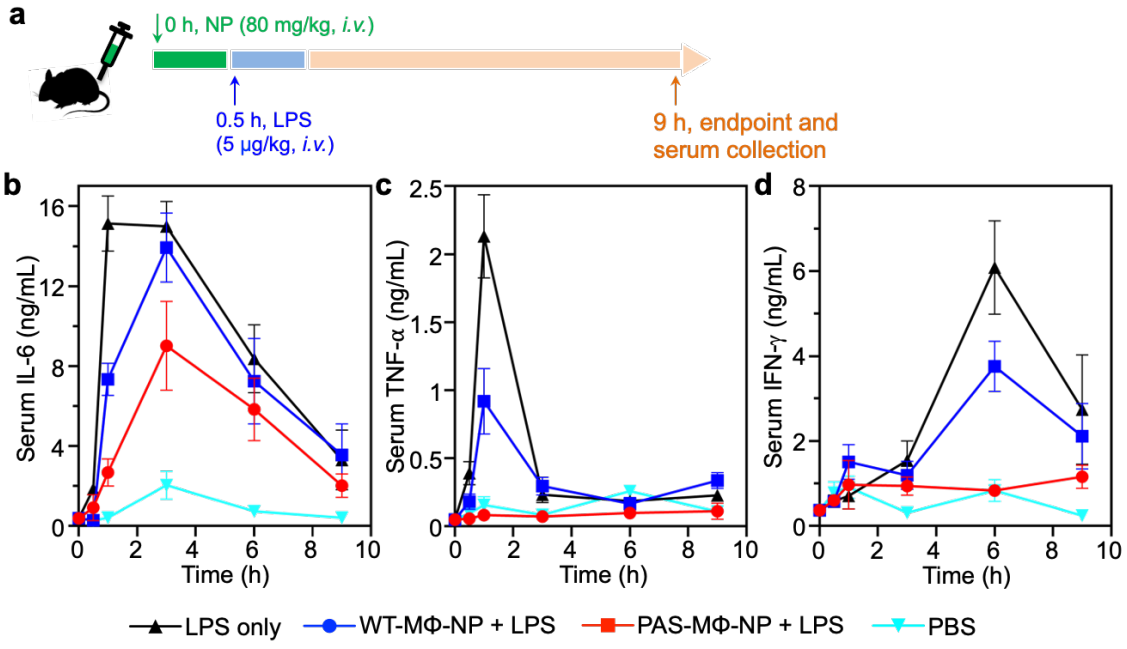

Figure 4.6 PAS-MΦ-NP enhancing systemic LPS neutralization efficacy in the blood of an LPS-induced endotoxemia mouse model. a) The study protocol. b-d) Quantification of serum inflammatory cytokines, including IL-6 (b), TNF-α (c), and IFN-γ (d), after intravenously injecting mice with LPS alone or LPS pretreated with WT-MΦ-NPs or PAS-MΦ-NPs (n = 6; mean ± s.d.). Mice injected with 1x PBS were included as a control group. Statistical analysis was between WT-MΦ-NP and PAS-MΦ-NP, and at 3, 1, and 6 h for IL-6, TNF-α, and IFN-γ, respectively, with unpaired two-tailed *t*-tests.

Finally, we evaluated the acute toxicity of PAS-MΦ-NPs following intravenous administration into mice. After 24 h, we collected blood and major organs from the mice and performed a comprehensive panel of assays. Blood count analysis showed no significant changes in the number of white blood cells, red blood cells, and platelets in mice injected with PAS-MΦ-NPs or WT-MΦ-NPs compared to mice treated with PBS only (**Figure 4.7A**). Moreover, when evaluating the serum metabolic panel, we observed no significant elevation in markers associated with liver or kidney functions in mice injected with either nanoparticle formulations (**Figure 4.7B**). We also collected the major organs of the mice, including the heart, liver, spleen, lungs, and kidneys, sectioned the tissues, and stained the sections with hematoxylin and eosin (H&E) for histopathological analysis (**Figure 4.7C**). We found that the overall structure, integrity, and immune infiltration of tissues in both PAS-MΦ-NP and WT-MΦ-NP treated groups were similar to those of the control mice, suggesting the absence of acute toxicity from these nanoparticles.

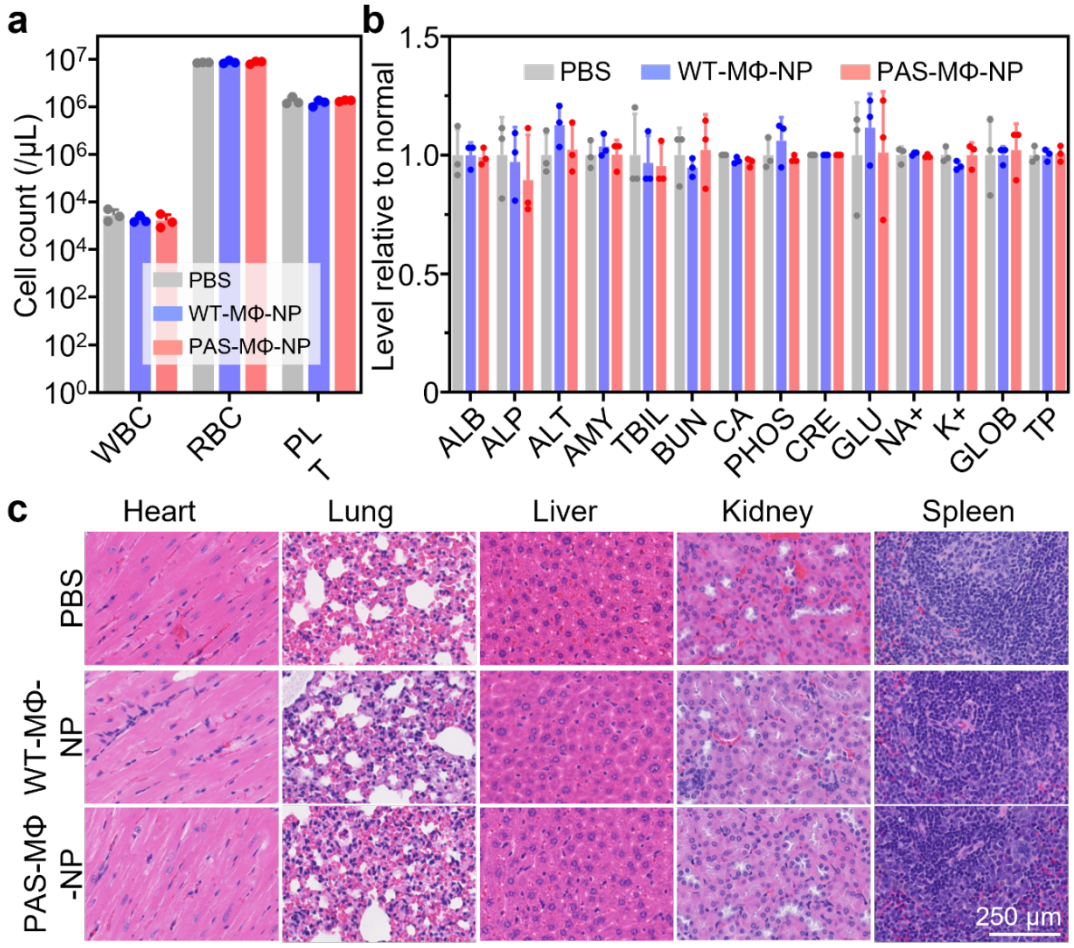

Figure 4.7 ***In vivo*** **safety of PAS-MΦ-NPs**. a) Blood cell counts 24 h after intravenous administration of WT-MΦ-NPs or PAS-MΦ-NPs (n = 3; mean + standard deviation). b) A comprehensive serum chemistry panel performed 24 h after intravenous administration of WT-MΦ-NPs or PAS-MΦ-NPs (n = 3; mean ± standard deviation). ALB, albumin; ALP, alkaline phosphatase; ALT, alanine aminotransferase; AMY, amylase; TBIL, bilirubin; BUN, urea nitrogen; CA, calcium; PHOS, phosphorus; CRE, creatinine; GLU, glucose; NA+, sodium; K+, potassium; GLOB, globulin (calculated); TP, total protein. c) H&E-stained histological sections from major organs 24 h after intravenous administration of WT-MΦ-NPs or PAS-MΦ-NPs. Scale bar = 250 μm.

4.3 Conclusions

In summary, we conducted genetic modifications on MΦ cells to express PAS sequences and utilized the modified cell membrane to create PAS-MΦ-NPs. The genetic modifications had minimal impact on the native cell membrane antigen profile and the physicochemical properties of the nanoparticles. The inclusion of PAS sequences provided additional protection to the

nanoparticles against uptake by MΦ cells *in vitro*. Upon intratracheal administration or intravenous injection to mice, PAS-MΦ-NPs exhibited significantly prolonged residence times compared to WT-MΦ-NPs. This increase in residence time further enhanced the therapeutic efficacy of the nanosparticles in animal models of LPS-induced lung inflammation and LPS-induced systemic endotoxemia. Overall, our study demonstrates that genetic modification of cell membranes represents an effective strategy to enhance *in vivo* residence times of nanoparticles, leading to improved therapeutic efficacy.

For future research, the residence time of PAS-MΦ-NPs can be further improved by controlling the density and length of PAS sequences.[19] The PAS-modified membrane may be hybridized with other types of membranes to enrich the nanoparticle functionality [35]. Additionally, apart from PAS, other emerging peptide amphiphiles can be incorporated into MΦ membranes using the same methodology, expanding the range of functionalities of MΦ-NPs [36, 37]. The genetic modification of MΦ-NPs opens new possibilities for broad applications associated with macrophage membrane coating. The success of genetic modification in MΦ-NPs suggests that a similar approach can be applied to other primary cells currently under active investigation for the development of cell membrane-coated nanoparticles. Moreover, the genetically modified cell membrane can also be used to coat onto other substrates, such as non-spherical cores [38] and cores with low mechanical modulus [39], to further improve the *in vivo* circulation time and biodistribution. With continued efforts, the full potential of cell membrane-coated nanoparticles will be released for broader biomedical applications.

4.4 Experimental Methods

4.4.1 Plasmid construction

To construct the pDisplay-PAS-mCherry plasmid, the complementary DNA (cDNA) sequences encoding the PAS-mCherry fusion protein were first synthesized by the Invitrogen GeneArt Gene Synthesis service (Thermo Fisher Scientific) based on a previously established method [19]. These cDNAs were then subcloned into the pDisplay plasmid (Thermo Fisher Scientific) using restriction enzymes (BamHI and XbaI, New England BioLabs). The resulting sequences encoding the pDispay-PAS-mCherry fusion protein were further subcloned into pLenti-CMV-Puro, a lentiviral transfer plasmid (Addgene), using restriction enzymes (Nhe I and BamH I, New England BioLabs). This construction process yielded the final plasmid of pLenti-Display-PAS-mCherry.

4.4.2 Lentivirus production

The lentivirus was produced according to a previously established protocol [25]. In brief, HEK293T cells (ATCC, CRL-3216) were seeded in a T75 cell culture flask at 50% confluency 12 h before the transfection. The transfer plasmid pLenti-Display-PAS-mCherry was mixed with the packaging plasmids (pMDL:pRev:pMD2.G = 1:1:1 weight ratio) at 1.5:1 weight ratio (transfer plasmid concentration = 4 μg/mL) in 5 mL of Minimum Essential Medium (MEM, Gibco). The plasmids were co-transferred using Lipofectamine 2000 (Thermo Fisher Scientific) into the HEK293T cells according to the manufacturer's protocol. Cells were cultured at 37°C and 5% CO_2 in Dulbecco's Modified Eagle Medium (DMEM, Gibco). After 6 h, the medium was replaced with DMEM containing 10% fetal bovine serum (FBS, Gibco) and 1% penicillin streptomycin (Pen-strep). Culture supernatants containing viral particles were collected 48 and 72 h after the transfection. The cell debris in the supernatants was removed by centrifugation at 800 ×g for 15 min, followed by filtration through 0.45-μm filters (Millipore Sigma). Following the filtration, the viral particles were pelleted with a Lenti-X concentrator (Takara) according to the manufacturer's

protocol and then resuspended in 100 μL 1X PBS. The concentrated virus suspension was stored at -80°C for subsequent uses.

4.4.3 Generation of MΦ cells expressing PAS

THP-1 cells, a human monocytic leukemia cell line, were obtained from American Type Culture Collection (ATCC, TIB-202) and cultured in RPMI 1640 medium supplemented with 10% fetal bovine serum (FBS) and 1% Pen-strep (all from Thermo Fisher Scientific). The cells were maintained at 37°C with 5% CO_2 in a humidity-controlled incubator. To generate MΦ cells expressing PAS, polybrene infection/transfection reagent (Millipore-Sigma) was added to the concentrated lentivirus containing genome encoding pDisplay-PAS-mCherry to a final concentration of 4 μg/mL. Then 100 μL of the mixture was added into each well of a 12-well plate containing 3×10^5 cells/well of THP-1 cells in RPMI 1640 medium supplemented with 10% FBS and 1% Pen-strep. The final volume of each well was 1 mL. Centrifuging the culture plate at 1200 ×g for 30 min facilitated viral transduction. After 48 h of the transduction, the culture media was replaced with RPMI 1640 medium supplemented with 10% FBS, 1% penicillin-streptomycin, and puromycin (10μg/mL, Invivogen). After 1 week of culture, monoclonal selection was conducted by plating the puromycin-selected cells in 96-well plates at an average density of 0.5 cell/well. The plate was cultured for 2 weeks in RPMI 1640 medium supplemented with 10% FBS and 1% Pen-strep. Then cells in each well were measured with flow cytometry (BD FACS Aria II Cell Sorter) to quantify PAS-mCherry expression levels. The clone with the highest expression was selected and expanded.

4.4.4 Quantitative reverse transcription PCR (qRT-PCR) measurement

RNA was extracted from 1×10^6 THP-1 or PAS-expressing THP-1 cells using a Direct-zol RNA Miniprep kit (Zymo Research) according to the manufacturer's protocol. The RNA was reverse transcribed into cDNA using the ProtoScript First Strand cDNA Synthesis kit (New England BioLabs). Quantitative PCR (qPCR) was performed with LUNA Universal qPCR Master Mix (New England BioLabs). The cycling condition was 95°C for 1 min and then 40 cycles of 95°C for 15 s followed by 60°C for 45 s. The relative expression of target genes was calculated using glyceraldehyde 3-phosphate dehydrogenase (GAPDH) as a reference gene.

4.4.5 Cell membrane derivation

Membranes of THP-1 cells and PAS-expressing THP-1 cells were derived based on a previously reported protocol [12]. Briefly, frozen cell stocks were thawed and washed with 1X PBS (three times, each time 800 ×g for 5 mins). Cells were then suspended in hypotonic lysing buffer containing 30 mM Tris-HCl (pH 7.5), 225 mM D-mannitol, 75 mM sucrose, 0.2 mM EGTA (all from Millipore-Sigma), and a protease and phosphatase inhibitor cocktail (Thermo Fisher Scientific). Next, cells were disrupted by using a Dounce homogenizer with a tight-fitting pestle (20 passes). The homogenized solution was centrifuged at 10,000 ×g for 25 min at 4°C. The pellet was discarded, and the supernatant was centrifuged again at 150,000 ×g for 35 min at 4°C. Following the centrifugation, membranes were washed once by resuspending in a 37 mL solution of 0.2mM ethylenediaminetetraacetic acid (EDTA, Millipore-Sigma) and centrifuging at 150,000 ×g for 35 min at 4°C. The final membrane stocks were resuspended in 1 mL of 0.2 mM EDTA. The membrane protein concentration was measured using a BCA kit (Pierce Thermo Scientific). The membrane suspension was stored at -80°C for subsequent uses.

4.4.6 Preparation of cell membrane-coated nanoparticles

Nanoparticles coated with THP-1 and PAS-expressing THP-1 membranes (denoted "WT-MΦ-NPs" and "PAS-MΦ-NPs", respectively) were prepared following a previously reported procedure.[12] In brief, 1 mL of poly(dl-lactic-co-glycolic acid) (PLGA, 50:50, 0.67 dl/g, Lactel Absorbable Polymers) in acetone (20 mg/mL) was added dropwise into 4 mL water. The mixture was vacuumed under an aspirator for 2 h to evaporate the acetone completely. For fluorescence imaging or flow cytometry experiments, 3,3-Dioctadecyloxacarbocyanine perchlorate (DiO, excitation/emission = 484/501 nm, Thermo Fisher Scientific) or 1,1'-Dioctadecyl-3,3,3',3'-Tetramethylindotricarbocyanine Iodide (DiR, excitation/emission = 748/780 nm, Thermo Fisher Scientific) was added to the PLGA solution before the mixture was added into the water. Encapsulated DiO or DiR showed negligible release within 48 h. Both dyes have been widely used to trace PLGA-based nanoparticles including cell membrane-coated PLGA nanoparticles for in vivo applications [3, 40, 41]. The dye concentration was 0.1 wt% of PLGA polymer. For cell membrane coating, WT-MΦ membrane or PAS-MΦ membrane was mixed with PLGA cores at a polymer-to-membrane protein weight ratio of 1:1. The mixture was then sonicated with a bath sonicator (Fisher Scientific FS30D) for 3 min.

4.4.7 Nanoparticle physicochemical characterization

The size and surface zeta potential of WT-MΦ-NPs and PAS-MΦ-NPs were measured with dynamic light scattering (DLS, Malvern Zetasizer Nano ZS). For nanoparticle morphology, the nanoparticle samples were adsorbed onto carbon-coated copper grids (400-mesh, Electron Microscopy Sciences) and stained with 0.2 wt% uranyl acetate (Electron Microscopy Sciences). The grids were imaged on a JEOL 1200 EX II transmission electron microscope. For stability study, the nanoparticle samples were stored in both 1X PBS and 10% sucrose at 4°C, and the sizes of the nanoparticles were measured daily with DLS for 72 h.

4.4.8 *In vitro* protein adsorption study

For *in vitro* protein adsorption assay, bovine serum albumin (BSA, Pierce Thermo Scientific) was first conjugated with Alexa Fluor 647 NHS (Thermo Fisher Scientific). Briefly, Alexa Fluor 647 NHS (excitation/emission = 650/671 nm, 1 mg/mL in dimethyl sulfoxide) was mixed with BSA (1 mg/mL in 1X PBS) at a molar ratio of 1:5 and incubated at 4°C overnight. The BSA with Alexa Fluor 647 conjugation was purified using Amicon Ultra-4 Centrifugal Filter Units (Millipore Sigma, molecular weight cut-off 100 kDa). The obtained BSA-Alexa 647 (50 μg, 1 mg/mL) was added to 0.5 mL and 2 mg/mL of WT-MΦ-NPs, PAS-MΦ-NPs, or uncoated PLGA cores. The mixture was incubated at 37°C for 1 h. After incubation, the nanoparticles were spun down by centrifugation (25,000 ×g for 15 min). The supernatant with the remaining BSA-Alexa 647 was removed. The nanoparticles were resuspended in 100 μL of ultra-pure water. The fluorescent signal from the nanoparticle samples was quantified with a Tecan Infinite M200 plate reader. All studies were carried out in triplicate.

4.4.9 *In vitro* MΦ uptake study

Mouse J774 MΦ cell line was purchased from ATCC and maintained in DMEM medium supplemented with 10% fetal bovine serum (FBS) and 1% penicillin-streptomycin (all from Thermo Fisher Scientific). The cells were maintained at 37°C with 5% CO_2 in a humidity-controlled incubator. For the nanoparticle uptake study, J774 MΦ cells were seeded at a density of 2×10^5 cells/well in 4-well Millicell EZ Slides (Millipore Sigma) and incubated for 24 h before the experiment. After the incubation, DiO-labeled WT-MΦ-NPs or PAS-MΦ-NPs were added to each well with a final nanoparticle concentration of 100 μg/mL, and the plate was incubated for 1 h. The cells were then washed with 1X PBS twice and imaged using a confocal microscope (Leica SP8).

For quantitative MΦ uptake evaluation, J774 MΦ cells were seeded at a density of 3×10^6 cells/well in a 6-well plate. DiR-labeled WT-MΦ-NPs or PAS-MΦ-NPs were added to the J774 MΦ cells with a final concentration of 150 μg/mL, and the cells were incubated for 5, 15, 30, and 60 min. At each time point, the cells were washed with 1X PBS twice and detached by scraping. The cells were resuspended in 100 μL 1X PBS and measured with flow cytometry (BD FACS Aria II Cell Sorter) for fluorescence intensity.

4.4.10 Animal care

Mice were housed in an animal facility at the University of California San Diego (UCSD), under federal, state, local, and National Institutes of Health (NIH) guidelines. Six-week-old ICR male mice were purchased from Envigo. Mice were maintained under standard housings with 12 h light/12 h dark cycle, ambient temperature, and normal humidity. All animal experiments were performed in accordance with NIH guidelines and were approved by the Institutional Animal Care and Use Committee (IACUC) of UCSD.

4.4.11 *In vivo* alveolar MΦ uptake study

For the *in vivo* alveolar MΦ uptake study, 50 μL of DiO-labeled WT-MΦ-NPs or PAS-MΦ-NPs at the concentration of 4 mg/mL were administrated intratracheally into 6-weeks-old ICR mice (n = 15, Envigo). Mice administered intratracheally with 50 μL 1X PBS were used as controls. At 0, 1, 2, 4, and 24 h, three mice from each group were euthanized, and bronchoalveolar lavage (BAL) was performed using 4 mL of 1X PBS containing 2mM EDTA and 0.5 wt% FBS. The cells were collected by centrifugation of the BAL fluid at 300 ×g for 10 mins. The resuspended cells were blocked with 1% BSA in 1X PBS for 15 min and then stained with DAPI, Pacific Blue-labeled anti-CD11c, and phycoerythrin (PE)-labeled anti-Siglec F (Biolegend) for 30 mins. Cells

were washed with 1X PBS containing 1% BSA. Alveolar MΦ cells were evaluated with a confocal microscope and flow cytometry for DiO-positive cells.

4.4.12 *In vivo* pharmacokinetic and biodistribution studies

To characterize the systemic pharmacokinetic profiles of WT-MΦ-NPs and PAS-MΦ-NPs, we administered DiR-labeled nanoparticles (40 mg/kg) to 6-weeks-old ICR mice (n = 3, Envigo) through intravenous injection. Mice injected with 100 μL 1X PBS were served as controls. At 1, 15, 30 min, and 1, 2, 4, 8, 24, and 48 h post-injection, whole blood was collected from each mouse via submandibular puncture. Serum was separated from the whole blood by centrifugation at 800 ×g for 15 min, followed by fluorescence measurements. For the biodistribution study, DiR-labeled WT-MΦ-NPs and PAS-MΦ-NPs were injected into 6-weeks-old ICR mice intravenously at a concentration of 40 mg/kg. At 0.5, 1, and 24 h post-injection, organs including the heart (tissue), liver, spleen, lung, kidney, and blood were collected from 3 randomly selected mice from each group. The collected organs were weighed and homogenized in PBS for fluorescence measurements. All fluorescent signals were quantified using a Tecan Infinite M200 plate reader.

4.4.13 *In vivo* LPS neutralization in the lungs

The therapeutic efficacy of WT-MΦ-NPs and PAS-MΦ-NPs were evaluated in an LPS-induced lung inflammation mouse model. In this study, mice were divided into 3 groups (n=6) and were anesthetized with a ketamine/xylazine cocktail containing 100 mg/kg ketamine (MWI Veterinary Supply) and 10 mg/kg xylazine (MWI Veterinary Supply). The mice were then intratracheally administrated with 30 μl of PBS, WT-MΦ-NPs, or PAS-MΦ-NPs at a dosage of 10 mg/kg. One hour after the pre-treatment, all mice were challenged with 30 μl of LPS at 400 μg/kg intratracheally. Mice treated with PBS only were used as healthy controls. Mice were sacrificed 6

h after the LPS challenge, and their lungs were extracted and homogenized. The inflammatory cytokine levels, including IL-6, TNF-α, and IL-12p40 were measured using ELISA assays according to the manufacturer's protocol (Biolegend).

4.4.14 Systemic LPS neutralization in a sublethal endotoxemia model

The systemic neutralziation capabilities of WT-MΦ-NPs and PAS-MΦ-NPs against LPS were evaluated in a sublethal endotoxemia mouse model by measuring the production of proinflammatory cytokines. In brief, 6-week-old BALB/c mice (Charles River) were divided into 3 groups (n=6), and were injected with PBS, WT-MΦ-NPs, or PAS-MΦ-NPs at a dosage of 80 mg/kg intravenously through the tail vein. Thirty minutes after the pre-treatment, the mice were challenged with 5 μg/kg LPS through intravenous injection. Mice injected with PBS were used as controls. After injection, blood samples were collected from the mice at predetermined time points through the submandibular puncture. The blood samples were allowed to clot at room temperature for 30 min, and the serum was collected through centrifugation. Serum IL-6, TNF-α, and IFN-γ levels were quantified using ELISA assays according to the manufacturer's protocol (Biolegend).

4.4.15 *In vivo* biosafety studies

For *in vivo* biosafety studies, 6-week-old ICR mice (n = 3, Envigo) were administered intravenously with WT-MΦ-NPs or PAS-MΦ-NPs at a dosage of 80 mg/kg. Mice injected with 100 μl of 1X PBS were served as controls. Mice were euthanized at 24 h after nanoparticle administration for sample collection. For blood chemistry analysis and blood cell counts, the mouse whole blood was collected into potassium–EDTA collection tubes (Sarstedt). The analysis was performed by the UCSD Animal Care Program Diagnostic Services Laboratory. For the

histological analysis, the major organs were sectioned and stained with H&E (Leica Biosystems), followed by imaging with a Nanozoomer 2.0-HT slide scanning system (Hamamatsu).

4.5 References

[1] R.H. Fang, A.V. Kroll, W. Gao, L. Zhang, Cell Membrane Coating Nanotechnology, Adv. Mater. 30(23) (2018) 1706759.

[2] S.Y. Wang, D. Wang, Y.O. Duan, Z.D. Zhou, W. Gao, L. Zhang, Cellular Nanosponges for Biological Neutralization, Adv. Mater. 34(13) (2022) 2107719.

[3] C.M.J. Hu, L. Zhang, S. Aryal, C. Cheung, R.H. Fang, L. Zhang, Erythrocyte membrane-camouflaged polymeric nanoparticles as a biomimetic delivery platform, Proc. Natl. Acad. Sci. U.S.A. 108(27) (2011) 10980-10985.

[4] C.M.J. Hu, R.H. Fang, J. Copp, B.T. Luk, L. Zhang, A biomimetic nanosponge that absorbs pore-forming toxins, Nat. Nanotechnol. 8(5) (2013) 336-340.

[5] D. Wang, S.Y. Wang, Z.D. Zhou, D. Bai, Q.Z. Zhang, X.Z. Ai, W. Gao, L. Zhang, White Blood Cell Membrane-Coated Nanoparticles: Recent Development and Medical Applications, Adv. Healthc. Mater. 11(7) (2022) 2101349.

[6] S. Thamphiwatana, P. Angsantikul, T. Escajadillo, Q.Z. Zhang, J. Olson, B.T. Luk, S. Zhang, R.H. Fang, W. Gao, V. Nizet, L. Zhang, Macrophage-like nanoparticles concurrently absorbing endotoxins and proinflammatory cytokines for sepsis management, Proc. Natl. Acad. Sci. U.S.A. 114(43) (2017) 11488-11493.

[7] Z.B. Ou, H. Zhong, L. Zhang, M.H. Deng, W.F. Zhang, J.Y. Wang, H.G. Feng, J.P. Gong, C.M. Miao, Z.J. Yi, Macrophage Membrane-Coated Nanoparticles Alleviate Hepatic Ischemia-Reperfusion Injury Caused by Orthotopic Liver Transplantation by Neutralizing Endotoxin, Int. J. Nanomedicine 15 (2020) 4125-4138.

[8] M.J. Xuan, J.X. Shao, L.R. Dai, Q. He, J.B. Li, Macrophage Cell Membrane Camouflaged Mesoporous Silica Nanocapsules for In Vivo Cancer Therapy, Adv. Healthc. Mater. 4(11) (2015) 1645-1652.

[9] C. Gao, Q.X. Huang, C.H. Liu, C.H.T. Kwong, L.D. Yue, J.B. Wan, S.M.Y. Lee, R.B. Wang, Treatment of atherosclerosis by macrophage-biomimetic nanoparticles via targeted pharmacotherapy and sequestration of proinflammatory cytokines, Nat. Commun. 11(1) (2020) 2622.

[10] J.N. Fu, Y. Li, Y. Zhang, Y.Q. Liang, Y.F. Zheng, Z.Y. Li, S.L. Zhu, C.Y. Li, Z.D. Cui, S.L. Wu, An Engineered Pseudo-Macrophage for Rapid Treatment of Bacteria-Infected Osteomyelitis via Microwave-Excited Anti-Infection and Immunoregulation, Adv. Mater. 33(41) (2021) 2102926.

[11] Q.Z. Zhang, J.L. Zhou, J.R. Zhou, R.H. Fang, W. Gao, L. Zhang, Lure-and-kill macrophage nanoparticles alleviate the severity of experimental acute pancreatitis, Nat. Commun. 12(1) (2021) 4136.

[12] Q.Z. Zhang, A. Honko, J.R. Zhou, H. Gong, S.N. Downs, J.H. Vasquez, R.H. Fang, W. Gao, A. Griffiths, L. Zhang, Cellular Nanosponges Inhibit SARS-CoV-2 Infectivity, Nano Lett. 20(7) (2020) 5570-5574.

[13] X.Z. Ai, D. Wang, A. Honko, Y.O. Duan, I. Gavrish, R.H. Fang, A. Griffiths, W. Gao, L. Zhang, Surface Glycan Modification of Cellular Nanosponges to Promote SARS-CoV-2 Inhibition, J. Am. Chem. Soc. 143(42) (2021) 17615-17621.

[14] M.J. Mitchell, M.M. Billingsley, R.M. Haley, M.E. Wechsler, N.A. Peppas, R. Langer, Engineering precision nanoparticles for drug delivery, Nat. Rev. Drug Discov. 20(2) (2021) 101-124.

[15] J.A. Mills, F.F. Liu, T.R. Jarrett, N.L. Fletcher, K.J. Thurecht, Nanoparticle based medicines: approaches for evading and manipulating the mononuclear phagocyte system and potential for clinical translation, Biomater. Sci. 10(12) (2022) 3029-3053.

[16] L. Rao, L.L. Bu, J.H. Xu, B. Cai, G.T. Yu, X.L. Yu, Z.B. He, Q.Q. Huang, A. Li, S.S. Guo, W.F. Zhang, W. Liu, Z.J. Sun, H. Wang, T.H. Wang, X.Z. Zhao, Red Blood Cell Membrane as a Biomimetic Nanocoating for Prolonged Circulation Time and Reduced Accelerated Blood Clearance, Small 11(46) (2015) 6225-6236.

[17] S. Ahmadpour, S.J. Hosseinimehr, PASylation as a Powerful Technology for Improving the Pharmacokinetic Properties of Biopharmaceuticals, Curr. Drug Deliv. 15(3) (2018) 331-341.

[18] U. Binder, A. Skerra, PASylation (R): A versatile technology to extend drug delivery, Curr. Opin. Colloid Interface Sci. 31 (2017) 10-17.

[19] S. Krishnamurthy, P. Muthukumaran, M.K.G. Jayakumar, D. Lisse, N.D. Masurkar, C. Xu, J.M. Chan, C.L. Drum, Surface protein engineering increases the circulation time of a cell membrane-based nanotherapeutic Nanomedicine 18 (2019) 169-178.

[20] M. Schlapschy, U. Binder, C. Borger, I. Theobald, K. Wachinger, S. Kisling, D. Haller, A. Skerra, PASylation: a biological alternative to PEGylation for extending the plasma half-life of pharmaceutically active proteins, Protein Eng. Des. Sel. 26(8) (2013) 489-501.

[21] C. Gray, C.A. Loynes, M.K.B. Whyte, D.C. Crossman, S.A. Renshaw, T.J.A. Chico, Simultaneous intravital imaging of macrophage and neutrophil behaviour during inflammation using a novel transgenic zebrafish, Thromb. Haemost. 105(5) (2011) 811-819.

[22] J.P. Rasmussen, G.S. Sack, S.M. Martin, A. Sagasti, Vertebrate epidermal cells are broad-specificity phagocytes that clear sensory axon debris, J. Neurosci. 35(2) (2015) 559-570.

[23] R. Paredes, S. Ishibashi, R. Borrill, J. Robert, E. Amaya, Xenopus: An in vivo model for imaging the inflammatory response following injury and bacterial infection, Dev. Biol. 408(2) (2015) 213-228.

[24] Y.C. Fu, L.H. Luo, N.L. Luo, W.T. Garvey, Lipid metabolism mediated by adipocyte lipid binding protein (ALBP/aP2) gene expression in human THP-1 macrophages, Atherosclerosis 188(1) (2006) 102-111.

[25] J. Elegheert, E. Behiels, B. Bishop, S. Scott, R.E. Woolley, S.C. Griffiths, E.F.X. Byrne, V.T. Chang, D.I. Stuart, E.Y. Jones, C. Siebold, A.R. Aricescu, Lentiviral transduction of mammalian cells for fast, scalable and high-level production of soluble and membrane proteins, Nat. Protoc. 13(12) (2018) 2991-3017.

[26] S.E.A. Gratton, P.D. PohhauS, J. Lee, I. Guo, M.J. Cho, J.M. DeSimone, Nanofabricated particles for engineered drug therapies: A preliminary Biodistribution study of PRINT (TM) nanoparticles, J. Control. Release 121(1-2) (2007) 10-18.

[27] M.T. Peracchia, E. Fattal, D. Desmaele, M. Besnard, J.P. Noel, J.M. Gomis, M. Appel, J. d'Angelo, P. Couvreur, Stealth (R) PEGylated polycyanoacrylate nanoparticles for intravenous administration and splenic targeting, J. Control. Release 60(1) (1999) 121-128.

[28] H. Domscheit, M.A. Hegeman, N. Carvalho, P.M. Spieth, Molecular Dynamics of Lipopolysaccharide-Induced Lung Injury in Rodents, Front. Physiol. 11 (2020) 36.

[29] S. Akira, K. Takeda, T. Kaisho, Toll-like receptors: critical proteins linking innate and acquired immunity, Nat. Immunol. 2(8) (2001) 675-680.

[30] R. Medzhitov, Toll-like receptors and innate immunity, Nat. Rev. Immunol. 1(2) (2001) 135-145.

[31] J. Dagvadorj, K. Shimada, S. Chen, H.D. Jones, G. Tumurkhuu, W.X. Zhang, K.A. Wawrowsky, T.R. Crother, M. Arditi, Lipopolysaccharide Induces Alveolar Macrophage Necrosis via CD14 and the P2X7 Receptor Leading to Interleukin-1 alpha Release, Immunity 42(4) (2015) 640-653.

[32] H. Domscheit, M.A. Hegeman, N. Carvalho, P.M. Spieth, Molecular Dynamics of Lipopolysaccharide-Induced Lung Injury in Rodents, Front. Physiol. 11 (2020).

[33] M. Holay, J.R. Zhou, J.H. Park, I. Landa, C.J. Ventura, W. Gao, R.H. Fang, L. Zhang, Organotropic Targeting of Biomimetic Nanoparticles to Treat Lung Disease, Bioconjug. Chem. 33(4) (2022) 586-593.

[34] A. Pagenstecher, A.K. Stalder, C.L. Kincaid, B. Volk, I.L. Campbell, Regulation of matrix metalloproteinases and their inhibitor genes in lipopolysaccharide-induced endotoxemia in mice, Am. J. Clin. Pathol. 157(1) (2000) 197-210.

[35] D. Dehaini, X.L. Wei, R.H. Fang, S. Masson, P. Angsantikul, B.T. Luk, Y. Zhang, M. Ying, Y. Jiang, A.V. Kroll, W.W. Gao, L.F. Zhang, Erythrocyte-platelet hybrid membrane coating for enhanced nanoparticle functionalization, Adv. Mater. 29(16) (2017) 1606209.

[36] A.N. Shirazi, R.K. Tiwari, D. Oh, A. Banerjee, A. Yadav, K. Parang, Efficient Delivery of Cell Impermeable Phosphopeptides by a Cyclic Peptide Amphiphile Containing Tryptophan and Arginine, Mol. Pharm. 10(5) (2013) 2008-2020.

[37] F. Qiu, Y.Z. Chen, C.K. Tang, X.J. Zhao, Amphiphilic peptides as novel nanomaterials: design, self-assembly and application, Int. J. Nanomedicine 13 (2018) 5003-5022.

[38] E. Ben-Akiva, R.A. Meyer, H.Z. Yu, J.T. Smith, D.M. Pardoll, J.J. Green, Biomimetic anisotropic polymeric nanoparticles coated with red blood cell membranes for enhanced circulation and toxin removal, Sci. Adv. 6(16) (2020) eaay9035.

[39] J.M. Guo, J.O. Agola, R. Serda, S. Franco, Q. Lei, L. Wang, J. Minster, J.G. Croissant, K.S. Butler, W. Zhu, C.J. Brinker, Biomimetic rebuilding of multifunctional red blood cells: modular design using functional components, ACS Nano 14(7) (2020) 7847-7859.

[40] Z.B. Lin, L. Xi, S.K. Chen, J.S. Tao, Y. Wang, X. Chen, P. Li, Z.P. Wang, Y. Zheng, Uptake and trafficking of different sized PLGA nanoparticles by dendritic cells in imiquimod-induced psoriasis-like mice model, Acta Pharm. Sin. B 11(4) (2021) 1047-1055.

[41] D. Wang, X.Z. Ai, Y. Duan, N.F. Xian, R.H. Fang, W.W. Gao, L.F. Zhang, Neuronal Cellular Nanosponges for Effective Detoxification of Neurotoxins, ACS Nano 16(11) (2022) 19145-19154.

Chapter 4, in full, is a reprint of the material as it appears in *Small*, 2023 by Yaou Duan, Jiarong Zhou, Zhidong Zhou, Edward Zhang, Yiyan Yu, Nishta Krishnan, Daniela Ailva-Ayala, Ronnie H. Fang, Anthony Griffiths, Weiwei Gao, and Liangfang Zhang. The dissertation author was the primary investigator and author of this paper.

Chapter 5

Conclusion

5.1 Multimodal enzyme delivery and therapy enabled by cell membrane-coated metal organic framework nanoparticles.

This chapter covered the design, synthesis, and characterization of a cell membrane-camouflaged metal organic framework (MOF) system with enhanced biocompatibility and functionality for potential gout treatment. The MOF core can efficiently encapsulate enzymes while maintaining their bioactivity. After the introduction of natural cell membrane coatings, the resulting nanoformulations can be safely administered in vivo. With the additional inflammatory cytokine neutralization ability provided by the macrophage membrane, this nanoformulation synergizes with the encapsulated enzyme to target disease pathology from multiple dimensions. Employing uricase as a model enzyme, we demonstrate the therapeutic efficacy of this approach in both murine hyperuricemia and gout models, showing significant reduction of serum uric level and amelioration of local joint inflammation. The results support the use of cell membrane-coated MOFs for enzyme delivery, and this treatment strategy could be easily applied across a wide range of enzyme payloads and different membrane coatings to improve the therapeutic efficacy of enzyme-based therapies in other areas of unmet clinical needs. Overall further development along these lines holds great promise for transforming the clinical landscape of current enzyme therapies.

5.2 Macrophage membrane coated nanosponges for the treatment of gastrointestinal diseases.

This chapter presented a unique oral formulation of macrophage cell membrane-coated nanoparticles for the treatment of inflammatory bowel diseases (IBD). IBD is a chronic gastrointestinal tract disorder characterized by uncontrolled inflammatory responses to the disrupted intestinal epithelial barrier and gut microbiome dysbiosis. Currently available small-molecule immunosuppressive agents and anti-cytokine biologics show limited potency, mainly due to the complexity of the inflammatory network involved in IBD. Here, we reported an oral formulation of macrophage membrane-coated nanoparticles encapsulated in enteric polymer-coated gelatin capsules (denoted 'cp-MΦ-NPs') for IBD treatment. The capsules protect the nanoparticles from gastric degradation and allow targeted delivery to the colon. At the inflamed colon, cp-MΦ-NPs act as macrophage decoys that bind and neutralize pro-inflammatory cytokines. The in vivo treatment efficacy of cp-MΦ-NPs is tested in a mouse model of dextran sulfate sodium-induced colitis. In both prophylactic and delayed treatment regimens, oral delivery of cp-MΦ-NPs significantly alleviates IBD severity, reflected by reduced intestinal inflammation and intestinal barrier restoration. Overall, cp-MΦ-NPs provide a biomimetic nanomedicine strategy for the treatment of IBD.

Encouraged by the promising results of cp-MΦ-NPs in treating IBD, we further investigated the combination of cell membrane-coating technology with micromotors to improve its pharmacokinetic profile. Here, we reported on two efficient algae-based motor platforms, pH-sensitive encapsulated algae and acidophilic algae, which take advantage of the fast and long-lasting swimming behavior of natural microalgae in intestinal fluid to prolong local retention within the GI tract. The cell membrane-coated nanoparticles are functionalized on either

acidophilic algae or algae motors that are embedded inside a pH-sensitive capsule, without compromising the algae motors' self-propelling ability for enhanced gastrointestinal delivery. In vitro, the algae motors displayed a constant motion behavior in simulated intestinal fluid after 12 hours of continuous operation. When orally administered in vivo into mice, the algae substantially improved distribution and retention of cell membrane-coated nanoparticles in the GI tract compared to traditional magnesium-based micromotors, which are limited by short propulsion lifetimes. Overall, adapting efficient motion and extended lifetime of natural algae-based motors results in a promising micromotor platform capable of achieving greatly improved nanoparticle delivery in gastrointestinal tissue for practical biomedical applications.

5.3 Extending the *in vivo* residence time of macrophage membrane-coated nanoparticles through genetic modification.

This chapter reported the development and engineering of macrophage cell membrane-coated nanoparticles for enhancement of bacterial toxins neutralization. As exhibited in numerous studies before, nanoparticles coated with natural cell membranes have emerged as a promising class of biomimetic nanomedicine with significant clinical potential. Particularly, macrophage membrane-coated nanoparticles hold promising clinical values due to their versatility in drug delivery and biological neutralization applications. In this chapter, we showed a genetic engineering approach to enhance their in vivo residence times, aiming to further improve their performance. Specifically, we engineered macrophages to PAS peptide chains, which provide additional protection against opsonization and phagocytosis. The resulting modified nanoparticles demonstrated prolonged residence times when administered intravenously or introduced intratracheally, surpassing those coated with the wild-type membrane. The longer residence times also contributed to enhanced nanoparticle efficacy in inhibiting inflammatory cytokines in mouse models of lipopolysaccharide-induced lung injury and sublethal endotoxemia, respectively. Our study underscores the effectiveness of genetic modification in extending the in vivo residence times of macrophage membrane-coated nanoparticles. This approach can be readily extended to modify other cell membrane-coated nanoparticles towards more favorable biomedical applications.